TECHNISCHE UNIVERSITÄT MÜNCHEN

Professur für Hybride Elektronische Systeme

Replacing Beryllium: Novel Graphenic Carbon X-ray Transmission Windows

Sebastian Hübner

Vollständiger Abdruck der von der Fakultät für Elektrotechnik und Informationstechnik der Technischen Universität München zur Erlangung des akademischen Grades eines

Doktor-Ingenieurs

genehmigten Dissertation.

Vorsitzender: Prof. Dr.-Ing. Erwin Biebl

Prüfer der Dissertation:

1. Prof. Dr.rer.nat. Franz Kreupl
2. Prof. Dr.-Ing. Thomas Mikolajick

Die Dissertation wurde am 18.04.2016 bei der Technischen Universität München eingereicht und durch die Fakultät für Elektrotechnik und Informationstechnik am 10.10.2016 angenommen.

Abstract

Energy dispersive x-ray spectroscopy (EDS) for element detection has profited from the significant improvements of the employed silicon x-ray detector technology. Today, EDS systems can easily be integrated into handheld devices, enabling mobile systems for element detection. In contrary to the detector technology, little improvement has occurred for the used x-ray transmission windows and toxic beryllium windows are still the most common choice in the field. The tight specifications that arise from the application requirements have left beryllium windows unchallenged as the proposed alternative window materials deteriorate the system performance.

In this work, a novel x-ray transmission window based on graphenic carbon (GC) was developed with superior performance compared to beryllium transmission windows. The novel x-ray transmission window exhibits an improved x-ray transmission for energies below 2 keV, while demonstrating excellent mechanical stability, as well as light and vacuum tightness. It was demonstrated that the available energy range of GC x-ray transmission windows can be extended to the energies below 1.5 keV by reducing the GC thickness and integrating a silicon support structure which results in a window configuration that fulfills the mechanical stability requirements. The presented GC low energy x-ray transmission window offers a superior x-ray transmission and optical light blocking levels compared to those of a commercial polymer low energy x-ray transmission window.

The GC material, deposited by a developed chemical vapor deposition process exhibits a highly laminar micro-structure and high mechanical strength. A bulge testing scheme was developed and combined with Raman spectroscopy measurements and finite element simulations to identify a Young's modulus of up to 170 GPa and a compressive stress of approximately 400 MPa. The GC material offers a high electrical conductivity with a bulk resistivity of 1 mΩ cm and a density of 2.2 g/cm^3. The identified material properties make the GC material attractive for a number of applications aside from x-ray transmission windows including microphones, loud speakers and other micro-electro-mechanical systems (MEMS) and is now available for evaluation.

The GC deposition and fabrication process was scaled up from the developed single window processing to wafer scale processing using substrates with a diameter of 150 mm, a requirement for the industrial fabrication of the windows in the future. The newly established GC material can therefore finally replace beryllium in x-ray transmission windows with a non-toxic and abundant material.

Table of Contents

1 Introduction **1**

1.1 Energy Dispersive X-ray Spectroscopy 2
1.1.1 Characteristic X-ray Radiation 2
1.1.2 Measurement Scheme 5
1.2 Semiconductor X-ray Detectors 7
1.3 The Silicon Drift Detector Module 12
1.4 X-ray Transmission Windows 13
1.4.1 Window Requirements 15
1.4.2 State of the Art 16
1.4.2.1 Beryllium Windows 18
1.4.2.2 Low Energy X-ray Transmission Windows 20
1.5 Graphenic Carbon: An Alternative to Beryllium 22
1.5.1 Graphene: The Ideal Window Material? 23
1.5.2 Proposal: Direct Graphenic Carbon Deposition onto Silicon Substrates 26
1.5.3 Graphenic Carbon as a Window Material 27
1.6 Objective of the Thesis 28

2 Methods **29**

2.1 Evaluation Schemes for X-ray Transmission Windows 29
2.1.1 X-ray Transmission 29
2.1.2 Mechanical Stability 31
2.1.3 Helium Leak Tightness 37
2.1.4 Light Tightness 38
2.1.5 Stability Against Ozone Exposure and X-ray Irradiation . 39
2.2 Evaluation Schemes for the Graphenic Carbon Window Material . 40
2.2.1 Surface Morphology 40
2.2.2 Raman Spectroscopy of the Graphenic Carbon Window Material 43
2.2.3 Thickness Measurements 46
2.2.4 Mechanical Characterization 53
2.2.4.1 Bulge Testing 54
2.2.4.2 Stress Measurements using Raman Spectroscopy 61
2.2.4.3 Wafer Curvature Measurements 63

2.2.5 Electrical Conductivity 64
2.3 Finite Element Simulations 65

3 Graphenic Carbon Deposition 67
3.1 Chemical Vapor Deposition of Graphenic Carbon: Theoretical Considerations 67
3.2 Deposition Process for Single X-ray Window Fabrication 72
3.2.1 Substrate Preparation 73
3.2.2 Deposition Process Scheme 74
3.2.3 Process Parameters 75
3.2.4 Process Development 75
3.3 Wafer Scale Deposition of the GC Window Material 84
3.3.1 Substrate Preparation 85
3.3.2 Deposition Process Scheme 85
3.3.3 Process Parameters and Process Development 86

4 Window Fabrication 93
4.1 Window Design 93
4.1.1 Window Design for an Open Window Geometry 93
4.1.2 Low Energy X-ray Transmission Window Design 94
4.2 Fabrication Scheme 97
4.2.1 Graphenic Carbon Structuring 100
4.2.2 Silicon Micromachining 103
4.3 Thickness Limitations of the Fabrication Scheme 111
4.3.1 The Implications of Compressive Stress During the Substrate Removal 113
4.3.2 Proposed Solution: Two Step Growth Process 120

5 Evaluation of Graphenic Carbon as a Window Material 125
5.1 Performance of Graphenic Carbon X-ray Transmission Windows . 125
5.1.1 X-ray Transmission 125
5.1.2 Helium Leak Tightness 127
5.1.3 Mechanical Stability 127
5.1.3.1 Burst Pressure 127
5.1.3.2 Cycle Stability 129
5.1.4 Light Tightness 130
5.1.5 Resistance Against X-ray Exposure and Ozone 132
5.1.6 Electrical Conductivity 133
5.2 Mechanical Characterization of the Graphenic Carbon Material . 133
5.2.1 Bulge Testing 133
5.2.1.1 Simulation of the Mechanical Behavior 136
5.2.2 Raman Spectroscopy: Stress Measurements 139

5.3 Performance of Graphenic Carbon Low Energy X-ray Transmission Windows . . . 142
5.3.1 X-ray Transmission . . . 143
5.3.2 Cycle Stability and Helium Leak Tightness . . . 144
5.3.3 Light Tightness . . . 145
5.3.4 Electrical Conductivity . . . 146
5.4 Wafer Scale Fabrication of Graphenic Carbon X-ray Transmission Windows . . . 146
5.4.1 Mechanical Stability: Burst Pressure . . . 146
5.4.2 Two Step Growth Method . . . 147
5.4.3 Mechanical Stability: Cycle Stability . . . 149
5.4.4 X-ray Transmission . . . 150
5.4.5 Electrical Conductivity . . . 151

6 Discussion **153**
6.1 Graphenic Carbon as a Material for X-ray Transmission Windows: Replacing Beryllium . . . 153
6.2 Comparison of the Developed Deposition Processes . . . 156
6.3 Graphenic Carbon as a Window Material for Low Energy X-ray Transmission Windows . . . 158
6.4 Material Properties of the Graphenic Carbon Material . . . 160

7 Summary and Outlook **163**

Acronyms **169**

List of Symbols **171**

Publications of the Author **173**

References **175**

Acknowledgement **198**

List of Figures

1.1 Schematic Generation Process of Characteristic X-ray Emission . 3
1.2 Atomic Shell Model and Electron Transitions of the Element Manganese . . . 4
1.3 Transition Energies of the Element Manganese and Fluorescence Yield Dependency on the Atomic Number . . . 4
1.4 K-Series Transition Energies for the Elements with an Atomic Number Between 2 and 34 . . . 5
1.5 Typical EDS Spectrum of a Calibration Sample . . . 6
1.6 Schematic Cross Section of a Silicon Drift Detector . . . 10
1.7 X-ray Intensity Decay in Silicon and Germanium . . . 11
1.8 Image and Schematic of a Silicon Drift Detector Module . . . 12
1.9 Silicon Drift Detector Module and the Effect of X-ray Transmission Windows . . . 14
1.10 Energy Dependent X-ray Transmission of Beryllium Windows . . 18
1.11 Energy Dependent X-ray Transmission and Optical Transmission of Low Energy X-ray Transmission Windows . . . 20
1.12 X-ray Image of Chronic Berylliosis . . . 22
1.13 The Atomic Structure of Graphene and Graphene Related Yearly Patent Numbers . . . 23

2.1 Detector Setup for X-ray Transmission Measurements . . . 30
2.2 Schematic of an X-ray Window Under a Pressure Load . . . 32
2.3 Schematic of the Employed Vacuum Test Equipment . . . 33
2.4 Schematic of the Employed Burst and Cyclic Loading Test Equipment 34
2.5 Pressure Values During Cyclic Fatigue Testing . . . 37
2.6 Schematic of the Employed Helium Leak Test Equipment . . . 38
2.7 Exemplary Surface Roughness Measurements . . . 42
2.8 Raman Spectroscopy: Measurement Schematic and the Typical Spectrum of Graphenic Carbon . . . 44
2.9 Schematic of the Step Fabrication Scheme for Thickness Measurements . . . 47
2.10 Step Height Measurements Employing Atomic Force Microscopy . 48
2.11 Schematic of White Light Interferometer and Thickness Measurement Setup . . . 49

2.12 Differential Thickness Measurement with WLI Sensor 51
2.13 2D WLI Measurements 52
2.14 Exemplary Bulge Test with a Silicon Nitride Membrane 57
2.15 Raman Measurements of a Pressure Loaded Graphenic Carbon Thin Film 62
2.16 Wafer Bow Measurement Scheme 63
2.17 Schematic of the 4-Point Probe Resistivity Measurement Setup . . 64

3.1 Diagram of Carbon Material Terminology and Micro-Structure . . 68
3.2 The Atomic Structure of the Carbon Precursors, the Gas Phase Evolution of Methane and Carbon Deposition Scheme 70
3.3 Schematic of the used Experimental CVD Equipment 73
3.4 SEM Image of Soot Particle Formation 77
3.5 Raman Spectra of Sooting and Non-Sooting Graphenic Carbon Material 78
3.6 SEM Cross Section Image of Graphenic Carbon Material 79
3.7 Graphenic Carbon Surface Morphology and Surface Roughness . . 80
3.8 Growth Rate of Graphenic Carbon Material 81
3.9 Raman Spectra of Graphenic Carbon Material Deposited with Different Deposition Parameters 82
3.10 Schematic of the used RTCVD Equipment 85
3.11 Optical Image of Graphenic Carbon Wafer Scale Deposition with a Sooting and non-Sooting Process 86
3.12 Raman Spectrum and AFM Surface Scan of Graphenic Carbon Material Deposited by the Wafer Scale Deposition System 87
3.13 Cross Section View of Graphenic Carbon Material Deposited by the Wafer Scale Deposition System 88
3.14 Slip-Line Dislocations and Silicon Edge Ring 89
3.15 RTP Heating Zones and Resulting Temperature Distribution . . . 90
3.16 Graphenic Carbon Thickness Homogeneity for Wafer Scale Deposition 91

4.1 Beryllium Window Reference Design 94
4.2 Low Energy X-ray Transmission Window Designs: Circular and Hexagonal Cells 96
4.3 Low Energy X-ray Transmission Window Designs: Bar Supported 96
4.4 Fabrication Process of Graphenic Carbon X-ray Transmission Windows: Open Window Geometry 97
4.5 Fabrication Process of Graphenic Carbon Low Energy X-ray Transmission Windows 99
4.6 Graphenic Carbon Structuring Process 101
4.7 Structured Graphenic Carbon Material 103
4.8 Anisotropic Wet Etching of Silicon 104

4.9 Silicon Etch Rates in KOH and KOH + IPA 105
4.10 Concentration Dependent Silicon Etch Quality 107
4.11 Window Fabrication with an Open Window Geometry 107
4.12 Window Fabrication with a Bar Supported Geometry 108
4.13 Window Fabrication from Pre-Structured Silicon Substrates . . . 110
4.14 Graphenic Carbon Low Energy X-ray Transmission Windows from Pre-Structured Silicon Substrates 111
4.15 Defect Graphenic Carbon X-ray Transmission Windows 112
4.16 2D Surface Profiles During Wet Etching 115
4.17 Photograph of a Graphenic Carbon Window During Wet Etching 115
4.18 Surface Deformation During Wet Etching 116
4.19 FEM Simulations of the Window Release 118
4.20 Wafer Bow Measurements for Different Graphenic Carbon Thicknesses 120
4.21 Demonstrated Window Regrowth 121
4.22 Graphenic Carbon X-ray Transmission Windows 123

5.1 X-ray Transmission of Graphenic Carbon X-ray Transmission Windows 126
5.2 Helium Leak Rate of Graphenic Carbon X-ray Transmission Windows 126
5.3 Graphenic Carbon X-ray Transmission Window Stability vs. Graphenic Carbon Thickness 128
5.4 Cyclic Stability of Graphenic Carbon X-ray Transmission Windows 130
5.5 Light Tightness of Graphenic Carbon X-ray Transmission Windows 131
5.6 Impact of Ozone and X-ray Exposure 132
5.7 Bulge Testing of Graphenic Carbon X-ray Transmission Windows 134
5.8 Simulation of Mechanical Window Behavior 137
5.9 Raman Spectroscopy of Stressed Graphenic Carbon Material . . . 140
5.10 Graphenic Carbon Low Energy X-ray Transmission Windows . . . 143
5.11 X-ray Transmission of Graphenic Carbon Low Energy X-ray Transmission Windows 144
5.12 Helium and Light Tightness of Graphenic Carbon Low Energy X-ray Transmission Windows 145
5.13 Wafer Scale Deposition and X-ray Transmission Window Fabrication 146
5.14 Mechanical Stability of Graphenic Carbon X-ray Transmission Windows Fabricated on a 150 mm Silicon Substrate 147
5.15 Mechanical Stability of Graphenic Carbon X-ray Transmission Windows Fabricated by the Two-Step Growth Process 148
5.16 Increased Pressure and Cyclic Loading Stability of Graphenic Carbon X-ray Transmission Windows 149
5.17 X-ray Transmission and Electrical Conductivity of the Graphenic Carbon Material 150

6.1 SDD Prototypes with a Graphenic Carbon X-ray Transmission Window, Theoretical Transmission Improvement and EDS Spectrum Acquired Therewith . . . 154
6.2 Comparison of the Mechanical Stability of the Developed Graphenic Carbon Deposition Processes . . . 157
6.3 X-ray Transmission of Graphenic Carbon Low Energy X-ray Transmission Windows Compared To Be Windows and Potential of Further Thickness Reduction . . . 159
6.4 Photograph of an Ultra Thin Graphenic Carbon x-ray Transmission Window . . . 160

List of Tables

1.1 Properties of Beryllium X-ray Transmission Windows 19
1.2 Properties of Polymer and Silicon Nitride Low Energy X-ray Transmission Windows 21

3.1 Employed Deposition Parameters for Small Scale Graphenic Carbon Deposition 84
3.2 Employed Deposition Parameters for Wafer Scale GC Deposition . 91

4.1 Characteristics of Different Low Energy X-ray Transmission Window Designs 95

5.1 Results of the Bulge Testing of Graphenic Carbon Thin Films . . 135

6.1 Comparison of the Properties of Graphenic Carbon and Beryllium X-ray Transmission Window 156
6.2 Summarized Material Properties of the Graphenic Carbon Material 161

1 Introduction

The introduction of silicon drift x-ray detectors (SDD) has transformed bulky, liquid nitrogen cooled x-ray detectors into compact detector modules that are cooled by Peltier elements. While advances in microelectronics and fabrication technologies, such as integrated junction field effect transistor (JFET) fabrication and high purity silicon substrates, have led to a constant improvement of detection efficiency and spectroscopic resolution [1–3], the fact that x-ray detectors can now be incorporated into handheld, stand-alone devices has made a big impact on the availability of systems for element detection [4]. The first handheld x-ray fluorescence (XRF) systems below 10k US-dollars are currently becoming available [5], making x-ray element detection attractive for a wide range of applications, aside from laboratory users. At the same time, improved signal processing algorithms, readout electronics and detector designs are helping to overcome the previous limitations of energy dispersive x-ray spectroscopy (EDS) systems including the low spatial resolution and limited element sensitivity. Burgess et al. [6] have shown that it is possible to achieve sub 10 nm resolution for scanning electron microscopy energy dispersive spectroscopy (SEM-EDS) applications, while Newbury et al. [7] demonstrated an element sensitivity, approaching that of wavelength-dispersive x-ray spectroscopy (WDS) systems, both of which are crucial aspects for high end laboratory applications.

While there have been impressive improvements in the detector technology as well as software algorithms, the available x-ray transmission windows that are a necessary component in most EDS applications, are still being fabricated from thin beryllium (Be) foils. Beryllium is a toxic material raising numerous handling precautions and poses a health risk if the window breaks during operation [8]. In this work, graphenic carbon (GC) is proposed and evaluated as a suitable window material.

The principles of energy dispersive x-ray spectroscopy (EDS), as well as the functionality of the used silicon drift detector (SDD) technology will be introduced in the following in order to set the scene for the upcoming chapters discussing the novel window material. Additional references are given to provide the interested reader with more detailed information on the covered aspects.

1.1 Energy Dispersive X-ray Spectroscopy

Energy dispersive x-ray spectroscopy (EDS) is a widely used method for element detection, offering simple sample preparation and element detection limits of approximately 0.1 wt% [9]. The measurement scheme is based on the fact that the characteristic x-ray emission spectrum of an element is a result of its unique atomic structure, as discussed in detail in reference [10]. By recording and analyzing the characteristic x-ray emission spectrum of a sample of interest, it is therefore possible to identify the individual contributing elements. A detailed, fundamental discussion of energy dispersive x-ray spectroscopy is given in reference [11].

1.1.1 Characteristic X-ray Radiation

Characteristic x-ray radiation is emitted by an element as it is de-excited by radiative relaxation from a highly energetic, ionized state. Ionization is induced either by electron bombardment with an electron beam, as it is typically available in scanning electron (SEM) or transmission electron (TEM) microscopy, denoted as SEM-EDS, by x-ray radiation, denoted as energy dispersive x-ray fluorescence (EDXRF), or other high energy particles, denoted as particle induced x-ray emission (PIXE).

The characteristic x-ray radiation is dependent on the electron configuration of the element. The atomic structure can be described as an atomic nucleus which is surrounded by electrons that are only allowed to occupy defined orbitals. These orbitals are successively filled as the atomic number, and thus the number of electrons, is increased. The energy of the electrons increases as one moves from a lower to a higher orbital, with the innermost orbital offering the lowest energetic state. Commonly, the x-ray level nomenclature is used which treats the orbitals as shells and sub-shells as described in reference [12]. The x-ray generation process for electron impact induced ionization and subsequent x-ray emission is shown schematically in figure 1.1. If the transferred energy of the incoming electron is sufficiently large, a vacancy can be created that is subsequently filled by an electron from a higher shell (fig 1.1 (b)). The energy difference is emitted in form of radiation, or as an Auger electron, with the corresponding energy. The shell transition energies are unique and responsible for the characteristic x-ray emission spectrum of an element.

A more detailed schematic of the atomic model is shown in figure 1.2 (a). The shells are classified as K, L and M and are further divided into sub-shells that exhibit different energetic levels within the same shell. The K shell can occupy a maximum of 2 electrons, the L shell a maximum of 8 electrons and the M shell a maximum of 18 electrons [15]. Heavier elements lead to the formation of addi-

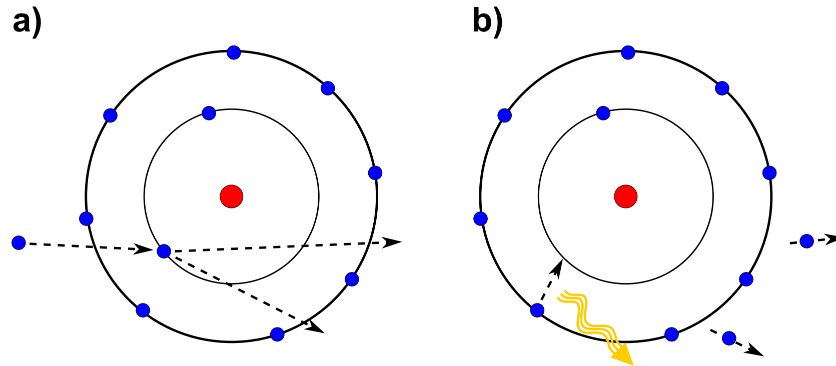

Figure 1.1: The generation process of the characteristic x-ray radiation of Ne is schematically shown for the case of electron excitation using the atomic shell model. A positively charged nucleus (red) is surrounded by electrons (blue) that occupy specific shells. In a) an inner electron is expelled from its position by the impact of an electron with a sufficiently high energy. An x-ray photon is emitted as the created vacancy is filled by the transition of an electron from a higher shell, as shown in b).

tional shells denoted as N, O, P and Q, which are successively filled. The elements hydrogen and helium do not exhibit characteristic x-ray radiation due to the absence of higher shells and can therefore not be detected using energy dispersive spectroscopy. Especially for heavier elements various different shell transitions are encountered. The possible electron transitions for the element manganese (Mn) using the Siegbahn notation are demonstrated in figure 1.2 (b), wherein the first letter denotes the shell with the electron vacancy and the ensuing Greek letter groups the electron transitions according to the transition energy [15]. The energy of the emitted photon, or Auger electron, is the energy difference of the states of the electron before and after the transition. Figure 1.3 (a) shows the transition energies of the corresponding transitions shown in figure 1.2 (b). The K series radiation always exhibits the highest transition energy and the α transition shows the highest intensity in the energy group [13].

The probability of the generation of a photon instead of an Auger electron during the electron transitions is dependent on the shell transition and the atomic number of the element and referred to as fluorescence yield [12]. The emitted radiation intensity is generally the highest for the $K\alpha$ series, if the excitation efficiency is disregarded, and heavier elements also emit significant amounts of L series radiation. The dependency of the fluorescence yield on the atomic number of the element and the transition series are shown in figure 1.3 (b). Higher series such as the M series exhibit an even lower fluorescence yield. Elements with a low atomic number emit only very little radiation as the fluorescence yield is low, making the detection of light elements more difficult.

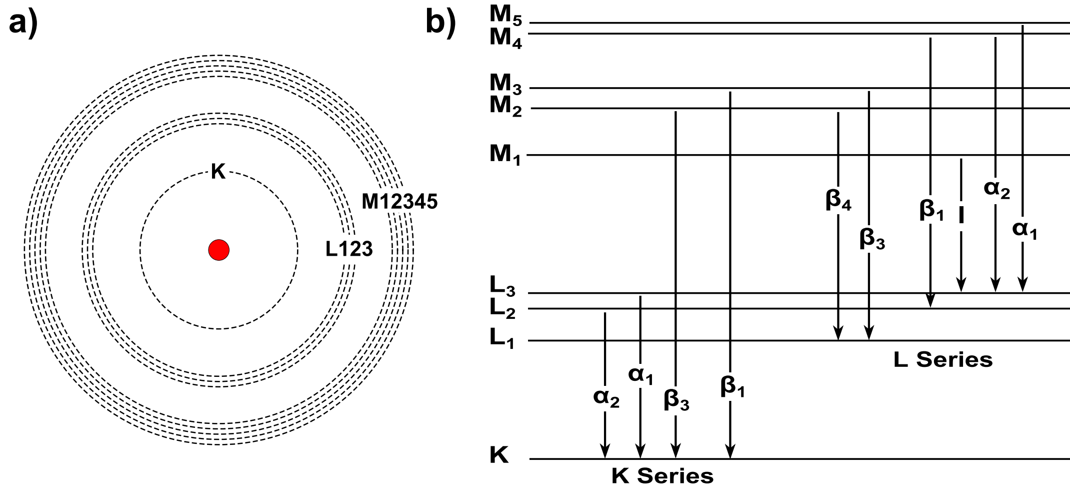

Figure 1.2: A detailed view of the atomic shell model of Mn is shown in a). The shells above the K shell are further divided in sub-shells. The electron transitions that are responsible for the characteristic emission spectrum of Mn using the Siegbahn notation are visualized in b) as discussed in reference [13].

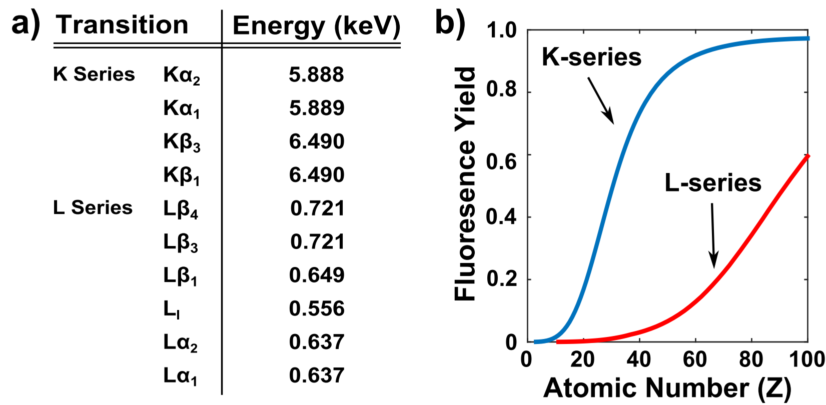

a)

Transition		Energy (keV)
K Series	$K\alpha_2$	5.888
	$K\alpha_1$	5.889
	$K\beta_3$	6.490
	$K\beta_1$	6.490
L Series	$L\beta_4$	0.721
	$L\beta_3$	0.721
	$L\beta_1$	0.649
	L_l	0.556
	$L\alpha_2$	0.637
	$L\alpha_1$	0.637

Figure 1.3: The corresponding energies of the electron transitions for the element Mn using the Siegbahn notation are given in a), and were taken from reference [13]. The dependency of the fluorescence yield on the atomic number of the element and the transition series is shown in b), based on the data found in reference [14]. K-series transitions exhibit a higher fluorescence yield compared to higher series.

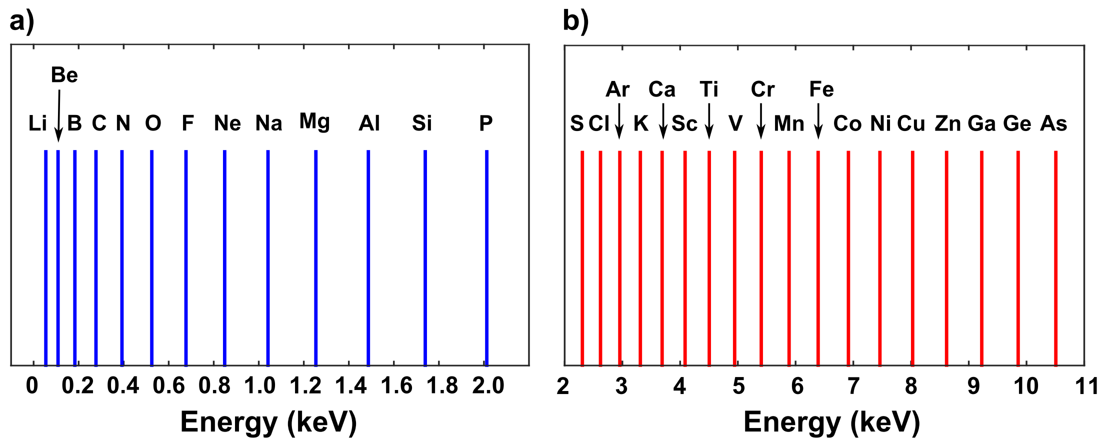

Figure 1.4: The elements for which the $K\alpha$ line energies are found below 2 keV are given in a) while b) shows the elements for which the $K\alpha$ line energies are found between 2 keV and 11 keV, as given in reference [17]. The line spacing increases with the increasing atomic number of the elements.

The specific characteristic energies of the elements have been measured with great accuracy in the past and are widely available, one example being reference [16]. The characteristic $K\alpha$ line energies of the elements for the energy range from 0.1 keV to 2 keV, which is regarded as low energy x-ray radiation, are shown in figure 1.4 a) and figure 1.4 (b) for the energy range from 2 keV to 11 keV. The energy and the energy spacing of the $K\alpha$ line energies increase with the atomic number of the elements, which was first recognized by Henry Moseley in 1913. As a consequence, the energy resolution required to distinguish the individual lines increases for lighter elements.

1.1.2 Measurement Scheme

By bringing the elements of a sample into an excited state and measuring the energy distribution of the emitted x-ray radiation it is therefore possible to determine the element composition of the sample. Ideally, the energy of each photon that reaches the detector is determined and accounted for, forming a histogram of the detected energies as the measurement is performed. The number of detection events for a given energy can therefore be used to quantify the elemental composition of the material, presuming a careful calibration and an in-depth understanding of the underlying physical mechanisms that lead to the x-ray generation are given as discussed in reference [7]. This presumes a sufficiently high energy resolution of the x-ray detection system in order to identify the single transitions that lead to the observed emission spectrum. This is more difficult for elements with a low atomic number due to the smaller energy spacing of the transitions and as the

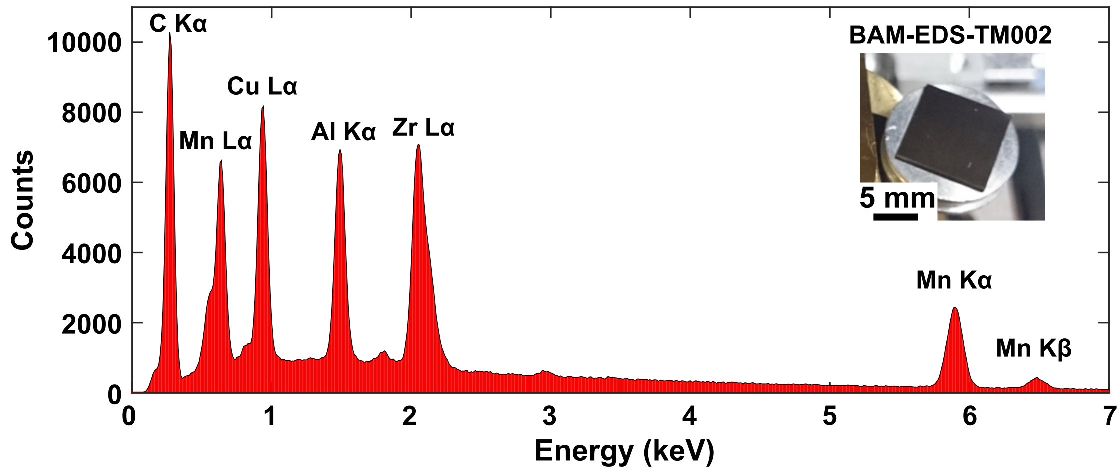

Figure 1.5: The EDS spectrum of a calibration sample (BAM-EDS-TM002, as shown in the inset), as obtained with an SEM-EDS system is shown. An acceleration voltage of 10 kV and an acquisition time of 400 seconds was used. The peaks exhibit a high peak to background ratio and the corresponding shell transitions were identified using reference [16].

transition energies of the L series from heavier elements ($Z > 20$) are also found in this low energy range [13].

A typical EDS spectrum, as it is obtained using an AXAS-D EDS system from Ketek in combination with an SEM, is shown in figure 1.5. A calibration sample (BAM-EDS-TM002 [18]) was excited using an electron beam with an energy of 10 keV and the x-ray emission of the sample recorded with an x-ray detector. A pulse processor interprets the voltage output of the x-ray detector and assigns each individual event, which ideally corresponds to a detected x-ray photon, to the corresponding channel of the spectrum acquisition software. A histogram of the encountered photon energies is subsequently available for interpretation. In the shown case, the sample includes the elements carbon (C), manganese (Mn), copper (Cu), aluminium (Al) and zirconium (Zr) and the corresponding peaks exhibit a high peak to background ratio. This element combination is used to optimize performance testing of EDS systems and in-depth information on the calibration sample can be found in reference [18]. The discussed $Mn\ K\alpha$ and $Mn\ K\beta$, as well as the $Mn\ L\alpha$ transitions are visible.

The line energies broaden due to the limited resolution of the detector as well as due to the noise of the acquisition system. The resulting resolution needs to be sufficiently high to separate the peaks, which would otherwise lead to misinterpretation. Deconvolution of the peaks and peak identification is available in most of the manufacturer supplied software, reducing the required time and background

knowledge of the user. The technique not only allows the identification of the elemental composition but also allows a quantitative analysis of the elements. A detailed discussion regarding the capabilities of SEM-EDS systems is provided in reference [7].

Aside from laboratory use in combination with SEM or TEM, handheld and tabletop EDS systems are available for element detection. These devices commonly rely on x-ray fluorescence instead of an electron beam for excitation. In this case, an x-ray source is used to excite the sample of interest. The energy of the x-ray radiation has to be sufficiently high to excite the elements of interest and the x-ray tubes are commonly operated at acceleration voltages of up to 50 kV. Especially handheld devices are used in ambient environments, which leads to a significant signal loss due to the absorption of x-ray radiation with an energy below 3.5 keV in the air. Systems that provide helium purging are available to reduce the impact of the air as helium offers a lower absorption at these energies [19]. None the less, if light elements such as carbon, boron and oxygen are to be detected, a vacuum is necessary as even helium purging is insufficient and the corresponding characteristic x-ray radiation is lost. Fortunately, heavier elements above 3.5 keV, such as hazardous lead, can easily be detected without helium purging, making handheld EDXRF systems highly attractive for applications including among others: archaeology [19], forensics [20] and environmental monitoring [21].

Handheld and tabletop devices with intelligent analysis algorithms have made EDS and EDXRF a widely used method for material analysis [22]. The introduction of semiconductor x-ray detection systems with a high energy resolution and low footprint were the basis for this development and will be discussed in the following.

1.2 Semiconductor X-ray Detectors

Energy dispersive spectroscopy requires x-ray detection systems with a high energy resolution, high count rates and reliable operation. The first lithium drifted silicon (Si(Li)) semiconductor x-ray detectors were developed in the 1960's but required liquid nitrogen cooling [23]. Current silicon drift x-ray detectors (SDD) provide high energy resolution [24], high count rates [25], and a low foot print due Peltier element cooling.

The underlying scheme of semiconductor x-ray detectors is the conversion of an incoming x-ray photon to a corresponding charge cloud of electron and hole pairs, as it is absorbed in the detector volume. The number of generated electron and hole pairs depends on the photon energy and the characteristic ionization energy

of the used detector material. In silicon, the generation of an electron hole pair corresponds to an average energy of $\omega_E = 3.66\ eV$ at a temperature of 300 K [26]. The fact that this is not a constant value sets a fundamental limit regarding the spectral resolution, which is accounted for by the Fano factor, describing the statistical spread of the amount of generated charge [27]. It has been shown that the product of the Fano factor and the average energy required to generate an electron hole pair in silicon is dependent on the temperature as well as on the energy of the incoming photon [28, 29]. The observed peak broadening in the EDS spectrum is quantified by the full width at half maximum (FWHM). The theoretical FWHM can be calculated following Fraser et al. [30] by equation 1.1. With ω_E denoting the average energy per electron hole pair, F denoting the Fano factor and E the energy of the incoming photon.

$$FWHM = \sqrt{8\, ln(2)} \times \sqrt{\omega_E\, F\, E} \tag{1.1}$$

Assuming a detector temperature of −60 °C and a photon energy of $E = 5.895\ keV$ results in an average energy per electron hole pair in silicon of $\omega_E = 3.70\ eV$ and a Fano factor of $F = 0.118$, as described in reference [28]. Using equation 1.1 results in a FWHM of 119.5 eV, which sets the theoretical limit for the energy resolution of a silicon radiation detector with the described working principle. It should be noted that the FWHM energy resolution of the $K\alpha$ line of Mn (5.895 keV) is often used as a figure of merit to describe the performance of an x-ray detector [31]. The newest generation of silicon drift detectors is approaching the Fano limit reaching a FWHM of 123 eV for the $K\alpha$ line of Mn (5.895 keV) [24], indicating the high maturity of the SDD detector technology [32].

The generated electron hole pairs need to be separated and quantified in order to deduce the energy of the absorbed photon. This can be achieved by applying a potential across the detection volume and the resulting electric field moves the electrons and holes to the electrode with the corresponding polarity. Subsequently, a high impedance transducer can be used to convert the collected electrons at the anode to a voltage output. In order to obtain the correct energy value, it is necessary to collect all of the generated electrons before recombination or trapping can take place. Therefore, silicon substrates with a high carrier lifetime are necessary, which implies high purity silicon with a low density of trapping states [1]. Evidently, any intrinsic charge carriers of the detector material will also be collected and contribute to, and thus deteriorate, the measurement. As the charge carrier density in high resistivity silicon is dominated by the thermal generation of electron hole pairs, cooling has a significant impact on the charge carrier densities

and detector performance. Equation 1.2 describes the temperature dependency of the intrinsic carrier density and demonstrates the importance of the detector temperature [33].

$$n_i \;=\; 9.15 \times 10^{19} \left(\frac{T}{300}\right)^2 exp\left(\frac{-6880}{T}\right) cm^{-3} \tag{1.2}$$

Early semiconductor x-ray detectors relied solely on cooling of the detector material in order to lower the charge carrier density. But the developed detectors still suffered from severe signal broadening due to thermal charge carrier generation, even at temperatures of 77 K which can readily be reached by liquid nitrogen cooling [1]. Instead, modern semiconductor detectors rely on a completely depleted absorption volume, which leads to a very low density of majority charge carriers. This was initially achieved by utilizing a reverse biased pin diode configuration. A highly doped p region, a high resistivity n doped or intrinsic region and a n doped region are brought into contact forming a p-n junction with a build in potential that removes the mobile majority carriers and separates the generated electron hole pairs. An additionally applied reverse bias in the order of 100 V results in a depletion width that can be larger than the substrate thickness and leads to a completely depleted detector volume with a very low charge carrier concentration throughout the detection volume [1].

Silicon drift detectors (SDD) elegantly combine the depletion zone of the pin diode configuration with a lateral drift field, which significantly reduces the overall capacitance of the detector [34]. It can be interpreted as a folded pin diode with complete sideward depletion of the semiconductor material, due to the applied reverse bias. The additional drift field is generated by a top electrode configuration of concentric rings. The applied differential voltage of the ring electrodes decreases towards the center anode with a resulting potential as described by Lechner et al. [35].

The schematic of a SDD detector is shown in figure 1.6. Electron hole pairs that are generated by the incident radiation are separated by the present electric field and the electrons drift along the drift field towards the anode, located at the center, where they are collected. An in-depth discussion of the SDD concept, its advantages and current state of the art can be found in the references [24, 36, 37]. A high impedance transducer converts the collected charge at the detector anode to a voltage signal and each collected charge cloud induces a step wise increase of the output level. The state of the detector anode is periodically reset in order to allow for a continuous detection scheme and a pulse processing unit is used to interpret the voltage output signal of the detector. The encountered voltage steps

are assigned to detection events with a corresponding energy and used to build a histogram showing the energy distribution of the detected photons.

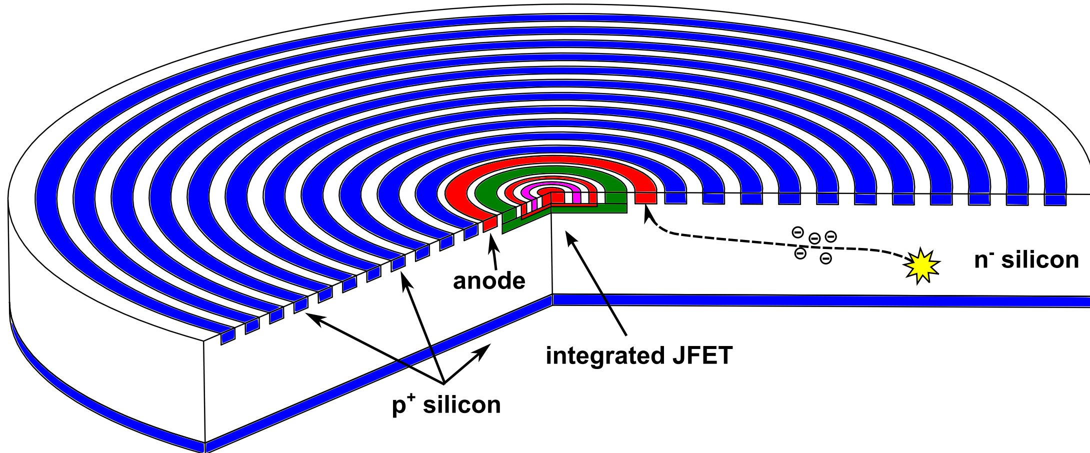

Figure 1.6: The cross section of a silicon drift detector is schematically shown. The top of the high resistivity, n doped silicon substrate is covered by concentric p+ doped ring electrodes that induce a drift field within the bulk material, which is used to channel the generated electrons towards the anode. An integrated JFET at the center of the device is used to convert the collected charge to a voltage signal. The radiation enters from the bottom through the p+ doped region and a charge cloud corresponding to the energy of the photon is generated if it is absorbed in the detector volume. The electrons subsequently drift along the drift field as indicated by the arrow. The schematic was redrawn and adapted from reference [3].

Apart from the detector resolution, which is limited by the Fano factor, the detector performance is governed by the detector efficiency. The interaction probability of the incoming photon and the detector volume, for a given detector thickness, depends on the material density and the atomic number Z of the detector material. In combination they determine the energy dependent absorption efficiency of the detector material, quantified by the mass absorption coefficient μ. A high density and Z value result in a high cross section of the element, which makes the photoabsorption of the incoming photon in the detector material more likely.

Equation 1.3 describes the exponential decay of the radiation intensity within a semiconductor detector volume, with I/I_0 denoting the relative intensity of the radiation, ρ the material density, μ the mass absorption, which is energy dependent, and x the thickness of the material [1].

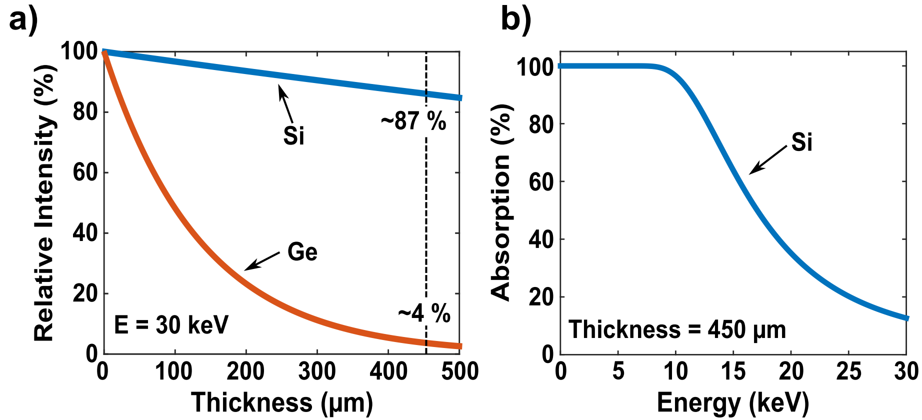

Figure 1.7: The intensity decay of x-ray radiation with an energy of 30 keV within a silicon and a germanium detector volume, as calculated with equation 1.3, is depicted in a). The remaining intensity at a thickness of 450 µm is indicated. The dependency of the x-ray absorption of a 450 µm thick silicon substrate on the energy of the x-ray radiation is given in b), as simulated by the web applet supplied by the Center of X-ray Optics (CXRO) at the Lawrence Berkeley National Laboratory [38].

$$\frac{I}{I_0} = e^{(-\rho\mu x)} \tag{1.3}$$

The implications are visualized in figure 1.7 a) by comparing the intensity decay of a silicon (Z=14) and a germanium (Z=32) detector volume for x-ray radiation with an energy of 30 keV. The relative signal intensity is significantly reduced for germanium compared to silicon at a thickness of 450 µm. The consequence is thus a smaller required thickness of the active region of the detector for a desired absorption efficiency, if the material offers a high Z value.

As the mass absorption coefficient is dependent on the energy of the incoming photons, a lower detection efficiency for high energy photons is observed as demonstrated in figure 1.7 b) for a silicon detector with a thickness of 450 µm. Whereas radiation with an energy below 10 keV is absorbed with a high probability, the absorption efficiency falls below 15 % for energies above 30 keV and therefore other type of detectors have to be used for high energy radiation detectors such as high purity germanium detectors, cadmium telluride detectors or a combination of silicon and other materials [24, 31]. Silicon drift detectors commonly exhibit a thickness of the active detector volume of 450 µm and therefore only offer a high detection efficiency within the range of 0.2 keV to 20 keV as shown in figure 1.7 b).

1.3 The Silicon Drift Detector Module

Silicon drift x-ray detectors (SDD) are cooled in order to reduce thermal noise generation and are commonly operated at a temperature of −60 °C to −20 °C, depending on the required energy resolution and operating environment. This temperature range can be achieved by a multi-stage Peltier element and poses a significant advantage compared to earlier Si(Li) x-ray detectors that required liquid nitrogen cooling.

A photograph of a typical detector module including the Peltier element, the bonded pins, the collimator, which shields the detector edge from irradiation, and the x-ray detector surface in the center is given in figure 1.8 a).

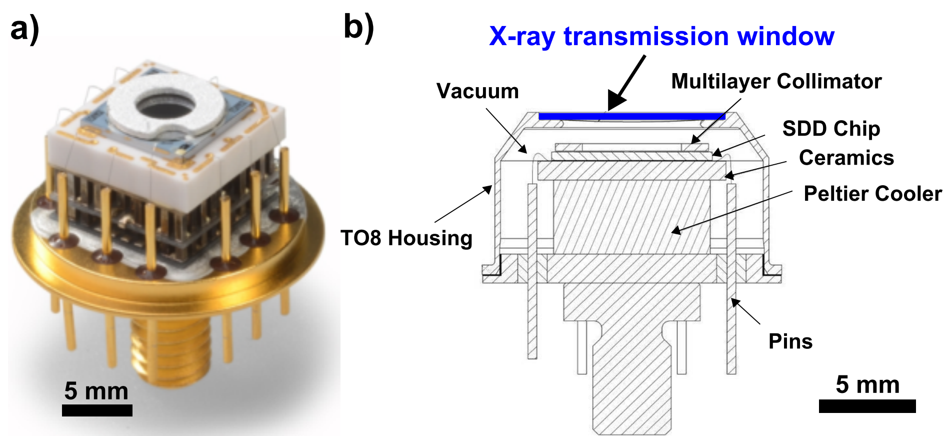

Figure 1.8: A photograph of a silicon drift detector is shown in a). The active detector volume is placed on top of a multistage Peltier element and surrounded by a collimator. The schematic cross section of a vacuum encapsulated detector module, as it is used for EDS and EDXRF applications, is depicted in b). It contains a highly x-ray transparent window on the top of the housing in order to pass the x-ray radiation to the detector. Images taken and adapted with permission from reference [32].

The efficiency of thermoelectric cooling is strongly dependent on the absolute thermal flux and corresponding current within the Peltier element, as discussed in reference [39]. An efficient cooling concept should therefore minimize the heat transfer between the cold detection volume and the ambient environment in order to obtain a minimal detector temperature. The thermal heat transfer consists of thermal conduction through the bulk material and bond wires, thermal radiation and thermal conduction due to convection.

The detector module is designed in a way to minimize the individual contributions by using materials with a low thermal conductivity and bond wires with a minimal diameter. In addition, thermal convection can be eliminated by placing the detector in a high vacuum of 1×10^{-6} mbar, with 1 mbar corresponding to 100 Pa. This has the additional advantage of shielding the detector surface from ambient contaminants by avoiding the adsorption and condensation of gaseous species. The SDD detector is therefore placed within an evacuated detector housing. The cross section of a vacuum encapsulated SDD detector module with an industry standard TO8 housing is schematically shown in figure 1.8 b). The top of the housing incorporates a highly x-ray transparent window element which passes the x-ray radiation through the housing and to the detector.

1.4 X-ray Transmission Windows

Beryllium (Be) is commonly used as a material for the x-ray transmission window and figure 1.9 a) shows a photograph of a vacuum encapsulated SDD detector module incorporating a Be x-ray transmission window.

Ideally, the x-ray transmission window should not alter the transmitted x-ray radiation. The effect of an x-ray transmission window on the detector signal is shown in figure 1.9 b). While the spectrum obtained with a windowless SDD module shows a high count rate across the given energy range, the signal obtained with a detector module that incorporates a standard Be window is significantly attenuated for x-ray energies below 2.5 keV. The detection efficiency of the detector system is therefore directly affected by the x-ray transmission of the x-ray transmission window [40], as well as indirectly by its ability to support the high quality vacuum inside the detector housing.

The x-ray transmission of a transmission window is dependent on the window thickness, the window material and the window geometry. Interestingly, the situation is comparable to the discussed implications of the detector material and thickness of the detection volume in regard to the efficiency of a semiconductor x-ray detector. But instead of a high absorption efficiency, the window material should transmit the x-ray radiation with as little attenuation as possible. The same considerations apply and the x-ray transmission window should therefore be as thin as possible and constitute of a material with a low atomic number. The interaction cross section is in general dependent on the energy of the incoming radiation, with an increased interaction probability for low energy radiation as described in section 1.2. This effect is apparent in figure 1.9 b) and results in a significant signal attenuation for the energies below 2.5 keV if a Be x-ray transmission window is used.

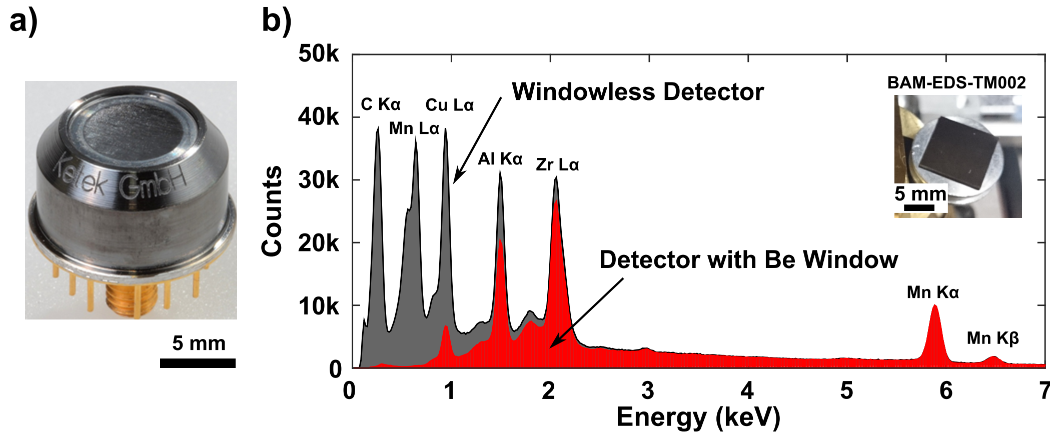

Figure 1.9: A photograph of a commercial, vacuum encapsulated, SDD detector module is shown in a). The image was taken with permission from reference [32]. The Be x-ray transmission window is visible on the top of the TO8 housing. The effect of a Be window on the measured EDS spectrum of a calibration sample (shown in the inset) is demonstrated in b) by comparing the spectrum obtained with a detector incorporating a Be window (red) to the spectrum obtained with a windowless detector (grey). The low energy radiation of the $C\ K\alpha$ and $Mn\ L\alpha$ transitions are not visible in the spectrum obtained with the Be window, as the radiation has been absorbed by the beryllium.

The vacuum inside the housing, with a low absolute pressure of 1×10^{-6} mbar, guarantees efficient detector cooling but results in a large differential pressure across the x-ray transmission window if the module is placed in a non-vacuum environment. The resulting load is dependent on the open diameter of the window and at an ambient pressure of 1 bar this results in a load of 3.85 N, or 385 g, for the standard window diameter of 7.0 mm employed for these type of detector modules. The x-ray transmission window has to be sturdy enough to withstand this load as well as additional stress that arises during normal operation of the detector module, which includes among others, pressure bursts if the specimen chamber is being vented or mechanical perturbations during module handling.

The contradicting goals of a minimal x-ray attenuation and the ability to withstand large pressure loads needs to be evaluated for the given application, depending on the energy range of interest, the required open geometry of the window and additional properties such as for example blocking of visible light.

1.4.1 Window Requirements

The x-ray transmission window is an integral part of the detector housing and the requirements of the window arise from the application and working environment of the detector module and will be derived in the following.

- The window has to transmit the radiation of interest in a sufficiently efficient manner to allow element detection. This corresponds to an energy range from 0.1 keV to 30 keV for the discussed SDD detector modules, although the exact range depends on the elements that are to be detected.
- The window has to withstand the differential pressure that acts across the window due to the vacuum inside the detector housing, if the module is placed in an ambient environment. The resulting load that weighs down on the window is dependent on the open diameter of the window geometry and unless otherwise noted, a standard window with a diameter of 7.0 mm is assumed. The pressure stability has to be sufficiently high to withstand at least the differential pressure of one atmosphere, but should ideally be larger in order to provide a safety margin.
- Aside from a static differential pressure load, the window also has to withstand dynamic pressure changes, as they occur if the measurement environment changes from vacuum to ambient pressure conditions or during the handling and resulting perturbations of the detector module. This results in a substantial stress on the window material which can lead to yielding, material fatigue and eventual window failure. The window therefore has to show a high resilience against material fatigue due to cyclic loads.
- The vacuum inside the detector housing is necessary for efficient cooling and a leak tight configuration of the housing and x-ray transmission window is a necessity for long time stability of the module performance. Helium leak rates below 3×10^{-10} mbar l/s are considered sufficient to provide a high cooling efficiency throughout the life time of the detector module, which is specified to two years.
- The x-ray transmission window should exhibit a high attenuation of optical and infrared radiation. Photons with an energy larger than the band gap of the used semiconductor material of the x-ray detector are able to generate unwanted electron hole pairs and should therefore be blocked by the window. At a temperature of −60 °C the silicon band gap is 1.145 eV, which corresponds to a wavelength of 1.08 µm [41]. Insufficient light blocking deteriorates the energy resolution and can even impede operation. The highly sensitive nature of SDD detectors requires a high attenuation of optical and

infrared radiation and a value of 1×10^{11} or higher is seen as sufficient if the detector module is to be used in daylight conditions [42].

- The window should be able to withstand the deterioration due to ambient contaminants such as moisture, low levels of oxidizing agents such as ozone and ionizing radiation, as they are encountered during operation.
- High temperature stability of the window is desirable as soldering processes are commonly used to join the x-ray window to the detector housing, which requires temperatures of up to 400 °C.
- Charging of the window should be avoided as it would otherwise deflect the electron beam in SEM-EDS applications and the window should therefore exhibit a sufficiently high electrical conductivity to dissipate the charge.

1.4.2 State of the Art

X-ray transmission windows need to satisfy partly contradicting requirements, namely the high x-ray transmission and the required mechanical stability and integrity. Only few materials have been identified that can comply to these requirements. Beryllium has been and is being used for applications in ambient environments, as well as for applications that do not require the detection of radiation with an energy below 1 keV [22]. This limits the detection to elements above sodium, making the detection of light elements including carbon, nitrogen and oxygen impossible.

Beryllium is used due to its high mechanical strength, high gas tightness, high light blocking ability, high electrical and thermal conductivity as well as high chemical stability if treated with a protective layer [43, 44]. Beryllium has a low atomic number (Z=4) and exhibits metallic properties with a high ultimate tensile strength of 454 MPa [43]. Using metallurgical techniques, such as rolling, it is possible to fabricate pin hole free beryllium foils with a thickness of 8 µm that are gas tight. Be windows with a thickness below 8 µm are usually not gas tight as the grain size of rolled beryllium is at a similar scale and diffusion along the grain boundaries becomes predominant [45].

The limited choice of window materials becomes apparent if one considers the downside of beryllium as a window material. Beryllium is toxic and seen as a serious health threat if inhaled [8]. Consequently, if the window ruptures, the detector module has to be disposed of and the workplace decontaminated. Especially high cost equipment, such as synchrotron beamlines, are affected from the down time if a window breaks and the Be window therefore poses a liability to the continuous operation. In addition, only very few suppliers for high quality beryllium foils are

available resulting in a price that is significantly higher than gold. Attempts using alternative window materials such as polymers [46,47], silicon nitride (SiN) [42,48] or synthetic diamond [49–51] have so far been unsuccessful as the windows lack a sufficiently high mechanical strength and light blocking ability, making beryllium unavoidable for most applications.

Low energy x-ray radiation is easily absorbed by most materials and if light element detection is required the x-ray transmission window therefore needs to be extremely thin. Consequently, alternative materials have to be used as the thickness of Be windows cannot be decreased to the required values. The minimal thickness is contradictory to the high mechanical stability that is required due to the differential pressure load that acts on the window. One way to comply to the stability requirements is by introducing a support structure that divides the open window geometry into numerous window elements with a reduced span width. The fact that the supporting elements cover a significant amount of the window geometry reduces the effective transmission area of the window. This signal loss is quantified by the fill factor (FF) of the window, which relates the open window area to the total area of the window. The FF therefore has a direct impact on the detection efficiency of the detector module [52].

Aside from a reduced signal transmission due to the incorporation of a support structure, ultra thin x-ray transmission windows exhibit a reduced light blocking ability for optical and infrared radiation due to their low thickness [47]. Additional light blocking layers are therefore required in order to shield the detector from low intensity light sources, such as often encountered optical fluorescence in SEM-EDS systems due to the electron beam interaction with the specimen sample. The additional light blocking layer commonly consist of aluminium and reduces the x-ray transmission of the window and leads to aluminium stray lines in the spectrum due to x-ray fluorescence. Special low energy x-ray transmission windows have been developed for light element detection but all exhibit significant setbacks such as a reduced temperature stability [53], low light blocking capability [47] and reduced mechanical stability [52, 53]. These disadvantages are tolerated due to the lack of an alternative. Low energy x-ray transmission windows fabricated from polymers [53] and SiN [42, 54] are available with the stated disadvantages including a reduced gas tightness as soldering is not possible due to the limited high temperature stability.

X-ray transmission windows for EDS applications can therefore be placed in two categories, Be windows for energies above 2 keV and low energy x-ray transmission windows for high-end applications that also require the detection of light elements with characteristic x-ray emission energies below 2 keV. The current state of the art of both will be elucidated in the following.

1.4.2.1 Beryllium Windows

Beryllium x-ray transmission windows are the most common choice for applications requiring a high x-ray transparency for energies above 2 keV. As beryllium is readily attacked by humidity in the air as well as oxidizing agents and acids, protective coatings are available in order to protect the Be windows against chemical attack [44].

Such windows are commercially available under the brand name DuraCoat Beryllium and exhibit a slightly lower x-ray transmission than standard Be windows [44]. Campbell et al. [55] have demonstrated that the passivation layer has the same influence on the x-ray transmission as an additional 2.24 µm of beryllium that is added to the nominal window thickness. The simulated energy dependent x-ray transmission of an 8 µm thick Be window and of an 8 µm thick DuraCoat Be window, as they are commercially available with an open geometry of 7 mm, are shown in figure 1.10. The transmission data were obtained by simulating the x-ray transmission of beryllium with a thickness of 8 µm and 10.24 µm, respectively, using the data provided by Henke et al. [17] in the form of a web applet supplied by the Center of X-ray Optics (CXRO) at the Lawrence Berkeley National Laboratory [38]. Both types of Be windows exhibit an x-ray transmission close to 100 % for energies above 3.5 keV, while energies below are increasingly absorbed by the window material.

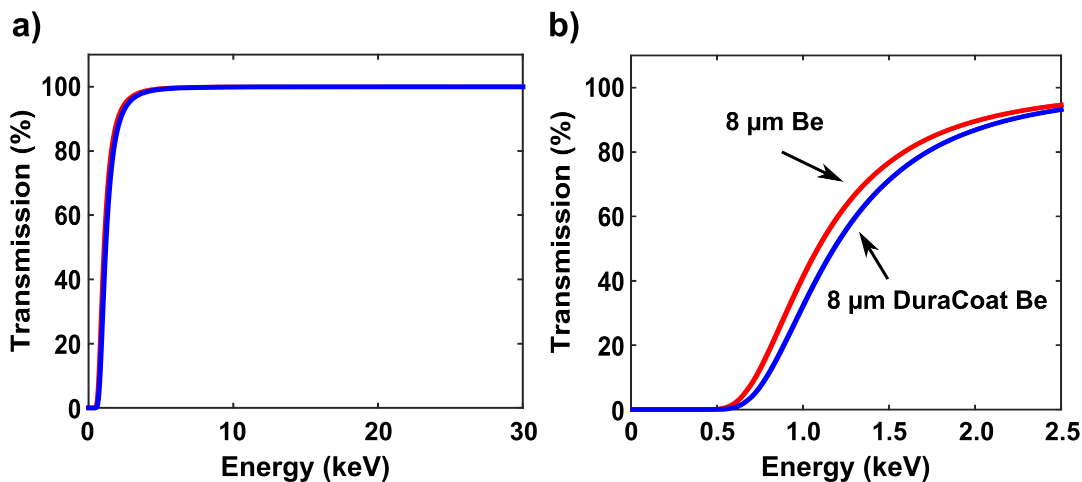

Figure 1.10: The energy dependent, transmission of an 8 µm thick Be window and of an 8 µm thick, corrosion resistant DuraCoat Be window, for the energy range from 0.1 keV to 30 keV, are shown in a) as simulated with the web applet provided by CXRO [38]. The low energy range from 0.1 keV to 2.5 keV is depicted in b) in more detail.

Be windows with a thickness of 8 µm and an open geometry with a diameter of 7 mm are specified to withstand a differential pressure load of up to 2 bar and more than 20k cycles of differential pressure loading with 1 bar of differential pressure applied per cycle [44, 56]. Be windows offer a high temperature stability and allow a soldering process to be used to join the Be window to the detector housing, resulting in an excellent gas tight configuration of the detector module. Helium leak rates below 1×10^{-10} mbar l/s are achievable with Be windows, which is sufficient to conserve the vacuum inside the detector housing. The metallic nature of beryllium and the relatively large nominal window thickness of 8 µm results in excellent light blocking capabilities of Be windows and are considered solar blind. This allows a detector module that incorporates a Be window to be used in ambient daylight conditions without a deterioration of the detector performance.

The thin beryllium foils are fabricated by rolling and the thickness tolerance of Be windows is specified with -0/+5 µm, which potentially leads to a lower x-ray transmission for energies below 3.5 keV than expected [56]. The employed passivation layer of DuraCoat Be windows exhibits a significantly increased electrical resistivity ($< 4 \times 10^4\ \Omega\ cm$) compared to passivation free beryllium ($4 \times 10^{-6}\ \Omega\ cm$) [43], but is still sufficiently high to avoid charging of the window during operation. The properties of Be x-ray transmission windows are summarized in table 1.1.

Table 1.1: Summarized window properties of a commercial DuraCoat Be window with a specified thickness of 8 µm and a window diameter of 7 mm, as specified in the references [44, 56].

X-Ray Window Property	**DuraCoat Beryllium**
X-ray Transmission	$> 80\ \%\ for\ E > 1.7\ keV$
Pressure Stability	$> 2\ bar$
Helium Leak Rate	$< 1 \times 10^{-10} \frac{mbar\ L}{s}$
Fill Factor	100 %
Pressure Cycle Fatigue	$> 20k$ cycles @ $\Delta p = 1\ bar$
Light Blocking Factor	$> 10^{11}$
Thickness Tolerance	$-\ 0\ \mu m\ /\ +\ 5\ \mu m$
Chemical Resistance	High
Electrical Resistivity	$< 4 \times 10^4\ \Omega\ cm$

1.4.2.2 Low Energy X-ray Transmission Windows

Low energy x-ray transmission windows need to exhibit a high x-ray transmission for the energy range from 0.1 keV to 2.0 keV. This is necessary to identify light elements including among others, boron (183 eV), carbon (277 eV), nitrogen (392 eV), and oxygen (525 eV), which is not possible with Be windows. The window properties of low energy x-ray transmission windows based on a polymer and silicon nitride window material, respectively, are discussed in the following and the low energy x-ray transmission window properties summarized in table 1.2 at the end of this section.

Polymer Low Energy X-ray Transmission Windows

Polymer windows were first introduced in 1982 and have been continuously improved, making them the most commonly used low energy window for light element detection [22]. The x-ray transmission is sufficiently high for energies below 2 keV as shown in figure 1.11 a) [53]. This is achieved by the use of low Z elements and a

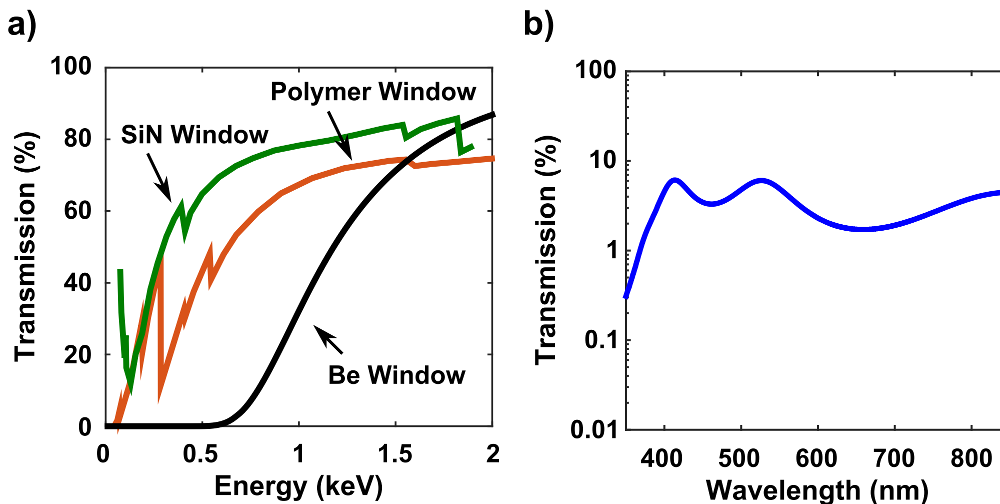

Figure 1.11: The x-ray transmission of a polymer and a SiN, fluorescent blind, low energy x-ray transmission window for the energy range below 2 keV are shown in a) [53, 54]. The transmission of a Be window is included as a reference. The measured optical transmission of a polymer x-ray transmission window, with an aluminium light blocking layer, is given in b) for the wavelengths 350 nm to 850 nm, with an average transmission of 3.3 %.

minimal window thickness. In order to provide the required mechanical strength the window incorporates a silicon beam support structure with a FF of 77 % [52]. An SEM image of the support structure is shown in reference [57]. Polymer windows with a window diameter of 6.2 mm are helium leak tight and withstand a differential pressure of up to 2 bar, as well as 10k cycles of differential pressure

loading with 1.2 bar. The high optical transparency of the polymer film requires an additional aluminium light blocking layer, which also avoids charging of the window. The resulting optical transmission of the polymer window including a light blocking layer, is shown in figure 1.11 b), with an average transmission of 3.3 % for the shown wavelengths. This is sufficiently high to block low intensity light sources and the window is considered fluorescent blind [47]. The polymer window properties are summarized in table 1.2.

Silicon Nitride Low Energy X-ray Transmission Windows

SiN low energy x-ray transmission windows have become available in 2013 and exhibit an unprecedented x-ray transmission for energies below 2 keV, as shown in figure 1.11, high gas tightness and high mechanical strength [42, 54]. The used low stress SiN window material is supported by an 8 µm thick, polycrystalline silicon support structure with a fill factor of 77 % [42]. An SEM image of the hexagonal support grid is shown in reference [57]. The high mechanical strength of the SiN window material allows the window thickness to be reduced to 40 nm while still withstanding a differential pressure of 3 bar for a window diameter of 6.2 mm [42, 54]. Cycle fatigue testing with a differential pressure of 1.2 bar and a total number of 250k pressure cycles does not lead to window failure [42]. An additional light blocking layer of aluminium is necessary due to the high optical transparency of SiN to block low levels of light, also avoiding charging of the window. The used aluminium leads to unwanted stray lines due to x-ray fluorescence of the aluminium. The light blocking ability is assumed to be similar to the values measured for the polymer window as SiN windows are considered fluorescent blind. The SiN window properties are summarized in table 1.2.

Table 1.2: Summarized window properties of commercial, fluorescent blind, polymer and SiN low energy x-ray transmission windows with a window diameter of 6.2 mm, as specified in the references [42, 53, 54].

X-Ray Window Property	Polymer Window	SiN Window
Low Energy X-ray Transmission	High	Highest
Pressure Stability	$> 2\ bar$	$> 3\ bar$
Helium Leak Rate	$< 1 \times 10^{-10} \frac{mbar\ L}{s}$	$< 1 \times 10^{-10} \frac{mbar\ L}{s}$
Fill Factor	77 %	77 %
Pres. Cycle Fatigue @ $\Delta p = 1.2\ bar$	$> 10k$ cycles	$> 250k$ cycles
Light Blocking Factor	> 16	unknown

1.5 Graphenic Carbon: An Alternative to Beryllium

Beryllium is known to cause berylliosis if inhaled making the fabrication, handling and disposal of EDS detector modules that incorporate a Be window a potential health threat. Beryllium inhalation can lead to a chronic sarcoidosis of the lung as well as acute reactions [58]. A thorax x-ray image of a patient suffering from berylliosis after beryllium exposure is shown in figure 1.12 [59].

Figure 1.12: The x-ray image of the thorax of a patient suffering from chronic berylliosis is shown. The left and right lung of the patient show inflammatory nodules (granulomas) that are a reaction to the beryllium exposure and ultimately led to a restrictive lung disease. The image was taken with permission from reference [59].

The partly contradicting requirements and tight specifications of x-ray transmission windows results in the fact that most x-ray transmission windows are still being fabricated from beryllium foils, despite the health risks, due to the high performance of Be x-ray transmission windows and the lack of alternative window materials.

This work proposes the use of graphenic carbon (GC) as a novel window material as elucidated in the following.

1.5.1 Graphene: The Ideal Window Material?

The fabrication of monolayer graphene films by Novoselov and Geim in the year 2004 complemented carbon nano tubes and fullerenes in the family of sp^2 bonded carbon allotropes [60]. The impressive properties of graphene has led to intense research and high expectations for graphene based electronics. More than 10 years later, the enthusiasm has slowed down as more and more drawbacks are being identified which hinder the use of graphene as a semiconductor material [61,62]. What remains untouched are the remarkable physical properties of monolayer graphene such as an ultra high mechanical strength [63, 64], high chemical stability [65], helium tightness [66] and high electrical conductivity [67]. This has sparked the interest in graphene as a material for micro-electro-mechanical systems (MEMS) and nano-electro-mechanical systems (NEMS) [68], membrane technologies [69], energy storage applications [70], chemical sensors [71] and as a filler material for composite materials [72–74].

Monolayer graphene offers the highest yet discovered mechanical strength with a Young's modulus of 1 TPa and an ultimate tensile strength of 130 GPa [63]. The high stability arises from a purely sp^2 bonded carbon network with the resulting characteristic hexagonal honeycomb structure, as schematically shown in figure 1.13 a).

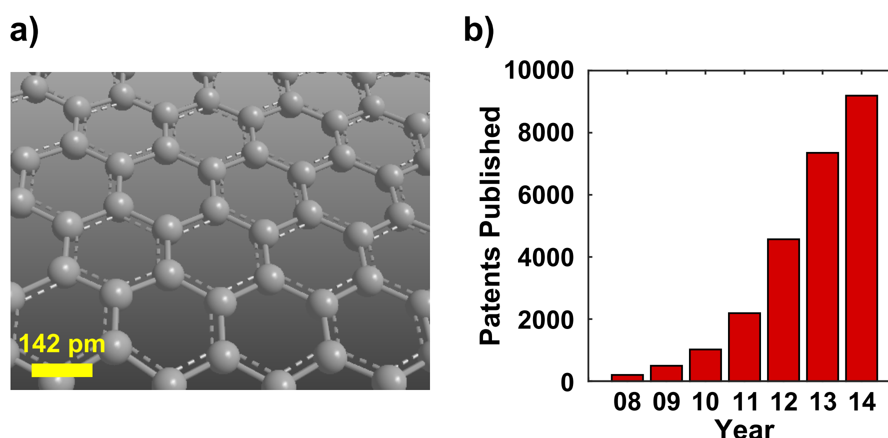

Figure 1.13: The atomic structure of monolayer graphene is schematically shown in a). The carbon atoms in graphene form a planar, hexagonal structure with a de-localized π electron orbital, as indicated by the dashed lines and a carbon-carbon bond length of 142 pm [75]. The number of graphene related, published patents for the specified year are visualized in b) [76].

Each carbon atom is bound to three adjacent carbon atoms and orientated in a single plane. The graphene monolayer can be interpreted as the building block

of carbon nanotubes, fullerenes as well as graphite, and exhibits a high chemical stability and in-plane electrical conductivity [77]. The growing number of yearly published patents that mention graphene, as shown in figure 1.13 b), indicates the gradual transition from fundamental to product orientated research. A steep increase is visible after the year 2009 and it should be kept in mind that it commonly takes 18 months for the patent publication following the application.

If it is possible to exploit the published material properties of graphene, an x-ray transmission window with an impressive performance would be possible, as implied by the following considerations:

- The high mechanical strength of graphene would allow for an x-ray transmission window with an extremely reduced window thickness, while still complying to the mechanical stability requirements.
- The low atomic number of carbon (Z=6) would result in a high x-ray transmission and even atomically thin graphene has been shown to be gas tight [66].
- The high chemical stability and electrical conductivity of graphene would allow the fabrication of a highly durable and conductive x-ray transmission window.

Graphene was mentioned for the first time as an x-ray window material in a patent in 2009, proposing to stack mechanically exfoliated graphene as a window material for x-ray transmission windows [78]. None the less, a number of problems remain which explains the absence of x-ray transmission windows exploiting the material properties of graphene. Foremostly, the synthesis of graphene is still under investigation and the published material properties were all extracted from high quality graphene obtained by mechanical exfoliation of highly ordered pyrolytic graphite (HOPG), which is not available as a large scale production method and only yields small samples of graphene. The second major obstacle is the physical integration of graphene into an x-ray window configuration that is gas tight and of high mechanical stability.

Open Question: Graphene Synthesis

Various synthesis methods of graphene, aside from the first presented mechanical exfoliation of HOPG by Novoselov and Geim in 2004 [60], have been proposed, including among others, epitaxial growth on silicon carbide substrates [79,80], the chemical reduction of graphene oxide [81], liquid phase exfoliation of HOPG [82] and chemical vapor deposition (CVD) [83]. The quality of mechanically exfoliated graphene excels with a low defect density and large regions of true mono-crystalline

composition, which has made this the method of choice for fundamental research and proof of concept device manufacturing [84]. Liquid phase exfoliation in combination with liquid phase deposition presents an easily scalable synthesis scheme but the resulting graphene films are of inferior quality [85]. The holy grail of graphene synthesis is therefore the combination of high graphene quality and simple fabrication, especially in regard to large scale processing. Chemical vapor deposition is considered one of the most promising methods due to the high quality of the obtainable graphene and the high level of scalability of CVD processing [83].

Chemical vapor deposition of graphene is based on the thermally activated decomposition of a carbon containing precursor gas and ensuing graphene film growth on a heated target substrate. Catalytic decomposition of the precursor and catalytic film growth has proven to produce high quality graphene films on a large variety of substrates [83]. An overview of the used catalytic materials and deposition schemes can be found in reference [83]. The transition metals copper and nickel are most commonly used and allow the relatively simple fabrication of few layer or even single layer, high quality graphene [86, 87]. Surprisingly, the first successful attempts at growing HOPG on transition metals has already been demonstrated as early as 1969 and many of the theoretical considerations remain valid [88]. Recently, graphene growth on hydrogen terminated germanium has led to a high graphene quality which was attributed, among others, to the very low adhesion between the resulting graphene film and the substrate surface [89]. The fact that the graphene material is grown on a catalytic growth layer implies a necessary transfer to an insulating substrate for electrical applications such as transistors and sensors. Various transfer schemes have been developed but all deteriorate the quality of the graphene material, and are a significant obstacle for large scale processing and integration of graphene [90].

Open Question: Graphene Integration

Presuming a graphene synthesis process is available, the graphene material still needs to be joined to the detector module housing in a gas tight, mechanically strong and reliable fashion, in order to realize a graphene based x-ray transmission window.

In a pioneering experiment, Bunch et al. [66] were able to seal micro cavities with an area of $4.75\,\mu m^2$ and a depth of 380 nm with monolayer graphene, by directly exfoliating HOPG onto a silicon dioxide substrate. The graphene layer adheres to the substrate due to van der Waals forces and gas impermeability of the membrane was shown. None the less, a slow diffusion into the cavity, independent on the number of graphene layers that sealed the chamber, was observed. Evidently a diffusion through the substrate or the substrate-graphene interface

was taking place. Therefore, if graphene material is to be used as a hermetic seal, not only the quality of the graphene is decisive, but also the substrate-graphene interface.

Aside from the gas tight configuration, the substrate-graphene interface needs to be strong enough to support the large mechanical loads that result from a differential pressure across the window. Experiments performed by Koenig et al. [91] with monolayer and few layer graphene membranes showed that the attracting van der Waals forces between graphene and a silicon dioxide substrate surface are insufficient to fully exploit the mechanical strength of graphene. The tested graphene membranes delaminated from the surface prior to material failure, as an increasing differential pressure was applied across the membrane.

The graphene integration into an x-ray window that can be joined to the module housing is seen as a major obstacle as the graphene synthesis methods require a transfer from the growth substrate to the desired target substrate. The adhesion due to van der Waals forces is insufficient and other alternatives such as clamping would require extremely smooth clamping surfaces and have not been demonstrated so far.

1.5.2 Proposal: Direct Graphenic Carbon Deposition onto Silicon Substrates

In this work, the direct deposition of graphene onto a silicon substrate without the use of a catalytic material such as copper, nickel or germanium is proposed. A sufficiently high deposition temperature results in the formation of silicon-carbide bonds at the interface which are much stronger than van der Waals forces and would lead to an intrinsic, high adhesion of the graphene layer onto the silicon substrate [92, 93]. The silicon substrate could subsequently be partially removed using standard micro machining methods to form the free standing geometry of the x-ray transmission window. The remaining silicon would form an integrated window frame making the transmission window sturdy enough to be handled and joined to the detector housing by soldering, as it is currently done with Be windows.

Catalyst free graphene growth has been of interest as to avoid the transfer process of CVD graphene, that has been grown on a catalytic substrate, to an insulator substrate for device fabrication. Graphene growth on, among others, silicon oxide [94], sapphire [95] and silicon nitride [96, 97] has been evaluated and discussed in literature. The absence of a catalytic growth layer results in a significantly reduced size of the graphene grains and a higher defect density, which

is problematic for electronic applications [84]. One advantage of catalyst free growth is the achievable, large film thickness as the growth is by condensation rather than segregation, as seen in nickel films, or surface adsorption, as it is seen with a copper catalyst surface [92]. This is advantageous for the fabrication of x-ray transmission windows, as the large opening dimensions requires a significant window thickness, even if the ideal mechanical properties of graphene are assumed.

The reduced grain size, of the catalyst free deposited graphene films, have led researchers to use the terms nanographene [98] and polycrystalline graphene [99], implying the structural differences to the general perception of graphene being a single crystal. Following the suggestions of Bianco et al. [100] it is refrained from using the discussed terms for a bulk material and instead the term graphenic carbon (GC) is employed. Bianco et al. postulate the use of the terminology GC for all bulk materials that are based on the graphene layer as the structural unit and therefore contain largely sp^2 hybridized carbon.

1.5.3 Graphenic Carbon as a Window Material

The question remains how the small grain size, which is found to be in the order of below 14 nm, for catalyst free graphene growth, effects the mechanical strength and gas tightness of the GC material [94, 95, 101]. Molecular dynamics simulations of single layer, nanocrystalline graphene with an average grain size of 2 nm by Zhang et al. [102] resulted in a Young's modulus of 432.26 $\pm$ 10.57 GPa and an ultimate tensile strength of 26.86 $\pm$1.12 GPa, instead of the introduced 1 TPa and 130 GPa for monolayer, single grain graphene. Interestingly, the simulations demonstrated that while nanocrystalline graphene exhibits reduced material constants, the fracture behavior was insensitive towards defects below a certain length scale and the critical stress for crack growth was found to be similar to single grain graphene [103]. This is attributed to the effect of grain boundaries on the crack propagation, a phenomenon that is known from ceramics [104].

While monolayer graphene has been shown to be helium gas tight, this is only the case for single crystalline, defect free, graphene films. In fact, soon after the first exfoiliation, graphene was proposed as an atomically thin anti-corrosion coating for materials such as copper, with seemingly promising results [105]. It was only later discovered that the graphene coating actually had a decremental effect in comparison to an uncovered sample due to gas diffusion along the grain boundaries and defects of the graphene film [106]. While this is true for atomically thin films, it is assumed that a large number of overlapping graphene grains as well as a certain amount of non-horizontally aligned carbon bonds should hinder gas diffusion across a bulk GC film.

The optical properties of the GC material are expected to be similar to those of graphene as indicated by the work of Dovbeshko et al. [107]. Graphene is known to have a high optical absorption of 2.3 % per atomic monolayer and the GC bulk material thus assumed to exhibit a sufficiently high light blocking ability to avoid the necessity of an additional light blocking layer.

The direct CVD deposition of GC onto a silicon substrate should therefore allow to utilize the impressive properties of graphene to fabricate high performance x-ray transmission windows. This would allow to finally replace toxic beryllium x-ray transmission windows with an abundant and safe carbon window.

1.6 Objective of the Thesis

The scope of this work is the fabrication and evaluation of a carbon x-ray transmission window in order to finally replace toxic beryllium as a window material. Commercial 8 µm thick Be windows are used as a benchmark in order to asses the performance of the proposed window material.

2 Methods

The employed methods to evaluate the properties of the deposited GC material as well as the performance of the GC x-ray transmission windows are introduced and discussed in this chapter. This includes the measurement schemes as well as the underlying theoretical considerations.

2.1 Evaluation Schemes for X-ray Transmission Windows

The performance of the proposed and developed GC x-ray transmission windows needed to be evaluated and the developed measurement schemes are discussed in the following section. These include the x-ray transmission, mechanical strength, helium leak tightness, optical attenuation and stability against ozone and x-ray radiation of the GC x-ray transmission windows.

2.1.1 X-ray Transmission

The transmission of the x-ray transmission windows was determined by measuring the signal intensity of an x-ray source with a windowless detector and comparing it to the signal intensity while the x-ray transmission window was placed in the x-ray signal path. Ideally one would use a "white" or tunable x-ray source in the range of 0.1 keV to 2.5 keV as it is available from a synchrotron x-ray source. Due to the absence of such, the characteristic emission spectrum of an EDS calibration sample was used instead (BAM-EDS-TM002 [18]). The sample contains the elements carbon (C), manganese (Mn), copper (Cu), aluminium (Al) and zirconium (Zr) and the spectrum therefore exhibits a number of well distinguishable emission peaks within the energy range of 0.1 keV and 2.5 keV [40].

The measurement setup is shown in figure 2.1 a). An SEM system with a dual EDS detector configuration was used. The electron beam was set to an acceleration voltage of 10 kV, which is sufficiently high to excite the elements of the calibration sample. The resulting characteristic x-ray emission spectrum of the sample was recorded simultaneously with two separate x-ray detectors. One of the detectors was defined as the reference detector in order to compensate for beam current variations and resulting differences in the emission spectrum, and

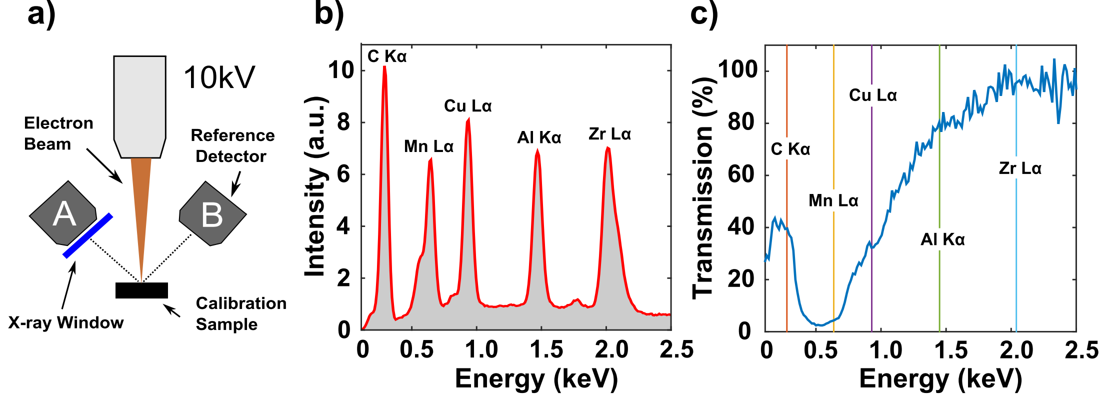

Figure 2.1: The used detector setup for the x-ray transmission measurements is shown schematically in a). The emission spectrum was recorded simultaneously with two EDS detector systems in order to calculate the energy dependent x-ray transmission. The spectrum, as recorded with the reference detector, of the calibration sample is given in b) and the corresponding, labeled peaks exhibit a high peak to background ratio. The calculated, continuous x-ray transmission of a test window with a GC thickness of 1 µm is shown in c). The vertical lines indicate the positions of the peaks shown in b).

the other defined as the measurement detector. The reference detector was a commercially available EDS system from Oxford Instruments (Oxford DryCol INCA 80 mm^2 SDD), which was equipped with a polymer low energy x-ray transmission window. The measurement detector was an AXAS-D system from Ketek with a windowless detector module. The to be tested x-ray window was glued into the cap of a TO8 housing which was subsequently placed on top of the windowless detector module in order to determine the x-ray transmission.

The actual measurement was performed in two steps. A first reference measurement with the windowless system and the reference system was simultaneously taken, followed by a second simultaneous measurement, with the to be tested x-ray window covering the windowless detector. The spectrum obtained with the reference detector system during a transmission measurement is shown in figure 2.1 b). The emission spectrum exhibits a high peak to background ratio and the corresponding elements are labeled. The energy dependent transmission, denoted as T(E), of the to be tested x-ray window was calculated using equation 2.1. With $I_{A1}(E)$ denoting the energy dependent signal intensity of the windowless detector A during the first measurement, $I_{A2}(E)$ denoting the energy dependent signal intensity of the detector A with the to be tested window attached during the second measurement, $I_{B1}(E)$ denoting the energy dependent signal intensity of the detector B during the first measurement and $I_{B2}(E)$ denoting the energy dependent signal intensity of the detector B during the second measurement. The

two reference measurements with detector B were therefore used to calibrate the intensity level of the two measurements obtained with detector A. This assumes that the deviation of the emission signal had the same impact on detector A and B.

$$T(E) = \frac{I_{A2}(E)\, I_{B1}(E)}{I_{A1}(E)\, I_{B2}(E)} \tag{2.1}$$

In general, it is possible to calculate a continuous transmission function using the measurement data and the introduced equation 2.1. The result for a 1 µm thick GC window is shown in figure 2.1 c). The obtained transmission values exhibit a poor signal to noise ratio which arises due to the fact that the signal intensity is low for the peak free segments of the emission spectrum. The transmission values are therefore, only calculated for the energies of the peak positions in the emission spectrum of the calibration sample, which offer a much higher signal to noise ratio. The energy values are indicated in figure 2.1 c) by the corresponding vertical lines at 0.277 keV ($C\ K\alpha$), 0.637 keV ($Mn\ L\alpha$), 0.930 keV ($Cu\ L\alpha$), 1.49 keV ($Al\ K\alpha$) and 2.04 keV ($Zr\ L\alpha$). The discrete transmission values are subsequently complemented with simulated transmission curves to evaluate the x-ray transmission of the window [108]. Simulations were performed using the data provided by Henke et al. [17] in the form of a web applet supplied by the Center of X-ray Optics (CXRO) at the Lawrence Berkeley National Laboratory [38].

2.1.2 Mechanical Stability

The mechanical stability of the x-ray transmission windows was evaluated by differential pressure loading. This includes the resilience against a gradually increasing differential pressure load as well as cyclic pressure loading to determine the effects of cyclic fatigue.

The resulting load that acts on the window is dependent on the open area of the window and the applied differential pressure and is given for circular windows by equation 2.2. With F denoting the resulting total load, Δp the applied differential pressure, A the window area and r the radius of the circular window.

$$F = \Delta p\, A = \Delta p\, \pi\, r^2 \tag{2.2}$$

The schematic cross section of an x-ray window under a pressure load is shown in figure 2.2 a). With r being the radius of the open, circular window and t the

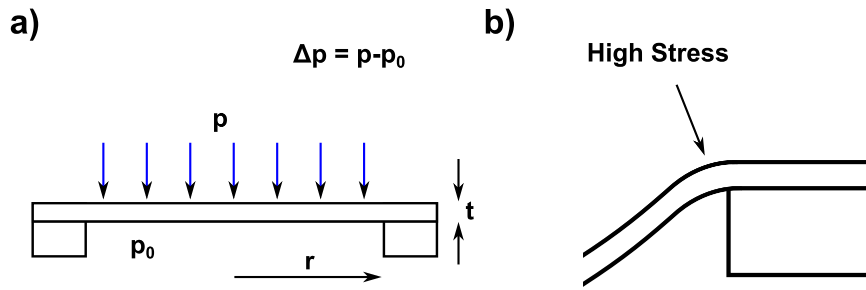

Figure 2.2: The schematic of an x-ray transmission window is depicted in a). The thin window material is supported by a sturdy frame. The differential pressure load typically weighs down on the window and the resulting mechanical load is dependent on the radius r and the differential pressure Δp. The implications that arise from the downward pressure load is shown in b). The window is deformed and deflected downwards.

window thickness. A frame structure holds the thin window material in place and gives the window the required ruggedness. This frame is also used to join the window to the detector housing. The resulting stress within the window material is dependent on the total load and the window thickness as stress is defined as force per area and the window thickness determines the cross section area of the window material.

Window failure occurs if the stress is larger than the ultimate tensile stress of the material and the mechanical stability of the window therefore defined by the ultimate tensile stress of the window material, the window geometry and the window thickness. The resulting load typically weighs down on the window and leads to a deflection and deformation of the window, which is schematically shown in 2.2 b). A bending moment results at the top of window material above the window frame which results in an additional, localized stress and corresponding deformation of the window material. The stress distribution is therefore not homogeneous within the window material but with a maximum near the window frame, with significant implications regarding the mechanical stability as will be discussed in more detail in section 2.2.4 and section 2.3.

A vacuum test setup was designed to probe the windows with a differential pressure of up to 950 mbar. This corresponds to the atmospheric pressure in Munich, which is on average 951 mbar, based on the elevation of 515 m above sea level. The schematic of the setup is shown in figure 2.3 a). A Pfeiffer MVP 035-02 diaphragm vacuum pump was used in combination with dosing valves to regulate the low pressure side of the window by controlling the pumping capacity.

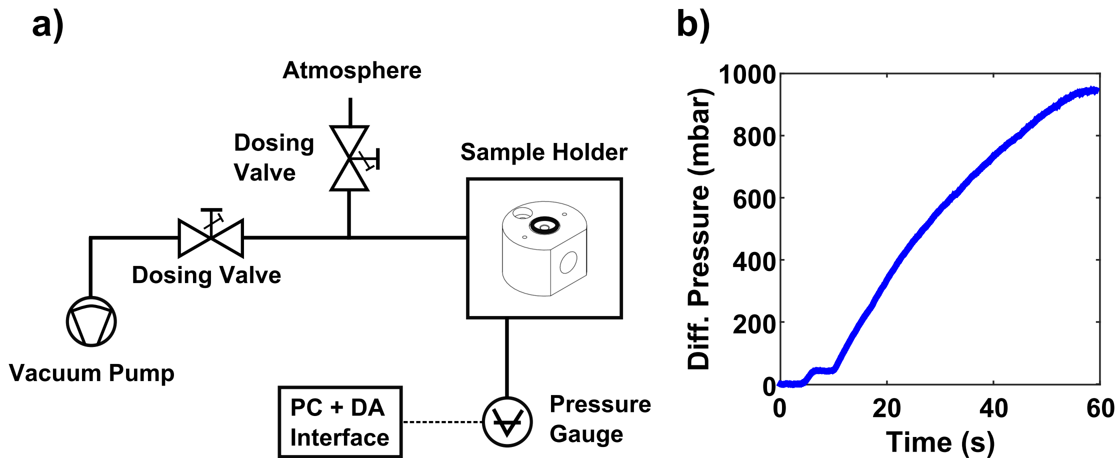

Figure 2.3: The layout of the developed vacuum test setup is schematically depicted in a). The window was placed on the o-ring of the sample holder for vacuum testing and the low pressure side of the sample holder was manually regulated using the two dosing valves. The differential pressure values during a vacuum test of a GC x-ray transmission window is shown in b). The window did not fail due to the applied differential pressure.

The differential pressure across the window was recorded using a pressure sensor (DP101AEP Panasonic) with a specified measurement range of -1 bar to 1 bar and a repeatability of ± 0.1 % full scale corresponding to ± 2 $mbar$. Analog to digital conversion was performed with a National Instruments 6008 USB box and the data was recorded using a LabVIEW software environment. The differential pressure was gradually increased by opening the dosing valve leading to the vacuum pump, while the dosing valve leading to atmosphere was available to vent the low pressure side of the sample holder. The to be tested window was placed on the seal and the low pressure side pulled the window towards the sample holder during testing, ensuring a sufficiently gas tight configuration. The typical pressure recording of a window that withstood the gradually increased differential pressure load until the atmospheric pressure limit was reached is depicted in figure 2.3 b).

Maximum Window Stability

The maximum pressure stability of the x-ray transmission windows was evaluated by applying a gradually increasing differential pressure across the window until window failure was induced. A second measurement setup was therefore designed to allow for higher differential pressures in order to determine the burst pressure values of x-ray windows that were larger than 950 mbar. The schematic of the test setup is displayed in figure 2.4 a). Compressed air was used to apply a differential pressure across the window. The compressor supplied a pressure reservoir with a maximum pressure of 7 bar. This could be reduced by a pressure reducer in order

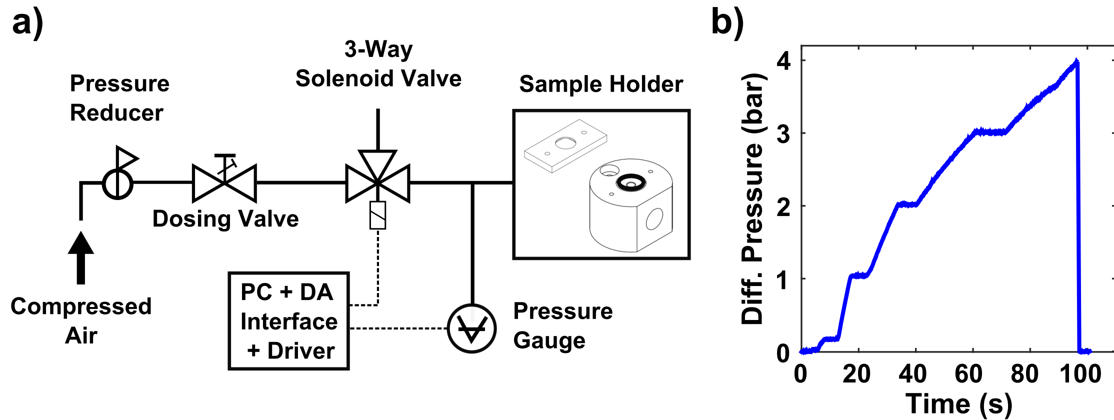

Figure 2.4: The layout of the pressure testing setup is schematically shown in a). A compressed air reservoir was used to apply a differential pressure across the window that was placed top down on the o-ring of the sample holder and was fixated by a teflon inlay and aluminium back plate. A PC interface was developed to actuate the 3-way solenoid valve and record the differential pressure. The recorded differential pressure during a burst pressure measurement of a GC x-ray transmission window with a GC thickness of 580 nm and a diameter of 7.4 mm is shown in b). The window failed at a differential pressure of 4 bar.

to allow for a finer pressure regulation by the dosing valve that was placed in-line to the compressed air supply.

A solenoid 3-way valve was chosen instead of a manual venting valve, which allowed a software based actuation of the setup. The required driver circuit was specifically designed and the solenoid valve was switched "on" for burst pressure testing, connecting the compressed air supply to the sample holder and switched "off" in order to vent the low pressure side to atmosphere. The differential pressure that acted across the window was recorded using a pressure sensor (DP102AEP Panasonic) with a specified measurement range of -1 bar to 10 bar and a repeatability of ± 0.2 % full scale, corresponding to $\pm 22\ mbar$. Analog to digital conversion was performed with a National Instruments 6008 USB box and the data was recorded using a LabVIEW software environment.

The to be tested x-ray window was placed "top-down" on the o-ring of the sample holder. A Teflon inset was used in combination with an aluminium back plate to press the window onto the o-ring. This was necessary to insure a gas tight configuration, as the high differential pressure load forced the window away from the o-ring. The recorded differential pressure across an x-ray window during burst testing is shown in figure 2.4 b). The solenoid valve was switched on and the differential pressure was gradually increased as the dosing valve was opened.

The dosing valve was closed at given time intervals in order to verify the gas tight configuration of the sample holder. Large differential pressure loads frequently required a re-tightening of the screws that press the back plate onto the x-ray transmission window in order to obtain a gas tight configuration. This was a critical aspect as too much pressure from the back plate would break the window frame. The differential pressure was increased until window failure occurred and the maximum differential pressure was used as a characteristic value for the mechanical stability of the window.

A figure of merit independent of the radius and the thickness of the window was introduced in order to use the burst pressure value to compare the stability of windows with varying opening diameters, due to either window design or process variations, as well as different window thicknesses. The figure of merit was developed based on the following considerations:

- The total load of the window is transferred to the window frame at the anchor points of the window material.
- The load, denoted as F, therefore acts on the area that is defined by the circumference, denoted as C, of the open window geometry and the window thickness, denoted as t, for a circular window with the radius r.

The maximum stress, denoted as σ_{max}, that results from the load that leads to window failure and acts on the described area was therefore interpreted as a figure of merit for the stability of the x-ray window and calculated as described by equation 2.3.

$$\sigma_{max} = \frac{F}{C\,t} = \frac{\Delta p\,\pi\,r^2}{2\,\pi\,r\,t} = \frac{\Delta p\,r}{2\,t} \tag{2.3}$$

The calculated stress corresponds to the average ultimate tensile strength of the material, as a homogeneous, perpendicular stress distribution across the defined area was assumed during the calculation. The ultimate tensile strength of a material is commonly used to identify the stress that is required to induce material failure [109]. It should be noted that the calculated figure of merit does not necessarily describe the strength of the GC material itself as defects in the material are assumed to locally reduce the mechanical stability, thus leading to early window failure and a significantly reduced value of the introduced figure of merit.

Cycle Stability

Aside from the burst pressure value of an x-ray transmission window, the resilience against cyclic loading is also of interest as material fatigue is a common

form of material failure [110]. Cyclic loading can lead to material failure even if the resulting stress that occurs in the material for each cycle is much smaller than the ultimate tensile stress of the specific material as fatigue failure occurs due to the nucleation and gradual growth of microscopic cracks and dislocations. An in-depth discussion about material fatigue is given in reference [110].

Cyclic fatigue testing of the x-ray transmission windows was performed by applying a differential pressure load across the window in a periodic manner. The same measurement setup that was used for the burst pressure experiments (fig. 2.4) was used in combination with an automatic actuation of the solenoid valve. The pressure reducer was used to set the maximum pressure while the dosing valve was used to adjust the rise time of the pressure cycle. The pressure transducer monitored the high pressure side of the sample holder and a LabVIEW program was developed to actuate the solenoid valve if the desired maximum and minimum pressure values were reached within the pressure cycle. The software includes an integrity checking algorithm that stops the cycle test and closes the solenoid valve if the window breaks. A specific number of cycles could be chosen or the program would run until window failure. The program recorded the number of cycles as well as the maximum and the minimum pressure per cycle and stored the values in a data file. The solenoid valve could operate with a specified maximum frequency of 20 Hz but the testing frequency was limited by the rise time of the pressure within the sample holder. This was dependent on the angular position of the dosing valve and absolute pressure of the pressure reservoir. Frequencies above 3 Hz resulted in a significant pressure overshoot as such short rise times were only achieved by a large over-pressure of the pressure reservoir due to the limited cross section of the solenoid valve.

The differential pressure that acts across an x-ray window during the cycle test, with the maximum differential pressure set to 3200 mbar and the minimum pressure set to 100 mbar, is shown in figure 2.5 a). The shown test was performed with a cycle frequency of approximately 2.5 Hz. The behavior of the pressure as the test parameters were being changed is demonstrated in figure 2.5 b). The set maximum value was successively changed from 1000 mbar to 2000 mbar to 2500 mbar and to 3000 mbar, leading to the shown pressure values. The pressure of the pressure reservoir was increased at the time of 120 s, resulting in an increased testing frequency but also in a slight overshoot of the reached maximum pressure. During cyclic pressure testing, the maximum pressure value before closing the solenoid valve and the minimum pressure before opening the solenoid valve was recorded for each pressure cycle and the number of performed cycles stored in a log file.

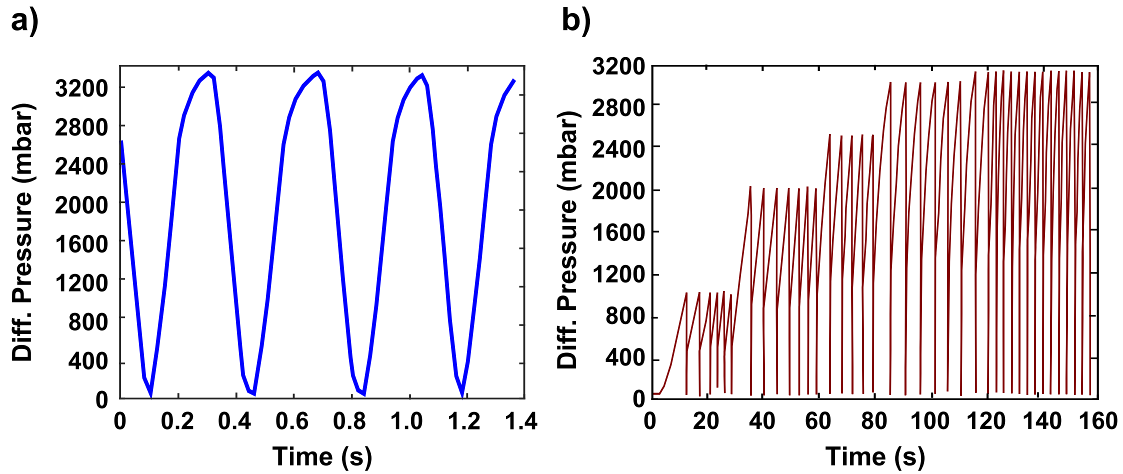

Figure 2.5: The pressure values during cyclic testing of a dummy window with a maximum differential pressure per cycle set to 3200 mbar and the minimum value set to 100 mbar, is shown in a). The resulting frequency was approximately 2.5 Hz. The influence of the chosen parameters on the pressure cycles are demonstrated in b). The maximum cycle pressure depends on the value set in the software, whereas the cycle frequency depends on the position of the dosing valve and the overpressure of the pressure reservoir.

2.1.3 Helium Leak Tightness

Helium is commonly used to evaluate the leak tightness of gas tight configurations as it exhibits a high diffusion rate, is chemically inert and only present at a very low concentration in the ambient environment as discussed in reference [111]. A commercial helium leak tester (Pfeiffer HLT 570) with a specified minimal detectable helium leak rate of 5×10^{-12} mbar l/s was used to measure the leak rates of the x-ray transmission windows. The to be tested x-ray window was glued into the cap of a TO8 housing, which was then placed in the sample holder of the helium leak tester, as shown in figure 2.6 a). The vacuum side of the helium leak tester and a helium reservoir at atmospheric pressure are separated by the cap and x-ray window. The helium detector is located within the vacuum side and the pressure difference across the window results in a high helium concentration gradient.

In order to obtain correct helium leak rate values, the helium diffusion through the sample holder and the interface of the x-ray window and the cap has to be minimized. The cap was therefore clamped by two sets of o-rings that are nitrogen purged in order to rule out diffusion through the seals, and the used adhesive was an epoxy with a very low gas diffusion rate that is commonly used for vacuum applications. A slight diffusion through the adhesive was sometimes observed

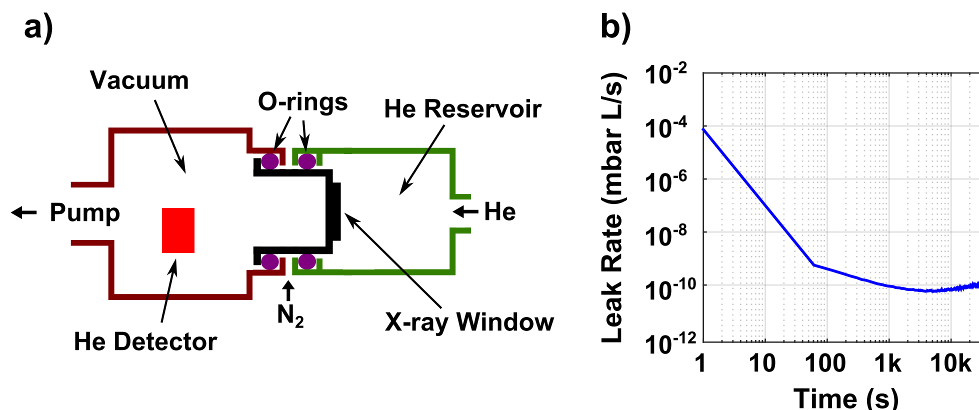

Figure 2.6: The schematic of the employed helium leak testing setup is depicted in a). A large helium concentration gradient was induced across the to be tested window and the diffusion rate measured by a helium detector. The helium leak rate for a tested GC x-ray transmission window is shown in b). A slight helium diffusion across the used adhesive appeared after 10k seconds of testing but was only observed if an insufficient amount of adhesive was used or the cross-linking was not conducted in an optimal manner.

during long time measurements of the helium leak rate as shown in figure 2.6 b). This occurred if an insufficient amount of adhesive was used or the cross-linking of the adhesive was not conducted in an optimal manner. Helium diffusion through the window was ruled out as this behavior was also observed during some of the helium leak rate measurements of very thin x-ray windows. The reduced thickness of the window should have otherwise led to an increased diffusion as well as a shorter time delay, which was not encountered.

2.1.4 Light Tightness

The light tightness of the x-ray transmission windows was evaluated depending on the application of the x-ray transmission window. X-ray transmission windows that are used in ambient lighting conditions need to be solar blind in order to shield the SDD detector from optical and infrared radiation. An attenuation of more than 1×10^{11} is seen necessary as discussed in Chapter 1.

Such high values of attenuation require a high efficiency low light detector such as a photomultiplier in order to measure the light intensity that passed the x-ray window as it was illuminated with a white light LED source. A commercial photomultiplier (Hamamatsu C10507-11-100C) with an active area of $1\,\mathrm{mm}^2$ and a photon detection efficiency of $45\,\%$ was used to record the ultra low intensity light levels. The detectable light intensity was limited by the noise level of the detector, which is specified with a typical value of 900 kcps and a maximum value

of 1500 kcps. Assuming an average energy of 1.84 eV per photon for the standard AM1.5 spectrum with an illumination intensity of 1000 W/m^2, results in a nominal photon flux of 1.22×10^{19} photons/s mm^2 during direct sunlight illumination [112]. An attenuation of up to 4×10^{12} can therefore be measured with the used photomultiplier before the transmitted light intensity falls below the detection limit. The to be measured x-ray windows were therefore illuminated and the intensity of transmitted light recorded with the photo-multiplier. A second measurement without illumination was taken in order to measure the dark count of the detector.

A more practical approach is to directly use the SDD as a low level light detector. The energy resolution of the SDD is strongly dependent on the intensity of the optical and infrared radiation, as the absorption leads to additional noise generation. It is therefore possible to determine whether the x-ray window is sufficiently light tight by measuring the energy resolution of the SDD detector under illumination. The window is seen as solar blind if the energy resolution is not altered due to the optical and infrared radiation. The resolution of the detector module was determined by irradiation with a narrow band radiative source such as a ^{55}Fe isotope source, emitting $Mn\,K\alpha$ radiation with an energy of 5.895 keV. X-ray spectra were acquired with and without direct illumination of the detector module and the FWHM value of the resulting $Mn\,K\alpha$ peak, as it was obtained from the detector readout electronics, was subsequently used to determine the detector resolution.

Low energy x-ray transmission windows are designed for a maximum x-ray transmission in the energy range below 2 keV and exhibit a reduced light blocking capability due to the minimal window thickness. Attenuation factors of less than 100 are common and the resulting light intensity, that passes the low energy x-ray windows, is too high to be measured with a photomultiplier [47]. The optical transmission of the low energy x-ray transmission windows was therefore measured with a commercial spectrometer (LD Didactic Compact Spectrometer) that incorporates a silicon photodetector with a specified resolution of 1 nm. The window was illuminated with a halogen light source with a maximum intensity at a wavelength of 580 nm and the optical transmission of the window was determined by measuring the spectrum of the light source with and without a window placed in front of the fiber input of the spectrometer.

2.1.5 Stability Against Ozone Exposure and X-ray Irradiation

Ozone is known to attack carbon compounds and is therefore seen as a potential threat to the integrity of carbon based x-ray windows. An ozone containing at-

mosphere was generated by placing an ultra violet (UV) light source within an airflow that was directed at the x-ray transmission window under test. The UV light source supplied a specified power of 4.5 W for the 184.9 nm wavelength that is relevant for ozone generation [113].

Radiation hardness is a crucial aspect for components that are used in an x-ray environment and Zhou et al. [114] have shown that the integrity of graphene can be deteriorated by soft x-ray radiation. The employed SDD detectors are guaranteed to withstand an irradiation with 1×10^{12} photons with an energy of 30 keV, which was subsequently seen as the minimum dose for the radiation hardness of an x-ray transmission window. The window under test was placed at a distance of 4 cm from a commercial x-ray tube (Oxford Eclipse 3), that was operated at an acceleration voltage of 30 kV and a current of 100 µA. The resulting dose per window area (for a window diameter of 7 mm) was calculated to be 9×10^8 photons per second. Irradiation of at least 18.5 minutes was therefore required to obtain the minimum required dose to evaluate the irradiation stability of the x-ray transmission window.

2.2 Evaluation Schemes for the Graphenic Carbon Window Material

The carbon window material was deposited by a chemical vapor deposition process and a detailed characterization of the material was necessary to optimize the deposition process and in order to evaluate the quality of the deposited material. A number of material properties were therefore determined, apart from the discussed window properties. These include the surface morphology, the GC thickness, the structural composition, the electrical conductivity and the mechanical properties including the Young's modulus and the residual stress of the deposited GC material.

2.2.1 Surface Morphology

The surface morphology of the deposited GC material is strongly dependent on the micro-structure of the material and the deposition process. While HOPG surfaces are atomically flat after cleaving, which is a result of nearly ideally orientated crystallites of sp^2 hybridized carbon atoms, isotropic pyrolytic carbon commonly exhibits a spherical growth from nucleation sites with a higher resulting surface roughness. Carbon black on the other hand is known for its low reflectivity due to a porous micro-structure and resulting low density. The analysis of the surface morphology of the deposited GC material is therefore a simple way for a first estimate of the material properties.

Visual Characterization

GC is known to deposit with a high surface conformity and the use of prime wafer grade silicon substrates results in an extremely smooth surface after deposition [115]. The deposited GC samples should therefore exhibit a metallic luster with high reflectivity.

Optical Microscopy

Optical microscopy was used to evaluate the surface morphology. Particles and surface deformations were identified using this method, which allows a first evaluation of the employed deposition parameters. A sufficiently high lateral resolution allowed to evaluate the structuring process of the silicon bulk and GC window material. A length calibration was performed and permitted the measurement of the dimensions of the window geometry and back illumination of the free standing GC films was employed to verify the absence of pin holes prior to helium leak testing.

Scanning Electron Microscopy

Scanning electron microscopy (SEM) was used for high resolution imaging of the GC surface and the window geometry. The used system (Hitachi S4500) allowed a detailed evaluation of the surface morphology and window geometry. Cross section images of the GC samples were obtained by breaking the GC coated silicon substrates along the sharp edge of a glass substrate and was subsequently imaged using a vertical sample holder.

Atomic Force Microscopy

The morphology and surface roughness of the deposited GC material was analyzed by tapping mode atomic force microscopy (AFM) measurements [116, 117]. Tapping mode AFM offers high resolution 3D imaging by scanning the surface of a sample with the atomic tip of an oscillating cantilever [118, 119]. The interaction between the cantilever tip and the sample surface results in a force that influences the resonance frequency of the cantilever. The change in amplitude and phase of the oscillation is therefore a measurement of the tip surface interaction. Topographical information of the surface is extracted by implementing a control loop that keeps the oscillation amplitude of the cantilever constant (constant force mode) by altering the tip to sample distance. The low frequency vertical motion of the cantilever is subsequently used to map the topography of the surface.

The obtained height values were used to determine the surface roughness of the sample [120]. A commonly used characteristic value is the root mean square (RMS)

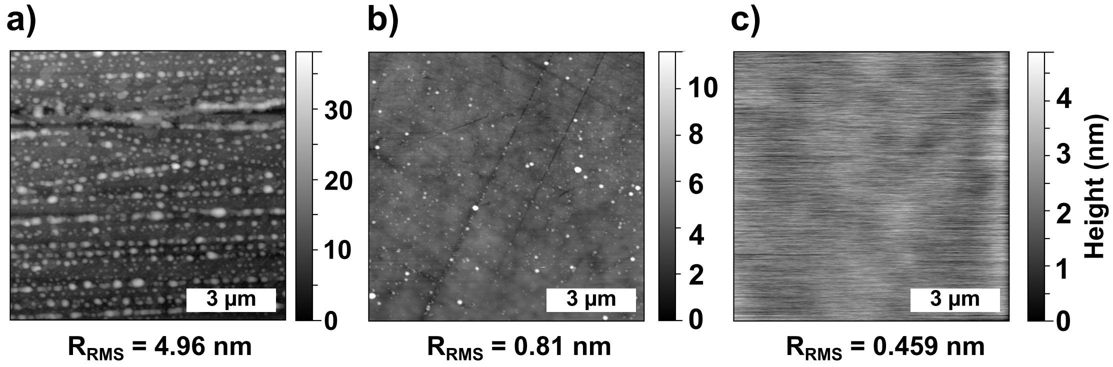

Figure 2.7: Atomic Force Microscopy was used to evaluate the surface morphology and surface roughness. A 10 µm × 10 µm AFM surface image of a quartz microscope slide is shown in a), of a polished quartz wafer in b) and of an extremely smooth TXRF quartz sample holder in c). The corresponding R_{RMS} values are given below the images and are in line to the observed surface morphology.

value of a surface. Equation 2.4 shows the used calculation method with n denoting the number of sampling points and z the corresponding height values [117]. The R_{RMS} value is therefore the standard deviation of the distribution of measured height values.

$$R_{RMS} = \left(\frac{1}{n} \sum_{i=1}^{n} z_i^2 \right)^{\frac{1}{2}} \tag{2.4}$$

The exemplary surface morphology and the extracted R_{RMS} values of the surface roughness for three different types of quartz substrates, as obtained with the used AFM system (Bruker Dimension Icon), are shown in figure 2.7. A large difference in the surface morphology is visible. The quartz slide (a) exhibits a high surface roughness ($R_{RMS} = 4.96\ nm$), whereas the surface of a polished quartz wafer (b) is much smoother ($R_{RMS} = 0.81\ nm$). Individual scratches from the used polishing slurry are visible. The third image (c) is from an ultra smooth quartz sample holder as it is used for total reflection x-ray fluorescence spectroscopy (TXRF), which requires an extremely smooth surface ($R_{RMS} = 0.459\ nm$). Line artifacts in the image are assumed to arise from the approaching resolution limit of the used imaging system. The demonstrated surface images of the quartz samples shows the capability of the used AFM measurement system in order to quantify the surface roughness.

2.2.2 Raman Spectroscopy of the Graphenic Carbon Window Material

Organic molecules exhibit a strong Raman signal, which has made Raman spectroscopy an important method for the analysis of carbon allotropes, including carbon nanotubes and graphene as well as other forms of carbon [121]. Raman spectroscopy is a non-destructive method of characterizing the deposited GC films and the theory and measurement scheme is discussed briefly.

A narrow band excitation source is used to illuminate the material of interest and a spectrometer employed to determine the wavelength dependent intensity of the returned light. Inelastic scattering leads to a characteristic wavelength shift, which can be associated with a specific binding type and scattering event. In the case of carbon allotropes, this allows the distinction between sp^2 and sp^3 hybridization [122], offers information regarding the structural composition [123] and is also sensitive to geometric differences such as the diameter of carbon nanotubes [124] and number of layers of graphene sheets [125].

Raman spectroscopy was conducted with a commercial Raman spectrometer from *B&W* Tek (inno-Ram-532H) with an excitation wavelength of 532 nm, a specified spot size of 10 µm and a maximum optical output power of 50 mW. The used Raman spectrometer is schematically shown in figure 2.8 a). The Raman spectrum of the deposited GC material is dominated by the Raman signal of sp^2 hybridized carbon as it is resonance enhanced compared to the response of the sp^3 hybridized carbon [126]. This leads to three dominant peaks, which are a result of the relative motion of sp^2 bonded carbon atoms (D-Peak), of the radial breathing mode of the typical sp^2 carbon hexagonal ring (G-Peak) and for sufficiently ordered pyrolytic carbon, a second order Raman feature that results from the same mechanism as the D-Peak (2D-Peak) [122, 127]. The position of the G-Peak is independent of the used excitation wavelength while the D and 2D peak are energy dispersive, as their position varies with the energy of the incident photons [126]. An excitation source with a wavelength of either 514 nm, 532 nm or 633 nm is commonly used for the analysis of graphitic carbon while UV Raman Spectroscopy with a wavelength of 229 nm or 244 nm is more suited for carbon compounds with predominantly sp^3 bonded carbon [127]. The following discussion and peak positions, are applicable for Raman spectroscopy with a wavelength of 532 nm, unless otherwise noted.

An integration time of 10 minutes was chosen for the GC samples and a dark measurement performed prior to the spectrum acquisition in order to increase the signal to noise ratio. A typical Raman spectrum, as it is obtained for GC that has been deposited onto a silicon substrate, is given in figure 2.8 b). The D and

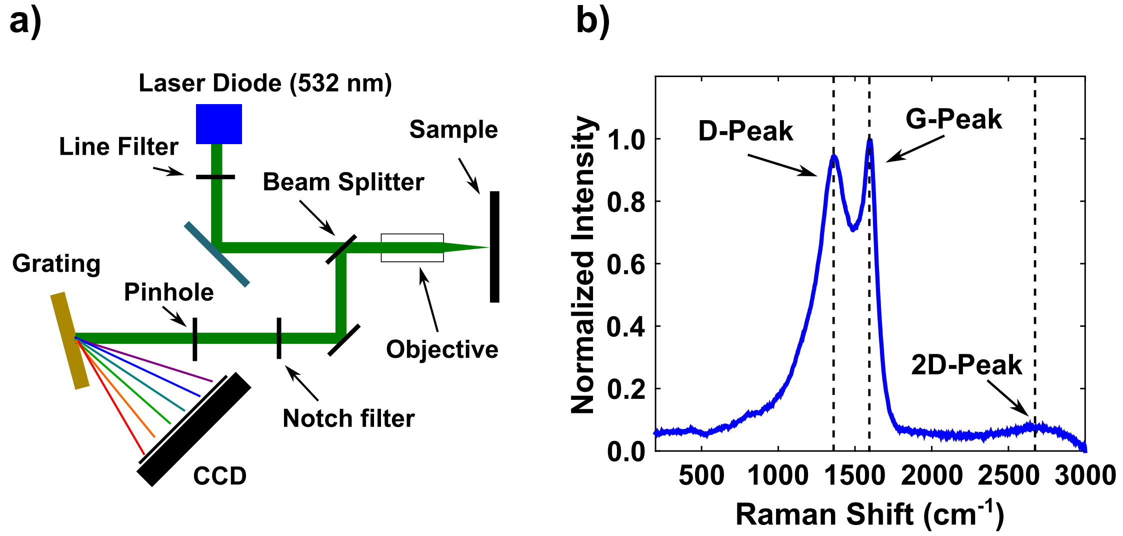

Figure 2.8: The used Raman Spectrometer is schematically shown in a). A laser diode with a wavelength of 532 nm was used as an excitation source and focused onto the sample with a microscope objective. The returned light was analyzed by a spectrometer and the spectral intensity distribution subsequently evaluated. A typical Raman spectrum of the GC material is given in b). The D-,G- and 2D-Peak positions are indicated.

G-Peak at 1365 cm^{-1} and 1595 cm^{-1} respectively, are clearly visible while the 2D Peak intensity, at a wave number of 2683 cm^{-1}, is low but still distinguishable.The observed Raman features are a result of the atomic structure of the GC material. Theoretical models that explain the signal formation have been developed and are available for interpretation of the Raman spectra and will be briefly discussed in the following.

The D-peak, located at a wave number of approximately 1360 cm^{-1}, is a defect induced Raman feature of sp^2 hybridized carbon [128, 129]. A perfect hexagonal carbon lattice therefore does not exhibit a D-peak feature in the Raman spectrum [130]. The intensity of the D-peak, compared to the other Raman features, is therefore commonly used as a figure of merit for graphene synthesis and transfer processes [125]. The interpretation of the D-peak intensity becomes more complex if polycrystalline and amorphous carbon containing materials are probed as described by Ferrari et al. [122].

The G-peak feature arises from the radial breathing mode of the hexagonal structure of sp^2 hybridized carbon and the existance of a G-peak feature is seen synonymously to the presence of sp^2 hybridized carbon [130]. The intensity ratio of the D- and G-peak is therfore generally used to quantify the defect density in

graphitic materials [130].

The Tuinstra-Koenig model (TK-model) relates the intensity of the G-Peak and D-Peak to the grain size of graphitic materials, as shown by equation 2.5 [131]. With L_a denoting the crystallite size, $C(\lambda)$ an excitation energy dependent constant and I(D) and I(G) the signal intensity of the D-peak and G-Peak, respectivly. The relationship is dependent on the used excitation wavelength of the Raman spectrometer and results in a value of $C(532\ nm) = 4.96\ nm$ for the used equipment [132]. More recent work has shown that this relationship is not valid in a general manner but depends strongly on the type of the carbon material [122,123,133]. The shown TK-model relation is seen applicable for a crystallite size above 2 nm and for materials with a high proportion of sp^2 hybridized carbon [122].

$$\frac{I(D)}{I(G)} = \frac{C(\lambda)}{L_a} \tag{2.5}$$

The development of the 2D-peak is attributed to the overall level of graphitization corresponding to a high ordering and planar orientation of the sp^2 hybridized crystallites, as the formation of the 2D-peak is highly sensitive towards disorder along the c-axis of the graphitic material [130].

Fitting the theoretical peak components to the obtained Raman spectrum is necessary in order to quantify the data, making the data available for comparison and analysis. Unless otherwise stated, the obtained data is normalized to the intensity of the Raman feature with the highest intensity of the obtained spectrum, which is in most cases the G-peak. This rules out the impact of altering signal strength which can be dependent on the sample position and optical properties.

Ferrari et al. postulate in reference [122] that any form of sp^2 hybridized carbon can be fitted by using a Lorentzian peak shape (equation 2.7) for the D-Peak and a Breit-Wigner-Fano (BWF) peak shape (equation 2.6) for the G-Peak with I_0 denoting the peak intensity, ω_0 denoting the peak position, Γ denoting the FWHM and Q^{-1} denoting the Breit-Wigner-Fano coupling coefficient. The BWF peak shape has the advantage of covering trailing peaks that are normally found on the right and left side of the G-Peak and is therefore an elegant alternative to a peak fitting with four instead of the postulated two peaks. It is stated by Ferrari et al. [122] that the choice of the peak shape is not possible a priori which means that the peak shape evolution is not fully understood.

Fitting was performed with Matlab utilizing the curve fitting package. The standard deviation of the G-Peak position, as measured on the same sample, was found to be $0.97\,\mathrm{cm}^{-1}$ for the used Raman spectrometer.

$$I(\omega) = \frac{I_0 \left[1 + \dfrac{2(\omega - \omega_0)}{Q\Gamma}\right]^2}{1 + \left[\dfrac{2(\omega - \omega_0)}{\Gamma}\right]^2} \tag{2.6}$$

$$I(\omega) = \frac{I_0}{1 + \left[\dfrac{2(\omega - \omega_0)}{\Gamma}\right]^2} \tag{2.7}$$

2.2.3 Thickness Measurements

The window thickness is a crucial aspect as it determines the x-ray transmission and mechanical stability of an x-ray window for a given window material. The thickness measurement is also a prerequisite in order to determine the deposition rate during the development of the deposition process.

The GC thickness was measured by removing parts of the thin GC material and measuring the height of the resulting step between the substrate and the GC material. The processing steps involved in structuring the GC material are schematically shown in figure 2.9 a). The GC coated silicon sample shown in sub-figure i) is cleaned with acetone and isopropanol to remove any residues in order to avoid adhesion problems. Radio Frequency Magnetron sputtering is used in combination with a shadow mask to partially cover the surface with a 100 nm thick titanium layer as depicted in sub-figure ii). An oxygen plasma treatment was subsequently used to remove the GC material that was not protected by the titanium mask as shown in sub-figure iii). A microwave plasma system was used with a high resulting GC etch rate of approximately 100 nm/min. The titanium masking layer was finally removed with hydrofluoric acid after visual inspection verified the complete removal of the GC material as shown in sub-figure iv). A micrograph of the sample surface after the structuring process of the GC layer is depicted in figure 2.9 b).

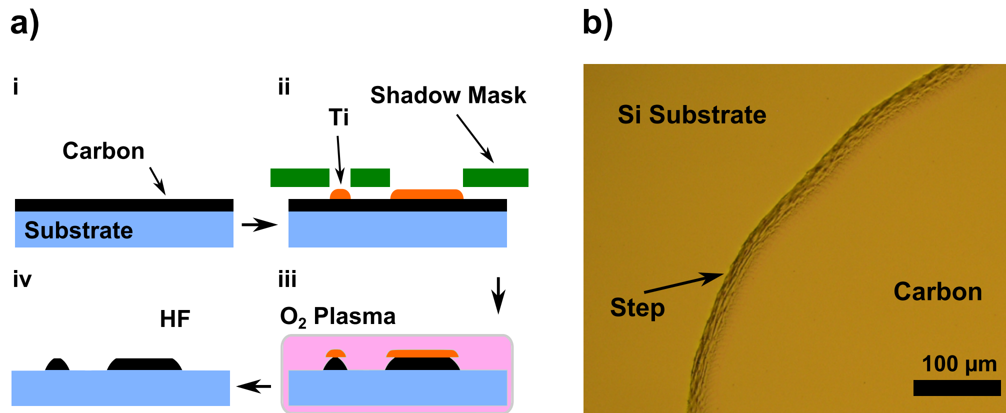

Figure 2.9: The process steps required for the step fabrication of the GC window material are schematically depicted in a). The carbon coated substrate was cleaned (i) and a titanium mask subsequently deposited onto the GC surface (ii). Oxygen plasma was employed to remove the uncovered GC material (iii) and the titanium was removed by a hydrofluoric acid bath (iv). A micrograph of the surface after the structuring process is shown in b). The top left of the image shows the bare silicon substrate while the bottom right is still covered by the GC material. The step is indicated by the arrow.

Atomic Force Microscope Measurements

AFM measurements were performed to determine the height of the fabricated steps of the GC material. The used AFM (Bruker Dimension Icon) has a vertical range of up to 12 µm, which is sufficient for the thickness measurements. A measured line profile is shown in figure 2.10 a). The line profile was extracted from the 3D data shown in figure 2.10 b). The large measurement area of 30 µm × 30 µm requires a scanning time of approximately 30 min due to the slow scanning speed of the AFM tip in order to avoid damage to the extremely sharp tip. The step transition separates the smooth silicon surface (left) and the smooth carbon surface (right). The step transition exhibits a rough surface due to the attack of the oxygen plasma in contrast to the carbon material that was covered by the titanium mask. A large scanning area is required in order to cover the complete step transition and to verify that the horizontal plateau of the carbon surface is the actual film height. The step height was extracted from the line profiles by setting the lower plane to zero and determining the height of the GC plane.

The AFM measurement scheme was found to be highly reliable for thicknesses below 800 nm but measurements of thicker samples led to a large deviation from measurement to measurement. In addition, the measurement and setup time for the AFM measurements is long which makes the thickness measurements a very time consuming task.

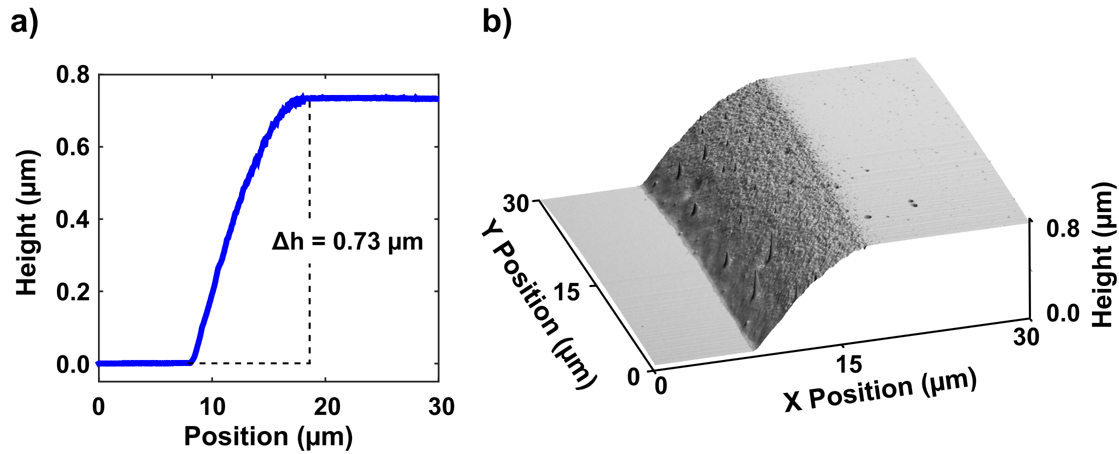

Figure 2.10: The extracted line profile across a measured step of the carbon material is shown in a). The corresponding 3D representation of the data obtained during the 2D scan of the carbon step is depicted in b). The left side of the image shows the silicon surface and the right side shows the carbon surface. The step transitions is seen in-between.

White Light Interferometry Measurements

As an alternative, an optical measurement setup was developed in order to measure window thicknesses above 800 nm and to reduce the required measurement time. Common, single wavelength, interferometric sensor systems are known for an extremely high resolution but are limited to continuous surface profiles as the unambiguous measurement signal repeats after a measurement range of $\lambda/2$ [134]. White light interferometry (WLI) overcomes this problem by employing a number of light sources with varying wavelengths and evaluating the wavelength dependent light intensity of the returned measurement signal [135]. The measurement setup of the used optical displacement sensor (Keyence SI-F01) is schematically depicted in figure 2.11 a).

A light source with a spectral range from 810 nm to 830 nm and an output power of 0.6 mW is used and the emitted light coupled into an optical fiber. A first reference reflection occurs at the sensor head at the end of the optical fiber. This reference signal and the measurement signal, which is reflected at the sample surface, is focused onto a diffraction grating that splits the signal into its spectral components by reflecting them onto a Charge Coupled Device (CCD) detector. The signal intensity of the pixels of the CCD detector are mapped to a specific wavelength and the resulting intensity distribution is used to determine the distance between the sensor head and sample surface. The underlying effect is the interference between the reference signal and measurement signal, which leads to

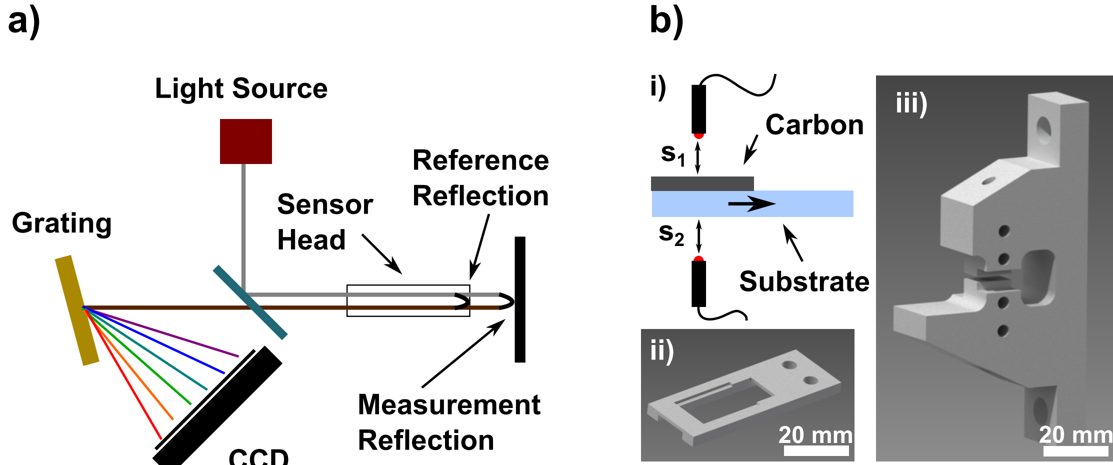

Figure 2.11: A schematic of the used optical displacement sensor system is given in a). The distance between the reference plane at the end of the sensor head and the sample surface was measured. The employed dual sensor head setup is schematically shown in b) and allows a differential measurement scheme as shown in sub-figure i). The sample was placed in the sample holder depicted in sub-figure ii), and sub-figure iii) depicts the designed dual sensor head holder. The sample holder passes through the gap between the two sensor heads during the measurement.

different path lengths requirements, for the different wavelengths of the light, in order for constructive interference to occur. The used WLI sensor therefore allows absolute distance measurements for a large unambiguous measurement range of 1.05 mm with a high resolution of 1 nm. The used system offers a spot size of 20 µm and a maximum sampling frequency of 5 kHz.

A dual sensor configuration was developed which allows a differential height reading. This has the advantage of canceling out any vertical motions, such as vibrations, of the sample. A schematic of the configuration is shown in the sub-figure i) of figure 2.11 b). The two sensor heads are placed at a fixed position facing each other with an overlapping measurement range. The sample that is to be measured is passed through the gap of the two sensors, each of them recording the measured distance between the sensor head and the sample surface, denoted as s_1 and s_2. The sum of the two values is used as a reference value and subtracted from the measurement signal $h = s_1 + s_2$ that is obtained while moving the sample perpendicular to the sensor arrangement. The step height and thus the film thickness is the absolute value of the measurement signal. The schematic of the used sample holder is depicted in sub-figure ii) of figure 2.11 b). The window or coated substrate is placed in the frame that is connected to an xyz stage (Newport M-562-XYZ) that offers a motorized x and y axis (CONEX-TRA12CC) with a lateral resolution of 1 µm. The schematic of the designed sensor holder is shown

in sub-figure iii) of figure 2.11 b). The sensors are introduced from the bottom and from the top and are each clamped by two plastic screws. The sample holder moves the sample through the gap that is formed by the two sensors.

A LabVIEW program and measurement environment was developed by the student Lukas Holzbaur. The program was designed to record the measurement data of the displacement sensors, that was made available by the sensor controller interface, and to control the x and y stepping motors of the motorized stage. The software user interface was used to position the sample holder accordingly and to define the lateral step size, the number of averaged measurements taken per step and the total length of the line scan. Data evaluation is included in the software environment, allowing the user to fit a step function to the obtained data. The resulting measured step height is displayed and the measurement data was subsequently written to a desired data file.

Line Profile Measurements

The measurement results obtained during the thickness measurement of an x-ray window are demonstrated in figure 2.12. In this case, the line scan moved down a structured step, from the carbon material (left) onto the silicon substrate (right). The determined step height and thus window thickness was 0.68 µm. Four successive measurements were taken, with a lateral step size of 5 µm and an averaging of 10 measurement values per position. Inset i shows the low noise level of the individual measurements with an approximate value of $\pm 10\ nm$ and a signal spread of approximately 25 nm. Inset ii shows the standard deviation that was calculated for the four measurements for each position. The value is below 11 nm apart from the actual step region. The large deviation at the transition region results from a lateral drift of the stage as can be seen in the main figure. An overshoot is visible at the abrupt edge transition, which is assumed to be a result of optical effects due to the relatively large spot diameter of 20 µm compared to the lateral step size of 5 µm.

3D Topography Measurements

WLI microscopes have reached a technological maturity making them a versatile tool for 3D topography measurements, offering a high vertical and lateral resolution [136]. The data is obtained by scanning the 2D surface of the sample and determining the vertical height of the surface, pixel by pixel. A similar approach is possible with the discussed white light interferometric displacement sensor in combination with a motorized stage and suitable a software.

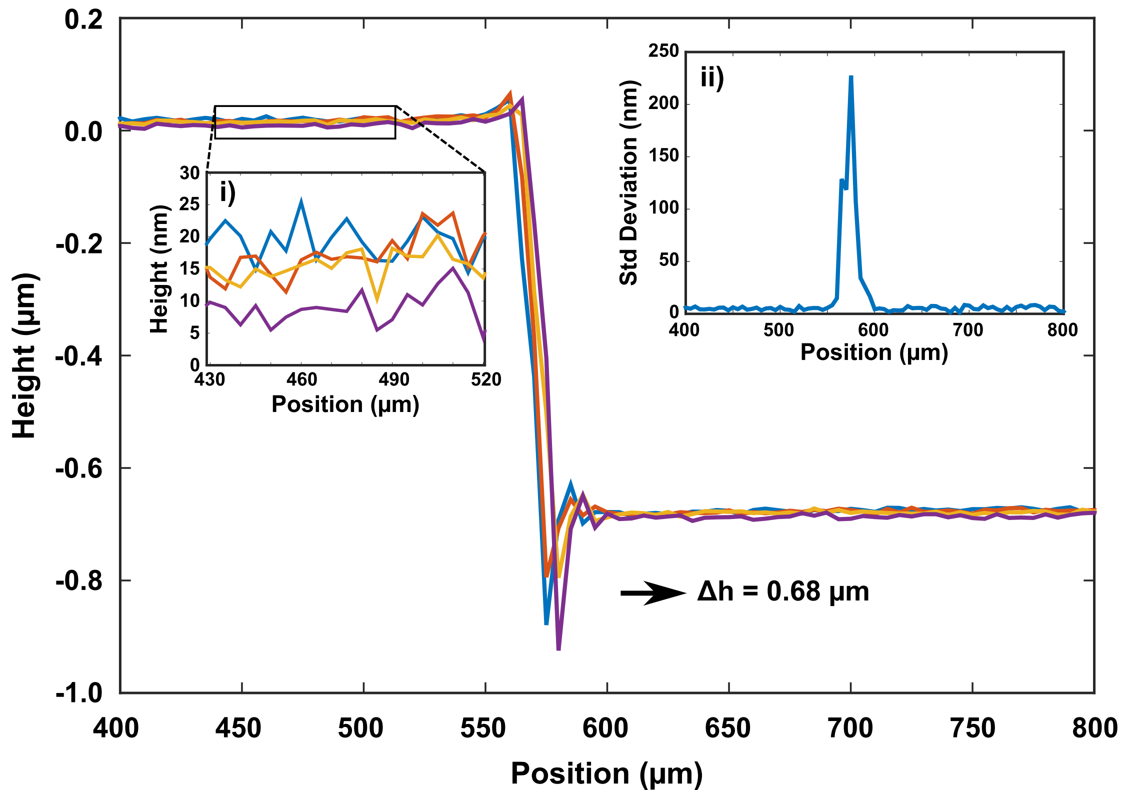

Figure 2.12: Four successive differential thickness measurements of a GC film, employing the dual sensor setup, are displayed. A low signal noise of $\pm 10\ nm$ was identified, as shown in inset i) offering a more detailed view of the measurements. Inset ii) shows the standard deviation of the four measurements for each position. A large value is only obtained at the step transition and results from the lateral drift of the stage.

A single sensor holder was designed that was placed above the motorized stage. The developed LabVIEW program was complemented by a 2D scanning mode. The x and y dimensions of the sample area, the x and y spacings and the number of averaged samples per height measurement are used to generate an automatic scanning motion of the motorized stage. The displacement sensor is used to measure the height of each pixel, which is then used to reconstruct the topographic information of the sample surface. The resulting 3D image of a structured window film is given in figure 2.13 a). The word KETEK was etched into a 1.2 µm thick GC film until the silicon surface was reached. The scan size is approximately 80 µm × 80 µm and the 3D image can be used to determine the film thickness by extracting a line profile. The line profile, as obtained by scanning across the letters "T" and "E", is shown in figure 2.13 b).

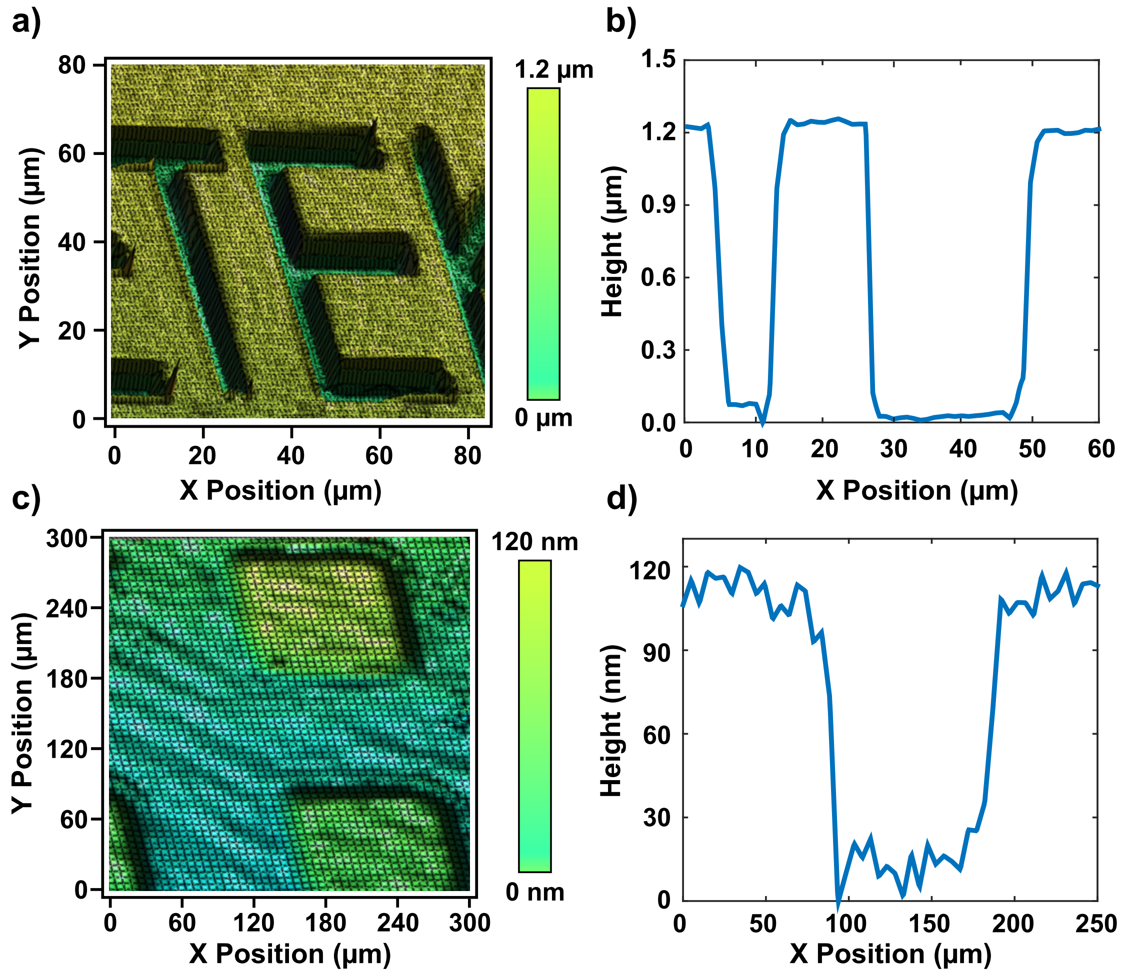

Figure 2.13: The 3D reconstructed data of a structured surface region of a 1.2 µm thick carbon film that has been deposited on a silicon substrate is shown in a). The word "Ketek" was etched into the carbon film with an oxygen plasma treatment and the extracted line profile across the letters "T" and "E" is depicted in b). Features with a reduced height can also be measured as demonstrated by the 3D reconstruction of a structured iron film with a height of 116.9 nm, as shown in c). The corresponding line profile is given in d).

The capability of the developed measurement system is demonstrated in figure 2.13 c). A structured iron thin film with a height of approximately 100 nm was deposited onto a silicon substrate. A measured height of 102 nm was extracted by a 2D scan with a scan size of 300 µm × 300 µm. The step height was verified by a commercial Dektak profilometer and determined to be 116.9 nm, which verifies a high measurement accuracy of the developed system.

Electrical Conductivity based Thickness Measurements

An alternative thickness measurement scheme is to use the thickness dependent conductivity of the deposited GC films in order to determine the film thickness. A linear dependency of the conductivity and GC thickness was identified and used to determine the GC thickness. This method was employed to determine the thickness distribution during the wafer scale deposition of the GC material. The measurement scheme is discussed in section 2.2.5.

2.2.4 Mechanical Characterization

Mechanical characterization schemes are necessary for an in-depth understanding of the GC window material.

Young's Modulus, Poisson's Ratio and Ultimate Tensile Strength

The Young's modulus, denoted as E, of a material describes the linear relationship of elastic strain and stress as defined in equation 2.8, with σ denoting the stress and ϵ the strain of the material [137]. Considering the uni-axial case, stress is defined as the force, denoted as F, per cross section area, denoted as A, and strain as the relative axial length change, as shown by equation 2.9 and 2.10, respectively.

$$E = \frac{\sigma}{\epsilon} \tag{2.8}$$

$$\sigma = \frac{F}{A} \tag{2.9}$$

$$\epsilon = \frac{l_0 - \Delta l}{l_0} \tag{2.10}$$

Elastic polymers exhibit a very low Young's modulus, for example the widely used elastomer polymethylsiloxan (PDMS) has a Young's modulus of 0.36 MPa to 0.87 MPa [138], whereas monolayer graphene exhibits a Young's modulus of 1 TPa [63]. While the Young's modulus describes the stiffness of the material in

the direction of stress and strain, the Poisson's ratio of a material is given by the ratio of in plane and out of plane deformation as a material is compressed or strained. A Poisson's ratio of 0.16 is assumed for the GC material as it corresponds to the bulk value of graphite in the basal plane and has been proposed for graphene [139, 140]. A high Young's modulus does not necessarily lead to a mechanically strong material but a high ultimate tensile strength is also required. The ultimate tensile strength is defined as the stress that needs to be applied in order to induce material failure.

Residual Stress

The residual stress of a material is of special interest as it has a significant impact on the material properties and processability if it is deposited onto a substrate. Residual stress is defined as the stress value that is present within the thin film at ambient conditions [141]. Such stress arises, among others, from a lattice mismatch in epitaxially grown films or from a difference in the thermal expansion coefficient (CTE) of the deposited film and the substrate, if the deposition takes place at non-ambient conditions.

Depending on the application, tensile, compressive or stress free films may be desirable. A high compressive stress is beneficial for protective coatings as compressive stress increases the hardness and scratch resistance, as exploited for modern touch screen technologies [142], but compressive stress can also lead to delamination from the substrate [143]. Stress free films are required for large free standing structures or for the fabrication of flat cantilevers [144], whereas a slight tensile stress is beneficial for membrane applications such as silicon nitride (MEMS) microphones or pressure transducers. This arises from the fact that compressively stressed thin films buckle if free standing structures are fabricated, while a tensile stressed film results in taut membranes that exhibit a reduced deflection if a differential pressure is applied [145, 146].

2.2.4.1 Bulge Testing

Bulge testing is a commonly used method to extract the Young's modulus of a thin film material [147]. The method is based on the pressure dependent deflection of a thin film membrane structure. Free standing membranes of the GC material are fabricated as described in Chapter 4 and subsequently used to employ the bulge testing technique. A differential pressure was applied across the free standing film and the pressure dependent deformation of the thin film material is dependent on the material properties. The mathematical models available to describe the deformation of the tested material, and thus allow the extraction of the material constants from the obtained measurements, are discussed in the following.

Catlin et al. [148] developed a first model to describe the center deflection of round membranes in dependence of the bi-axial modulus of the material, the film thickness, the radius of the membrane and the applied differential pressure. The model is based on the assumption of a spherical bulge shape and a homogeneous bi-axial stress and strain distribution throughout the membrane. This allows the relatively simple extraction of the Young's modulus by simultaneously recording the center deflection and differential pressure using equation 2.11. With Δp denoting the applied differential pressure, t the film thickness, r the membrane radius, ν the Poisson's ratio of the material, Y the bi-axial modulus of the material and s the center deflection. The bi-axial modulus is defined as $E/(1-\nu)$, with E denoting the Young's modulus and ν the Poisson's ratio of the material [149].

$$\Delta p = \frac{8Yt}{3r^4}s^3 \tag{2.11}$$

The introduced model by Catlin et al. [148] ignores the fact that a truly bi-axial stress and strain state is only present at the membrane center, whereas a uni-axial stress and strain state exists at the membrane edges. The bulge model has therefore been continuously improved by various groups based on energy minimization methods [150] and finite element simulations [151], in order to obtain a better model. Equation 2.12 shows the derived model for round membranes with Δp denoting the applied differential pressure, t the film thickness, r the membrane radius, σ_0 the residual stress of the thin film material, ν the Poisson's ratio of the material, E the Young's modulus of the material and s the center deflection.

$$\Delta p = \frac{t}{r^2}s\left[4\sigma_0 + \frac{7-\nu}{3r^2}\frac{E}{1-\nu}s^2\right] \tag{2.12}$$

The idea of bulging long rectangular, instead of circular or square membranes was introduced by Vlassak et al. [152] with the postulated advantage of a solely uni-axial stress and strain state throughout the thin film, across the narrow region of the membrane. It was shown that this is the case for rectangular membranes with a side aspect ratio greater than four [153]. Using rectangular structures therefore avoids the transition from a bi-axial stress and strain state at the membrane center to a uni-axial stress and strain state at the membrane edge. This leads to a slightly different relation between the applied pressure and resulting center deflection as given by equation 2.13 with Δp denoting the applied differential pressure,

t the film thickness, r the membrane radius, σ_0 the intrinsic stress of the thin film material, ν the Poisson's ratio of the material, E the Young's modulus of the material and s the center deflection.

$$\Delta p = \frac{t}{r^2} s \left[2\sigma_0 + \frac{8}{6r^2(1+\nu)} \frac{E}{1-\nu} s^2 \right] \tag{2.13}$$

The introduced models assume a stress free or taut thin film membrane. Compressive stress of the thin film leads to buckling of the window material as the substrate material is removed to fabricate the free standing membrane. Unfortunately, carbon materials deposited from the gas phase at elevated temperatures are known for their compressive stress including for example ultra-crystalline diamond and pyrolytic carbons, with some groups reporting residual compressive stress levels of up to 85 GPa [154]. The wrinkles, that are subsequently formed in the free standing GC material, have a significant effect on the observed pressure dependent deflection of the thin film as discussed below while introducing the developed measurement scheme.

Measurement Scheme

The discussed WLI sensor system (Section 2.2.3) was used in combination with the discussed vacuum test setup (Section 2.1.2) in order to measure the differential pressure dependent center deflection of a thin film membrane. The vacuum sample holder was placed on an xyz-stage below the WLI sensor. The x and y axis are motorized and allow a minimal step size of 1 µm. The differential pressure that acts across the membrane was pre-set by regulating the pumping speed with two dosing valves and recorded using a pressure transducer.

The center deflection of the membrane was determined for a given differential pressure by scanning across the window geometry by moving the stage below the WLI displacement sensor. The schematic of the measurement setup is shown in figure 2.14 a). The stage movement was controlled by a PC user interface that allows the simultaneous recording of the deflection and differential pressure. The introduced LabVIEW software environment was complemented by a script to automatically find the membrane center. This was achieved by scanning the pressure loaded membrane in a cross wise manner until the point of maximum deflection was found. This is necessary as line profiles across the membrane that do not intersect the membrane center result in an incorrect measurement of the membrane deflection.

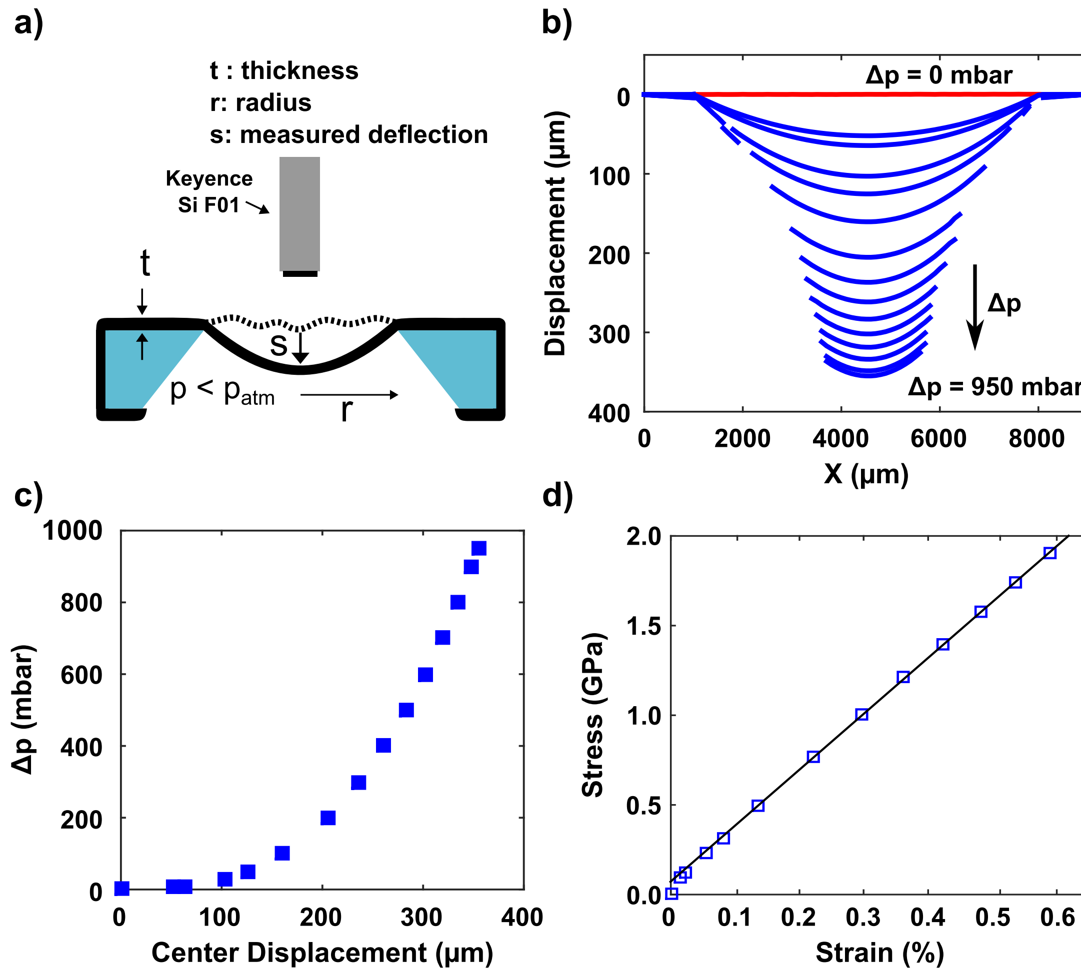

Figure 2.14: The measurement principle during bulge testing is schematically shown in a). A differential pressure Δp is applied across the membrane geometry with the radius r and the membrane, with a thickness t, is deflected downwards. A WLI displacement sensor (Keyence SiF01) is used to scan across the membrane geometry in order to acquire the membrane deflection s. The wrinkles, that are formed in a free standing GC film, are indicated. The obtained line profiles of a SiN test membrane with a diameter of 7 mm and a thickness of 400 nm are given in b) for increasing differential pressures. The maximum, applied, differential pressure is 950 mbar and results in a center deflection of approximately 350 µm. The extracted, pressure dependent, center deflection of the SiN membrane is depicted in c) and the calculated strain-stress values of the SiN membrane material, as calculated with equations 2.14 to 2.16 are shown in d).

The developed bulge test setup was evaluated with a silicon nitride (SiN) membrane in order to determine the feasibility of the proposed measurement scheme. The thin film exhibited a slight tensile residual stress and is therefore seen compatible with the introduced models.

The measured membrane profiles for increasing differential pressures of a SiN membrane with a diameter of 7 mm and a thickness of 400 nm, are shown in figure 2.14 b). The top most profile (red) is obtained without a differential pressure and the deflection increases as the differential pressure is increased up to a maximum of 950 mbar. It should be noted that the differential pressure was set in a non-monotonical order to rule out any hysteresis effects. The sensor signal is lost at the edge of the SiN membrane as the large center deflection results in a significant membrane slope towards the edges and the reflected signal intensity is insufficient.

The Young's modulus E and intrinsic stress σ_0 of the material can be extracted by applying equation 2.12, if the contributing values are known. The center deflection s, the film thickness t, the differential pressure Δp and the radius a of the circular membrane geometry therefore have to be determined. A Poisson's ratio of 0.23 for low stress SiN is found in literature [155]. The used WLI sensor offers a high specified resolution of 1 nm and the measurement of the deflection is regarded as highly accurate as the total center deflection is in the order of several hundred micrometers. The thickness of the membrane thin film was determined as discussed in section 2.2.3 and an accuracy of approximately $\pm 10\ nm$ is seen as realistic for the used measurement setup. The radius of the circular membrane geometry was measured with a calibrated optical microscope and as equation 2.12 is highly sensitive on the radius a the radius, also measured using a profile scan with the WLI sensor and a step size of 10 µm. The measured radius is subsequently assumed to be within $\pm 5\ \mu m$ of the real value. The applied differential pressure was measured with a pressure sensor (DP101AEP Panasonic) with a specified measurement range of −1 bar to 1 bar and a repeatability of ±0.1 % full scale, corresponding to $\pm 2\ mbar$.

The center deflection of the membrane at a corresponding differential pressure was extracted from the line scans and shown in figure 2.14 c). The obtained data were fitted to the introduced deflection model that led to equation 2.12 and resulted in a Young's modulus of 262 GPa and a residual tensile stress of 87 MPa. The fitting procedure was seen as highly accurate with an R-square value of 0.9999 and the previous considerations regarding the measurement accuracy of the individual components of equation 2.12 resulted in an uncertainty of $\pm\ 8GPa$ for the Young's modulus and $\pm\ 2\ MPa$ for the residual stress. The extracted values approach those found in literature as Edwards et al. [155] measured a Young's modulus of $255\ \pm\ 5\ GPa$ and a residual tensile stress of 114 MPa to 130 MPa for

low stress silicon nitride films. The measurement system was therefore regarded as sufficiently accurate for estimating the Young's modulus and residual stress of a thin film material.

Measurements performed with the deposited GC material were fitted to the presented deflection models but the results were inconsistent and the fitting of poor quality. It was assumed to be a result of the compressive residual stress of the GC material. It has been shown by Small et al. [150], that even if a large differential pressure is applied across the membrane, the edge region still exhibits a significant amount of compressive stress and they concluded that the discussed models cannot be used to extract the Young's modulus from compressively stressed thin films.

Therefore an alternative approach was chosen. The definition of the Young's modulus is the ratio of strain and stress within the material as given by equation 2.8. If the stress and strain states of the membrane are known it is therefore possible to directly determine the Young's modulus of the material. Strain ϵ is defined as the relative length change as described by equation 2.14 with b denoting the length at a given load and b_0 denoting the original length. Assuming a spherical bulge shape, it is possible to calculate the arch length of the deflected membrane depending on the vertical deflection of the membrane center. Geometric considerations for the arch length of a sphere lead to equation 2.15 with b denoting the arch length, s the center deflection and r the radius of the circular membrane geometry. A low differential pressure of 6 mbar was applied in order to smooth the wrinkles and was considered a pre-loading step and the resulting deflection used for the calculation of the initial arch length b_0.

$$\epsilon = \frac{b - b_0}{b_0} \tag{2.14}$$

$$b = \frac{s + r^2}{s} arcsin\left(\frac{2rs}{r^2 + s^2}\right) \tag{2.15}$$

The stress of the GC material can be estimated by assuming a homogenous stress distribution throughout the GC material and was calculated by equation 2.16, which is commonly used to determine the homogenous stress within the material of a thin walled, spherical pressure vessel [150]. With σ denoting the homogeneous stress through out the material, Δp the applied differential pressure, s the deflection, r the radius of the circular membrane geometry and t the thickness of the membrane material.

$$\sigma = \frac{\Delta p(s^2 + r^2)}{4st} \tag{2.16}$$

The values of the stress (σ) and strain (ϵ) were subsequently used to calculate the bi-axial modulus of the material. The calculated stress and strain values of the bulged SiN membrane, for each of the applied differential pressures, are given in figure 2.14 d). The bi-axial modulus is therefore the slope of the resulting data points. A linear fit is used and a bi-axial modulus of 297 GPa and a residual tensile stress of 57 MPa extracted. Small et al. [150] developed equation 2.17 to derive the Young's modulus, denoted as E, from the bi-axial modulus, denoted as Y, while taking the transition from bi-axial strain at the membrane center, a to uni-axial strain state at the membrane edge into account. Assuming a Poisson's ratio of 0.23 for low stress SiN, the measurement scheme results in a Young's modulus of 242 GPa, which is close to the value obtained for the direct fitting approach. The difference of approximately 8 % is assumed to arise from the assumption of a spherical bulge shape and a homogeneous stress and strain distribution.

$$E = \frac{1 - \nu}{1 - 0.241\nu} Y \tag{2.17}$$

Rectangular bulge structures were also probed in order to identify any differences and possible improvements to the bulge setup. The uni-axial strain and stress states of the membrane material results in a different dependency of the Young's modulus from the uni-axial modulus that is obtained from the extracted strain-stress curve as described by Xiang et al. [153] with equation 2.18.

$$E = (1 - \nu^2)\, Y \tag{2.18}$$

The proposed evaluation scheme allows the bulge testing of compressively stressed thin films in a reproducible manner. The implications that arise from the compressive stress need to be kept in mind during the interpretation of the bulge test results of the GC material as the systematic error is unknown. In order to obtain a better understanding of the implications of the compressive stress state of the window material and as an alternative approach to determine the Young's modulus, Raman spectrometry was used to probe the GC material.

2.2.4.2 Stress Measurements using Raman Spectroscopy

Raman spectroscopy is a versatile tool for the analysis of the GC material and the obtained data not only contains information about the structural composition, as described in section 2.2.2, but Raman spectroscopy is also capable of probing the stress state of the GC material.

While the position of the G-Peak feature is independent of the used excitation wavelength, it is sensitive to the deformation of the atomic structure of the carbon network [122]. This wave number dependency arises from the stress that acts on the carbon bonds [156]. Interestingly, if we keep the definition of the Young's modulus, as defined by equation 2.8, in mind it is possible to determine the Young's modulus of the GC material by relating the stress induced Raman shift to the applied strain [157]. Mohiuddin et al. [158] showed that an applied bi-axial strain shifts the G-Peak position of monolayer graphene with a rate of $-62\,\mathrm{cm^{-1}}/\%$. Theoretical work has shown that this is applicable not only to graphene but also other forms of sp^2 hybridized carbon containing compounds by tracing the origin of the peak shifting to the Grüneisen parameter, relating the lattice vibration frequencies to the volumetric change of the crystal lattice [159]. The slope of the strain induced shift of the G-Peak position, denoted as $\delta\omega_G/\delta\epsilon$, was shown to exhibit a linear dependency on the Young's modulus of the graphenic material and can therefore be used to determine the Young's modulus of a sp^2 hybridized carbon containing material [156]. The slope $\delta\omega_G/\delta\epsilon$ of the GC material under bi-axial strain therefore needs to be identified and the Young's modulus could subsequently be estimated by equation 2.19, which relates the observed Raman shift of the GC material to the Raman shift of graphene by normalizing the $\delta\omega_G/\delta\epsilon$ of graphene with the Young's modulus of graphene (1 TPa) [158].

$$E_{GC} = \frac{\delta\omega_{G-GC}/\delta\epsilon}{\delta\omega_{G-Graphene}/\delta\epsilon} E_{Graphene} = \frac{\delta\omega_{G-GC}/\delta\epsilon}{62\ cm^{-1}/\%}\ 1\ TPa \tag{2.19}$$

A measurement procedure was developed which compromises of two stages:

- The pressure dependent strain of the membrane material was determined in Stage 1. The discussed bulge test setup was used and the pressure dependent center deflection of the round GC membrane recorded for differential pressures between 6 mbar and 950 mbar. The relative length change of the membrane material was calculated using equation 2.15 and used to determine the bi-axial strain state of the material at the given differential pressure.

- Raman spectra of the membrane center were taken at the evaluated differential pressures in Stage 2. A photograph of the vacuum sample holder as it is placed below the microscope lens of the Raman spectrometer, during the measurements, is shown in figure 2.15 a). The bi-axial stress state of the membrane material was probed at the center of the membrane by acquiring a Raman spectrum as schematically shown in figure 2.15 b). A fitting procedure was used to determine the G-Peak position for the corresponding differential pressures and subsequently related to the determined strain value. The slope $\delta\omega_G/\delta\epsilon$ was extracted by a linear fit of the obtained data and used to estimate the Young's modulus of the GC material.

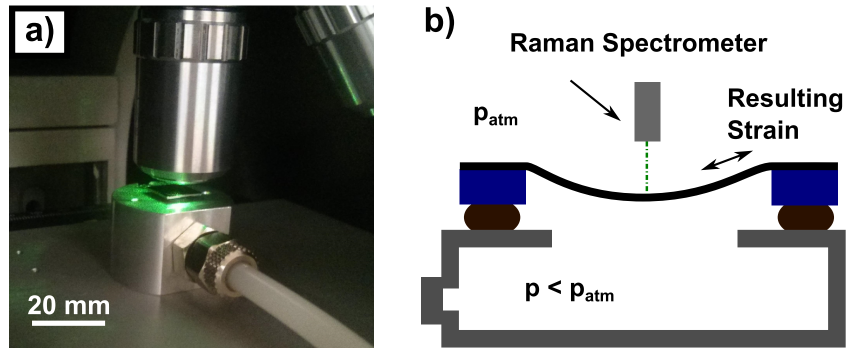

Figure 2.15: A photograph of the vacuum sample holder, as it is placed below the microscope objective of the used Raman spectrometer, is shown in a). The membrane geometry under a differential pressure load is schematically depicted in b). The thin membrane material is deflected downwards and results in an in plane, bi-axial tensile strain state at the center of the membrane.

Raman measurements were also employed in order to probe the stress state of the membrane material across the window geometry and the window frame. This was employed to obtain a better understanding of the mechanical implications that arise from the compressive stress state of the GC material.

The introduced vacuum sample holder was placed onto the xyz stage that has been used for the bulge experiments. The motorized x or y axis was used to determine the G-Peak position of the GC material along a line scan across the window geometry. This was performed with an applied differential pressure as well as in the relaxed membrane state and the obtained data were used to interpret the stress and strain state of the deflected GC material.

2.2.4.3 Wafer Curvature Measurements

A common way to determine the residual stress of deposited thin films are curvature measurements. The basic scheme is shown in figure 2.16 a). A thin film that is deposited onto a substrate results in a deformation if the stress of the deposited film deviates from zero. Positive stress values are interpreted as tensile stress and result in the upward bending of the substrate-thin film stack (i) whereas a negative stress value is interpreted as compressive stress, which results in a downwards bending of the stack (ii) [160].

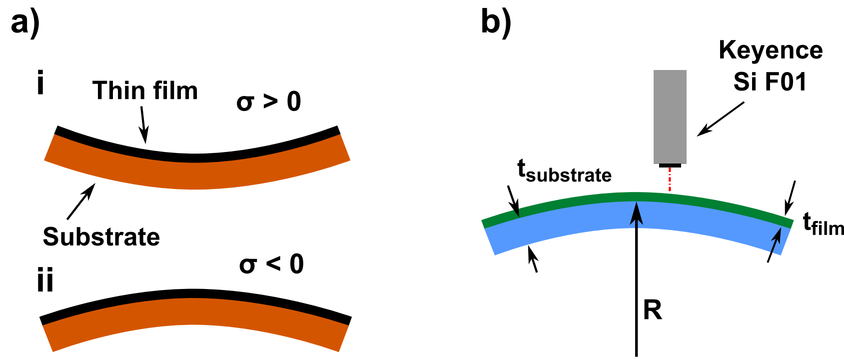

Figure 2.16: The implications of a thin film that is deposited onto a substrate exhibiting a tensile residual stress is schematically shown in a)(i), and in a)(ii) for a compressive residual stress. The measurement scheme of the sample curvature using a WLI sensor is schematically depicted in b). Line profiles of the surface deformation were obtained by moving the sample below the displacement sensor (Keyence Si F01). A sphere with radius R was fitted to the surface deformation.

A mathematical approximation of the observed curvature was published in 1909 by Stoney, following his work on the deposition of metallic films [161]. The amount of deformation is dependent on the ratio of the substrate and thin film thickness, the mechanical stability of the substrate and thin film, and therefore on the values of the Young's modulus, and of the stress value of the thin film [162]. Stoney's equation for the extraction of the film stress (eq. 2.20) is based on a thin film approximation and it has been shown that serious errors are avoided if the thickness of the substrate exceeds the thickness of the thin film by a factor of 10 [162]. With σ denoting the film residual stress, Y_s the bi-axial modulus of the substrate, t_s the thickness of the substrate, t_f the thickness of the thin film and K denoting the curvature which is the reciprocal of the radius of the deformed substrate, assuming a circular shape of deformation.

$$\sigma = \frac{Y_s t_s^2}{6 t_f} K \tag{2.20}$$

A measurement scheme was developed to perform curvature measurements in order to identify the stress of the deposited GC material. The employed measurement scheme is given in figure 2.16 b). The sample was placed on the motorized xyz stage and the WLI displacement sensor used to acquire line profiles across the sample surface. A Matlab script was written in order to fit the obtained data to a sphere with the radius R. Silicon substrates with a thickness of 500 µm and 250 µm, respectively, were used and the thickness of the GC film measured as discussed in section 2.2.3. The bi-axial modulus of mono-crystalline silicon is dependent on the wafer orientation and for (100) orientated silicon substrates a bi-axial modulus of 180 GPa was used [163].

2.2.5 Electrical Conductivity

The conductivity of the deposited GC thin films was evaluated by four-point probe measurements using a commercial Jandel Four-Point Probing System. The measurement principle is schematically shown in 2.17.

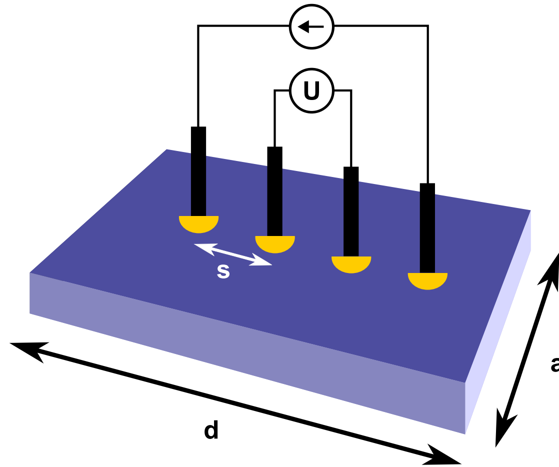

Figure 2.17: The employed four point probe resistivity measurement setup is schematically shown for a probe spacing s and a sample with the lateral dimensions a and d. A specified current was driven through the outer probes and the resulting potential difference between the two inner probes measured.

The outer two probes drive a current with a specified value through the sample and the inner two probes are used to measure the resulting potential difference. Assuming an infinite sheet size and and equidistant probe spacing, allows the sheet resistance to be calculated by equation 2.21 [164]. With R_s denoting the sheet resistance, V the measured potential difference between the two inner probes and

I the current flowing through the two outer probes. The used system exhibits a probe spacing s of 1 mm, probe tips with a large radius of 500 µm and a low downward weight of 20 g in order to avoid damaging the surface. The contribution of the substrate is assumed to be negligible as high resistivity substrates were used and the conductivity of the GC material is known to be high [165].

$$R_s = \frac{V}{I}\frac{\pi}{ln2} = \frac{V}{I}4.5324 \tag{2.21}$$

The presented equation 2.21 assumes an infinitely large surface and care must be taken when measuring samples with confined lateral dimensions. Depending on the ratio of lateral dimension of the sample and probe spacing, different correction factors have to be applied. The measured samples are either wafers with a diameter of 150 mm or square samples with an area of 1 cm^2. For the former the ratio of the probe spacing to the lateral dimension is approximately 150, which is sufficiently large and no correction factor is needed. For samples with a lateral size of 1 cm the ratio is reduced to 10 and a correction factor of 0.93 is recommended by Smits [164]. The sheet resistance is defined by equation 2.22 with ρ denoting the bulk resistivity of the material and t the thin film thickness.

$$R_s = \frac{\rho}{t} \tag{2.22}$$

It is therefore possible to deduct the bulk resistivity of the GC material from the sheet resistance measurements, if the GC thickness is known or deduct the GC thickness if the bulk resistivity is known, respectively.

The used four-point probe system allows multi-position measurements of the 150 mm wafers at predefined positions. This was used to measure the position dependent sheet resistance and the introduced measurement scheme therefore allows to evaluate the thickness distribution during the wafer scale deposition of the GC material.

2.3 Finite Element Simulations

Multi-physics finite element (FEM) simulations on a window geometry were performed for a better understanding of the underlying mechanical dependencies using the Ansys 14.5 Workbench simulation environment. The static-structural

simulation scheme is employed to simulate the three dimensional stress and strain state of the GC material. The derived material constants were used to identify the influence of the compressive stress of the window material during the window fabrication and differential pressure loading.

The window geometry was generated within the Workspace environment and the required boundary conditions applied using the graphical user interface. Meshing was performed automatically and a high node density was required due to the large aspect ratio of the very thin membrane and the macroscopically large lateral dimensions of the window geometry.

The compressive stress of the GC material was generated by a pre-step prior to the actual Static-Structural simulation. A steady-thermal simulation scheme was developed that induces a compressive stress of approximately 400 MPa to 500 MPa. The stress level can be tuned by altering the temperature load or the ratios of thermal expansion coefficient (CTE) of the GC and substrate material.

The simulation results were analyzed in regard to the stress and strain state of the GC material as well as the material deformation. The obtained 3D results are vector quantities that comprise of magnitude and direction. Therefore not only the magnitude of the stress and strain vectors are analyzed, but also the scalar value of the corresponding equivalent or "von-Mises" stress and strain. The equivalent values are calculated by determining the resulting distortion energy of the vector quantities thereby deducting a scalar value independent of the orientation. The equivalent stress and strain values are calculated according to equation 2.23 and equation 2.24 respectively.

$$\sigma_e = \sqrt{\frac{1}{2}\left[(\sigma_1 - \sigma_2)^2 + (\sigma_2 - \sigma_3)^2 + (\sigma_3 - \sigma_1)^2\right]} \tag{2.23}$$

$$\epsilon_e = \sqrt{\frac{1}{2}\left[(\epsilon_1 - \epsilon_2)^2 + (\epsilon_2 - \epsilon_3)^2 + (\epsilon_3 - \epsilon_1)^2\right]} \tag{2.24}$$

3 Graphenic Carbon Deposition

The proposed GC window material was directly deposited onto silicon substrates using a chemical vapor deposition (CVD) process. Theoretical considerations regarding the deposition process are given and the development of the deposition process is discussed in the following chapter.

3.1 Chemical Vapor Deposition of Graphenic Carbon: Theoretical Considerations

Catalytic free, chemical vapor deposition of graphene is discussed in literature in respect to the fabrication of transparent electrodes [165–167], Schottky junction diodes [168], DRAM capacitors [115] and interconnects [169].

Interestingly, the catalyst free deposition of carbon materials from a carbonaceous gas phase has been studied for decades, for example in the form of pyrolytic carbon (PyC) and pyrolytic graphite (PyG) deposition [170, 171]. Carbon gas phase deposition from a carbon containing precursor gas results in carbon materials with largely varying properties, that strongly depend on the chosen deposition parameters. The deposited material ranges from insulating diamond [172] to highly conductive graphene [83], from porous carbon black to high density graphite and includes such intriguing micro-structure formations such as carbon-nanotubes and fullerenes [173].

The observed material properties result from the hybridization of the carbon atoms, which can be sp^2, sp^3 and even sp^1, the level of incorporation of hydrogen, which is always present during the pyrolysis of carbon containing precursor gases, and the micro-structure of the material including density, crystallinity and the crystallographic orientation of the crystallites [173]. The terminology used to describe the composition of amorphous and disordered carbon material, in regard to hybridization and hydrogen content, as described by Ferrari et al. [122], is shown in figure 3.1 a). Graphitic carbon contains almost purely sp^2 hybridized carbon while diamond like carbon is largely sp^3 hybridized. Sputtered amorphous carbon (a-C) and tetrahedral amorphous carbon (ta-C) exhibit an increasing sp^3 content compared to graphitic carbon.

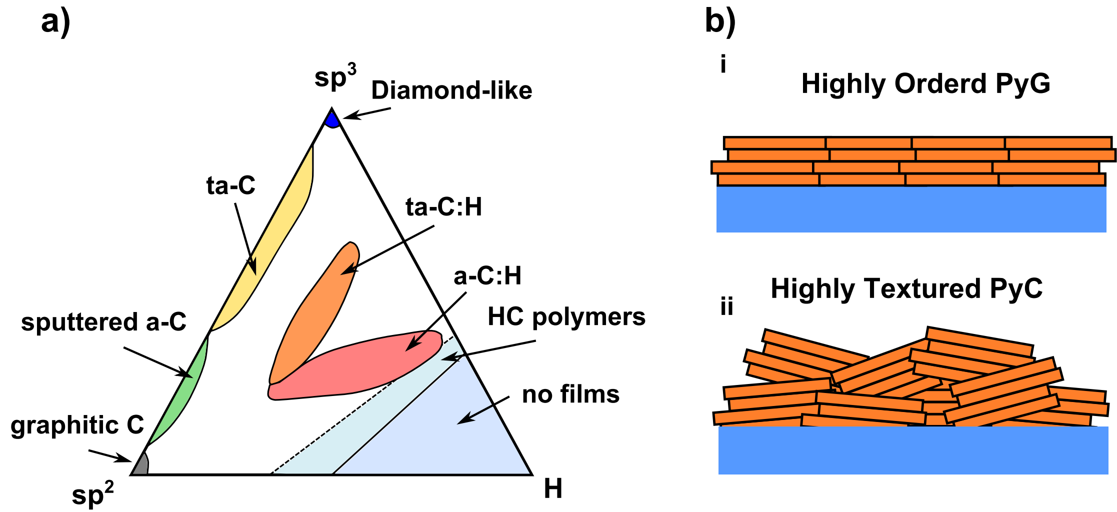

Figure 3.1: The terminology used to describe amorphous and disordered carbon materials based on their content of sp^2 and sp^3 hybridized carbon and incorporated hydrogen, is schematically shown in a) and has been adapted and redrawn from reference [122]. The micro-structure of HOPG and HT-PyC is schematically depicted in b) and the individual grains of single crystal, hexagonal carbon networks are shown as they are deposited onto a substrate.

Increasing hydrogen incorporation results in hydrogenated tetrahedral amorphous carbon (ta-C:H) and hydrogenated amorphous carbon (a-C:H) with modified properties such as a reduced electrical conductivity [174]. An even higher hydrogen content leads to the formation of hydrocarbon polymers.

Extra dimensions are added if the crystallinity and crystallographic orientation of the crystallites are taken into consideration, as the micro-structure of the carbon material has a significant impact on the material properties [173]. For example, single crystal diamond is highly ordered and almost completely sp^3 hybridized carbon [172] and as the grain size and ordering are reduced, nano-crystalline [175], ultra nano-crystalline [176] and amorphous diamond like carbon are formed [177], with varying material properties.

Highly ordered pyrolytic graphite (HOPG) is the sp^2 hybridized pendant to single crystal diamond and consists of almost perfectly stacked, large grain, sp^2 hybridized carbon layers which leads to highly anisotropic material properties. The crystallographic orientation and arrangement of the single crystal, hexagonal carbon networks in HOPG in comparison to highly textured pyrolytic carbon (HT-PyC) is schematically shown in figure 3.1 b). The highly planar micro-structure leads to the high in-plane electric and thermal conductivity as well as high mechanical strength of HOPG [170]. The highly ordered nature results in a low out of

plane flexibility and low interlayer adhesion, as single layers can easily be cleaved as demonstrated by the exfoliation of graphene mono-layers from HOPG [60]. HT-PyC exhibits a slightly higher disorder [178]. While the carbon network is highly ordered within the individual grains, the grain size is limited and the crystallographic orientation of the single grains shows an increased deviation between one another, compared to HOPG. This results in an increased out of plane flexibility as demonstrated by Guellali et al. [178].

The astonishing variability of the carbon family, even if the carbon allotropes, nanotubes and fullerenes are left aside, results in a wide range of processing parameters that need to be controlled in order to obtain a material with the desired properties. Pyrolytic carbon, especially if it is of a highly textured nature, is very similar to the discussed GC material and the theoretical considerations regarding the gas phase deposition of PyC are of great interest to the catalyst free deposition of the postulated GC window material.

The molecular structure of typical gaseous precursors, that are used for the CVD deposition of PyC materials, are schematically shown in figure 3.2 a). Methane (i), ethylene (ii) and acetylene (iii) exhibit an increasing carbon to hydrogen ratio and a decreasing thermal stability, which means that pyrolysis takes place at lower temperatures [179]. Ethanol (iv) incorporates a small amount of oxygen and has proven useful for some applications such as carbon nanotube (CNT) growth [180].

The precursor gas acts as the feedstock for the carbon deposition from the gaseous phase and a sufficiently high temperature is required to induce the thermal decomposition (pyrolysis) of the used precursor gas. The resulting, complex, gas phase composition depends on the processing parameters and the used precursor. The temperature dependent gas phase composition for the precursor gas methane, in thermal equilibrium as simulated by Gueret et al. [181], is given in figure 3.2 b). The simulation takes five gaseous species into account and assumes an atmospheric pressure and demonstrates the impact of the process temperature on the gas phase composition. The fraction of methane (CH_4) is gradually reduced as the temperature is increased, while the hydrogen (H_2) fraction grows monotonically. The fraction of benzene (C_6H_6), ethylene (C_2H_4) and acetylene (C_2H_2) also increases until approximately 1100 °C. The benzene and ethylene fractions start to diminish as the temperature is further increased, while acetylene and hydrogen become predominant for temperatures above 1300 °C. It should be noted that the simulated gas fractions are for an atmospheric pressure and at thermal equilibrium, calculated by minimization of the Gibbs energy and no solid carbon deposition was taken into account by Gueret et al. [181].

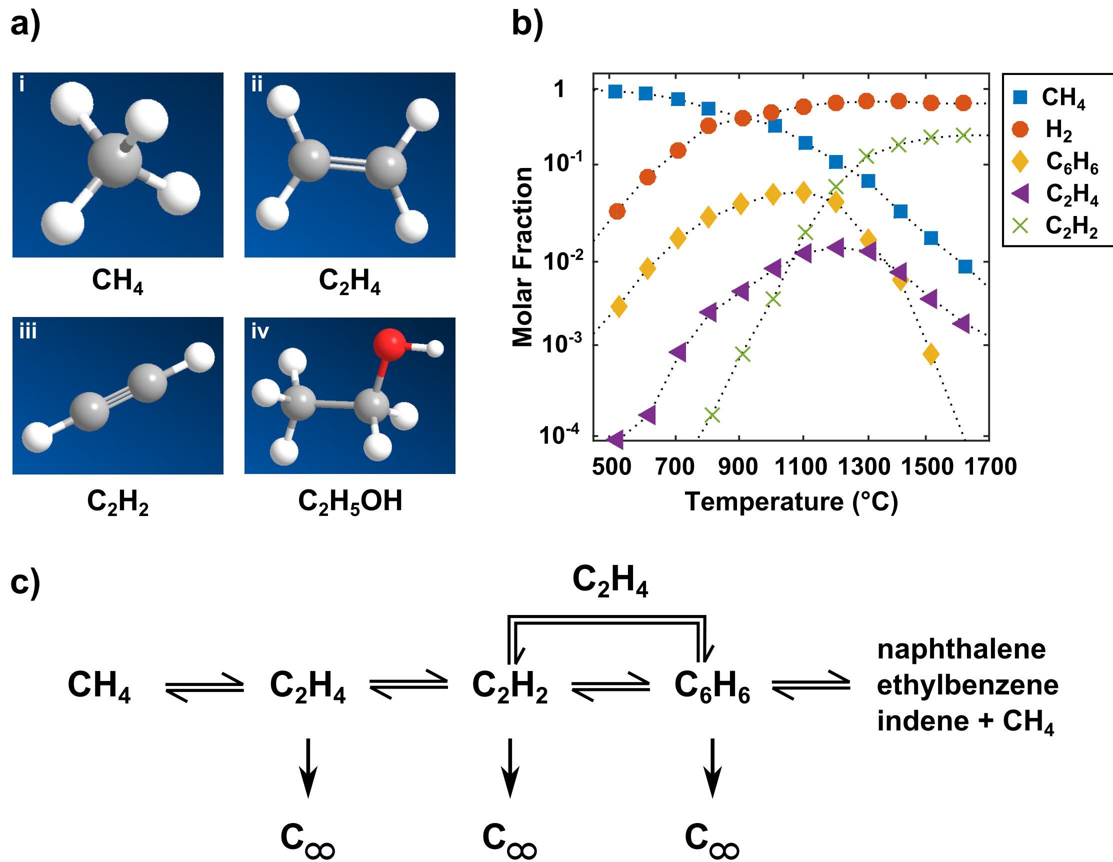

Figure 3.2: The atomic structure of the commonly used precursor gases, methane (i), ethylene (ii), acetylene (iii) and ethanol (iv) are schematically depicted in a). The temperature dependent gas phase composition of the methane precursor at an atmospheric pressure, as simulated by Gueret et al. [181], is given in b) and was adapted and redrawn from reference [181]. The reactions governing the gas phase evolution and solid carbon deposition scheme, as postulated by Becker et al. [182], are given in c). Acetylene is seen as the major contributor to the deposition of solid carbon [183].

The simulation results demonstrate the complexity of the gas phase evolution that takes place in the hot reactive zone of the deposition system. The reactions that occur within the gas phase, including the assumed deposition mechanism for elemental carbon, indicated by C_∞, as postulated by Becker et al. [182], are shown in figure 3.2 c). Interestingly, no direct carbon deposition from methane is assumed to be possible and the solid carbon formation thought to predominantly originate from acetylene, as discussed in the references [165, 183]. The high temperature decomposition of methane to other carbonaceous gas species, especially to acetylene, is therefore crucial for carbon deposition.

The reaction rates for the transition schemes shown in figure 3.2 c) are process dependent and the resulting gas phase composition is therefore governed by:

- The process temperature, as demonstrated by figure 3.2 b).
- The absolute process pressure as well as the individual partial pressures of the gaseous components, which can be altered by introducing for example additional hydrogen [182, 184].
- The reactor geometry, which is commonly defined as volume per surface area, which alters the amount of carbon that is withdrawn from the gas phase [185].
- The residence time of the molecules within the gas phase, which describes the time that is available for the gas phase reactions to take place before the molecules leave the reaction volume. This was not taken into account in figure 3.2 b) as only the composition at the thermal equilibrium is shown. The thermal equilibrium is only reached for very long residence times, whereas low residence times shift the gas phase composition towards shorter hydrocarbons and primary reaction partners [184].

The above considerations describe the reaction mechanisms that lead to the carbon deposition. Further complexity is added to the deposition process model if the properties of the deposited carbon material are to be described. Different growth models have been developed to explain the mechanisms that govern the micro-structure evolution. The growth models distinguish between two main modes of carbon deposition that dominate, depending on the gas phase composition, as postulated by Hu and Hüttinger [183]:

- Carbon deposition based on chemisorption of carbonaceous species at active sites of the deposited carbon material. These are predominantly available at the edges of the basal planes.
- Carbon deposition based on gas phase nucleation. Large polycyclic hydrocarbons develop in the gas phase and are deposited on the substrate by physisorption. The process can therefore be regarded as a condensation process.

Chemisorption dominates at low pressures, low temperatures and short residence times, whereas the gas phase nucleation mechanism is predominant at high pressures, high temperatures and high resident times, as described by De Pauw et al. [186]. The micro-structure evolution is dependent on the dominant deposition mechanism and the encountered gas phase composition, but a highly laminar micro-structure has been obtained for both growth regimes [186]. The evolution of

a highly laminar micro-structure in a chemisorption governed deposition process is obtained if an optimum ratio of cyclic hydrocarbons and linear hydrocarbons are present in the gas phase. This is described by a particle-filler model by Hu et al. [183] and takes place at intermediate temperatures and pressures. The nucleation based growth model results in a highly laminar micro-structure only if planar, polycyclic hydrocarbons are present in the gas phase, which is difficult to predict in a general manner, but it is known to require high resident times [185].

Independent of the growth model, it is observed that higher processing temperatures result in larger grain sizes and an overall increase in a planar orientation of the crystallites [123, 178]. In fact, high temperature post deposition annealing at temperatures above 2500 °C of PyC materials leads to graphitization and a micro-structure approaching that of HOPG [178]. Evidently, the high temperature allows a reorganization of the carbon material.

It was therefore the objective to identify a suitable CVD process that allows the deposition of a GC material that exhibits a highly laminar micro-structure and incorporates the desired, discussed properties of graphene. The direct deposition on a silicon surface was assumed to result in an inherently high adhesion of the GC material to the substrate due to the formation of strong silicon-carbon bonds and poses a significant advantage compared to a transfer mediated graphene integration. In a first stage, the proof of concept for a GC x-ray transmission window was intended and an experimental CVD setup used to deposit the carbon material onto 1 cm by 1 cm silicon substrates. The proof of concept stage was followed by the development of a wafer scale deposition process. The employed equipment, capable of processing silicon substrates with a diameter of up to 200 mm, would allow to fabricate x-ray transmission windows on an industrial scale and therefore demonstrates the scalability of the GC deposition.

3.2 Deposition Process for Single X-ray Window Fabrication

An experimental CVD setup was utilized during the first stage, allowing the GC material to be deposited onto silicon substrates with a size of 1 cm x 1 cm. This permits the fabrication of single x-ray transmission windows without the implications of large scale processing such as inhomogeneous deposition rates and large reactor volumes. The use of small substrates allowed a high throughput with a reduced consumption of resources. The schematic of the deposition system is given in figure 3.3.

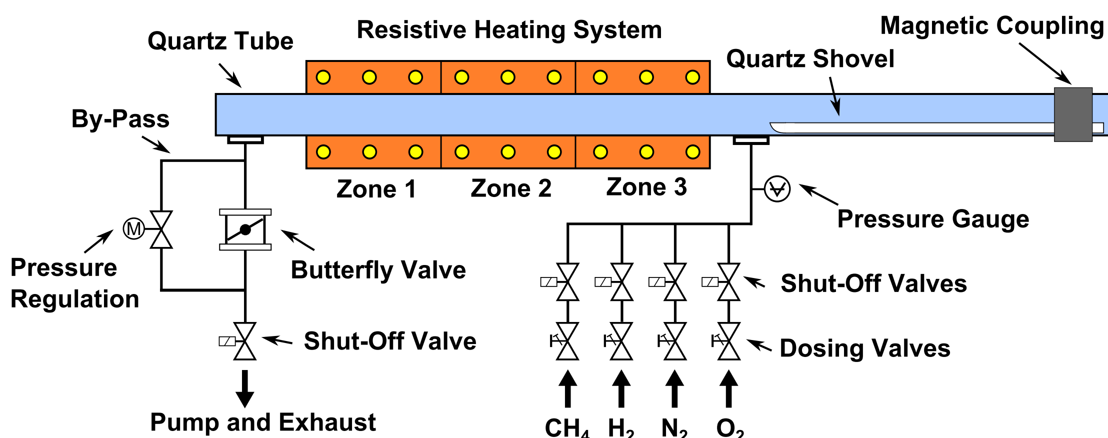

Figure 3.3: The schematic of the used experimental CVD equipment is depicted. The precursor gas entered the heated reaction zone from the right and the process pressure and gas flow were regulated by the gas line dosing valves and the pumping capacity. A magnetic loading mechanism was employed to transfer the substrate into the reaction zone. The system was capable of low pressure processing at temperatures of up to 1100 °C.

The system provided 3-zone resistive heating and was capable of process temperatures of up to 1100 °C. Low pressure as well as atmospheric pressure CVD was possible and the precursor gas, hydrogen, oxygen and nitrogen were available as processing gases. A motorized throttling valve, placed in line to the vacuum pump, was used in combination with a pressure gauge for pressure regulation. This allowed to adjust the flow rate of the processing gases, independently of the process pressure, using the manual dosing valves for each of the gas lines. A manual butterfly valve was available to realize high flow rates at low chamber pressures with a high pumping capacity.

The substrates were placed in the quartz shovel and were moved into the hot zone by a magnetic loading mechanism. This allowed for high heating and cooling rates and thus a high sample throughput. Oxygen was used to remove the deposited carbon material on the quartz ware at temperatures above 600 °C. A thermocouple was located outside of the quartz tube but within the resistive heating system and was used for temperature regulation.

3.2.1 Substrate Preparation

High resistivity (>20 Ω cm) p-doped, silicon wafers with a surface orientation of either (100) or (110), a diameter of 150 mm and a thickness of either 250 µm, 500 µm or 675 µm, were cut into square, 1 cm by 1 cm samples using a wafer sawing system. Current beryllium x-ray transmission windows exhibit a circular window

frame that is subsequently soldered into the cap of the TO8 detector housing. In order to directly evaluate the GC x-ray tranmsission windows, circular substrates with a diameter of 9.75 µm were also used. The required round, purchased, silicon substrates were fabricated utilizing the stealth dicing technology and subsequently available for GC deposition [187].

The individual silicon samples were cleaned using heated acetone and isopropanol in combination with an ultrasonic bath in order to remove the resist layer, that was applied to protect the wafer surface during sawing. A cleaning step comprising of heated (H_2O:HCl:H_2O_2) with a mixing ratio of (5:1:1) was performed in order to avoid a reactor contamination with inorganic contaminants during the deposition process.

The native silicon oxide that covers the surface of the silicon samples was removed by a dip in hydrofluoric acid with a concentration of 5 %, immediately before the GC deposition, in order to obtain an oxide free, hydrogen terminated surface. The hydrogen termination of a silicon (100) surface is stable for several tens of minutes before the hydrogen termination is lost and a native oxide starts to form at ambient conditions [188, 189]. It was therefore seen necessary to directly proceed with the deposition process in order to guarantee unhindered silicon-carbide bonding during the GC deposition.

3.2.2 Deposition Process Scheme

The prepared silicon substrates were placed in the loading position of the reactor. The magnetic loading mechanism allowed the hot zone of the reactor to remain at the deposition temperature while loading and unloading the silicon samples. The loading position was kept at room temperature throughout the deposition process due to active water and air cooling.

The complete reactor volume was vented during the loading and unloading process, and nitrogen counter-flow purging employed in order to avoid the introduction of ambient air into the reactor volume. The chamber was immediately evacuated to a base pressure of below 1×10^{-1} mbar after loading the silicon samples and subsequently thoroughly purged with nitrogen gas. A leak test of the reactor volume was performed after five minutes of purging. This was necessary in order to rule out any leakages in the system and to avoid a gas phase contamination with ambient oxygen and water, which is known to affect the growth process and could facilitate the formation of carbon soot particles during the deposition process [190].

High purity hydrogen (99.9999 %) with a flow rate of 250 sccm was introduced

into the reaction volume, provided that the leak test was successful, and chamber purging continued for an additional 5 minutes. High purity methane (Air Liquide, 99.9995 %) was employed as the carbonaceous precursor gas and introduced into the reaction volume to initiate the deposition process.

3.2.3 Process Parameters

Following the theoretical considerations, introduced in section 3.1, the properties of the GC material are strongly dependent on the deposition conditions. The influence of the individual process parameters were evaluated and are discussed in the following.

The available process equipment allowed the following process parameters to be manipulated:

- The process temperature
- The employed processing gases and resulting gas mixture
- The absolute process pressure
- The flow rates of the processing gases

The complex interaction of the introduced parameters determined the gas phase composition during the deposition process. Methane was chosen as the carbonaceous precursor gas as the pyrolysis of methane requires temperatures at and above 1000 °C and higher temperatures are desirable for the deposition of highly textured GC materials [186]. In addition, the high temperature necessary for the methane pyrolysis was seen favourable for the formation of strong silicon-carbon bonds, as discussed in section 3.1.

3.2.4 Process Development

The introduced theoretical considerations offer an in-depth understanding of the assumed deposition mechanisms and the influence of the individual processing parameters. None the less, the processing parameters are strongly dependent on the used equipment and experiments were conducted in order to identify a parameter set that results in the soot free deposition of a highly textured GC material. For the following discussion, methane with a flow of 30 sccm was employed as the precursor gas, unless otherwise noted.

Soot Formation

Soot formation is a common observation during the combustion and pyrolysis of hydrocarbons and assumed to originate from gas phase nucleation and the subsequent growth from heavy, polycyclic aromatic hydrocarbons (PAH) [191]. PAH form during the pyrolysis of methane as described in section 3.1 and are a prerequisite for GC deposition during the physisorption growth regime. While the deposition and subsequent film growth on the substrate is desired, the growth of soot from the PAH's in the gas phase results in the development of spherical soot particles. The resulting GC material, that is deposited on the substrate, is dominated by condensation and agglomeration of these soot particles. Larger particles form in the gas phase by sticking collisions of individual soot particles and the resulting GC material exhibits an isotropic micro-structure and a low density [192]. Soot formation was therefore seen as a critical aspect during the GC deposition process and had to be avoided in order to obtain a highly textured GC material.

The employed, silicon substrates offered a very smooth surface finish and exhibited a mirror like appearance. GC films are known to deposit with excellent surface conformity and the resulting GC films should therefore offer a very low surface roughness and highly reflective appearance [115]. Depending on the chosen process parameters, either dull surfaces or surfaces with a highly reflective metallic luster were obtained.

SEM imaging was performed in order to obtain high resolution images of the surface morphology. An SEM image of the surface of a sample exhibiting a dull surface appearance is given in figure 3.4 a). The deposited GC material is comprised of spherical structures as shown in an enlarged section in figure 3.4 b). The spherical structure is typical for soot particles that have grown in the gas phase and have eventually conglomerated .

Soot formation can be significantly reduced by lowering the concentration of PAHs in the gas phase, as this hinders the development of soot particles from the present PAHs [193]. This can be achieved by reducing the residence time of the carbonaceous molecules in the reaction volume, by lowering the process temperature and pressure and thus the formation rate of PAHs, or by the introduction of additional hydrogen. An SEM image of the surface morphology of a sample that had been deposited with an optimized gas phase composition is depicted in figure 3.4 c). The surface is extremely smooth apart from single conglomerates of condensed soot found on the surface of the sample as shown in detail in figure 3.4 d). It is assumed that these were formed during the termination of the deposition process, as the bulk material is free of spherical structures.

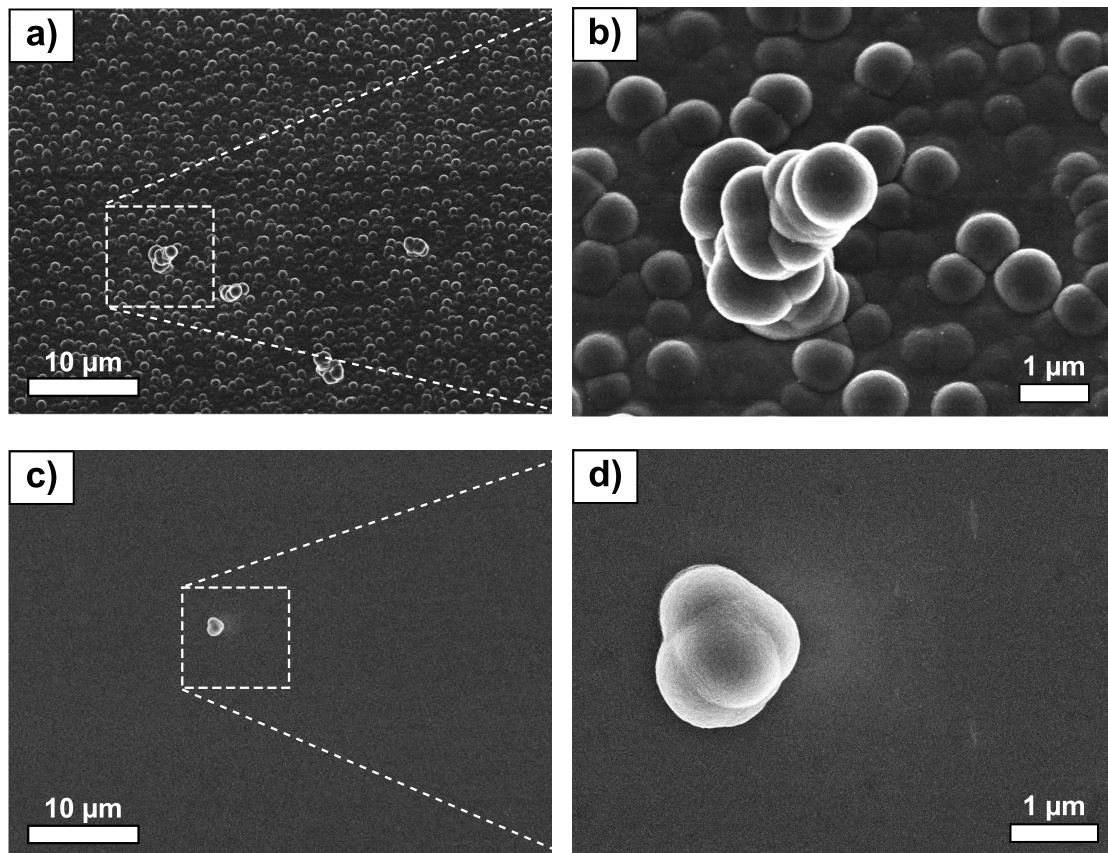

Figure 3.4: An SEM image of the surface of a GC sample with a high level of soot formation in the gas phase during the deposition process is shown in a). A close up image of the spherical soot particles is given in b) and a typical conglomerate of soot particles was identified. The surface of a soot free deposition process is depicted in c) and a close up of a spherical soot particle that was found on the surface of the sample is shown in d) to demonstrate the low surface roughness. The identified soot particle was assumed to have formed during the termination of the deposition process. The SEM images were obtained with a working distance of 6 mm and an acceleration voltage of 3 kV.

Raman spectroscopy is commonly used to characterize carbon materials as discussed in section 2.2. The Raman spectrum of the GC sample that exhibited a high soot concentration is given in figure 3.5 a), whereas figure 3.5 b) shows the Raman spectrum of the soot free sample. Interestingly, the Raman spectra are almost identical. It is therefore not possible to directly deduce the surface morphology from Raman measurements.

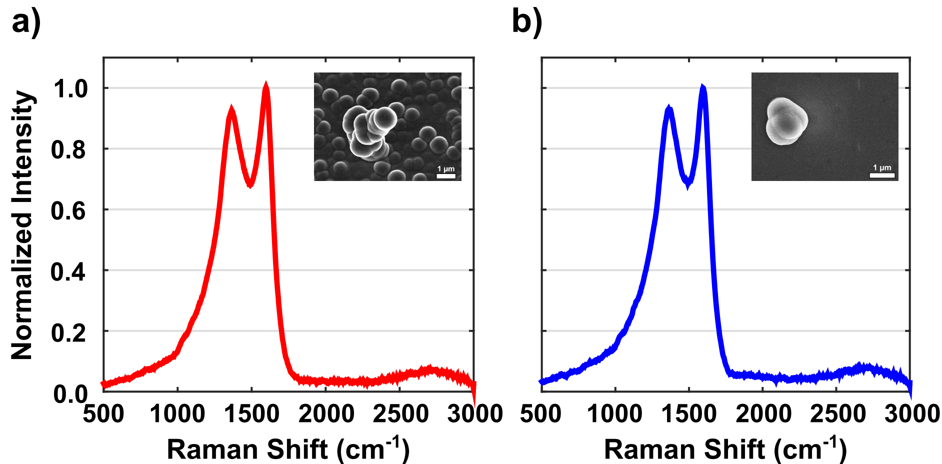

Figure 3.5: Raman spectroscopy of the sample with a high soot concentration led to the spectrum shown in a) whereas the non-sooting deposition process led to the spectrum given in b). No differences were identified and Raman spectroscopy therefore unsuitable to resolve the surface morphology.

Micro-structure of the Deposited GC Material

SEM cross section images of the discussed samples were obtained in order to identify the micro-structure of the deposited GC material, as shown in figure 3.6, and reveal the highly textured micro-structure of the GC material. Interestingly, both deposition processes exhibit a highly laminar structure, independent of the strong soot formation that is visible in figure 3.6 a), as indicated by the arrow. The incorporation of such spherical soot particles into the GC film, and subsequently into the x-ray window, results in inhomogeneous film properties and the window material is assumed to fail at the mechanically weakest point. The highly laminar structure of the GC material, which was deposited on the silicon substrate is apparent in the enlarged image shown in 3.6 b).

Evidently a significant substrate gas-phase interaction took place during the deposition of the GC material, as is indicated in 3.6 c) by the arrow. The removal of the GC material (not shown) revealed that the indicated structural changes of the silicon surface were in fact hollowed out portions of the substrate. It is assumed

that the hydrogen containing atmosphere at the initiation of the deposition process has led to silicon etching due to some sort of metallic contamination of the surface. In comparison, a high resolution image of the GC cross section of a sample obtained with an optimized growth process did not show the discussed silicon etching or soot formation, and the resulting GC material exhibits a highly laminar structure, as shown in figure 3.6 d).

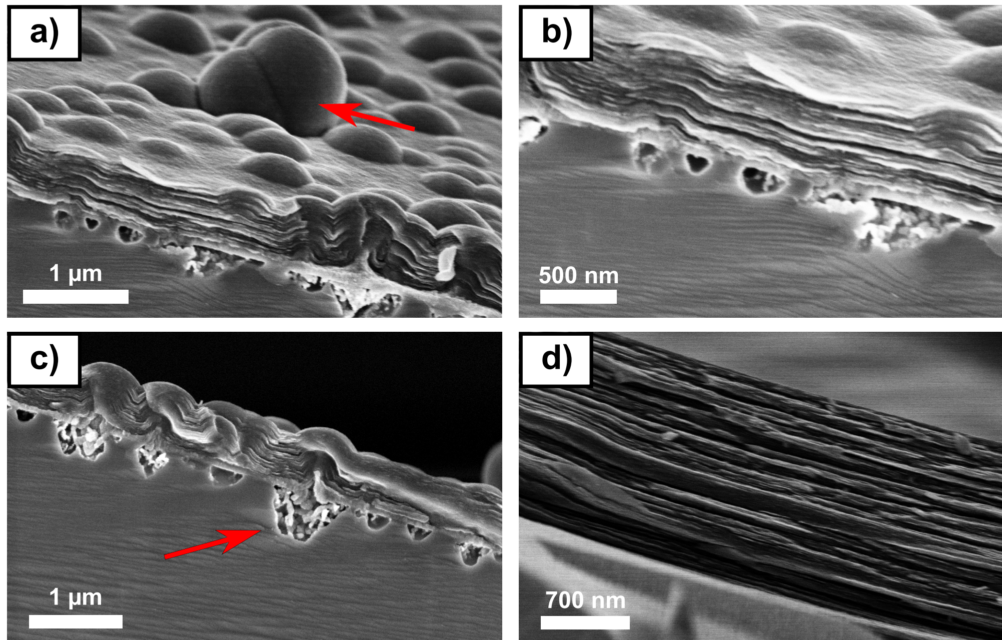

Figure 3.6: An SEM cross section image of the GC material deposited by the examined, sooting deposition process is shown in a). Soot particles are incorporated into the GC film as indicated by the arrow. The GC material exhibits a highly laminar structure as demonstrated in b), showing an SEM image with a higher magnification. A strong interaction of the gas phase with the silicon substrate was identified as indicated by the arrow in image c). The highly laminar structure of the GC material deposited by the developed non-sooting process is depicted in d).The SEM images were obtained with a working distance of 6 mm and an acceleration voltage of 3 kV.

Surface Roughness of the Deposited GC Material

The surface roughness of the GC material is dependent on the process parameters, as shown in figure 3.7. AFM measurements of the GC surface were used to calculate the surface roughness of the deposited GC material and was subsequently available to compare different process parameters. A low surface roughness is assumed to indicate homogeneous film properties and is therefore seen desirable. The surface AFM image of GC material deposited at a temperature of 1100 °C and

a pressure of 20 mbar is shown in figure 3.7 a) and compared to the GC material deposited at a temperature of 1000 °C and a pressure of 65 mbar with otherwise identical deposition parameters, as shown in figure 3.7 b). The high residence time during the deposition of sample b) resulted in a very smooth surface with an R_{RMS} of 0.23 nm compared to a value of 1.14 nm for sample a). Both sets of deposition parameters resulted in high quality GC deposition with low soot formation and similar growth rates but the surface roughness is nearly one order of magnitude lower for the sample grown at a higher residence time.

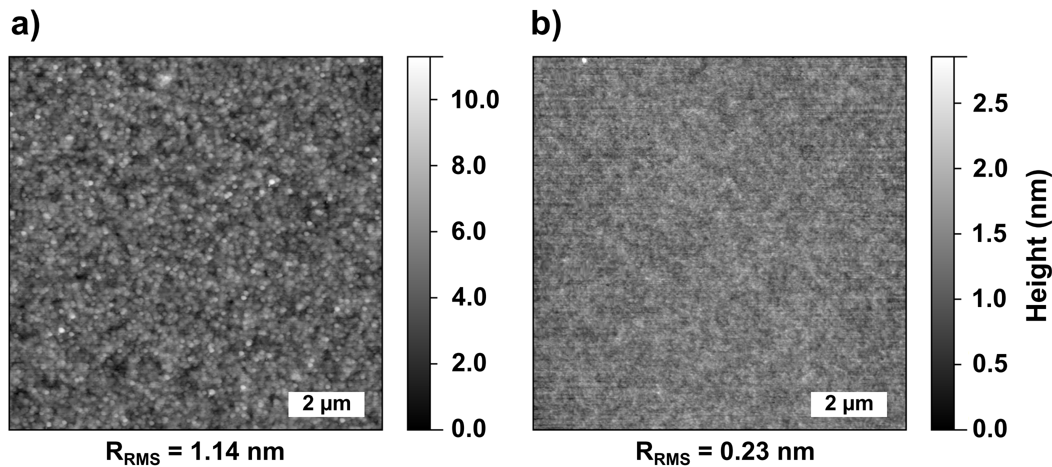

Figure 3.7: AFM measurements of the GC surface were employed to determine the surface roughness. The surface roughness is process dependent and the surface roughness shown in a) is significantly higher compared to the surface roughness of sample b), which was deposited with a deposition process exhibiting a higher residence time.

Growth Rate and Thickness of the Deposited GC Material

The thickness of the deposited GC material is found to depend linearly on the duration of the deposition process as shown in figure 3.8 for two sets of deposition parameters. The lower process temperature of 1000 °C compared to 1100 °C results in a significant reduction of the deposition rate, even though the process pressure was increased from 20 mbar to 35 mbar. The growth rate was determined by depositing GC material for different deposition times and measuring the film thickness with the discussed methods introduced in section 2.2. The growth rate is closely linked to the micro-structure of carbon materials deposited from the gas phase and therefore seen as a further parameter that needs to be taken into consideration [186]. In general, the low, observed growth rates of the GC material allow for a high thickness control of the deposited films and thus also for the GC x-ray transmission windows.

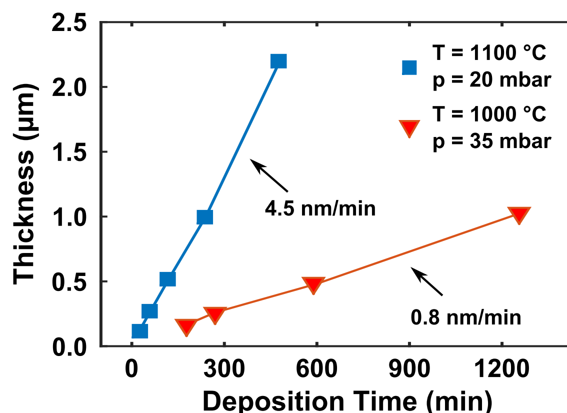

Figure 3.8: The deposition rates of the GC material for two different sets of deposition parameters are shown. The GC thickness is dependent on the deposition time, the temperature and the process pressure. For both deposition processes, methane was employed as the precursor gas with a constant flow of 30 sccm.

Raman Spectra of the Deposited GC Material

Raman spectroscopy offers a contact free characterization of the deposited GC material and is highly sensitive to the molecular structure of the GC material as discussed in Chapter 2.

The process parameters had a significant impact on the GC material, as demonstrated by the Raman spectra given in figure 3.9. The deposition rate of the samples was determined as described in Chapter 2 and are also given in the diagrams and ranged from 0.3 nm/min to 5.0 nm/min. The samples shown in the figures 3.9 a), b) and c) were deposited using a process temperature of 1100 °C and the process pressure was successively increased from 6 mbar, 10 mbar to 20 mbar, respectively. The remaining process parameters were kept constant. The deposition rate of the GC material increased with a higher process pressure from approximately 1 nm/min to 5 nm/min. A reduction of the process pressure below 6 mbar led to very low deposition rates, whereas higher process pressures resulted in soot formation. The Raman spectra all exhibit the characteristic D-, G- and 2D-Peaks and a predominantly sp^2 hybridized carbon material is therefore assumed. The intensity of the 2D-Peak is highest for the GC material deposited with the minimal growth rate and indicates an increased ordering along the c-axis of the graphitic crystallites, as discussed in Chapter 2. Interestingly, the intensity ratio of the D- and G-peak, and therefore the defect density increases with a lower deposition rate.

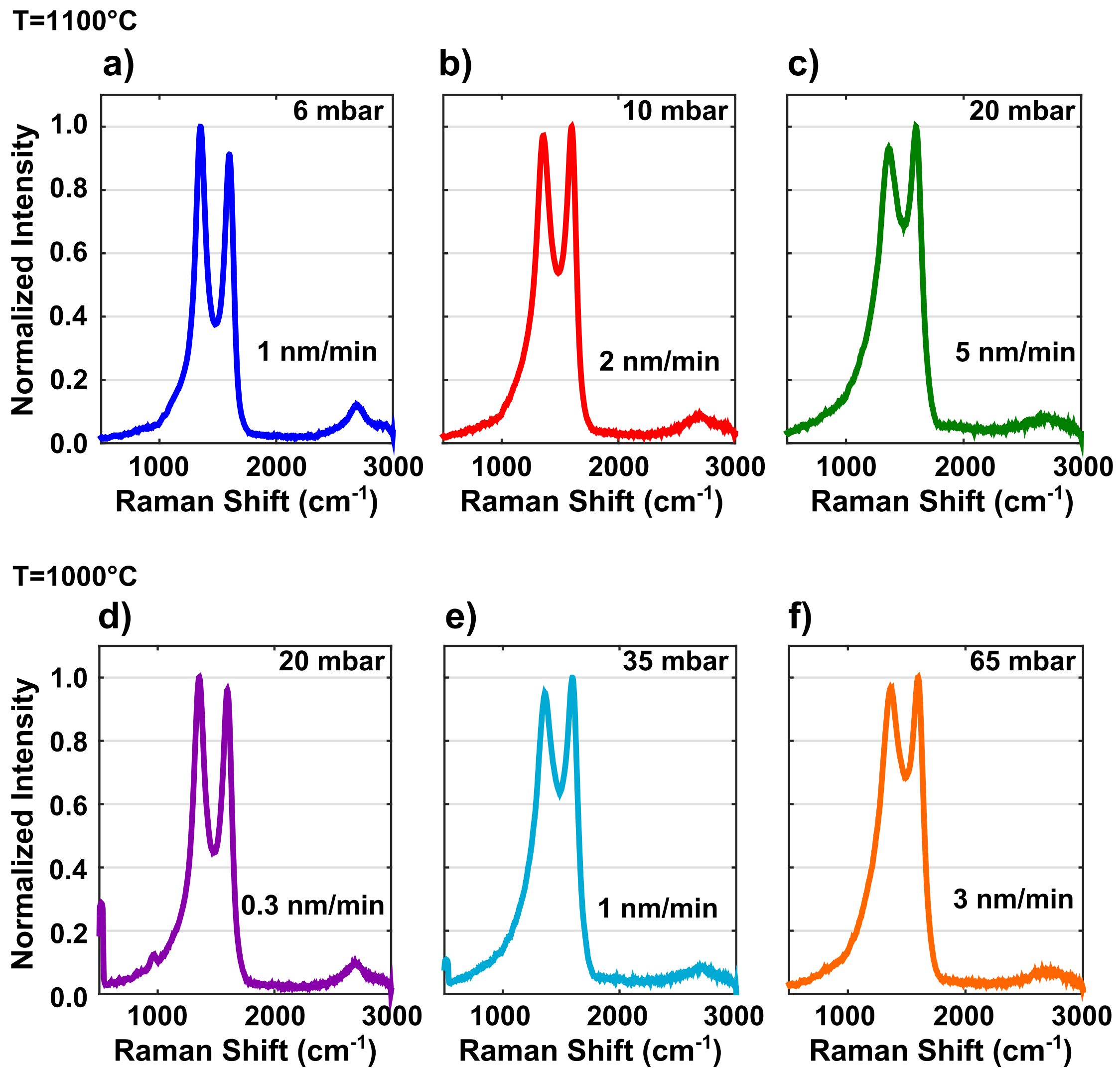

Figure 3.9: The Raman spectra of the GC material deposited by the corresponding deposition process parameters are shown. The temperature and gas pressure was varied, all other process parameters were kept constant. The Raman spectra obtained from GC material that was deposited with a low growth rate exhibit a more pronounced 2D-peak and sharper D- and G-Peak formations.

The figures 3.9 d), e) and f) show the Raman spectra obtained from GC samples deposited at a reduced process temperature of 1000 °C and an increasing pressure of 20 mbar, 35 mbar and 65 mbar, respectively. The remaining processing parameters were kept the same. The deposition rate was significantly reduced by more than an order of magnitude at a pressure of 20 mbar compared to the deposition rate at a temperature of 1100 °C, and indicates the importance of the thermal decomposition of the precursor gas and the gas phase evolution.

Interestingly, the Raman spectrum of figure 3.9 d) is very similar to that of 3.9 a). This is also the case for that of figure 3.9 f) and c). Very similar Raman spectra can evidently be obtained using different process parameters. The high process pressure of 65 mbar, as shown in figure 3.9 f), results in an increased deposition rate, compared to figure 3.9 a) and b), although the process temperature is lower. The experiments at a temperature of 1000 °C seem to indicate the same relation for the intensity of the D-Peak as the experiments at 1100 °C. The lower deposition rate results in a higher D-peak and 2D-Peak intensity. The individual process parameters evidently compensate each other and exemplify the complexity of the gas phase deposition process.

The Raman spectra of the GC material deposited with a low growth rate exhibit a more pronounced 2D-Peak which indicates a higher ordering of the crystallites along the c-axis of the micro-structure, as discussed in Chapter 2. It is also apparent that the shape of the D- and G-Peak is sharper and the resulting peak valley is extended to lower intensities. A deep inter-peak valley has been assumed to indicate a reduced amount of amorphous carbon within the GC material [125]. If we apply the TK model, as discussed in Chapter 2, to the obtained Raman spectra the grain size is found to range between 4.5 nm for the samples deposited with a low deposition rate, to 5.3 nm for the samples deposited with a high deposition rate. This is close to the values reported in literature for nano-crystalline graphene, ranging from 5 nm to 19 nm [94,167]. The value of the defect related D- to G-peak intensity ratio is minimal for the sample deposited at a temperature of 1100 °C and a pressure of 20 mbar and SEM cross section images verified a soot free, highly laminar micro-structure.

Identified Deposition Parameters

A promising set of deposition parameters was chosen and subsequently employed for the GC deposition, as summarized in table 3.1. It should be noted, that the deposition process is dependent on numerous parameters that are indirectly defined by the used equipment, including among others the size of the reactor volume, the reactor geometry, and the heat transfer in the hot zone of the reactor.

Table 3.1: The identified deposition parameters that were used for the GC deposition are summarized.

Precursor Gas	Temperature	Pressure	Gas Flow	Growth Rate
CH_4	1100 °C	20 mbar	30 sccm	4.5 nm/min

3.3 Wafer Scale Deposition of the GC Window Material

While the use of small scale substrates was advantageous for the process development and proof of concept of the GC x-ray transmission window material, the deposition and fabrication process needs to be scaled up to larger substrates for industrial mass fabrication, if the GC window material is to replace beryllium. The developed deposition process was therefore transferred to a reactor system, capable of processing wafers with a diameter of up to 200 mm. Using silicon wafers with a diameter of 150 mm would allow the simultaneous deposition for up to 170 x-ray transmission windows, assuming a required area of 1 cm^2 per window. The use of large silicon substrates was also a prerequisite for the fabrication of GC x-ray transmission windows with a diameter of more than the discussed 7 mm.

The schematic of the used rapid thermal chemical vapor deposition (RTCVD) system is given in figure 3.10. Single wafer processing and radiative heating allowed high process temperatures of up to 1200 °C and short processing times. The reactor chamber remained cool during the deposition process due to an active water cooling system. A pyrometer was available for optical temperature measurements of the silicon wafer and a motorized butterfly valve was available for pressure regulation. Each gas line was equipped with a mass flow controller and the process recipes were fully programmable. The gas was injected into the reaction chamber by four radial and two tangential injectors in order to improve the gas phase homogeneity. An ozone generator was placed in-line of the oxygen gas line and allowed the introduction of ozone into the reaction chamber in order to remove remaining, volatile carbonaceous compounds.

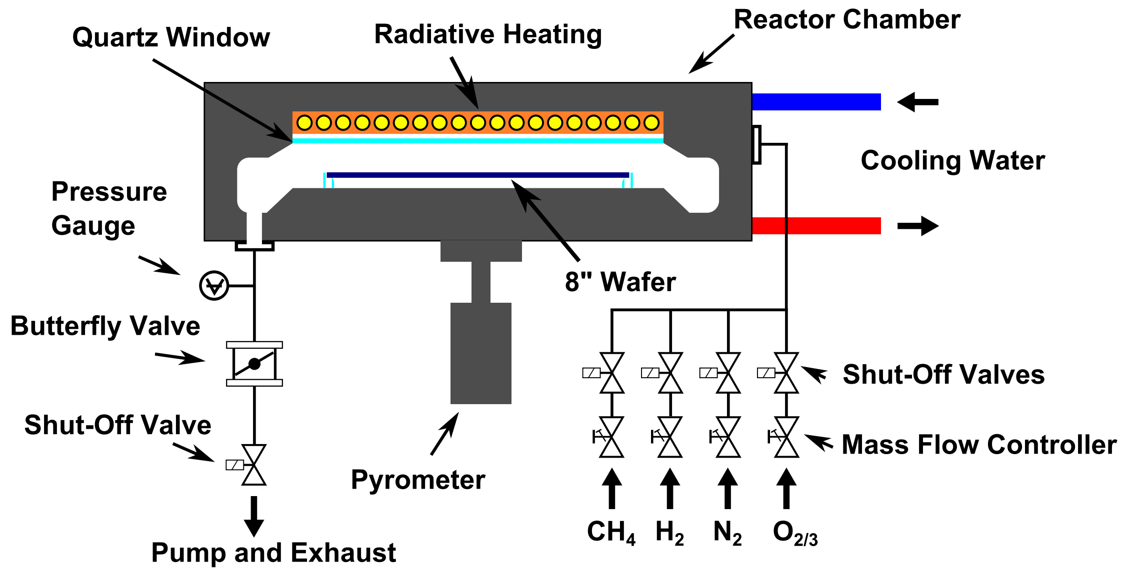

Figure 3.10: The used RTCVD equipment for wafer scale GC deposition is schematically depicted. Radiative heating was used to process substrates with a diameter of up to 200 mm. A quartz window separates the reactor chamber from the heating system and the walls of the reactor remained cool as they are continuously cooled by water.

3.3.1 Substrate Preparation

High resistivity (>20 Ω cm), p-doped, double side polished, 150 mm diameter silicon wafers with a thickness of 250 µm and 500 µm, respectively, were used and cleaned using a full RCA clean. This includes a bath within a solution comprising of (NH_4OH:H_2O_2:H_2O) with a ratio of (1:1:5), denoted as R1 solution, to remove organic residues, a hydrofluoric acid dip to remove the native oxide of the silicon substrate and a final bath within a cleaning solution comprising of (H_2O:HCl:H_2O_2) with a mixing ratio of (5:1:1), denoted as R2 solution, in order to remove remaining inorganic contaminants. The native oxide of the silicon wafer substrate was removed by a hydrofluoric acid dip with a concentration of 5 % prior to the GC deposition.

3.3.2 Deposition Process Scheme

The silicon wafer substrate was placed in the reactor and the chamber immediately evacuated to a base pressure of below 1×10^{-2} mbar and a purging cycle with nitrogen gas executed. A leak test of the system was performed in order to rule out any gas phase contamination with ambient oxygen and water, which could facilitate the formation of carbon soot particles during the deposition process.

The silicon wafer was heated to the deposition temperature of 1200 °C under high purity hydrogen (99.9999 %) flow with a flow rate of 250 sccm or in vacuum. High purity methane (Air Liquide, 99.9995 %) was employed as the carbonaceous precursor gas and introduced into the reaction chamber with a flow rate of 2000 sccm to initiate the deposition process. The film thickness was determined by the deposition rate and the deposition time.

3.3.3 Process Parameters and Process Development

The considerations remain valid for the wafer scale deposition and a set of process parameters was identified that resulted in a soot free deposition of highly textured GC material.

Similarly to the single window process discussed in the previous section, a high amount of gas phase nucleation and subsequent soot growth resulted in an isotropic micro-structure and low density of the GC material. Severe soot formation was identified by a dull GC surface appearance. A photograph of a 150 mm silicon wafer that was coated with a GC film using a set of process parameters that resulted in significant soot formation is shown in figure 3.11 a).

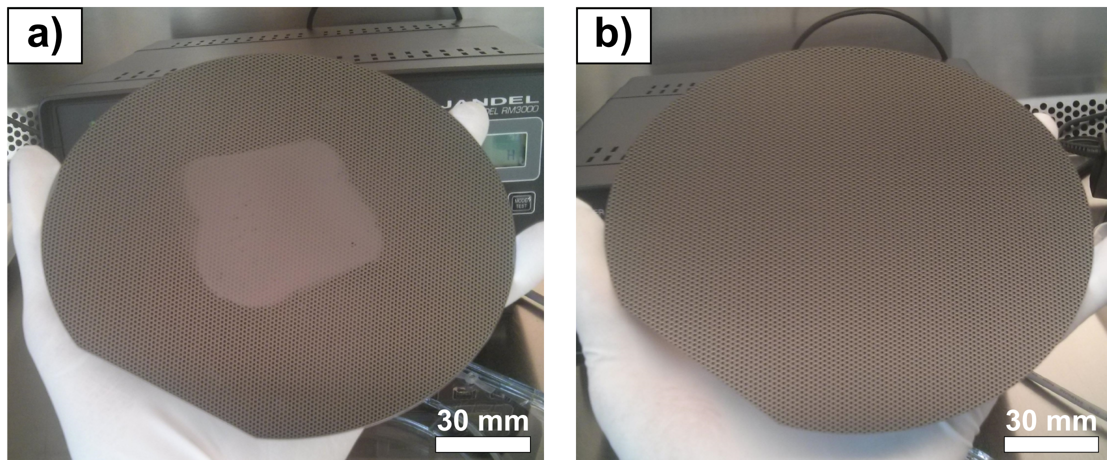

Figure 3.11: Photographs of processed silicon wafers after the GC deposition are shown. The center of the wafer in a) exhibited significant soot formation whereas optimized deposition parameters resulted in a soot free GC material, as demonstrated in b). It should be noted that the highly reflective wafer surface reflects the bottom cover of the above flow box.

The center region exhibits a dull appearance, whereas the process parameters used to deposit the GC material shown in figure 3.11 b) resulted in a highly reflective, metallic appearance of the GC surface. The square shape of the dull region

indicates an inhomogeneous gas phase composition which is assumed to arise from the gas injectors of the RTCVD system.

The RTCVD system was operated in constant power mode instead of employing feed-back based temperature regulation. For deposition processes that alter the emissivity of the substrate wafer, this mode of operation is seen favourable as the changing emissivity of the substrate influences the temperature reading of the pyrometer [194]. It has been shown that single wafer deposition processes exhibit a higher repeatability using the constant power mode. [195].

Process parameters were identified that resulted in a GC material with similar Raman features and a surface roughness close to the values obtained for the GC material deposited by the experimental, small scale CVD process. The Raman spectrum of the deposited GC material is given in figure 3.12 a) and an AFM surface scan image, shown in figure 3.12 b), demonstrates an R_{RMS} of 0.98 nm and a similar surface morphology compared to the samples obtained with the small scale deposition process.

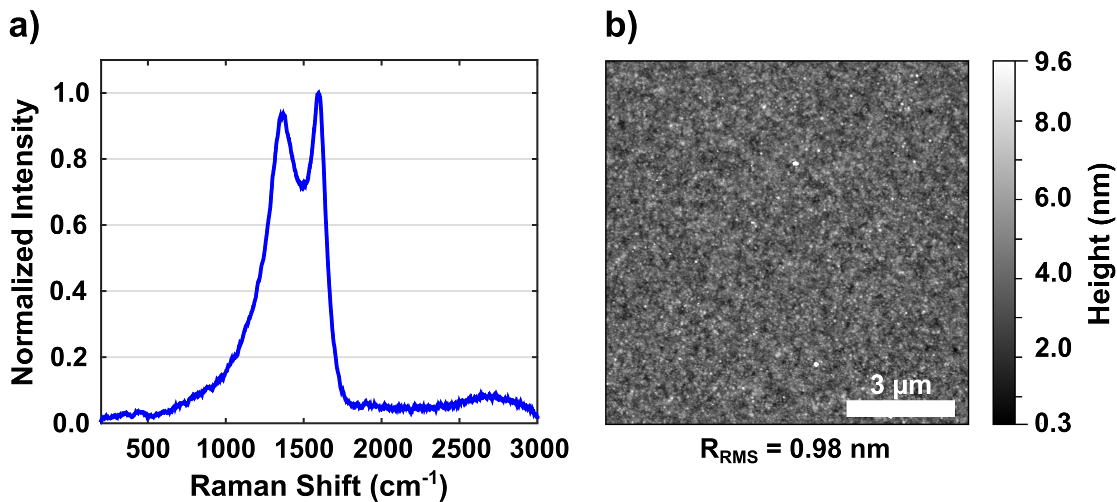

Figure 3.12: A Raman spectrum obtained from the GC material deposited by the wafer scale deposition system is shown in a) and exhibits the typical, discussed Raman features. The AFM surface scan of a GC sample deposited using the wafer scale deposition system is given in b) and the corresponding surface roughness is $R_{RMS} = 0.98\ nm$. Both, the Raman spectrum and the surface roughness are similar to those obtained from the GC material deposited by the small scale process.

In order to verify the highly laminar micro-structure of the deposited GC material a cross section of the GC film was prepared. The SEM image obtained after breaking the GC coated silicon substrate is shown in figure 3.13 a). The highly

laminar micro-structure is apparent in the high resolution image shown in figure 3.13 b), and is very similar to images found in literature of HT-PyC that had been annealed at 2900 °C [178].

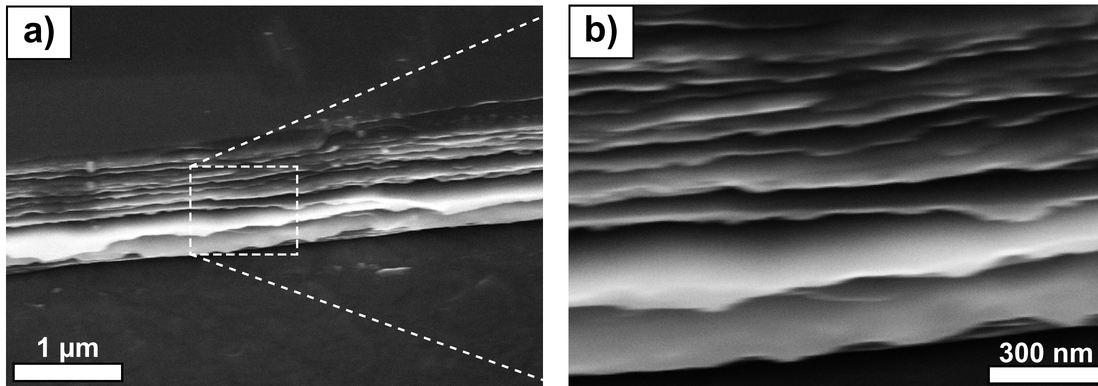

Figure 3.13: An SEM image of the cross section of a GC film that was deposited onto a silicon wafer is demonstrated in a). The highly laminar micro-structure becomes apparent in image b), showing the GC material with a higher magnification. The SEM images were obtained with a working distance of 6 mm and an acceleration voltage of 3 kV.

Temperature and Deposition Homogeneity

A common challenge for wafer scale processing schemes is the aspect of process homogeneity across the wafer substrate [196]. The inhomogeneities arise from temperature differences across the wafer substrate and, in the case of gas phase deposition processes, an inhomogeneous gas phase composition in the reactor volume. Temperature gradients are especially pronounced in cold wall reactor systems as the radiative losses of the wafer substrate are substantially larger at the edges of the substrate, compared to the substrate center [197]. The variation of the surface temperature of the substrate results directly in a spatial variation of the gas phase composition, either due to increased carbon deposition and thus removal of carbonaceous components, or an increased pyrolysis of the carbonaceous components. The temperature and resulting gas phase inhomogeneity therefore leads to a spatial variation of the deposition rate of the GC material. In addition, the resulting temperature gradient within the wafer substrate is known to produce line dislocations due to a different volumetric expansion of the substrate material and high resulting stress [198]. Single wafer processing of crystalline silicon wafers can produce line dislocations at processing temperatures above 1000 °C, if the temperature gradient within the substrate is exceedingly large [199].

Line dislocations occur predominantly at the wafer edge due to the discussed temperature gradient evolution [199]. A micrograph of a processed silicon wafer exhibiting strong slip line formation is depicted in figure 3.14 a). The used RTCVD system is capable of processing substrates with a diameter of up to 200 mm. By employing silicon wafers with a diameter of 150 mm and combining the wafer substrate with a silicon ring with an outside diameter of 200 mm, it was possible to significantly decrease the edge effects for the used 150 mm wafer. The employed silicon ring is shown in figure 3.14 b) and allowed an improved GC thickness distribution and a reduction of the observed line dislocations.

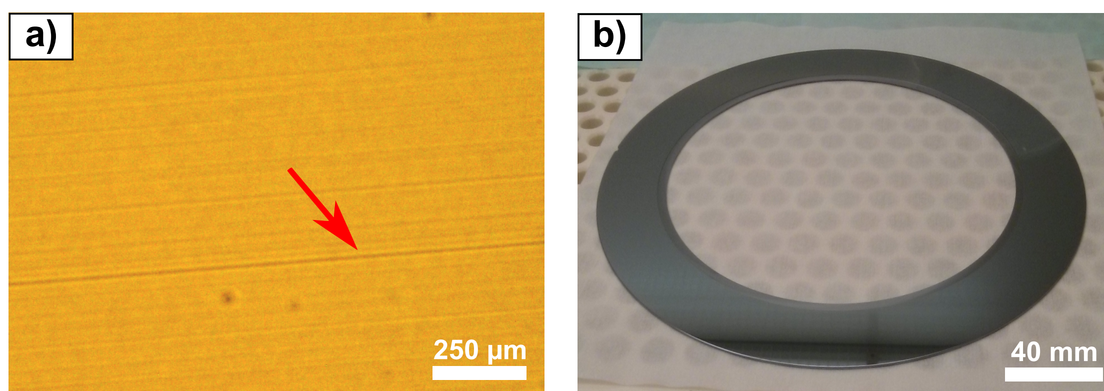

Figure 3.14: A micrograph image of GC material deposited onto a silicon wafer is shown in a). Slip-line dislocations are visible, as indicated by the arrow. A photograph of the used silicon edge ring is depicted in b) and the silicon wafer substrate with a diameter of 150 mm can be placed within the silicon ring.

Apart from using a silicon edge ring, different methods have been proposed in order to achieve an improved temperature homogeneity. These include rotating the wafer substrate, an optical thin film filter on the bottom side of the quartz window [200], a reflective coating on the wafer substrate itself [197] and the regulation of the illumination intensity by spatially varying the applied power to the illumination system [201]. The later was available for the used RTCVD system and the silicon wafer substrate was heated by radiation from the top of the reactor chamber. The heating system was comprised of three separate heating zones in order to achieve an improved temperature homogeneity across the substrate, as shown in figure 3.15 a). It was therefore possible to partially compensate the radiative losses of the wafer edges by increasing the heating power of the zones 1 and 2. A pyrometer was available to measure the temperature of the silicon wafer with a spot size of approximately 2.5 mm from below the reaction chamber. The pyrometer position could be varied as indicated in figure 3.15 a), with a pyrometer port located at the wafer center and one located towards the front of the chamber.

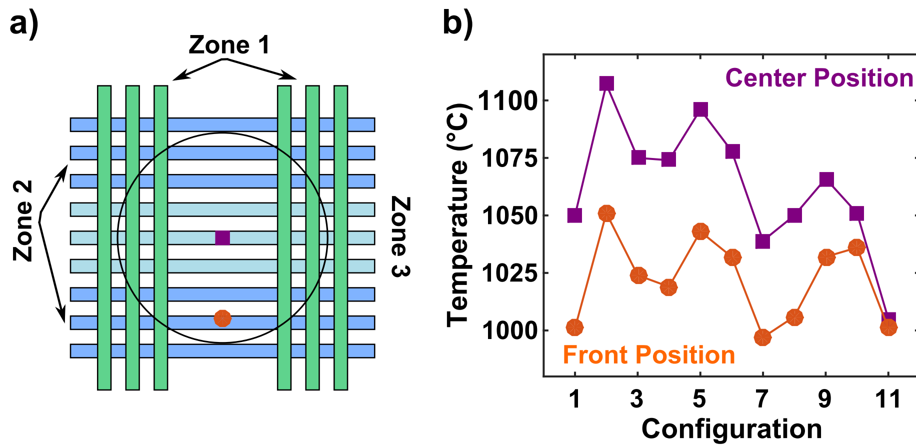

Figure 3.15: The lamp layout of the used reactor system is schematically shown in a). The three heating zones can be addressed independently and allow to compensate the radiative edge effects of the substrate. The pyrometer can either be located at the wafer center or 75 mm towards the front of the reactor volume, as indicated. The shown circle indicates the position of a substrate with a diameter of 200 mm. The measured temperatures for the two pyrometer positions, for the corresponding heating zone configuration, are given in b). Configuration 1 corresponds to a uniform heating profile.

The measured temperatures corresponding to the two described pyrometer positions for different combinations of correction factors, that regulate the power of the separate heating zones, is shown in figure 3.15 b). A silicon wafer with a diameter of 200 mm was used for the experiments and a low pressure of 5×10^{-3} mbar chosen. Configuration 1 corresponds to a uniform heating profile, with each heating zone receiving the identical amount of power. This resulted in a measured temperature difference of approximately 50 °C. Various heating configurations were tested until the measured temperature difference was close to zero (Configuration 11).

The identified heating zone configurations were employed to deposit the GC material, while the pressure, flow and overall power setting of the system were kept constant. The GC thickness was examined by measuring the sheet conductivity of the GC material across the wafer substrate. A linear relationship between the thickness of the GC material and the measured sheet conductivity was identified as described in section 2.2. The measured thickness values were normalized for a better comparability and the influence of the heating zone configurations are shown in figure 3.16. Using a homogeneous heating zone distribution resulted in the thickness distribution denoted as setting A. The large temperature deviation between the wafer center and the wafer edge lead to a thickness difference of a factor of two. Interestingly, the identified configuration 11 that led to the minimal

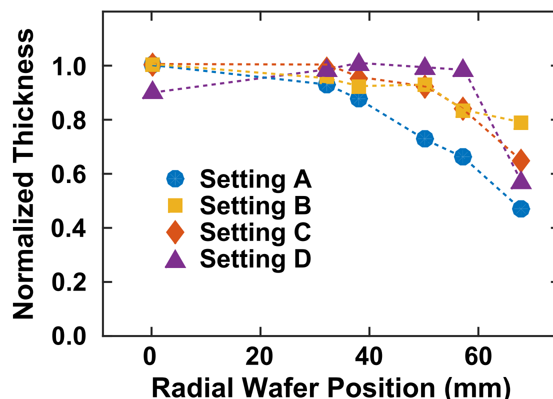

Figure 3.16: The resulting GC thickness distribution across a silicon wafer with a diameter of 150 mm is shown for four sets of heating zone correction factors. The thickness was normalized in order to visualize the effect of the different correction factors. Setting A corresponds to a uniform heating configuration.

temperature deviation shown in figure 3.15 b) showed a reduced GC thickness at the wafer center, denoted as setting D in figure 3.16. This effect was assumed to arise from the introduced gas phase during the deposition process. Settings B and C exhibited a significantly improved thickness distribution and setting B was finally chosen for the GC deposition process.

A set of promising deposition parameters was chosen to deposit highly structured GC material onto silicon substrates with a diameter of 150 mm, as summarized in table 3.2. The GC material was evaluated by fabricating x-ray transmission windows and the processing steps for the window fabrication will be discussed in the following chapter.

Table 3.2: The identified deposition parameters that were used during the wafer scale GC deposition process are summarized.

Precursor Gas	**Temperature**	**Pressure**	**Gas Flow**	**Growth Rate**
CH_4	1200 °C	140 mbar	2000 sccm	30 nm/min

4 Window Fabrication

GC x-ray transmission windows were fabricated from GC coated silicon substrates. The direct deposition of the GC material onto the silicon substrate allows the fabrication of GC x-ray transmission windows with an integrated silicon frame by removing parts of the silicon substrate. The inherently high adhesion of the GC material onto the silicon frame due to strong silicon-carbon bonds avoids the problems that arise otherwise from joining the very thin window material to a sturdy frame.

The employed silicon substrates enables the use of widely available silicon processing technology and the high chemical stability of the GC material opens the route to straight forward window fabrication. The window design and fabrication scheme for the replacement of beryllium as well as for GC low energy x-ray transmission windows are discussed in this chapter.

4.1 Window Design

The window design of the GC x-ray transmission windows follows the design of Be x-ray transmission windows, that are seen as reference windows as discussed in Chapter 1, and therefore allows a direct replacement without altering the detector module housing.

4.1.1 Window Design for an Open Window Geometry

The window design of the Be x-ray transmission windows is shown in figure 4.1, with a circular open window geometry with a diameter of 7 mm and a circular window frame with an outside diameter of 9.75 mm [56].

The GC x-ray transmission windows were designed to exhibit an open geometry with a diameter of 7 mm in order to demonstrate the suitability of the GC material. Circular silicon substrates with a diameter of 9.75 mm were employed, allowing the testing systems that were available, for the qualification process of detector housings incorporating beryllium windows, to be used. The free standing radiation passage was fabricated by removing the central part of the GC coated silicon substrate. The remaining silicon substrate material elegantly forms the

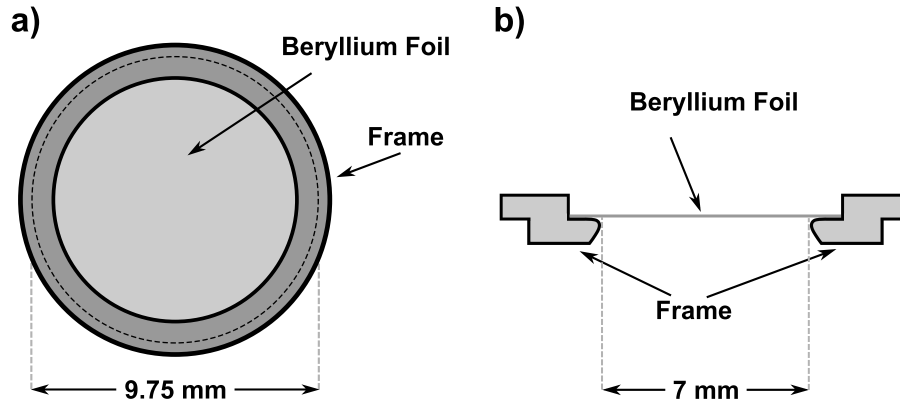

Figure 4.1: The schematic top down view of a Be x-ray transmission window is depicted in a) and a schematic cross section view is given in b), as found in reference [56]. The thin beryllium foil is joint to the sturdy window frame by metallic bonding and forms the radiation passage.

window frame that can be subsequently joined to the TO8 detector housing.

In order to determine the properties of the GC x-ray transmission windows, GC films with a thickness ranging from 30 nm to 3 µm were deposited onto silicon substrates as described in Chapter 3. The desired GC film thickness was obtained by varying the deposition time and a low growth rate of 1 nm to 5 nm per minute allowed excellent thickness control, which is assumed to be better than 10 nm.

The window fabrication process development was performed using square 1 cm by 1 cm silicon substrates due to the high availability and subsequently transferred to the circular substrates.

4.1.2 Low Energy X-ray Transmission Window Design

Low energy x-ray transmission windows require a significantly reduced window thickness and thus a supporting structure in order to sustain the differential pressure that acts across the window, as discussed in Chapter 1. GC low energy x-ray transmission windows therefore require a more elaborate window design.

Circular silicon substrates with a diameter of 9.75 mm were used in order to comply to the dimensions of the standard detector housing. The silicon substrate was used to fabricate an integrated silicon support grid that is part of the window frame. The optimal layout of the supporting grid is dependent on the mechanical strength of the GC material and the chosen GC thickness, as well as the required mechanical stability of the x-ray transmission window. The supporting silicon grid is radio opaque and blocks the incoming x-ray radiation and it is therefore

desirable to minimize the coverage of the supporting grid, which results in a higher FF of the window as discussed in Chapter 1.

A number of window designs were proposed that offer different FF and different grid designs. In general it is expected that a lower FF results in a higher mechanical strength of the resulting window as this either reduces the span width of the individual open window regions or increases the width, and thus the mechanical strength of the supporting grid structure.

Four low energy x-ray transmission window designs with increasing FF are shown in figure 4.2. The open window geometry is divided into smaller window cells with either a circular or a hexagonal shape, with a cell width of either 0.6 mm or 1 mm. The remaining silicon supporting grid has a minimal width of 80 µm and the thickness of the support structure is the silicon substrate thickness which corresponds to 500 µm for the employed substrates. Design a) divides the window region into 91 circular cells with a diameter of 0.6 mm, design b) into 91 hexagonal cells with a width of 0.6 mm, design c) into 37 circular cells with a diameter of 1 mm and design d) into 37 hexagonal cells with a width of 1 mm.

An alternative approach is shown in figure 4.3, employing a bar support structure dividing the window geometry into rectangular cells. Design e) comprises of 6 supporting bars with a width of 200 µm and a span width of 1 mm, whereas design f) comprises of 6 supporting bars with a reduced width of 100 µm and a span width of 1 mm. The use of a bar grid structure has the advantage of a reduced influence of the incident angle of the incoming x-ray radiation, as shadowing only occurs for incident angles perpendicular to the grid structure. In addition, the bar grid windows can be fabricated using wet etching techniques, which is a considerable advantage in regard to the fabrication complexity. Table 4.1 shows the detailed characteristics of the proposed window geometries including the theoretical FF.

Table 4.1: The characteristics of the different window designs for GC low energy x-ray transmission windows are summarized.

Design	**Fill Factor**	**Cell Geometry**	**Cell Width**	**Grid Width**
a)	70 %	Circular	600 µm	80 µm
b)	77 %	Hexagonal	600 µm	80 µm
c)	76 %	Circular	1000 µm	80 µm
d)	85 %	Hexagonal	1000 µm	80 µm
e)	85 %	Bar	1000 µm	200 µm
f)	90 %	Bar	1000 µm	100 µm

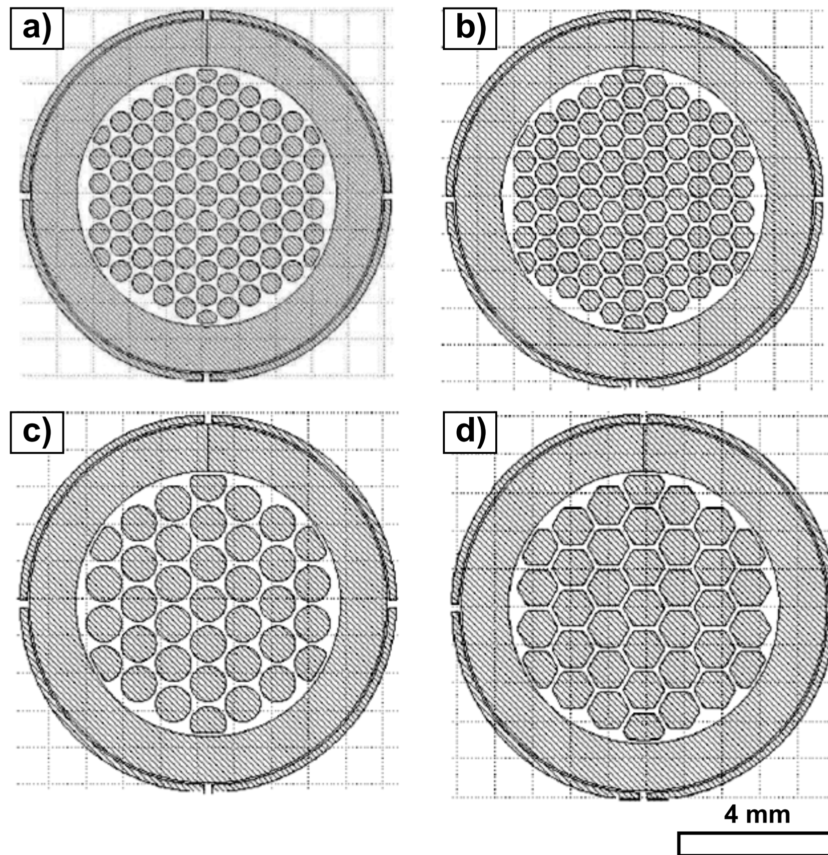

Figure 4.2: The evaluated window designs for GC low energy x-ray transmission windows are shown and divide the open window area into cells with a reduced span width. A circular cell design with a diameter of 0.6 mm (a), a hexagonal cell design with a cell width of 0.6 mm (b), a circular cell design with a diameter of 1 mm (c) and a hexagonal cell design with a cell width of 1 mm (d) are shown.

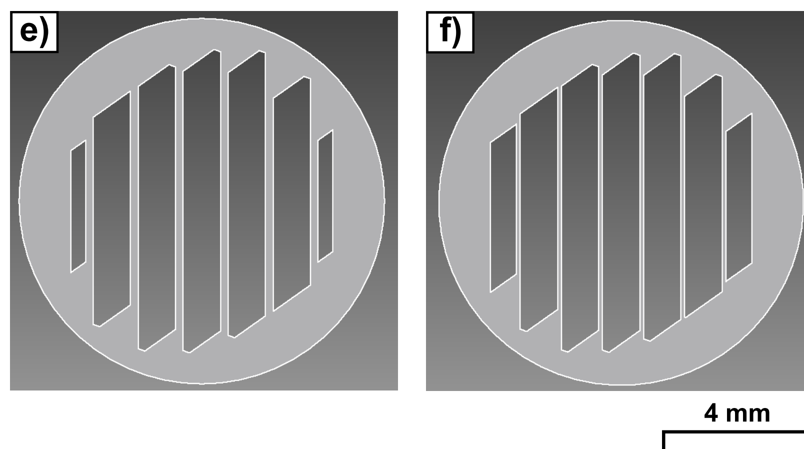

Figure 4.3: The evaluated support structure designs for GC low energy x-ray transmission windows with a bar support structure are depicted. The design e) exhibits a bar width of 200 µm and design f) a reduced bar width of 100 µm. The span width for both designs is 1 mm.

4.2 Fabrication Scheme

The GC x-ray transmission windows were fabricated by partly removing the silicon substrate, thus creating free standing regions of the GC material with a high x-ray transparency. The remaining silicon forms the window frame and, for the low energy x-ray transmission windows, the supporting structure. The fabrication process is described in the following and the individual components of the process discussed in more detail in the next section.

The developed fabrication process for GC x-ray transmission windows with an open window geometry is schematically given in figure 4.4 a). The GC material was deposited onto the (100) orientated silicon substrates as described in Chapter 3. The high stability of the GC material against commonly used wet etchants such as heated potassium hydroxide allows it to be used as the masking material. The window geometry of the GC x-ray transmission windows was subsequently defined by partially removing the GC material on the back of the substrate. Wet chemical etching was employed to remove the silicon substrate in the regions where the silicon was not protected by the GC material.

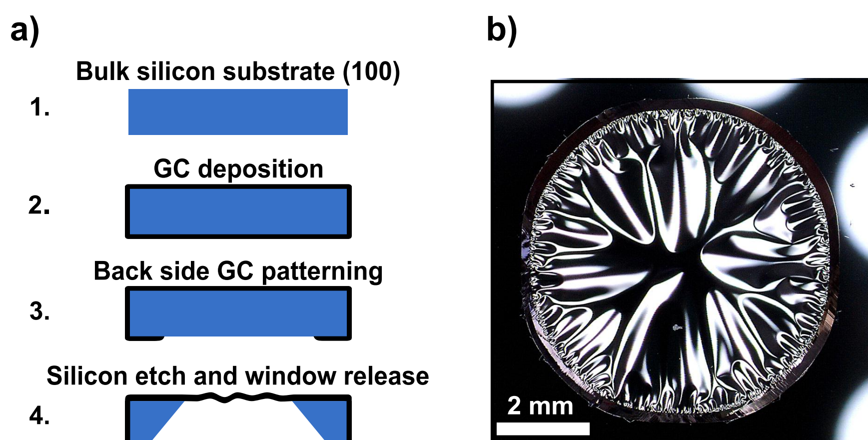

Figure 4.4: The fabrication process for GC x-ray transmission windows with an open window geometry is schematically depicted in a). A photograph from the back of a GC x-ray transmission window, as it was obtained after wet etching, is presented in b). The reflections of the LEDs used for illumination are visible and wrinkles were formed in the free standing GC material as the bulk silicon material was removed due to the compressive stress of the GC material.

Etching was completed once the free standing GC film was formed. A photograph of a typical GC x-ray transmission window fabricated by the described process is shown in figure 4.4 b). The image was taken from the back side of the window and the bright spots near the substrate edge arise from the LEDs used for

illumination. The free standing GC film develops wrinkles as soon as it is released from the silicon substrate due to the compressive stress of the GC material.

The fabrication process for the GC low energy x-ray transmission windows is schematically depicted in figure 4.5. The window design utilizing a bar support structure offers the advantage that it can be realized using wet chemical etching, whereas the hexagonal and circular cell design requires more elaborate micromachining schemes.

The fabrication scheme for the bar supported GC low energy x-ray transmission windows is depicted in figure 4.5 a). Silicon substrates with a (110) surface orientation were used and the GC material deposited as described in Chapter 3. The use of silicon substrates with a (110) crystallographic orientation of the surface plane allows the fabrication of a high aspect support structure in one direction of the wafer, using anisotropic wet etching. A detailed discussion regarding the crystallographic orientation and the wet etching process is given in section 4.2.2. The GC material on the back of the substrate was used as an etch mask and the GC material removed in the regions that were to form the radiation passage. The silicon substrate was subsequently removed in the regions that were not covered by the GC material using wet chemical etching. A photograph from the back of a GC low energy x-ray window with a support bar structure is shown in figure 4.5 b). The free standing GC film forms the characteristic wrinkles and is supported by the vertical, silicon support structures that are an integral part of the window frame.

The complex design of the low energy x-ray windows incorporating circular and hexagonal cells required high aspect, vertical structures, independent of the crystallographic orientation and cannot be achieved using anisotropic wet chemical etching. Instead pre-structured silicon substrates were used that exhibit only a thin silicon film that covers the cell regions as shown in figure 4.5 c), which schematically shows the fabrication process. The GC material was deposited onto the pre-structured silicon substrates with a (100) surface orientation, with the deposition process discussed in Chapter 3. The GC material on the back of the substrate was removed across the entire window region. Wet chemical etching was employed to etch the remaining, thin silicon film that covers the window cells in order to fabricate the free standing GC regions. A photograph from the back of a GC low energy x-ray transmission window with a hexagonal support grid design is depicted in figure 4.5 d).

The presented fabrication schemes offer a direct route to the GC x-ray transmission window fabrication and the individual processing steps are discussed in the following.

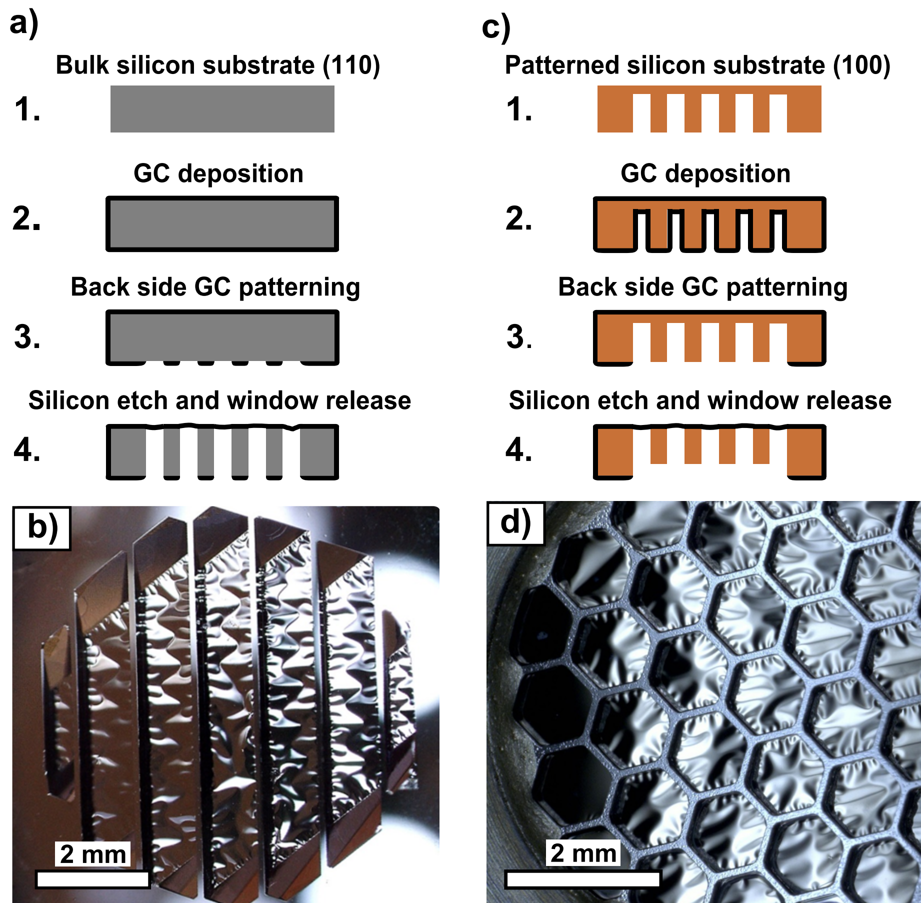

Figure 4.5: The fabrication process for GC low energy x-ray transmission windows with a bar support structure, utilizing a (110) orientated silicon substrate, is schematically depicted in a). A photograph from the back of a fabricated GC window with a bar support structure is shown in b) and the vertical silicon support structures separate the free standing GC material. The fabrication process for a GC low energy x-ray transmission window with an arbitrary support structure design is given in c). The (100) orientated silicon substrates need to be pre-structured according to the support structure design using a RIE process. A photograph from the back of a window incorporating a hexagonal support structure is shown in d).

4.2.1 Graphenic Carbon Structuring

The GC material was conveniently used as the masking material during the silicon structuring due to its high resilience against potassium hydroxide, a commonly used wet etch solution for anisotropic silicon etching.

The GC material therefore had to be structured in a reliable manner in order to define the resulting window geometry of the GC x-ray transmission windows. While the GC material is chemically inert against most etching solutions, high etch rates can be obtained in highly oxidative environments and a number of etching techniques were therefore considered.

- Carbon composites are known to be etched by oxygen exposure at temperatures above 600 °C [202]
- Polymers such as polymethylmethacrylate (PMMA) are known to be etched by oxygen exposure in combination with illumination at a wavelength of 172 nm [203]
- HOPG can be etched by the exposure to an oxygen containing plasma [204].

The structuring process should exhibit sufficiently high etch rates as the GC material has a thickness of up to 3 µm, should offer a sufficiently high resolution in order to fabricate delicate support structures and avoid any deterioration of the GC material covering the front of the silicon substrate. The last aspect was seen as especially crucial, as pinholes of any size were unacceptable in the window region of the substrate as this would deteriorate the gas and light tightness and reduce the mechanical strength of the GC x-ray transmission window.

The use of a shadow masking scheme significantly reduces the necessary processing steps in order to structure the GC material compared to the deposition and lithographic structuring of a deposited masking material such as titanium. While shadow masking offers a reduced resolution due to under etching, the relaxed geometries necessary for the discussed window designs permit its use. Both, an oxygen containing capacitively coupled plasma (CCP) and photo-induced etching with a high power UV source were seen as promising candidates and were subsequently evaluated.

A sample holder was designed that protected the front of the GC coated substrate and simultaneously aligned the shadow mask, in order to obtain repeatable results. The shadow masks were fabricated from 100 µm thick steel sheets and laser cutting offered a sufficiently high resolution of 50 µm to realize the mask designs.

Photo-induced Etching

A shadow mask with an open diameter of 7 mm was used and the front of the GC sample was protected against illumination. A UV lamp, emitting at a wavelength of 254 nm and 185 nm with a power of 4.8 W, was placed directly above the sample in an oxygen containing atmosphere. The result of 216 hours of UV exposure in an oxygen atmosphere is shown in figure 4.6 a). A discoloration of the GC material in the open region of the shadow mask is apparent, but the removal of the GC material was seen as insufficient even at such an elevated duration. The sample substrate has a non-polished back side which is advantageous in order to visualize the etching behavior as double-polished substrates are highly reflective.

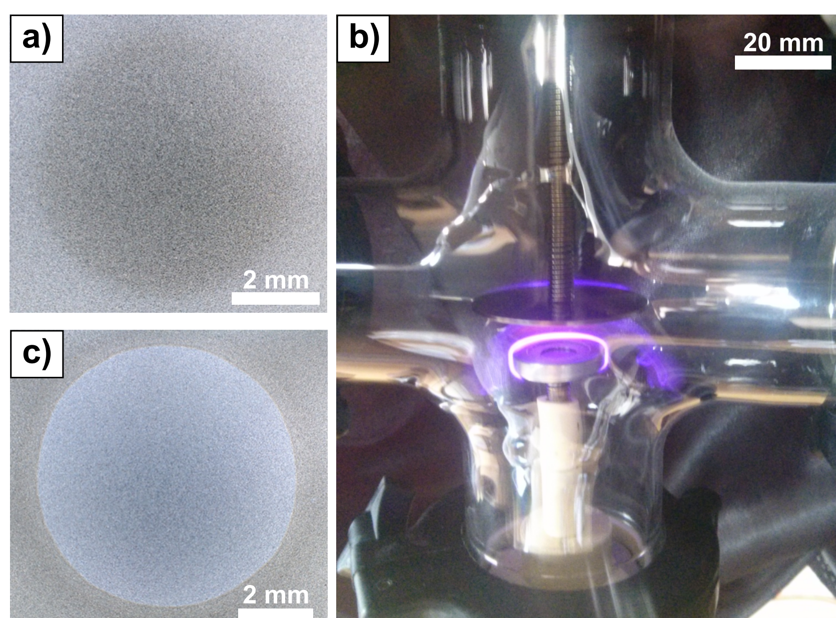

Figure 4.6: A photograph of the GC material after an extended exposure of 216 hours to UV illumination in an oxygen atmosphere is shown in a) and the GC material was attacked but not removed. A photograph of the employed CCP setup for oxygen plasma etching of the GC material is given in b) and high etch rates of 140 nm/min and a good mask transfer were possible as shown in c), as the GC material was removed in the center.

Oxygen Plasma Etching

A photograph of the used CCP system is shown in figure 4.6 b). The simple setup was comprised of two electrodes and a voltage source operating at a frequency of 45 kHz. This led to an anisotropic etching behavior that was used to transfer

the mask design into the GC material. A control unit was designed and built that allows to manually set the process duration. The temperature increase of the sample with prolonged processing times led to an increasing etch rate and a cyclic mode of operation therefore included in the control unit. It was possible to set the "on" and "off" time of the plasma process independently and high substrate temperatures were avoided by choosing a sufficiently long cool off period before the etching process was resumed.

The results of 7 min of plasma etching using a shadow mask with an open geometry of 7 mm is shown in figure 4.6 c). The GC material was completely removed in the open region of the shadow mask, which was verified by Raman spectroscopy (not shown). The etch rate of the GC material was determined to be approximately 140 nm/min and thus sufficiently large, even for thick GC films. The use of a shadow mask commonly results in an under etch of the mask structure due to the space that is present between the mask and the to be etched material. The minimal size of the mask features and the amount of under etching were therefore seen as the limiting factors for the resolution of the GC structuring using the discussed processing scheme.

A micrograph of a structured GC film that was deposited on a silicon substrate and etched using oxygen plasma, with an open window design, is shown in figure 4.7 a). The GC material was completely removed in the center region, whereas the remaining substrate is still covered with the GC material. The presented GC structuring scheme allowed the fabrication of the narrow masking structures required for the GC low energy x-ray transmission windows with a bar support structure, as shown in figure 4.7 b). The resulting GC mask exhibited a bar width of 185 µm instead of the targeted width of 200 µm and an under etching of 7.5 µm was therefore identified. Considering the GC film thickness of only 140 nm this is substantial but for the minimal structure size of the proposed window designs seen as sufficient and can be compensated by adjusting the mask dimensions.

An SEM image of the structured GC material is shown in figure 4.7 c) and a close up of the under etched region is given in figure 4.7 d). The GC material that was protected by the shadow mask still exhibits a smooth surface and the line roughness was interpreted as sufficiently smooth for the dimensions of the window designs.

GC structuring with an oxygen plasma in combination with a shadow mask was therefore seen as a suitable structuring scheme and employed to fabricate the GC x-ray transmission windows.

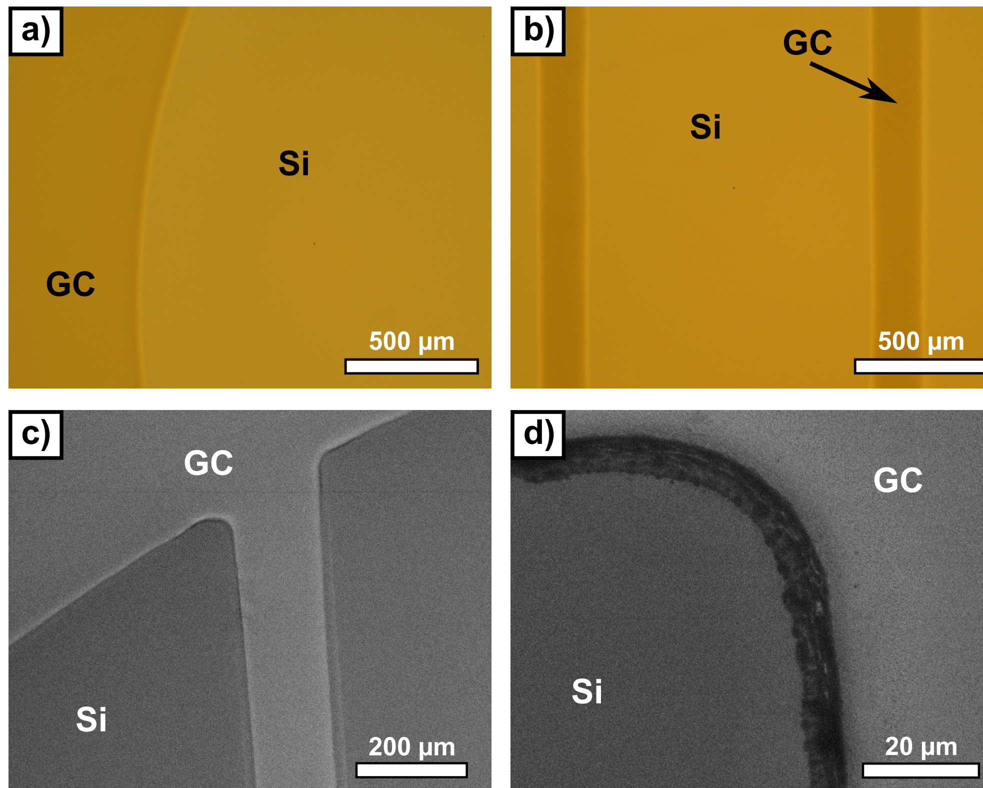

Figure 4.7: A micrograph of a structured GC coated silicon substrate is shown in a). The GC material was removed in the center of the sample and the round shape of the window geometry is visible on the left side of the image. The developed structuring scheme allows the mask fabrication for the bar supported GC low energy x-ray transmission window design, as demonstrated in b), showing the narrow GC mask required for the etching of the vertical support structures. An SEM image of the structured GC film shown in b) is depicted in c). An SEM image with a higher magnification is given in d) and shows the under etched GC region in more detail. The SEM images were obtained with a working distance of 6 mm and an acceleration voltage of 3 kV.

4.2.2 Silicon Micromachining

The silicon substrate needs to be removed in the regions that resemble the open window geometry. In the case of the windows intended for the replacement of beryllium, a circular window design and for the more elaborate low energy x-ray transmission windows the discussed window designs were employed.

Wet Chemical Etching

Wet chemical etching has the advantage of a simple processing scheme offering high throughput and low cost. The GC material exhibits a very high chemical re-

silience against potassium hydroxide and is therefore a suitable masking material.

Potassium hydroxide solution is an anisotropic wet etchant for silicon substrates and commonly used during the micro-machining for MEMS applications [205]. The etch rate is dependent on the crystallographic orientation and doping of the silicon substrate, as well as the temperature and composition of the etchant solution. The (111) plane is the slowest etching crystallographic direction and ratios of up to 1:400 for the etch rate compared to the (100) plane and 1:600 for the etch rate compared to the (110) plane have been reported [205]. The direction dependent etch rates results in the typical pyramidal structures due to the very low etch rate in the (111) direction for (100) orientated silicon wafers, as demonstrated in figure 4.8 a), as the (111) planes intersect the (100) plane at an angle of 54.74° [205]. The use of (110) orientated silicon wafers allows the fabrication of structures with vertical sidewalls and was therefore seen suitable for the fabrication of a bar support structure as shown in figure 4.8 b), due to the vertical intersection of the (111) and (110) planes [206].

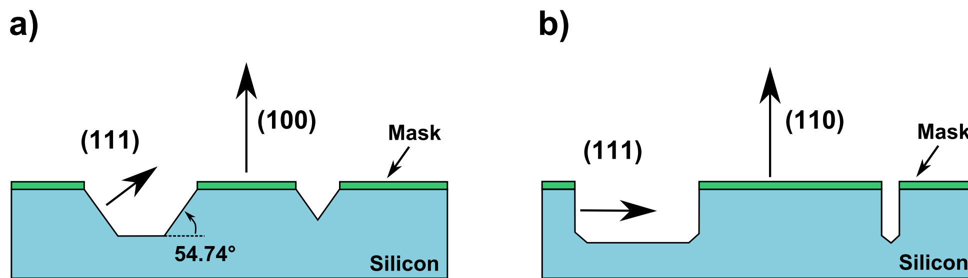

Figure 4.8: The typical pyramidal structures that develop for (100) orientated silicon substrates, if etched with a potassium hydroxide solution, are shown in a) and result from the intersection of the (111) planes and the wafer surface at an angle of 54.74°. Structures with a vertical sidewall can be etched into a correctly orientated (110) silicon substrate with potassium hydroxide, due to the perpendicular intersection of the (111) planes and the wafer surface, as demonstrated in b). The schematics were adapted and redrawn from reference [205].

Open Window Geometry

The etch masks for the circular window design were therefore altered in order to compensate for the formation of the (111) plane with an angle of 54.74° relative to the (100) surface. The final window diameter is subsequently smaller than the open mask diameter and has to be increased by an amount that is dependent on the substrate thickness. Following a simple trigonometric approach the mask diameter was chosen as 7.7 mm for a substrate thickness of 500 µm based on equation 4.1 and results in a final window diameter of 7.0 mm. With D denoting the

required diameter of the mask for a resulting window diameter of 7.0 mm.

$$D = 7.0\ mm + 2 \times \frac{t}{tan(54.74°)} \approx 7.7\ mm \quad (4.1)$$

The anisotropic etching for potassium hydroxide etched silicon substrates leads to a strong deviation of the final window geometry. The circular shape of the GC mask eventually leads to a square window geometry for long etching times. The concentration dependent etch rates for different crystallographic directions of a (100) orientated p-type silicon wafer ($5 - 10\ \Omega\, cm$) at a temperature of 80 °C, as determined by Zubel et al. [207], are shown in figure 4.9 a).

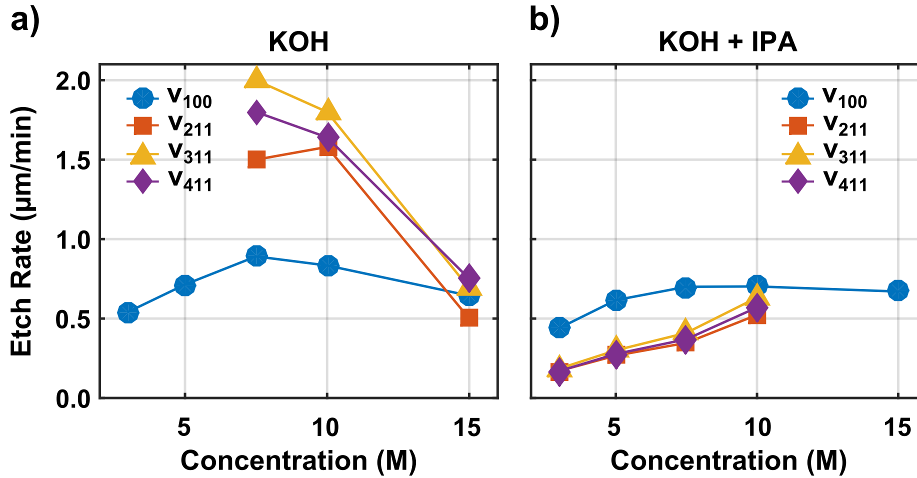

Figure 4.9: The concentration dependent etch rates for different crystallographic silicon planes in a potassium hydroxide solution with the specified molar concentration are given in a). The corresponding etch rates can be altered if the potassium hydroxide solutions are saturated with isopropanol as a surfactant, as demonstrated in b). The etch rates were determined by Zubel et al. [207] for a temperature of 80 °C and low doped p-type silicon with a resistivity of $5 - 10\ \Omega\, cm$. The diagrams were adapted and redrawn from reference [207].

The etch rate of the (311) plane, for example, is significantly higher than the (100) plane, which has to be etched in order to remove the silicon material, and results in the aforementioned deviation between the transferred window geometry and the original mask design.

Adding a surfactant, such as isopropanol, to the potassium hydroxide solution reduces the direction dependent etch rates compared to the (100) plane, as

shown in the diagram depicted in figure 4.9 b), and allows circular patterns to be etched [208,209]. The etch rate of the (100) plane is only slightly reduced, whereas the other directions exhibit a much more pronounced reduction of the etch rate for potassium hydroxide solutions with a concentration at and below 10 M. The underlying mechanism of the added surfactant is assumed to be an enhanced adsorption of the isopropanol molecules on the higher indexed planes, thus blocking the access of OH^- ions to the silicon surface [210]. The direction dependent etch rates of a potassium hydroxide solution saturated with isopropanol was therefore seen as much more favorable for transferring arbitrary mask designs into the (100) silicon substrate.

The concentration of the potassium hydroxide solution not only determines the direction dependent etch rates of silicon, but also has a significant impact on the quality of the etching process [210]. The influence of the potassium hydroxide concentration on the roughness of the silicon surface is shown in figure 4.10. Both images show the back side of a silicon substrate with a circular, GC free center region that has been etched with a potassium hydroxide solution. The substrate shown in figure 4.10 a) was etched in a 4 M potassium hydroxide solution, saturated with isopropanol, while the window shown in figure 4.10 b) was etched in a 5 M potassium hydroxide solution, also saturated with isopropanol. The developed (111) plane of the silicon substrate is visible on the right side of the images and indicated by the arrows. The intersecting silicon plane exhibits a smoother surface for the five molar solution. This is is seen as highly advantageous as the intersection of the (111) plane and the (100) surface forms the edge and thus anchor point of the free standing GC window material. Any irregularities, especially formations that point towards the window center result in regions of increased stress that reduce the mechanical stability of the GC window.

The discussed potassium hydroxide solution with a concentration of 5 M, a temperature of 80 °C and isopropanol as a surfactant was subsequently chosen for the window fabrication. The resulting etch times were found to be approximately nine hours for the (100) orientated silicon substrates with a thickness of 500 µm and the etch rate therefore identified to be approximately 0.9 µm/min. The use of the surfactant allowed the etching of circular structures and the presented scheme was found to be highly reliable as demonstrated in figure 4.11. A top view photograph of a GC x-ray transmission window with a circular window geometry is given in figure 4.11 a) and exhibits an excellent circular shape, which manifests in a radial symmetry of the formed wrinkles. A back view photograph is shown in b) and the resulting intersection of the (111) silicon plane and the GC material is free of hillocks, as verified in the micrographs of the back side of the GC x-ray transmission window given in figure 4.11 c) and d).

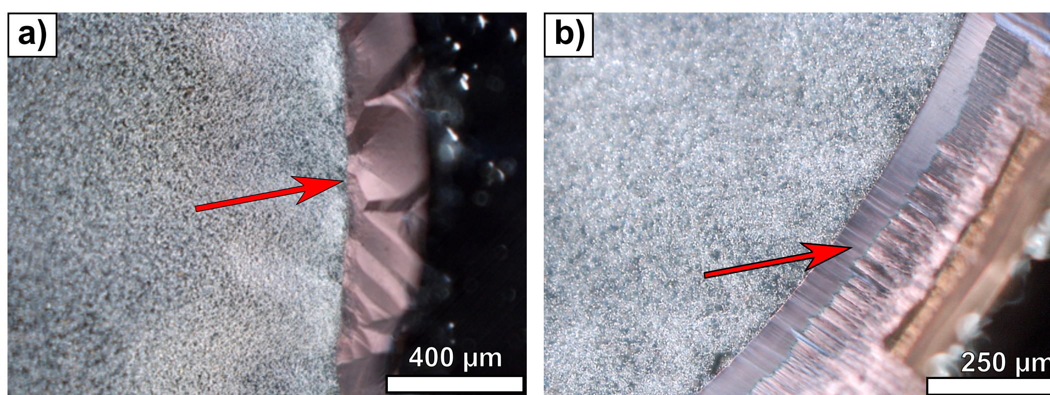

Figure 4.10: A photograph from the back of an etched silicon substrate using a 4 M potassium hydroxide solution is depicted in a), whereas b) shows a photograph of a much smoother silicon plane, as indicated by the arrows, of a silicon substrate that was etched with a 5 M potassium hydroxide solution. Both solutions were kept at a temperature of 80 °C and saturated with isopropanol.

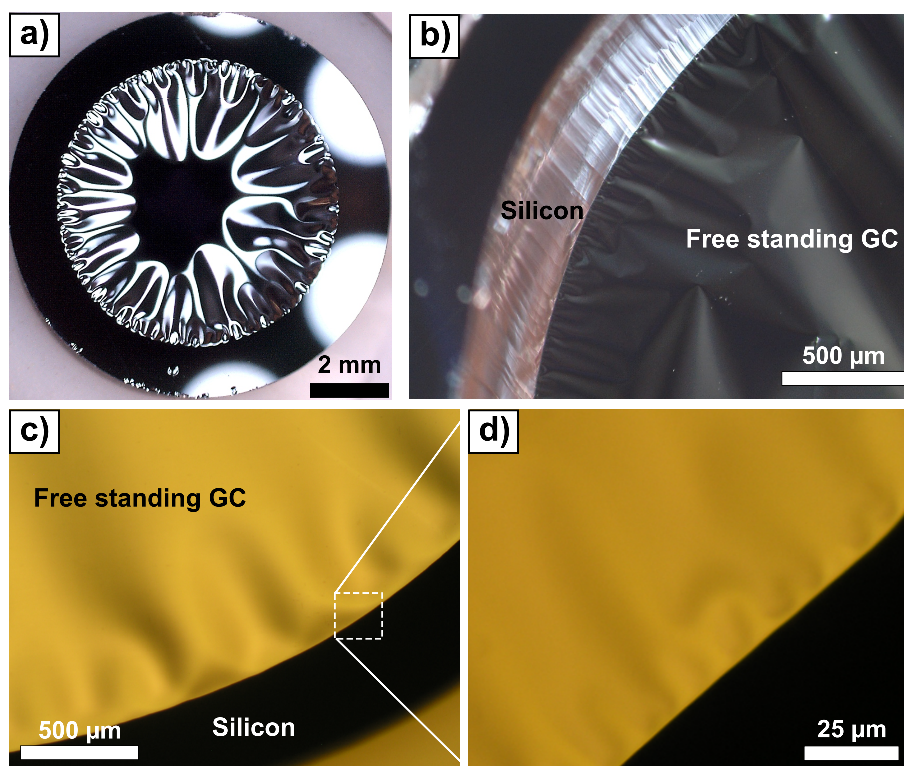

Figure 4.11: A top view photograph of a GC x-ray transmission window with a diameter of 7.15 mm and a GC thickness of 1 µm is presented in a). The magnified view from the back side of the GC x-ray transmission window, given in b), demonstrates the smooth finish of the silicon sidewall surface. The intersection of the silicon (111) plane (left side) and the GC material (right side) is visible. The micrographs given in c) and d) show the back side of the GC window and demonstrate the hillock free silicon-GC intersection in the right side of the images.

Window Designs with a Bar Support Structure

High aspect, vertical structures can be fabricated by anisotropic wet etching by carefully aligning the etch mask with the crystallographic orientation of a (110) orientated silicon substrate [211]. A photograph from the back side of a GC low energy x-ray transmission window, incorporating a bar supported window design, with a GC thickness of 140 nm is given in figure 4.12 a).

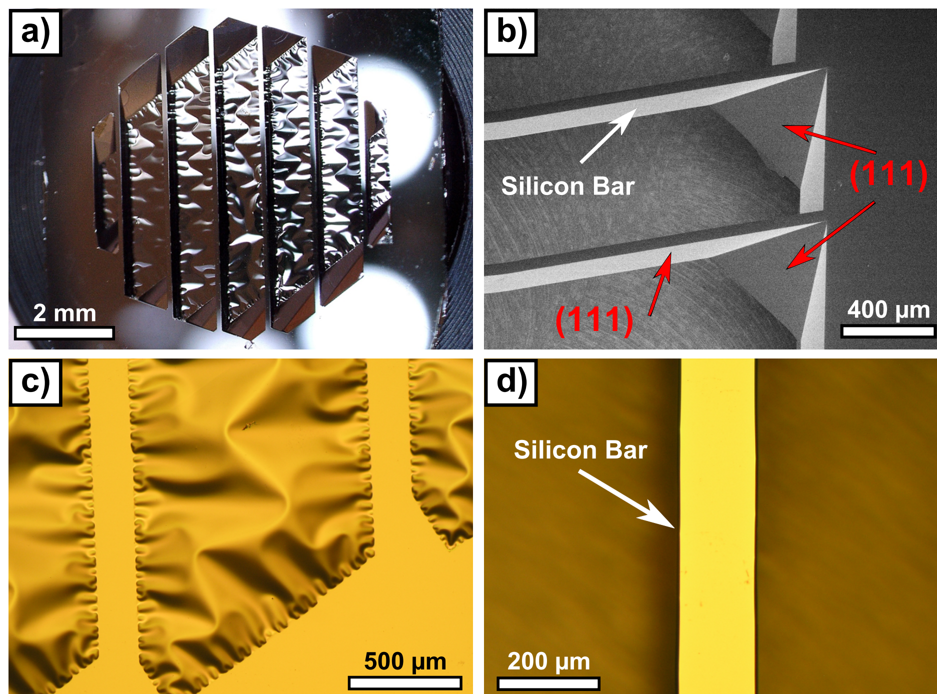

Figure 4.12: A photograph from the back side of a GC low energy x-ray transmission window with a bar support structure is given in a). An SEM image of the silicon bar support structure is shown in b) and the (111) silicon planes are indicated by the arrows. The SEM image was obtained with a working distance of 6 mm and an acceleration voltage of 3 kV. A micrograph of the front side of the GC low energy window is depicted in c) and a micrograph image from the back of a silicon bar structure is given in d).

The large difference of the etching rates of the (110) and (111) silicon planes results in the emergence of almost atomically flat silicon structures. The thin GC film is supported by a silicon bar structure with a nominal width of 200 µm and a nominal span width of 1 mm. An SEM image of the silicon grid structure is shown in figure 4.12 b) and the (111) planes are indicated by the arrows. Aside from the (111) planes that form the vertical bar structure, an additional (111) plane emerged at the intersection of the bar structure and the window frame. The plane

intersects the (110) substrate surface at an angle of 35.3°, which reduces the length of the open geometry and had to be accounted for in the GC mask design [206]. A micrograph image of the front of the GC low energy x-ray transmission window with the parallel bar structure is given in figure 4.12 c). The thin GC film forms wrinkles as it is released from the substrate due to the compressive stress of the GC material. The highly parallel nature of the bar structure becomes apparent in figure 4.12 d) and the absence of step like edges in the silicon bar structure demonstrates the excellent alignment of the GC etch mask and the crystallographic orientation of the silicon wafer.

Pre-structured Silicon Substrates for Arbitrary Window Designs

The discussed wet etch processing allows the fabrication of a bar support structure and, with the addition of isopropanol, circular window geometries. Arbitrary window designs are not possible as vertical features can only be realized along the vertical (111) planes of the employed silicon substrate.

The use of pre-structured silicon substrates that can be obtained using a dry etching process, such as reactive ion etching (RIE) using the Bosch Process, allows high aspect structures with an arbitrary design [212]. Silicon substrates were pre-structured based on the discussed low energy x-ray transmission window designs exhibiting a circular or hexagonal cell layout. The structuring process was terminated before the silicon substrate was completely removed and a thin silicon layer, covering the open area of the window cells, remained. The GC carbon was subsequently deposited onto the pre-structured silicon substrates as discussed in Chapter 3. The GC material covering the back of the silicon substrate was etched using an oxygen containing plasma and the thin remaining silicon film removed with the introduced potassium hydroxide solution used for the circular window geometries. The thin, remaining, silicon was etched within minutes, resulting in only marginal under etching of the pre-structured window features, and a free standing GC film was subsequently formed.

The micrograph images shown in figure 4.13 a), c) and e) show the back side of three of the proposed low energy window designs prior to the GC deposition. The support structure is clearly visible and the open regions of the window cells are still covered by a thin silicon film. The corresponding front side micrograph images of the resulting GC low energy x-ray transmission windows, as obtained after the GC deposition and wet etching, are shown in figure 4.13 b), d) and f). The thin GC material forms wrinkles after the thin silicon substrate material was removed due to the compressive stress of the GC material. The resulting support structure exhibits an excellent uniformity and closely resembles the corresponding window design.

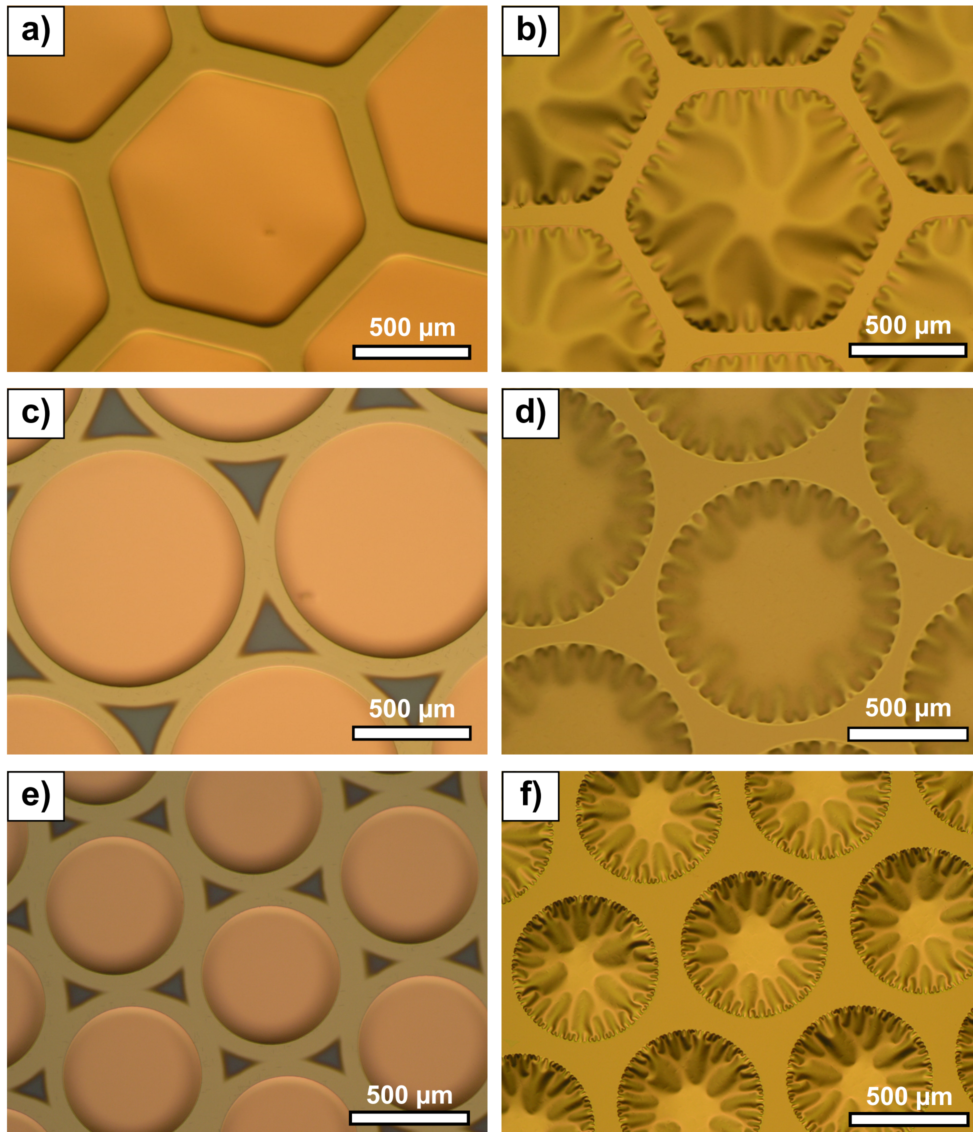

Figure 4.13: Micrographs from the back of the pre-structured silicon substrates, employed for the fabrication of GC low energy x-ray transmission windows, with a hexagonal and circular cell design are shown in the images a), c) and e). The silicon support structure is visible and the radiation passage region is still covered by a thin silicon layer. The corresponding GC low energy x-ray transmission windows, as obtained after the deposition of the GC material and subsequent wet etching are demonstrated in the micrographs b), d) and f), respectively. The GC material in the free standing regions forms the characteristic wrinkles due to the compressive stress of the GC material.

Photographs of the GC low energy x-ray transmission windows with a circular and hexagonal cell design are shown in figure 4.14. The support structure and the open window regions are clearly visible and the reduced span width of 600 µm of the corresponding window designs allows the GC material to be significantly reduced. The shown windows exhibit a GC thickness of 140 nm.

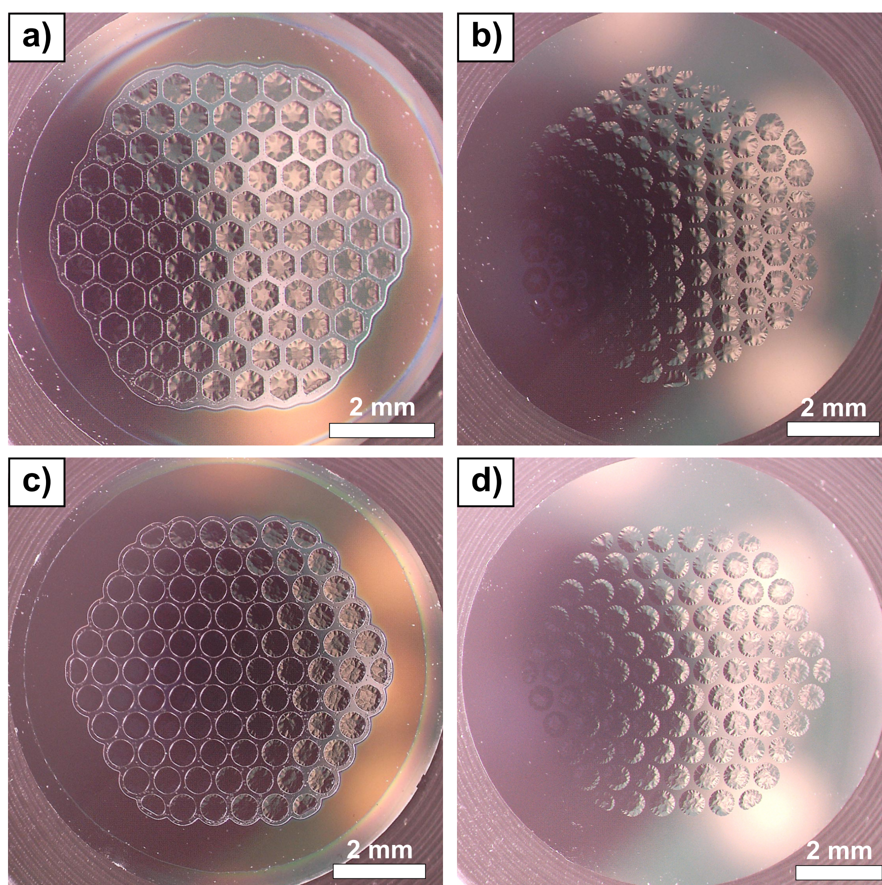

Figure 4.14: Photographs of the back side of GC low energy x-ray transmission windows with a hexagonal and circular cell design are given in a) and c) and the photographs depicted in b) and d) show the corresponding GC low energy x-ray transmission windows from the front.

4.3 Thickness Limitations of the Fabrication Scheme

The presented fabrication scheme was found to be highly reliable and more than 600 windows with varying GC thicknesses, window geometries and substrates were

fabricated and evaluated.

GC x-ray transmission windows with a GC thickness above a certain, deposition process dependent, threshold were found to exhibit tears in the free standing GC material after the wet etching process. The tears were predominantly found near the window edge, close to the silicon frame and a micrograph of a typical tear is shown in figure 4.15 a). The tears were found to be either closely following the window edge or, if located further to the window center, to follow the crystallographic orientation of the silicon substrate.

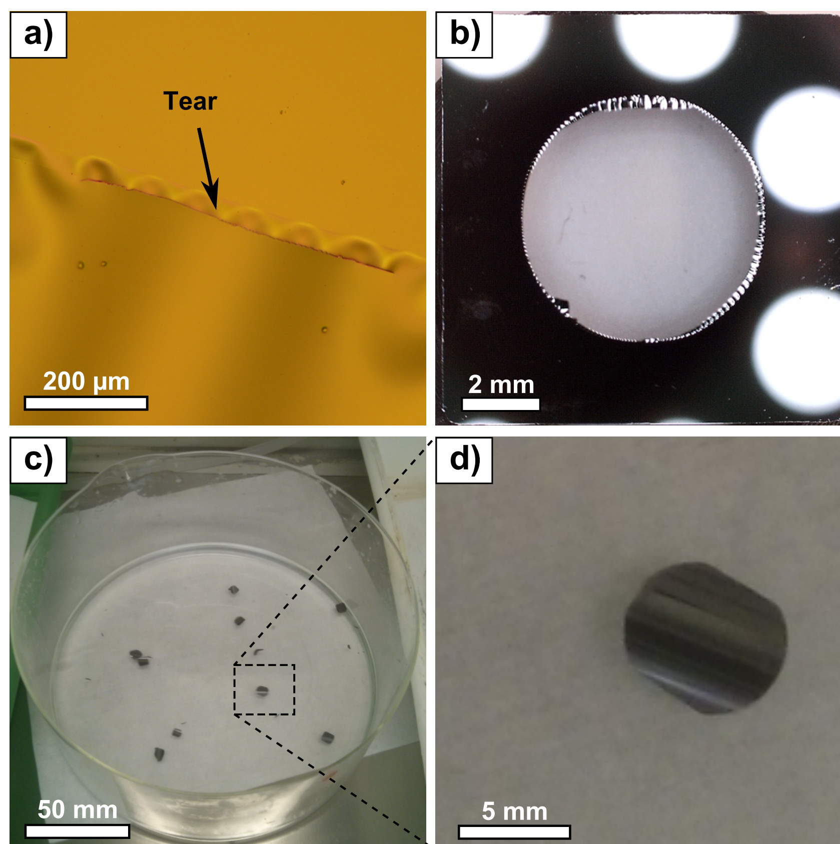

Figure 4.15: A micrograph of a typical tear in the free standing GC material is shown in a), and the tear indicated by the arrow. A photograph from the front of a GC x-ray window after wet etching is given in b) and the free standing GC material was completely removed due to a continuous tear along the window edge. The GC material was subsequently found floating on the surface of the etchant solution, as depicted in the photograph shown in c). The floating GC material exhibited a shape closely resembling the window geometry and was otherwise found to be intact, as demonstrated by the magnified image shown in d).

The thickness threshold was found to be dependent on the GC deposition process and identified at approximately 4 µm for the developed single window deposition process and at approximately 1 µm for the wafer scale deposition process. An increase of the GC thickness above the thickness threshold resulted in the formation of tears in the free standing GC material during wet etching. The tears were found to be localized or even continuous, depending on the GC thickness. Continuous tears in the free standing GC material resulted in a complete removal of the free standing GC material during the silicon substrate etching, as demonstrated in figure 4.15 b). The removed GC material was found floating in the etchant solution at the end of the wet etching process, as indicated in figure 4.15 c). The floating GC material was otherwise intact and exhibited no additional tears and closely resembled the circular shape of the window as demonstrated in figure 4.15 d).

The fact that the tears of the GC material only occurred in films above a certain thickness implies a mechanism that is related to the compressive stress of the material. It is a commonly observed phenomenon that a deposited material with a large compressive stress results in delamination or cracking, if films above a certain thickness are deposited [213]. In contrary to the observed cracking of thick diamond films as reported by Jeong et al. [214], the deposited GC films were found to be crack free prior to the wet etching. In addition, the fact that the tears were predominately formed at the vicinity of the window frame indicates a mechanism that arises from the etching process itself.

4.3.1 The Implications of Compressive Stress During the Substrate Removal

The considerations indicate that the tear formation is related to the compressive stress of the GC material and the implications of the compressive stress during the substrate removal were therefore evaluated.

The deposition of a compressively stressed material onto a substrate results in a deformation of the material stack, which is commonly measured during wafer bow measurements in order to determine the stress of the deposited material, as discussed in Chapter 2. Let us consider the Stoney equation (eq.4.2) used to relate the surface deformation to the stress of a deposited material [161], with R denoting the radius of the sample curvature, Y_s denoting the bi-axial modulus of the substrate material, t_s the thickness of the substrate material, σ the stress and t_f the thickness of the deposited thin film material. It is apparent that the radius of curvature is not only dependent on the stress and thickness of the deposited material, but also on the substrate thickness itself. The radius of the sample curvature

R is therefore dependent on the substrate thickness in a quadratic manner and the continuous reduction of the substrate thickness during the wet etching process results in an increasing ratio of the GC to substrate thickness. This consequently leads to a reduction of the local radius of curvature, as the compressive stress and thickness of the GC material remain constant. The wet etching process in combinations with the large compressive stress of the GC material was therefore identified as a possible cause of the observed tear formation.

$$R = \frac{Y_s t_s^2}{6\sigma t_f} \tag{4.2}$$

Based on these considerations, a detailed analysis of the etching process was performed. The in Chapter 3 introduced, two dimensional laser scanning system was used to visualize the sample behavior during the wet etching process. A sample with a GC thickness of 1.2 µm and a silicon substrate thickness of 250 µm was prepared for wet etching by structuring the GC material on the back of the silicon substrate with a circular window geometry exhibiting an open diameter of approximately 6 mm. The sample was placed in a heated potassium hydroxide solution for 5 hours and a 2D surface scan was subsequently performed. The laser distance sensor was moved across the front surface in a scanning manner and the distance measured with a high vertical resolution and an x-y spacing of 200 µm. The scan size was 8 mm and therefore covered the region of interest.

The resulting 2D surface profile is shown in figure 4.16 a) and only a very slight surface deformation is visible. Wet etching was continued and surface scans acquired at a 15 minute interval. The corresponding 2D surface profiles are shown in figure 4.16 b), c) and d). The reduction of the silicon substrate thickness results in a significant deformation of the remaining material that is covering the window region with a center deflection of more than 60 µm after 5 hours and 45 minutes of wet etching.

The deformation of the sample surface after a processing time of 5 hours and 45 minutes was clearly visible, even with the eye, as shown in figure 4.17 a), depicting a front view photograph of the scanned sample. The window surface almost resembles the shape of a highly reflective bubble and the reflection of the LEDs, used for illumination, are strongly deformed. Etching was continued for an additional 30 minutes and the resulting free standing GC film exhibits the typical wrinkles, as demonstrated in figure 4.17 b). The free standing GC film exhibited the discussed tears near the window frame and the large, observed, deformation of the sample surface during the wet etching was assumed to be the cause.

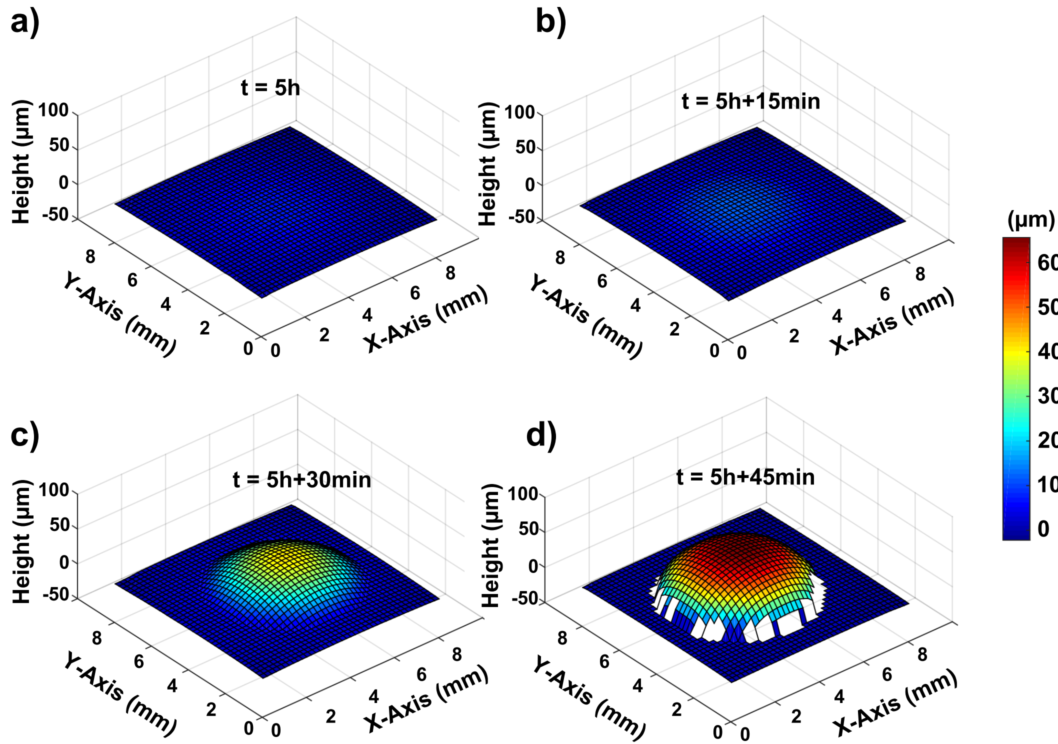

Figure 4.16: 2D surface profiles of a GC coated silicon substrate, with the back side GC material structured to ultimately form a free standing GC film with a diameter of 6 mm, were obtained during the wet etching process. The measurements were performed at the indicated etching times and an increasing deformation of the surface was observed in the center region, as shown in the diagrams a) to d). The surface height was measured by scanning across the surface with a laser distance sensor in an x-y scanning manner.

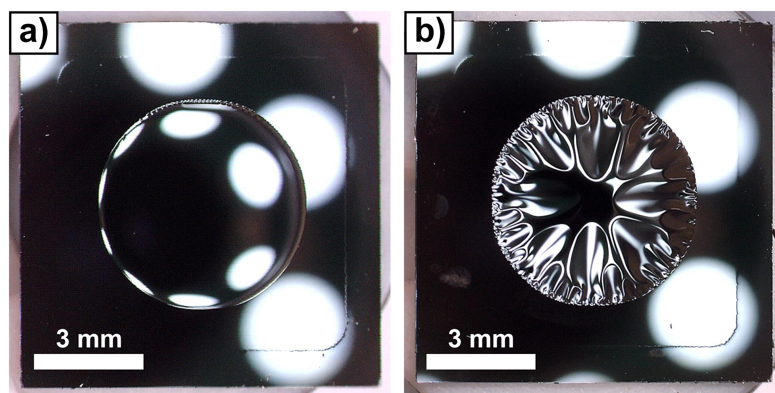

Figure 4.17: A photograph from the front of a GC coated silicon substrate after 5 hours and 45 minutes of wet etching is given in a). The remaining substrate was significantly deformed in the center region and the white spots from the LED illumination are distorted. The typical wrinkles were formed as the silicon material was completely removed by an additional 30 minutes of wet etching, as demonstrated by the photograph shown in b).

Line profiles were therefore extracted from the 2D surface scans and revealed a very sharp angle at the intersection of the open window geometry and the window frame, especially for the measurement obtained after 5 hours and 45 minutes of wet etching as depicted in figure 4.18 a).

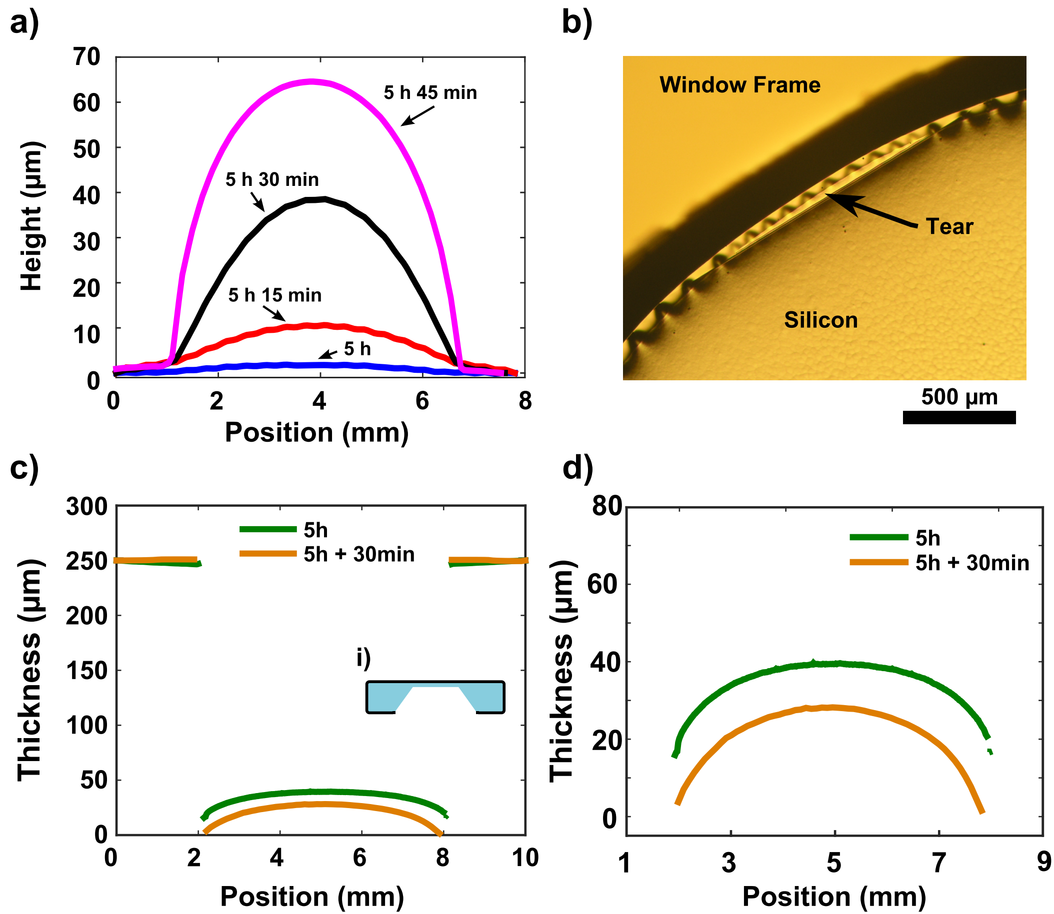

Figure 4.18: The extracted line profiles of the surface deformation across the sample, as obtained from the 2D scans, are shown in a), and demonstrate a sharp angle of deflection at the edge of the free standing window region. A micrograph of the back side of the sample after 5 hours and 45 minutes of etching is given in b) and the silicon substrate is removed first near the window edge and a tear is visible as indicated by the arrow. The thickness profiles of the sample after 5 hours and after 5 hours and 30 minutes of wet etching are shown in c) and in greater detail in d), and demonstrates the inhomogeneous etching of the silicon substrate material.

Further analysis of the etching process revealed that the silicon material was not etched in a uniform manner, but an increased etch rate was observed near the

window frame. The micrograph shown in figure 4.18 b) was taken from the back of a sample that was etched until the first free GC material appeared. The window frame is visible in the top left corner and the bottom right corner of the image shows the window region that is still covered by silicon. The free standing GC material appeared first at the window edge and a tear is visible as indicated by the arrow. The region exhibiting the sharp angle due to the surface deformation was thus the region where the silicon substrate was first completely removed. The free standing GC material in this region was subsequently exposed to a large stress as the remaining surface material was bulging upwards. The tears were therefore assumed to have appeared at the moment that the silicon substrate was removed in the region near the window frame.

The inhomogeneous etching of the silicon substrate was verified by thickness measurements using the double sensor setup described in Chapter 2. The sample thickness after 5 hours of etching and after 5 hours and 30 minutes of etching in hot potassium hydroxide is demonstrated in figure 4.18 c). The thickness profile was obtained by scanning across the window and inset i) schematically shows the scanned window geometry. The substrate thickness of 250 µm was verified by the measurement as can be seen at the X-positions between 0 mm and 2 mm and 8 mm and 10 mm, corresponding to the window frame. The thickness of the center region was already significantly reduced but exhibits a non uniform thickness. The laser signal was lost in the transition region due to the formation of a highly reflective (111) silicon plane with a steep slope. The center region is given in more detail in figure 4.18 d). The thickness of the sample after 5 hours and 30 minutes of etching was almost zero near the window frame and increases to almost 30 µm at the window center.

The resulting etch profile was considered undesirable as the region with the highest angle of deformation is released first. FEM simulations were therefore performed in order to obtain a better understanding of the stress and strain state of the GC material during the wet etching and especially during the last moments of the window release. The critical moment was assumed to be the removal of the silicon material near the window edge and thus a window geometry, as shown schematically in figure 4.19 a), was used as the simulated geometry. A thin film with a thickness of 1 µm represented the GC material and a Young's modulus of 130 GPa, a Poisson's ratio of 0.16 and a density of 2.2 g/cm^3 assigned as material constants, based on the results discussed in Chapter 5. The thin film was supported by a silicon frame with a thickness of 250 µm and the remaining silicon attached to the membrane modeled by a center region of silicon with a thickness of 20 µm that was attached to the thin film material. A region with a width of 100 µm that is free of the silicon material separates the center material from the window frame material, as indicated in the inset of a).

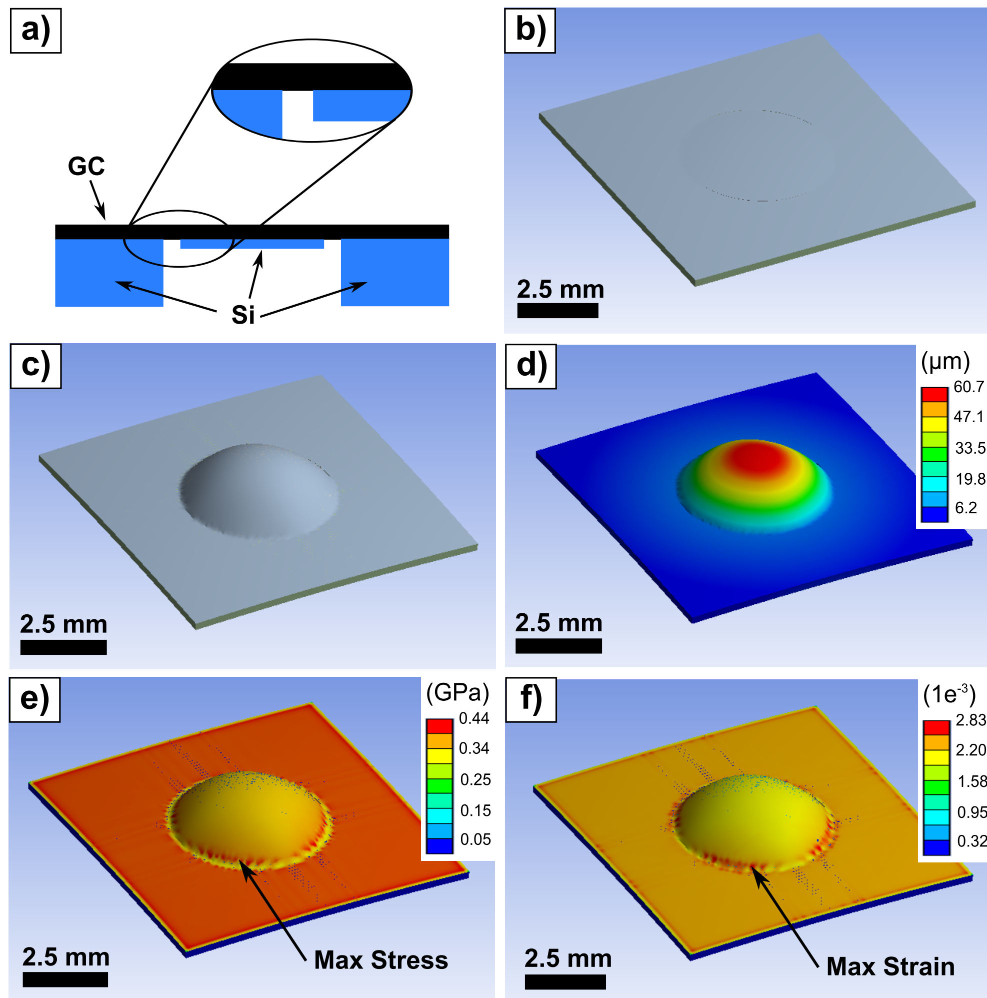

Figure 4.19: The simulated window geometry is schematically depicted in a) and resembles the GC window state during the final moments of the wet etching process. A small region of free standing GC material has already been formed near the window frame, as indicated in the inset. The resulting top view of the simulation results, if no residual compressive stress is applied to the thin film material, is given in b). A large deformation occurs if the geometry is simulated with an applied residual compressive stress of the thin film material of approximately 400 MPa, as shown in image c). The vertical deformation of the sample is given in d) and approaches 60 µm. The simulated values of the von Mises stress and strain are shown in the images e) and f) respectively and the maximum values for both are encountered in the region indicated by the arrows.

A front view of the model, before the compressive stress was induced in the thin film material by thermal loading as described in Chapter 2, is shown in figure 4.19 b). A compressive stress of approximately 400 MPa was applied to the GC material and led to a significant deformation of the material that covers the center region of the sample, as shown in figure 4.19 c), (not to scale). The perpendicular center deformation was approximately 60 µm, as demonstrated in figure 4.19 d). The substrate deformation was therefore much larger for the region above the open window geometry compared to the region that was not affected by substrate thinning, and thus closely represents the measured sample deformation. The simulation results were used to identify the stress and strain state of the deformed thin film material. A maximum of the von Mises stress with a value of 440 MPa was found exactly at the region where the silicon material had been completely removed, as depicted in figure 4.19 e) and the deformation results in a maximum strain of 0.28 %, also found at the described region of the thin film material, as shown in figure 4.19 f).

The simulation results indicated a high stress and strain level in the region that was found to predominantly exhibit the tear defects. The wet etching, in combination with the compressive stress of the GC material was therefore assumed to be the reason of the observed tears in the GC windows that exceed a certain thickness threshold.

Wafer curvature measurements were therefore performed using the measurement scheme described in Chapter 2. GC material with a thickness of between 550 nm and 1.8 µm was deposited onto silicon substrates with a thickness of 250 µm utilizing the wafer scale deposition system. The backside GC material was removed in the center forming a circular etch mask with a diameter of 7 mm. The surface bow of the 1 cm by 1 cm samples was measured by scanning across the surface and recording the distance to the sensor head and are given in figure 4.20 a). The deflection increases monotonically with the GC thickness and the profiles were fitted to a circle with the radius R and a high value of R corresponds to a low surface curvature. Wet etching was performed following the bow measurements and the windows identified that exhibited tears in the GC material. The thickness of the GC material was measured as described in Chapter 2 and the radius of curvature of the sample related to the GC thickness as shown in figure 4.20 b). The average stress of the evaluated GC samples was obtained by employing the Stoney's equation introduced in Chapter 2 and results in an average, compressive stress of 420 MPa. The samples that exhibited tearing during the window etching are marked by the color red and a thickness threshold of approximately 1.1 µm was found for the employed GC material.

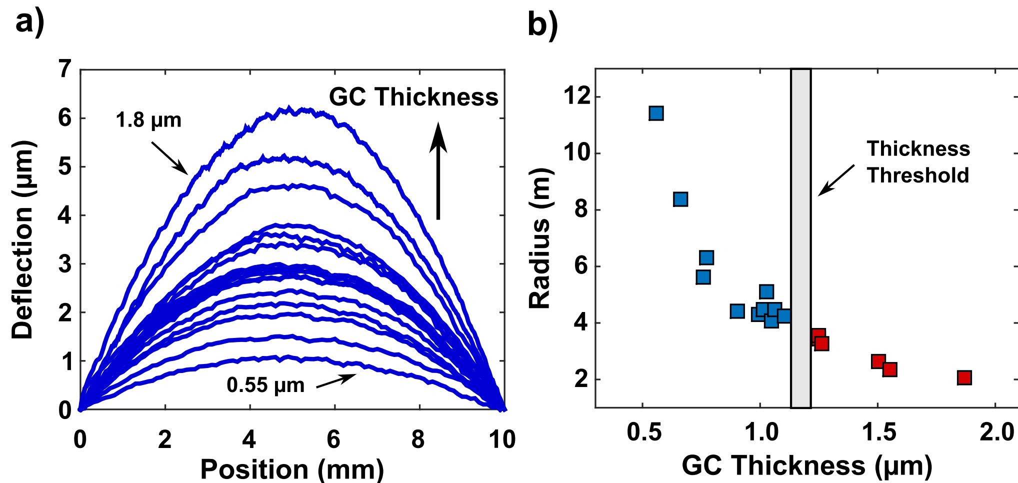

Figure 4.20: The measured sample deformation, due to the compressive residual stress of the GC material, of GC coated silicon substrates with a thickness of 250 µm are given in a). Each line profile corresponds to an individual sample with increasing GC thicknesses. The corresponding radius of the substrate curvature, as obtained by fitting a circle to the data shown in a), is related to the GC thickness as presented in b). The red colored data points correspond to samples that led to tear formation during wet etching. The thickness threshold is indicated and a GC thickness above the threshold assumed to induce tear formation.

4.3.2 Proposed Solution: Two Step Growth Process

The observed thickness limitation was seen as a direct result of the compressive stress of the deposited GC material and the wet etching process. A two step growth process was therefore proposed and evaluated.

A GC x-ray transmission window with a thickness significantly below the thickness threshold that leads to tear formation was fabricated as described in section 4.2. In a second step, additional GC material was deposited onto the GC window surface until the desired total GC thickness was obtained. A front view photograph of the GC x-ray transmission window with an initial GC thickness of approximately 500 nm is given in figure 4.21 a).

The sample exhibited the typical wrinkle formation. Additional GC material was subsequently deposited onto the window until a thickness of approximately 8 µm was obtained. The thickness increase of the free standing GC film resulted in a reduced number of wrinkles that exhibited a wider structure, as can be seen in the photographs that were taken at intervals during the additional growth processes.

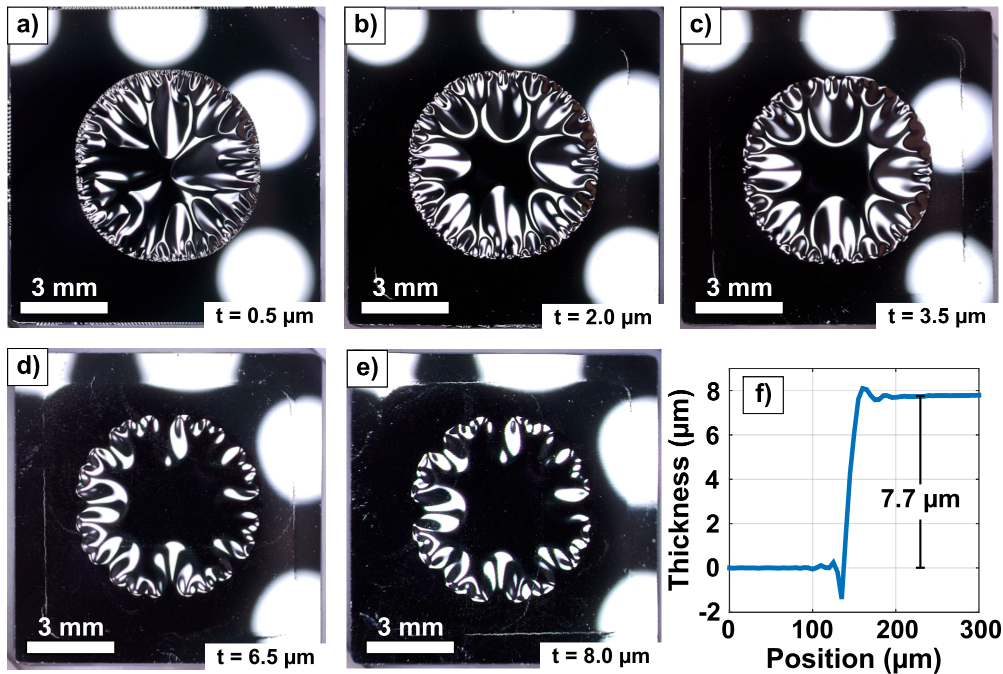

Figure 4.21: A front side photograph of a GC window with a thickness of 500 nm is depicted in a) and was subsequently employed as a substrate for the deposition of additional GC material. The photograph shown in b) depicts the GC window after one, in c) after two, in d) after four and in e) after five additional GC deposition processes. Each process is assumed to add 1.5 µm of GC material. The measured step height of the GC material deposited during the additional deposition processes onto a silicon reference sample is demonstrated in the diagram shown in f).

The photographs shown in figure 4.21 were taken after one additional deposition process, shown in b), after two, shown in c), after four, shown in d), and after 5, shown in e), additional deposition processes. Each process was assumed to deposit approximately 1.5 µm of GC material. The GC thickness was measured on a silicon sample that was placed in the reactor as a reference during the additional deposition processes. The step height measurement, obtained as discussed in Chapter 2, of the reference sample with a step height of 7.7 µm is given in figure 4.21 f).

The final window thickness was therefore assumed to be 8.2 µm. The GC thickness was seen as an estimated value, as the reference thickness was measured on a silicon sample and it is unclear how the deposition on a free standing GC film influences the GC deposition rate. None the less, the observed changes in the wrinkle formation and the mechanical behavior indicated that a substantial amount of additional material was deposited onto the GC window.

The thus fabricated GC x-ray transmission window did not exhibit tears or other defects and the proposed two step deposition process was therefore seen as a viable route to fabricate GC windows with much larger GC thicknesses compared to the discussed thickness thresholds.

Final Windows

The developed and presented processing scheme allows the fabrication of GC x-ray transmission windows with a circular window geometry and GC low energy x-ray transmission windows with a bar support structure as well as with an arbitrary window design using pre-structured silicon substrates. The use of round silicon substrates with a diameter of 9.75 mm allows a direct replacement of currently used x-ray transmission windows and the standard detector housing does not have to be adjusted.

The GC x-ray transmission windows were decontaminated after wet etching, as potassium hydroxide is not CMOS compatible, in order to rule out contamination of the used equipment. A hot bath in a solution comprising of (H_2O:HCl:H_2O_2) with a mixing ratio of (5:1:1) for 20 minutes, followed by rinsing with de-ionized water was therefore performed.

The GC x-ray transmission windows with a round silicon substrate, as shown in figure 4.22 a), can subsequently be glued into a TO8 detector housing for testing. A photograph from the bottom of a TO8 housing incorporating a GC x-ray transmission window is shown in figure 4.22 b). The detector housing subsequently offers a highly x-ray transparent opening for the incoming x-ray radiation. A photograph of the final housing configuration employing a GC window with an open window diameter of 7 mm is shown in figure 4.22 c) and employing a GC low energy x-ray transmission window with a hexagonal cell design is shown in 4.22 d) and are subsequently available for evaluation.

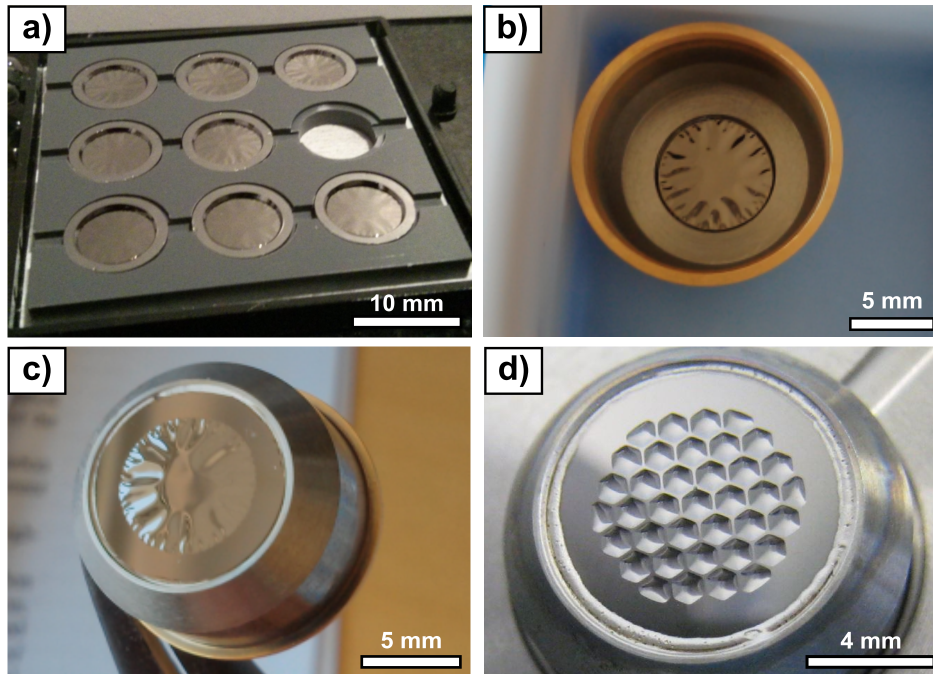

Figure 4.22: A photograph of GC x-ray transmission windows that are ready for evaluation is depicted in a), and the GC windows can subsequently be glued into a TO8 housing as demonstrated in b). The photograph was taken from the bottom of a TO8 housing, with a GC x-ray transmission window glued into the corresponding window position. A front view photograph of a TO8 housing with an incorporated GC x-ray transmission window with an open diameter of 7 mm is shown in c) and a TO8 housing incorporating a GC low energy x-ray transmission window with a hexagonal cell design is presented in d).

5 Evaluation of Graphenic Carbon as a Window Material

The deposited GC material was evaluated by fabricating GC x-ray transmission windows and probing the window properties. In addition, bulge testing and Raman spectroscopy were employed to extract the material properties of the deposited GC material. The results are presented in this chapter and complemented by finite element simulations for an in-depth understanding of the mechanical behavior of the GC x-ray transmission windows.

5.1 Performance of Graphenic Carbon X-ray Transmission Windows

GC x-ray transmission windows, fabricated as described in Chapter 4, were evaluated in regard to the window requirements discussed in Chapter 2. This includes the energy dependent x-ray transmission, helium leak tightness, mechanical stability, light tightness, resistance against ozone and hard x-ray exposure and the electrical conductivity of the GC x-ray windows.

5.1.1 X-ray Transmission

The x-ray transmission of the GC x-ray transmission windows was measured as described in Chapter 2. The energy dependent x-ray transmission of GC windows with a thickness of 2 µm and 1 µm, respectively, are shown in figure 5.1 for the energies between 0.1 keV and 6 keV. The measured x-ray transmission of a DuraCoat beryllium window is given as a reference and corresponds to a beryllium thickness of 10.76 µm, excluding the passivation layer, which is within the specified thickness tolerance of 8 µm thick commercial Be windows, as discussed in Chapter 2.

The x-ray transmission of both GC windows is higher than the x-ray transmission of the Be window and an especially high transmission for the carbon $K\alpha$ radiation is observed. The difference in transmission becomes indistinguishable for energies approaching 6 keV and above.

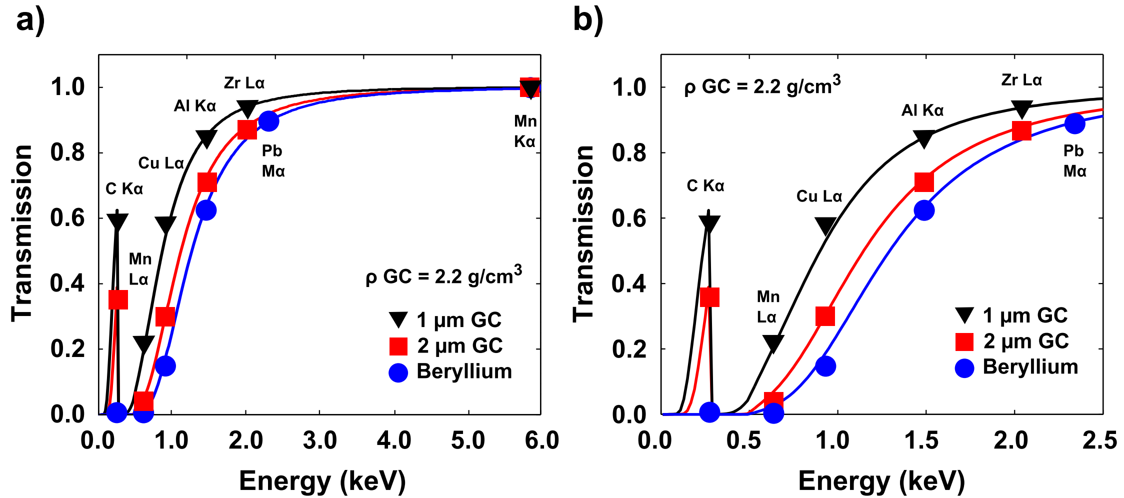

Figure 5.1: The measured x-ray transmission of GC x-ray transmission windows with a GC thickness of 2 µm and 1 µm and of a DuraCoat Be window for the energy range of 0.1 keV to 6 keV are given in a). The GC x-ray transmission windows offer a superior transmission for energies below 2.5 keV as demonstrated in b). The discrete data points correspond the the measured transition lines and the continuous data were generated with the web applet supplied by the CXRO [38] for a GC density of 2.2 g/cm^3.

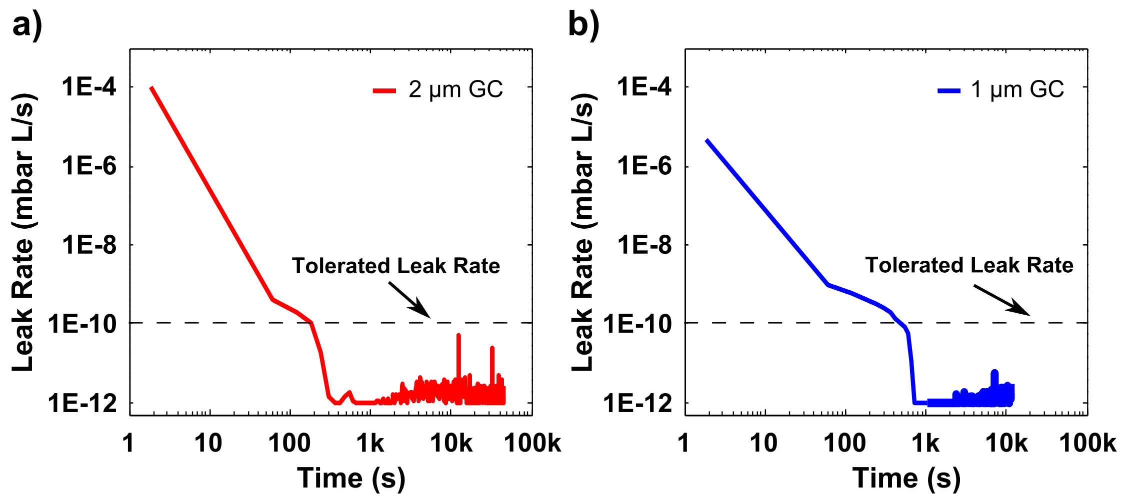

Figure 5.2: The measured helium leak rate of a 2 µm, as shown in a), and of a 1 µm, as shown in b), thick GC x-ray transmission window with an open diameter of approximately 7 mm remained below the tolerated leak rate of 1×10^{-10} mbar l/s, as indicated by the dashed line. The leak test was performed for a sufficiently long time to exclude the measurement of desorbing helium from the inside of the test chamber, which manifests as an increased leak rate at the beginning of the measurements.

The continuous data were obtained by simulating the transmission for the element carbon with the corresponding thickness and fitting the material density to the discrete date points, utilizing the web applet supplied by the CXRO [38]. A density of $2.2\,g/cm^3$ was found to offer the best fit for the GC material, which is close to the theoretical value of single crystal graphite ($2.25\,g/cm^3$) [215].

5.1.2 Helium Leak Tightness

GC x-ray transmission windows with an open window diameter of approximately 7 mm and a GC thickness of 2 µm and 1 µm, respectively, were glued into the cap of a TO8 housing and subsequently tested for helium leak tightness as described in Chapter 2. Both GC x-ray transmission windows exhibited a helium leak rate below the required limit of 1×10^{-10} mbar l/s as shown in figure 5.2 and were therefore considered helium leak tight.

5.1.3 Mechanical Stability

The mechanical stability of the GC x-ray transmission windows was evaluated by measuring the burst pressure of the GC x-ray transmission window by applying an increasing differential pressure across the window until failure, as described in Chapter 2. The resilience against dynamic pressure variations was tested by cyclic pressure loading of the GC windows.

5.1.3.1 Burst Pressure

The burst pressure values of GC x-ray transmission windows with a varying GC thickness were determined in order to identify the required GC thickness necessary to comply to the mechanical stability requirements discussed in Chapter 1. A GC x-ray transmission window during burst pressure testing, with a GC thickness of 1.7 µm and a window diameter of 6.9 mm, is shown in figure 5.3 a). The photographs were taken from the back of the window at increasing differential pressure values. The free standing GC material was consequently deflected upwards and the wrinkles were gradually smoothed out, as the differential pressure was increased. The large deflection and bulging of the window center becomes visible as the reflections of the LED light sources are deflected in a radial manner, which are visible as bright spots on the window material. The differential pressure was increased until window failure occurred at a differential pressure of 1400 mbar. The GC material was completely removed after the window failure and little free standing GC material remained visible.

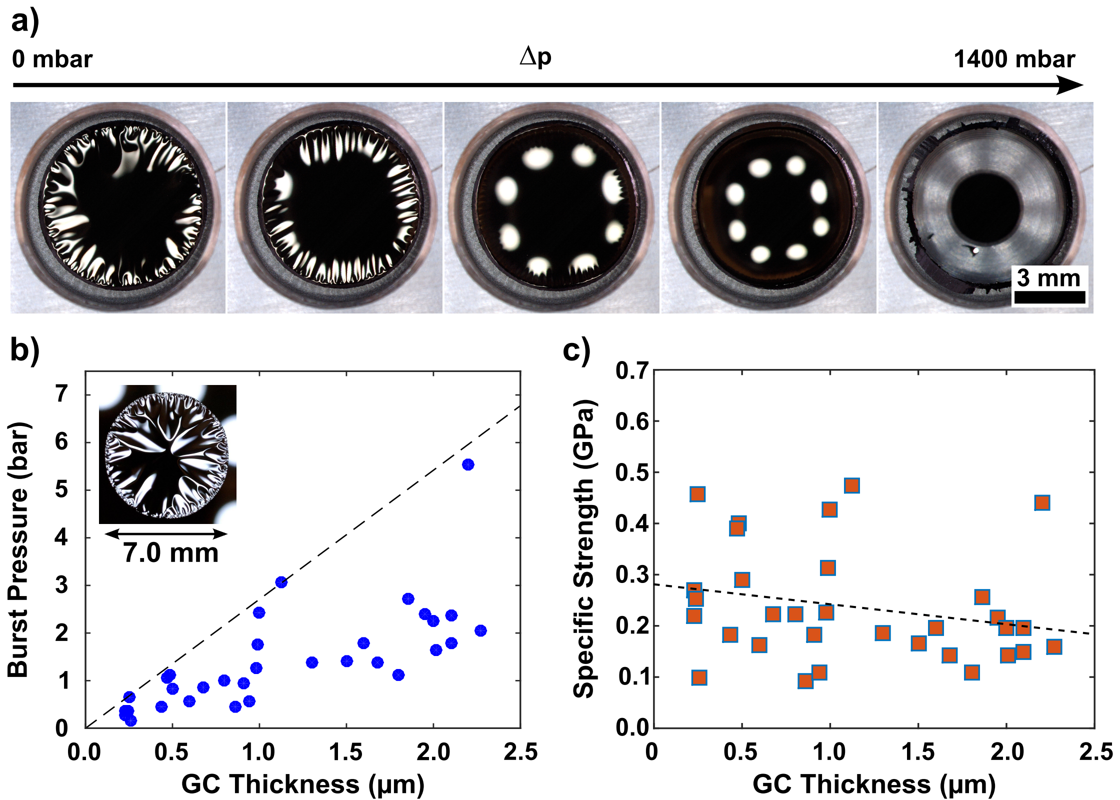

Figure 5.3: Burst pressure testing of the GC x-ray transmission windows results in a large deflection and bulging of the GC window material as demonstrated in a), depicting bottom view photographs of a burst pressure tested GC window with a GC thickness of 1.7 µm and an open window diameter of 6.9 mm. The differential pressure was increased from 0 mbar until window failure occurred at a differential pressure of 1400 mbar and the free standing GC material was completely removed. The measured burst pressure values of GC x-ray transmission windows with an open window diameter of 7 mm and the corresponding GC thicknesses are given in b). The dashed line serves as a guide for the eye indicating the maximum encountered values. The extracted specific strength values for the tested GC windows and the corresponding GC thickness are shown in c). A linear fit results in a negative correlation with the GC thickness, as indicated by the dashed line.

The stability of the GC x-ray transmission windows against a differential pressure load that acts across the window geometry was measured for GC thicknesses ranging from 230 nm to 2.3 µm, as shown in figure 5.3 b). The obtained burst pressure values were normalized to an open window diameter of 7 mm to account for fabrication variations and generally show an increasing pressure stability for an increasing GC thickness. A large variation in the burst pressure values was observed, even for windows with a nearly identical GC thickness and assumed to arise from defects in the GC material. The discussed window geometry exhibits a critical area of 38.5 mm^2, which is large for the class 1000 clean room environment used for the window fabrication. Hence for most of the tested windows, the limiting factor was assumed to not be the intrinsic strength of the GC material but window failure assumed to occur at defects of the GC material and thus at the weakest point of the open window region. The dashed line, in figure 5.3 b), was therefore seen as a lower limit for the intrinsic stability of GC x-ray transmission windows. A GC window thickness of 1 µm was subsequently seen sufficient to withstand the targeted differential pressure load of 2 bar for an open window diameter of 7 mm.

The calculated, specific strength of GC x-ray transmission windows, as introduced in Chapter 2, is seen as a figure of merit for the mechanical stability of the windows, as it is independent of the window diameter and GC thickness. The specific strength of the tested GC windows is shown in figure 5.3 c) and a standard deviation of 0.11 GPa identified and attributed to the discussed defects in the GC material. A negative correlation with an increasing GC thickness is apparent as indicated by the dashed line of best fit. The negative correlation is assumed to arise from the compressive stress of the GC material, which ultimately leads to the formation of tears and window failure during the window fabrication, as discussed in Chapter 4. It is assumed that although no tears or cracks were visible, the increased GC thickness resulted in a growing number of minor defects that reduce the overall stability of the GC x-ray transmission windows.

5.1.3.2 Cycle Stability

Cyclic testing of the GC x-ray transmission windows was performed by applying a differential pressure of at least 1200 mbar across the GC window in a cyclic manner, as discussed in Chapter 2. A GC window that was glued into a TO8 housing with no differential pressure acting on the thin window is shown in sub-figure (i) of figure 5.4 a). The wrinkles of the GC material are clearly visible. The application of a vacuum to the inside of the detector housing results in a differential pressure across the GC window. The GC thin film is significantly deflected downwards and the wrinkles are smoothed out as the differential pressure weighs down on the free standing GC material, as shown in sub-figure (ii). The cyclic loading therefore

leads to a large stress on the window material near the window frame due to the pressure induced deflection of the GC material.

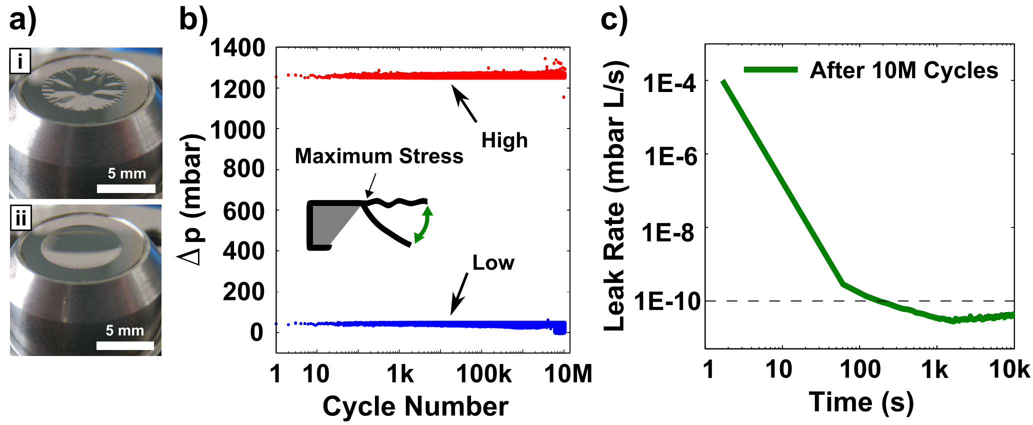

Figure 5.4: Dynamic pressure changes across the GC x-ray transmission window result in a large deflection and deformation of the window material as indicated in the photographs of a TO housing incorporating a GC window without (i) and with an applied vacuum (ii) to the inside of the detector housing. The maximum and minimum differential pressure of each pressure cycle during cycle testing of a GC window with a diameter of 6.9 *mm* and a thickness of 1 µm are given in the diagram shown in b). The cycle tested GC window remained helium leak tight after ten million pressure cycles as demonstrated in c).

Cyclic testing was performed with a frequency of 3 Hz and ten million pressure cycles did not lead to window failure as shown in figure 5.4 b), for a GC x-ray transmission window with an open window diameter of 6.9 mm and a GC thickness of 1 µm. The maximum and minimum differential pressure values across the GC window were recorded for each pressure cycle. The tested GC material showed a high resilience against material fatigue as no visual alteration was observed and the window remained intact. A subsequent helium leak test was performed with the cycle tested window in order to rule out micro crack formation and a helium leak rate below the required 1×10^{-10} mbar l/s was measured, verifying the window integrity as shown in figure 5.4 c).

5.1.4 Light Tightness

The light tightness of the GC material was tested as described in Chapter 2. The count rates of the low light detector for front side illumination of the detector housings incorporating a 1 µm and 2 µm thick GC x-ray transmission window and a 8 µm thick Be window, respectively, are shown in figure 5.5 a).

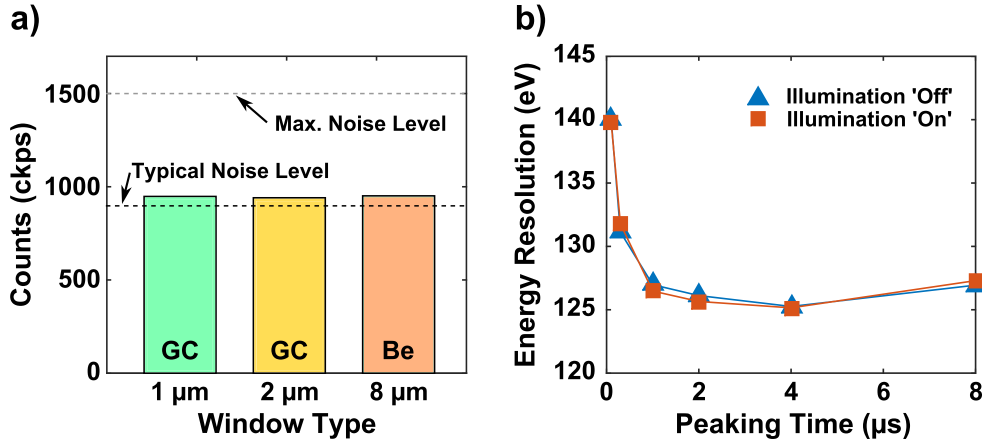

Figure 5.5: The measured output counts of a low light detector placed behind the different window types under front illumination are shown in a). The typical and maximum specified dark count rates of the low light detector are indicated by the dashed lines. The energy resolution of a SDD detector module incorporating a 1 µm thick GC x-ray transmission window was determined for peaking times between 0.1 ms and 8 ms for $Mn\ K\alpha$ radiation. Illuminating the detector during the measurements did not lead to a deterioration of the measured energy resolution, as demonstrated in b).

The measured count rates were close to the typical dark count rates of the low light detector, specified with 900 kcps, and significantly below the maximum dark count rates as specified with 1500 kcps. No significant change in the output count rate of the low light detector was observed for the three window types during illuminated, compared to non-illuminated measurements. No difference in the light blocking ability between the Be window and the GC windows was therefore identified with the described measurement scheme.

In order to verify the light tightness of 1 µm thick GC x-ray transmission windows and to rule out an insufficient sensitivity of the low light detector, the influence of illumination on the energy resolution of a SDD detector module incorporating a 1 µm thick GC x-ray transmission window was evaluated. The measured energy resolution for the $Mn\ K\alpha$ (5.895 keV) radiation of the tested detector module, is shown in figure 5.5 b). While the different peaking times have an influence on the detector resolution, no deterioration is induced by changing the illumination source from the 'off' to the 'on' state. The temperature of the detector was kept at −55 °C during the measurements and the light tightness of the 1 µm thick GC x-ray transmission window was consequently verified.

The energy resolution shows the typical dependency on the chosen peaking time of the detector. The highest resolution was obtained at a moderate peaking time.

The peaking time is equivalent to the time available to integrate the generated charge at the output node. A reduced peaking time limits the averaging of the generated thermal noise and can even lead to incomplete charge collection, deteriorating the energy resolution, whereas long peaking times lead to a larger contribution of the current noise, introduced from the amplifier electronics. For a more detailed discussion of the individual noise components, responsible for the resolution dependency on the peaking time of the detector module, it is referred to reference [1].

5.1.5 Resistance Against X-ray Exposure and Ozone

The resilience of GC x-ray transmission windows against x-ray and ozone exposure was evaluated for GC windows with a GC thickness of 1 µm and an open window diameter of 7 mm as described in Chapter 2.

The GC windows were exposed to a total ionizing dose of 6×10^{12} photons with an energy of 30 keV, which corresponds to a six-fold of the guaranteed irradiation stability of the SDD detector. No visible deterioration of the GC material or increased helium leak rates were observed after exposure, compared to a helium test performed prior to the experiment. The measured helium leak rate stayed below 1×10^{-10} mbar l/s, as shown in figure 5.6 a).

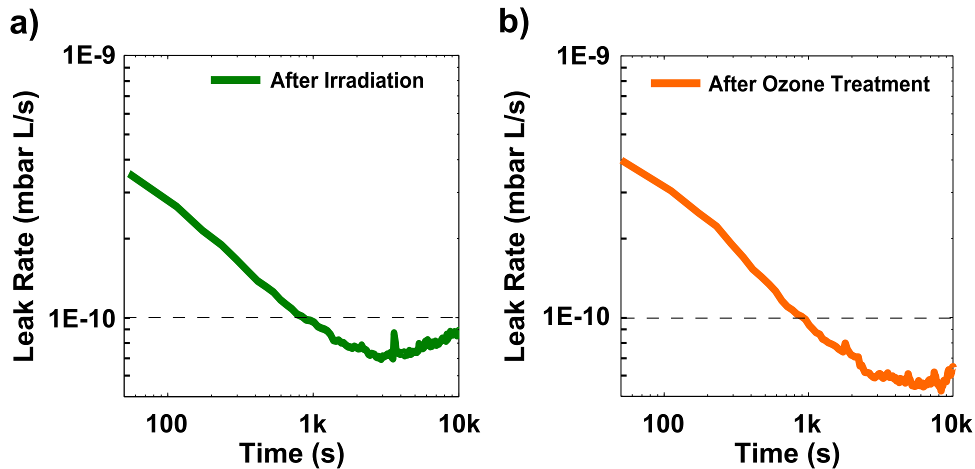

Figure 5.6: The measured helium leak rate of a 1 µm thick GC x-ray transmission window after irradiation with a total ionizing dose of 6×10^{12} photons with an energy of 30 keV is shown in a) and after ozone exposure testing in b). The helium leak rate remained below the required 1×10^{-10} mbar l/s.

In a second experiment, GC windows were placed in front of an ozone containing gas flow for a total of three days for ozone exposure testing. A subsequent

helium leak test did not show an increased helium diffusion compared to a test performed before the ozone exposure and the measured helium leak rate was below 1×10^{-10} mbar l/s, as shown in figure 5.6 b).

5.1.6 Electrical Conductivity

The electrical conductivity of the GC window material was measured as described in Chapter 4. GC material with a thickness of 1 µm was deposited onto a silicon substrate and a sheet resistance of 10.77 Ω/□ determined. The corresponding bulk resistivity of the GC material was subsequently identified to be 1.1 mΩ cm.

5.2 Mechanical Characterization of the Graphenic Carbon Material

The mechanical properties of the GC x-ray window material were characterized by bulge testing and Raman spectroscopy. In addition, FEM simulations were performed in order to obtain an in-depth understanding of the mechanical behavior of the GC x-ray transmission windows and to verify the implications that arise from the compressive residual stress of the GC material.

5.2.1 Bulge Testing

Bulge testing is a common method to extract the Young's modulus and residual stress of thin film materials. The implications that arise from the compressive stress of the GC material and the employed measurement setup were introduced and discussed in detail in Chapter 2.

Free standing GC films were fabricated as discussed in Chapter 4 and the differential pressure induced film deflection was measured using a WLI displacement sensor. Samples with varying GC thickness and circular as well as rectangular window geometries were employed for bulge testing as shown in figure 5.7 a). The pressure induced thin film deflection was measured by performing line scans across the window geometry at the positions indicated by the arrows.

The typical deflection profiles, as obtained by bulge testing a circular, free standing GC film with a diameter of 6.9 mm and a GC thickness of 950 nm, are shown in figure 5.7 b).

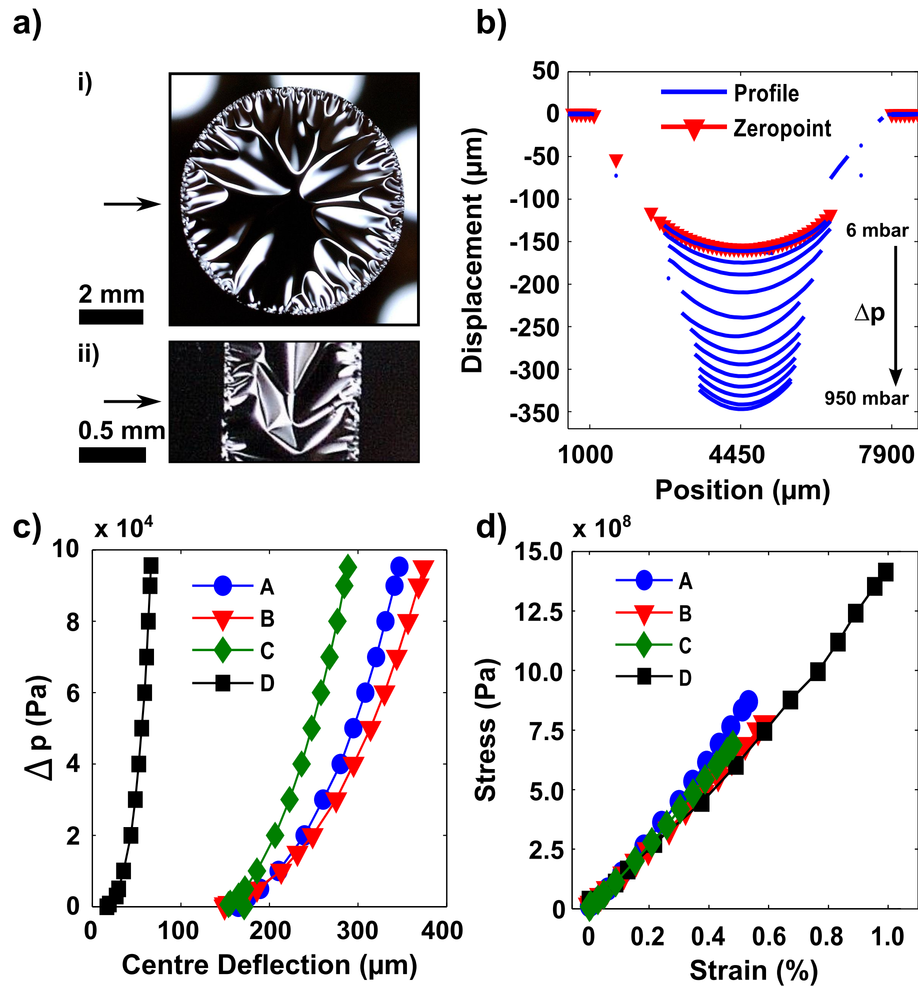

Figure 5.7: The probed window geometries for bulge testing are shown in the photographs in a). Line scans were performed along the direction indicated by the arrows. The measured deflection profiles of a GC window with an open diameter of 6.9 mm and a GC thickness of 950 nm, under an increasing differential pressure are demonstrated in b). A low differential pressure of 6 mbar was applied to smooth the wrinkles of the GC material and was subsequently considered the reference height. The measured pressure dependent center deflection of four different windows are shown in c). Samples A, B and C exhibited a circular and sample D a rectangular window geometry. The corresponding strain-stress values of the window material was calculated as discussed in Chapter 2 for the probed windows and are given in d).

Each line profile corresponds to a pre-set differential pressure that was increased in a non monotonically manner until the maximum differential pressure of 950 mbar was reached. A low differential pressure of 6 mbar was applied as a pre-stressing step in order to reduce the impact of the present wrinkles. The corresponding deflection was subsequently interpreted as the starting point for the deflection measurements. This was necessary due to the compressive stress of the GC material as discussed in Chapter 2.

The line scans were subsequently used to extract the center deflection of the free standing GC films for a given differential pressure. The pressure dependent center deflection of four samples are shown in figure 5.7 c). Sample A, B and C correspond to a circular geometry with a diameter of 6.9 mm, 7.3 mm and 5.4 mm and a GC thickness of 950 nm, 1100 nm and 1000 nm, respectively. Sample D exhibited a rectangular design with an aspect ratio greater than four, a rectangle width of 1.04 mm and a GC thickness of 140 nm. The impact of the open diameter of the thin film geometry is clearly visible and an increased diameter leads to a larger center deflection.

The pressure deflection curves were subsequently used to calculate the strain and stress state of the free standing GC films for each of the samples, based on the equations introduced in Chapter 2. The extracted strain-stress curves of the four samples are given in figure 5.7 d). A linear fit of the data was employed to extract the bi-axial modulus, respectively the uni-axial modulus for the rectangular sample, of the GC material. The Young's modulus of the samples was subsequently calculated as described in Chapter 2 and the results are given in table 5.1.

Table 5.1: Summary of the discussed, bulge tested samples and the obtained values for the Young's Modulus of the GC material. The maximum calculated stress, as obtained at the maximum differential pressure, is also indicated but does not represent the ultimate tensile strength as the windows were still intact.

Sample	**Diameter**	**GC Thickness**	**Young's Modulus**	**Max Stress**
A	6.9 mm	950 nm	142 GPa	870 MPa
B	7.3 mm	1100 nm	115 GPa	780 MPa
C	5.4 mm	1000 nm	124 GPa	690 MPa
D	1.04 mm	140 nm	136 GPa	1.4 GPa

The maximum stress value calculated for sample D was found to be 1.4 GPa and was substantially larger than for the other samples, as shown in figure 5.7 d) and table 5.1. This is due to the reduced GC thickness of sample D. The uni-axial

stress and strain state of the rectangular sample D therefore allows the stress value to be regarded as an indication of the high ultimate tensile strength of the GC material, which is commonly determined by tensile testing that results in a similar uni-axial stress loading.

A standard deviation of 12.09 GPa was identified for the determined values of the Young's modulus with an average value of 129.3 GPa. The origin of the large variation is unclear but assumed to result from the compressive residual stress state of the GC material. FEM simulations were therefore performed in order to obtain a better understanding of the implications that arise from the compressive stress of the GC material in regard to the bulge testing experiments.

5.2.1.1 Simulation of the Mechanical Behavior

The workspace environment provided by ANSYS 14.5 was employed to design the GC x-ray transmission window geometry comprising of a thin film material that is supported by a window frame. The material properties of silicon, which are available within the software suite, were allocated to the frame material and a Young's modulus of 130 GPa, a Poisson's ratio of 0.16 and a density of 2.2 g/cm^3 chosen for the thin film material in order to resemble the GC material. The material constants were chosen based on the previous experiments. A bottom view image of the designed window geometry with an open diameter of 1 mm and a thin film thickness of 1 µm is shown in figure 5.8 a).

The reduced window diameter was necessary in order to reduce the number of nodes during the meshing process of the simulated geometry. The high aspect ratio of the thin, free standing material and the large lateral dimensions of the window geometry is known to be problematic for FEM simulations and increases the required number of nodes dramatically. The reduction of the window diameter to 1 mm was assumed to not alter the general validity of the simulation results.

A pre-loading step was performed in order to induce a compressive residual stress within the thin film material of approximately 400 MPa, as described in Chapter 2, and wrinkles were subsequently formed in the free standing thin film material as shown in figure 5.8 b).

In the following step, a differential pressure of 1 bar was applied across the window geometry and the free standing material was deflected downwards, as shown in figure 5.8 c). The wrinkles were smoothed out but remain clearly visible near the window frame and the simulated window closely represents the visual appearance of GC x-ray transmission windows under a differential pressure load, as shown throughout this thesis.

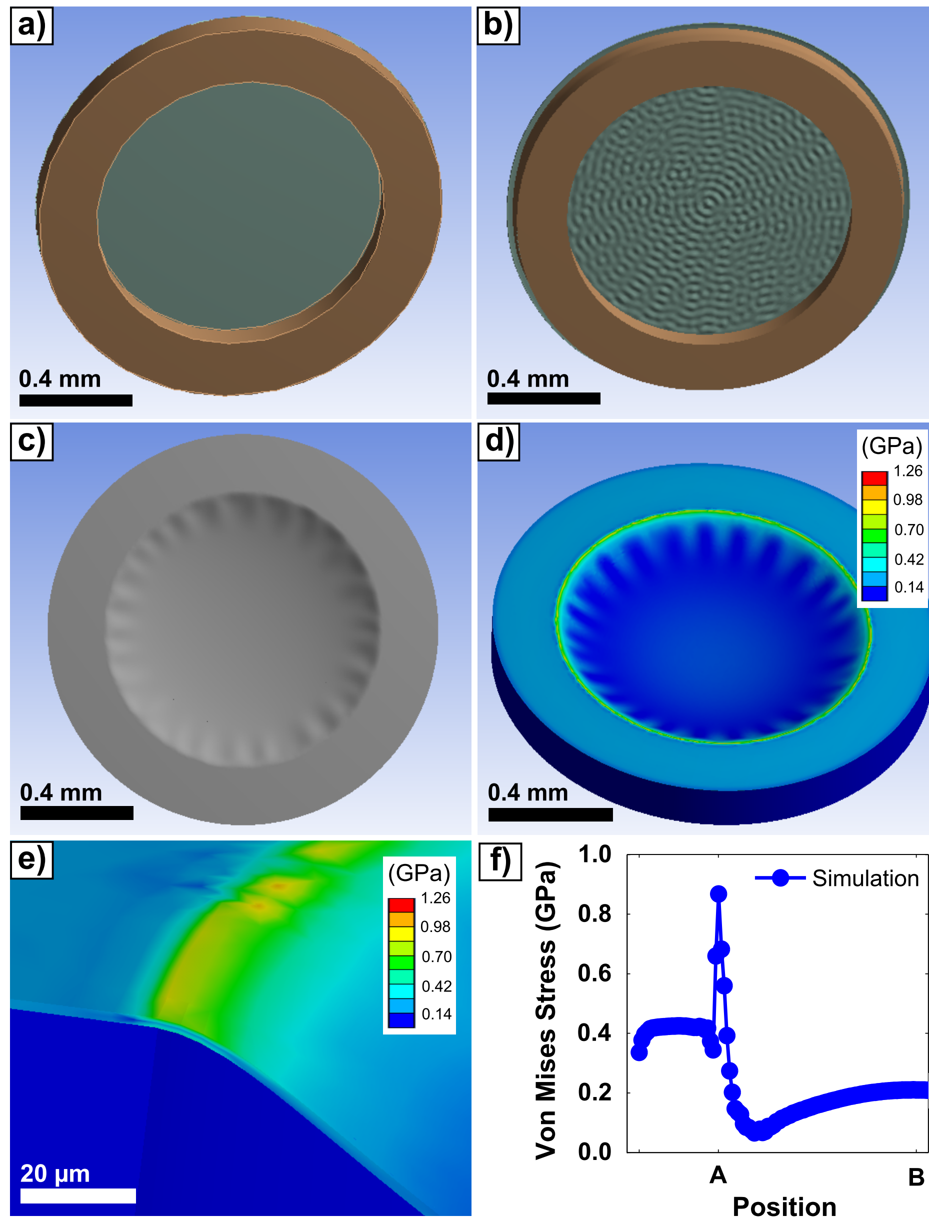

Figure 5.8: a) The back side view of the simulated GC window geometry is depicted in a). A 1 µm thick film is supported by a silicon frame. The same window geometry, after the pre-loading step, is shown in b) and the resulting compressive stress leads to wrinkle formation within the free standing material. A front view image of the simulated window under an additional pressure load of 1 bar is demonstrated in c). The free standing film is deflected downwards and the wrinkles are smoothed out in the window center but remain present near the window frame. The calculated von Mises stress distribution of the thin film material at a differential pressure of 1 bar is shown in d) and a maximum is observed near the window frame. The window frame region of the pre-stressed and pressure loaded window is shown in e) in more detail. The von Mises stress values along a path across the window geometry are shown in f), with A denoting the the material at the window frame edge and B the window center.

The simulated von-Mises stress distribution of the window and frame material is shown in figure 5.8 d). The stress distribution does not exhibit a homogeneous distribution and significantly increased stress values were identified at the edge of the free standing region. In contrary to simulations performed without a compressively stressed thin film material (not shown), a periodic stress pattern was visible that closely resembles the wrinkles near the window frame. The resulting, complex stress distribution exhibits a maximum stress value of 1.26 GPa near the window frame.

The cross section view of the window edge region is shown in figure 5.8 e) in more detail. The high stress values were confined to a small area directly above the edge of the window frame. The von-Mises stress values were extracted from a line path across the tested window geometry under a pressure load of 1 bar, as demonstrated in figure 5.8 f). An increase by a factor of approximately 4.5 was found for the material stress at the window edge, denoted as position A, compared to the window center, denoted as position B. The region near the window frame was therefore identified as a critical area, as material failure is assumed to occur predominantly in this high stress region.

While the von Mises stress values are useful to determine the intensity of the encountered stress, the simulation results also contain the direction of the stress vectors. A bi-axial tensile stress state was only observed near the window center but the transition to a uni-axial state near the window frame, as postulated by Small et al. [150] was only observed for thin films without a residual compressive stress state. Instead the simulations with the compressively stress material, as shown in figure 5.8, verified that circumferential compressive stress remains present near the window frame, even at an applied differential pressure of 1 bar. The complicated stress and strain state at the window frame was not taken into account by the equations during the bulge testing experiments and the results therefore have to be considered with care.

In order to obtain a better understanding of the results obtained by the bulge testing experiments, the simulated center deflection data was used as measurement input for equation 2.16 that was employed to calculate the stress of the GC material during bulge testing. In contrary to the simulated, maximum stress value of 1.26 GPa, encountered near the window frame, the calculated stress is determined to be only 248 MPa. This corresponds to a reduced stress value by almost a factor of five. On the other hand, the calculated stress corresponds closely to the stress values found in the center of the window as shown in figure 5.8 f).

The stress values determined during the bulge test experiments are therefore interpreted as a lower limit, as the simulations have shown that the stress value of the material is significantly enhanced in the region close to the window frame. It is assumed that the encountered maximum stress value is responsible for the overall window stability and the ultimate tensile strength of the GC material is therefore substantially larger than the discussed value of 1.4 GPa.

The simulation results indicating an enhanced stress value near the window frame were supported by the observations made during the burst pressure measurements, as it was encountered that the GC material was completely removed and little free standing GC material remained after window failure. This was seen as an indication that the window failure occurred near the window frame, which would be in line with the simulated stress distribution.

5.2.2 Raman Spectroscopy: Stress Measurements

The fact that bulge testing of compressive thin film materials is seen as problematic in regard to the unknown systematic error of the measurements, as discussed in Chapter 2 and verified by the FEM simulations, Raman spectroscopy was additionally employed to probe the stress and strain state of the GC material, as it was deformed due to differential pressure loading. A detailed discussion of the underlying theory and the used measurement setup was given in Chapter 2.

A front view photograph of the probed GC window with an open diameter of 6.9 mm and a GC thickness of 950 nm is shown in figure 5.9 a). The Raman spectra were obtained along the indicated line, subsequently moving from the window frame to the center of the free standing GC material. The position of the G-peak was determined for each of the measured Raman spectra and used to evaluate the stress state of the GC material.

The G-peak positions of the Raman spectra obtained at the indicated sample positions, for the relaxed window state and for a deflected window state, are shown in figure 5.9 b). The deflection was induced by applying a differential pressure of 900 mbar across the window and a significant downward shift of the G-peak positions was observed due to the deformation of the GC material. The G-peak position for Raman spectra that were obtained from the window frame region, exhibited an upward shift to higher wave numbers which corresponds to a compressive stress state, as discussed in Chapter 2. While the G-peak positions of the Raman spectra obtained from the window frame region were not affected by an applied differential pressure, the G-peak positions of the Raman spectra obtained from the free standing GC material were downward shifted, indicating a tensile stress state.

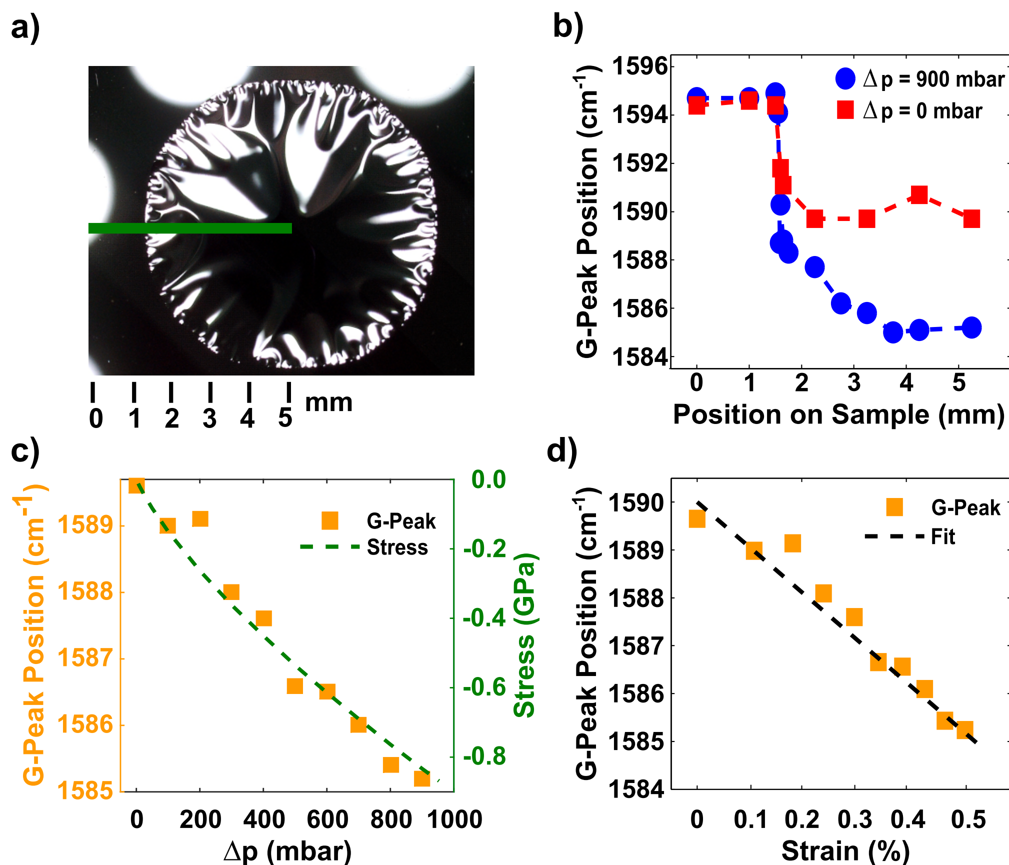

Figure 5.9: A front view photograph of a free standing, circular GC film with a thickness of 950 nm is shown in a) and Raman spectra were measured along the indicated line. The extracted G-peak positions of the Raman spectra, that were obtained at the corresponding positions of the sample shown in a), are given in the diagram b). Measurements were performed for the relaxed GC state and with an applied differential pressure of 900 mbar. The G-peak position and the calculated stress of the GC material at the center of the free standing region, for the given differential pressure, is depicted in c). The extracted strain to G-peak position relation of the probed GC material is demonstrated in d).

Interestingly, the shift of the G-peak position was highest at the center of the free standing material and decreases towards the window frame. This is in contrary to the assumptions made during the bulge testing scenario that assumed a constant stress and strain value throughout the GC material. Raman measurements performed on tilted GC samples did not show an angular dependency of the Raman spectrum and the influence of the slope of the GC material in the window frame region was therefore discarded as the source of the reduced shift of the G-peak position. Mohiuddin et al. [158] demonstrated that uni-axial stress reduces the shift of the G-peak position in comparison to a bi-axial stress state. The increasing G-peak positions near the window frame region were therefore partly attributed to the gradual shift of a bi-axial stress and strain state at the window center to an increasingly uni-axial stress and strain state at the window edge, as discussed in Chapter 2.

The FEM simulation results, shown in figure 5.8f) correspond well to the stress distribution of the central window region, but the stress enhancement in the vicinity of the window edge was not verified by the Raman measurements and was attributed to the rather large spot size of the used Raman spectrometer. The measurements indicate an abrupt change from compressively stressed to tensile stressed GC material at the window edge and it is assumed that the large stress indicated by the FEM simulations and the abrupt change in the stress state poses a significant mechanical burden on the window material near the window frame and makes the high mechanical strength of the GC x-ray transmission windows even more astonishing.

Further experiments were performed at the center of the free standing region where the FEM simulations verified a bi-axial stress state, even for materials that exhibit a compressive residual stress. Combining the Raman spectrometer measurements with deflection measurements therefore allowed the extraction of the Young's modulus of the GC material as discussed in detail in Chapter 2. The evolution of the G-peak position to lower wavenumbers, as the differential pressure was increased from zero to 950 mbar, is demonstrated in figure 5.9 c). The same sample was used to measure the corresponding center deflection of the free standing GC material and the stress of the GC material was calculated as described in Chapter 2. The stress of the GC material correlated well with the G-peak position, as shown by the second y-axis of the figure 5.9 c). By plotting the strain of the GC material, as obtained from the deflection measurements, against the G-peak position it was subsequently possible to calculate the Young's modulus of the GC material by measuring the G-peak shift for a given strain value and comparing the slope of the linear fit to that of a predominantly sp^2 containing carbon material of which the value of the Young's modulus is known, as discussed in Chapter 2.

The linear fit led to a slope of $\delta\omega_G/\delta_\epsilon = -9.4\ cm^{-1}/\%$. Metten et al. [140] determined the slope of monolayer graphene to be $\delta\omega_G/\delta_\epsilon = -57\ cm^{-1}/\%$, compared to $\delta\omega_G/\delta_\epsilon = -63\ cm^{-1}/\%$ obtained by Mohiuddin et al. [158] for monolayer graphene under bi-axial strain. None the less, both postulated a Young's modulus of graphene of approximately 1 TPa, with 1.05 TPa and 1.09 TPa, respectively. Employing these values in the aforementioned manner resulted in an approximated Young's modulus of the GC material of 173 GPa and 163 GPa respectively, which is slightly higher than the average value of 129.3 GPa obtained during bulge testing.

5.3 Performance of Graphenic Carbon Low Energy X-ray Transmission Windows

The impressive properties of GC x-ray transmission windows with a thickness of 1 µm and 2 µm led to the development of the fabrication scheme for GC low energy x-ray transmission windows described in Chapter 4. The x-ray transmission, helium leak rate, mechanical stability, optical transmission and electrical conductivity were therefore evaluated in order to identify, whether the GC thickness can be sufficiently reduced, while complying to the requirements introduced in Chapter 2. Especially the mechanical strength and helium leak and light tightness were seen as problematic as they strongly depend on the GC thickness.

The window design d), as described in Chapter 4, incorporating a hexagonal cell design with a cell width of 1 mm, was identified as the most promising layout of the pre-structured silicon substrate fabrication scheme, as the other proposed designs exhibited a significant shadowing effect due to the grid layout. Correspondingly, design e), as described in Chapter 4, incorporating a bar support structure with a cell width of 1 mm and a bar width of 200 µm, was identified as the most promising window design of the fabrication scheme employing (110) orientated silicon substrates as the structuring of the GC material to form the 100 µm thick bar structures was found to be unreliable using the shadow mask fabrication scheme.

Two low energy GC x-ray transmission windows, incorporating the aforementioned window designs were fabricated and are shown in the photographs of figure 5.10. Both windows passed vacuum testing, performed as described in Chapter 2. The GC thickness of the window with the bar support structure, shown in figure 5.10 a), was 140 nm, whereas the GC thickness of the window with the hexagonal cell design, shown in figure 5.10 b), exhibited a GC thickness of 220 nm. The presented windows were employed to evaluate the feasibility and properties of a

GC low energy x-ray transmission window.

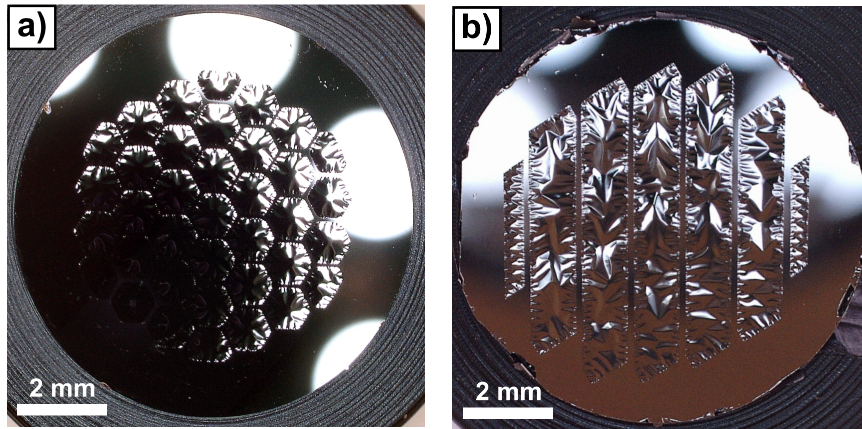

Figure 5.10: A front view photograph of a GC low energy x-ray transmission window with a hexagonal cell design is shown in a) and a front view photograph of a GC low energy x-ray transmission window with a bar grid design is depicted in b). The typical wrinkles are formed in the free standing GC regions.

5.3.1 X-ray Transmission

The x-ray transmission of the depicted GC low energy x-ray transmission windows was measured, as described in Chapter 2, for the energies ranging from 0.1 keV to 2.5 keV. Both GC low energy x-ray transmission windows exhibited a significantly increased x-ray transmission for energies below 2 keV compared to a 1 µm thick GC x-ray transmission window with an open window geometry, as shown in figure 5.11 a).

The GC low energy x-ray transmission window with the bar support structure exhibits a higher x-ray transmission for the low energy radiation due to the reduced GC thickness. The x-ray transmission saturates for energies above 1.5 keV with a transmission of 84.6 % and 75.4 %, for the window with the bar support structure and the hexagonal cell design, respectively. While the thin GC material is almost completely transparent for energies above 1.5 keV, the supporting grid remains radio opaque, blocking the x-ray radiation. The saturation transmission is therefore only dependent on the FF of the window design, unless high energies above 10 keV are taken into account, as discussed in Chapter 1.

A large difference in the saturation transmission of the two window designs was encountered even though the specified FF was identical, as described in Chapter 4. While the bar supported design exhibited only a slight reduction compared to the specified FF of 85 %, the hexagonal cell design showed a significant reduction

of the measured FF. This is assumed to arise from shadowing effects as the hexagonal grid design leads to shadowing in all angular directions in contrary to the bar supported design, which only induces shadowing for the angular distribution perpendicular to the bar structure.

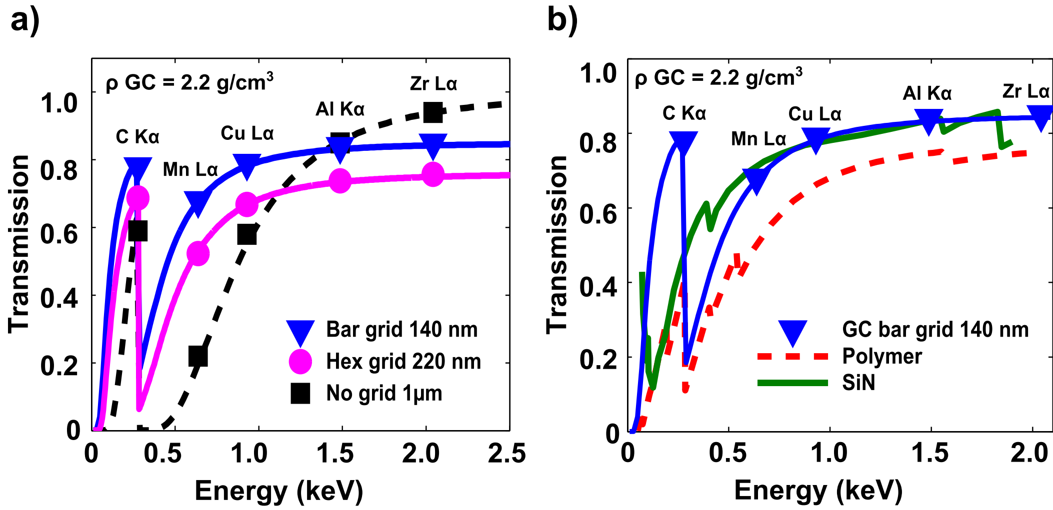

Figure 5.11: The measured x-ray transmission of a GC low energy x-ray transmission window with a hexagonal and a bar supported design, for the energies between 0.1 keV and 2.5 keV, are shown in a). The measured x-ray transmission of a 1 µm thick GC window with an open window geometry is included as a reference. The measured x-ray transmission of the window with the bar supported design was found to be more favorable and was compared to the measured x-ray transmission of a commercial polymer and the literature values of a silicon nitride [54], low energy x-ray transmission windows, as shown in b). The discrete, measured, data points were complemented by simulated values using the web applet supplied by the CXRO [38]

The x-ray transmission of the GC low energy x-ray transmission window with a bar supported design and a GC thickness of 140 nm is compared in figure 5.11 b) to the transmission of a commercial polymer and a commercial silicon nitride low energy x-ray transmission window. The x-ray transmission of the GC window is superior to the polymer window for all energies, while the silicon nitride window exhibits a higher x-ray transmission for energies below 90 eV, between the energies 280 eV and 870 eV and a similar x-ray transmission for the remaining energies that are shown.

5.3.2 Cycle Stability and Helium Leak Tightness

The discussed GC low energy x-ray transmission windows with a hexagonal cell and a bar supported design were exposed to a cyclic differential pressure for 17k

cycles without window failure. The maximum differential pressure of each cycle was 950 mbar and the differential pressure was applied with a cycle frequency of 0.5 Hz. Subsequent helium leak testing did not result in a helium leak rate above the required leak rate of 1×10^{-10} mbar l/s, as shown in figure 5.12 a).

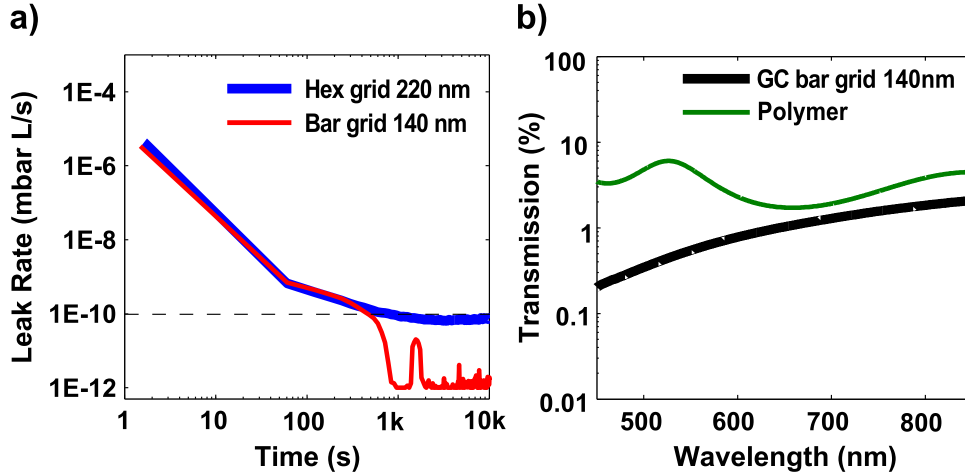

Figure 5.12: The measured helium leak rates of the discussed GC low energy x-ray transmission windows after cyclic testing with an atmospheric differential pressure and 17k pressure cycles are given in a). The measured, optical transmission of the 140 nm thick GC window with a bar supported window design is shown in b) for the wavelengths between 450 nm and 850 nm. The measured optical transmission of a polymer window, including an aluminium light blocking layer, is included as a reference.

5.3.3 Light Tightness

The light tightness of the bar supported GC low energy x-ray transmission window with a GC thickness of 140 nm was evaluated using the measurement scheme discussed in Chapter 2. The reduced GC thickness results in a significantly reduced light blocking ability compared to the discussed GC x-ray transmission windows with a GC thickness of 1 µm. The optical transmission for the wavelengths ranging from 450 nm to 850 nm was therefore determined and compared to the transmission of a commercial polymer window, as shown in figure 5.12 b). The light blocking ability is superior compared to a commercial, fluorescent blind polymer low energy x-ray transmission window and exhibits a wavelength dependency that is similar to that known from graphene and other graphitic materials [165, 167]. No information regarding the light blocking ability of the SiN low energy x-ray transmission window was available, but it is assumed to be similar to the polymer window as a thin aluminium layer is also employed as the light blocking layer [42].

5.3.4 Electrical Conductivity

The electrical conductivity of a 140 nm thick GC low energy x-ray transmission window was measured on a GC coated silicon substrate and a sheet resistance of 64.0 Ω/□ determined which corresponds to a bulk resistivity of the GC material of 0.9 mΩ cm.

5.4 Wafer Scale Fabrication of Graphenic Carbon X-ray Transmission Windows

The wafer scale deposition of the GC material introduced in Chapter 3 allows the use of silicon substrates with a diameter of 150 mm, as shown in figure 5.13 a), and was seen as a prerequisite for industrial fabrication of GC x-ray transmission windows.The wafer substrates were subsequently cut into 1 cm by 1 cm samples as shown in figure 5.13 b, which allows the window fabrication with the fabrication scheme developed for the single window process as described in Chapter 4.

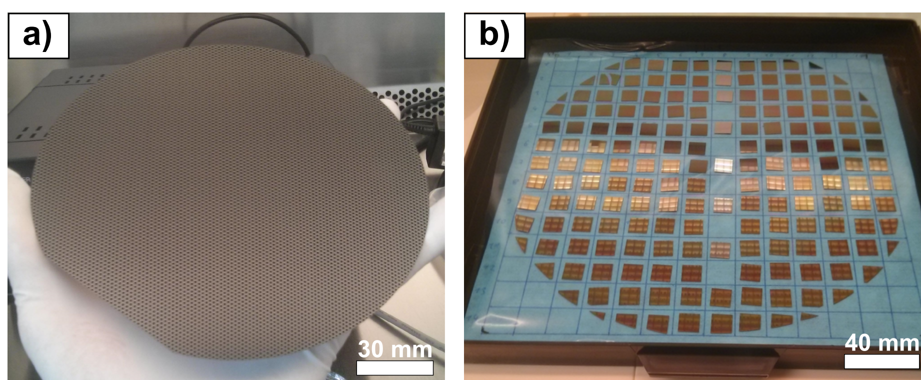

Figure 5.13: A photograph of a silicon wafer with a diameter of 150 mm after the GC deposition is depicted in a). The wafer substrates were subsequently cut into 1 cm by 1 cm GC coated silicon samples as shown in the photograph given in b).

5.4.1 Mechanical Stability: Burst Pressure

GC x-ray transmission windows fabricated from the GC material that was deposited using the wafer scale deposition process exhibited an excellent mechanical stability, as shown in figure 5.14 a). The burst pressure values of GC x-ray transmission windows with an open window diameter of approximately 7.2 mm and GC thicknesses between 530 nm and 1060 nm range between 2.5 bar and 6.9 bar. Bulge test experiments were conducted and an increased value of the Young's modulus of

170 GPa was encountered and seen as the reason for the improved pressure stability. Surprisingly, the highest stability against pressure loading was found at a GC thickness of 700 nm to 800 nm and decreased for larger GC thicknesses. The negative correlation of the GC thickness and the mechanical strength becomes even more apparent if the specific strength value of the tested windows is plotted versus the GC thickness, as shown in figure 5.14 b). The specific strength decreases significantly with the GC thickness, an aspect that has already been identified for the GC windows fabricated using the single sample deposition process, but the impact is much more pronounced.

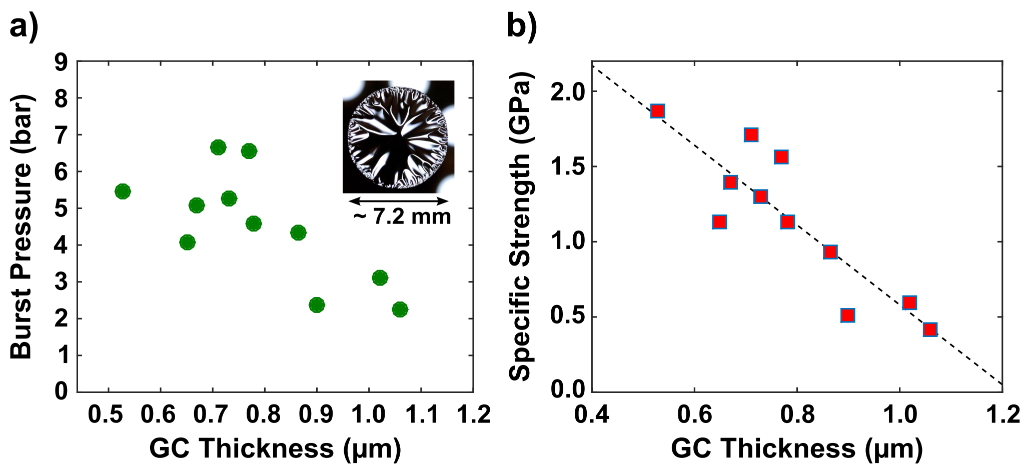

Figure 5.14: The measured burst pressure values for GC x-ray transmission windows fabricated from GC material deposited by the wafer scale deposition process, with a diameter of approximately 7.2 mm and the corresponding GC thickness, are shown in a). The corresponding specific strength values of the tested windows is given in b). A negative correlation with an increasing GC thickness is encountered as indicated by the dashed line of best fit.

The negative correlation of the encountered window stability is again attributed to the large compressive stress and the resulting implications during the wet etching of the GC windows, as described in Chapter 4. The line of best fit in figure 5.14 b) intersects the x-axis at a GC thickness value of approximately 1.2 µm and indeed, windows with a GC thickness above 1.1 µm displayed tears and cracks after the wet etching process as discussed in Chapter 4.

5.4.2 Two Step Growth Method

Therefore a two step deposition scheme was developed as introduced in Chapter 4 and experiments were conducted in order to determine whether the additional GC material improves the mechanical stability of the GC x-ray transmission window.

A number of GC x-ray transmission windows were fabricated with GC thicknesses below the identified thickness threshold, ranging from 420 nm to 720 nm. The obtained burst pressure values for the corresponding GC thicknesses are shown in figure 5.15 a). The burst pressure values were normalized to an open window diameter of 7 mm for better comparability. The resulting burst pressure values were subsequently seen as reference values. A window with an initial GC thickness of 500 nm was used to demonstrate the feasibility of the two step deposition scheme. Additional GC material was added to the fabricated GC x-ray transmission window by subsequent deposition processes that led to a total GC thickness of approximately 8 µm.

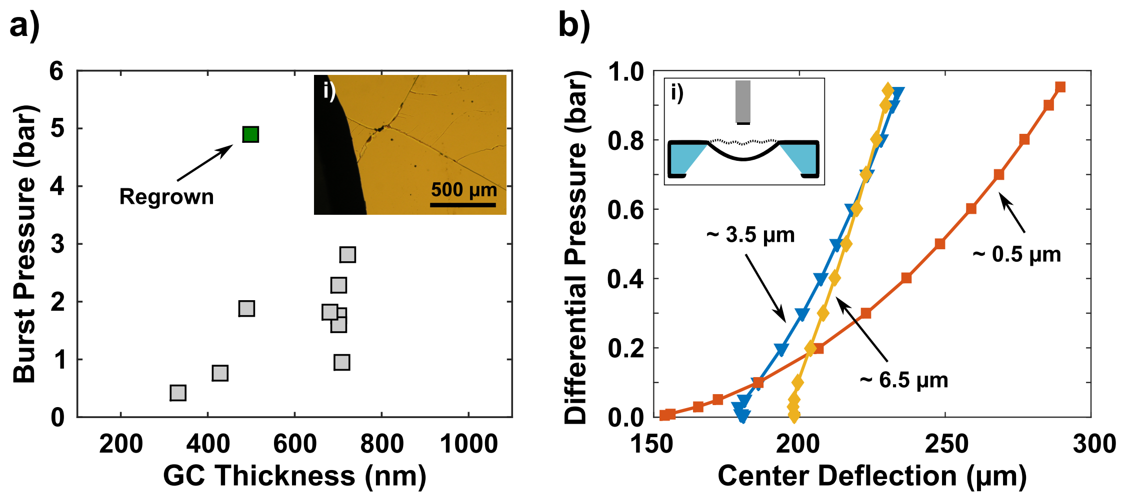

Figure 5.15: The measured burst pressure values for GC x-ray transmission windows with an open window geometry of 7 mm and the corresponding GC thickness are shown in a). The burst pressure value of a regrown GC window with an approximate GC thickness of 8 µm is indicated by the arrow, which is seen as a lower limit as the silicon window frame broke during the measurement and not the GC material. A photograph of the broken silicon window frame is shown in the inset i). The pressure induced center deflection of the GC window for varying amounts of added GC material are demonstrated in b). The inset i) schematically depicts the used measurement geometry.

Bulge test experiments were conducted with the regrown GC x-ray transmission window in order to determine whether the additional GC material improved the mechanical stability of the GC x-ray transmission windows. The extracted pressure deflection curves are given in figure 5.15 b). The pressure induced center deflection was significantly reduced as the GC material thickness was increased from 500 *nm* to 3.5 µm and 6.5 µm, respectively. This was interpreted as an indication that the additional GC material forms an integral part of the free standing

GC material. Burst pressure testing of the regrown GC x-ray transmission window with an assumed final GC thickness of 8 µm resulted in a burst pressure of 4.9 bar. The window material did not fail but instead the integrated silicon window frame broke during pressure testing as shown in inset i) of figure 5.15 a). Unfortunately, a silicon substrate with a reduced thickness of 250 µm was used for this experiment exhibiting a reduced mechanical stability. None the less, the obtained burst pressure value was significantly higher compared to the reference burst pressure values for a GC window with a thickness of 500 nm, as indicated in figure 5.15 a). The additional GC material therefore results in an increase of the mechanical stability of the GC x-ray transmission window.

5.4.3 Mechanical Stability: Cycle Stability

Burst pressure testing of the GC x-ray transmission windows was complemented by cyclic pressure testing. The encountered, high, mechanical stability of GC x-ray transmission windows fabricated from the GC material deposited by the wafer scale deposition process made cyclic pressure testing with a higher differential pressure feasible as a GC x-ray transmission window with an open diameter of 7.2 mm and a GC thickness of 650 nm, withstood a differential pressure of 4 bar, as shown in figure 5.16 a).

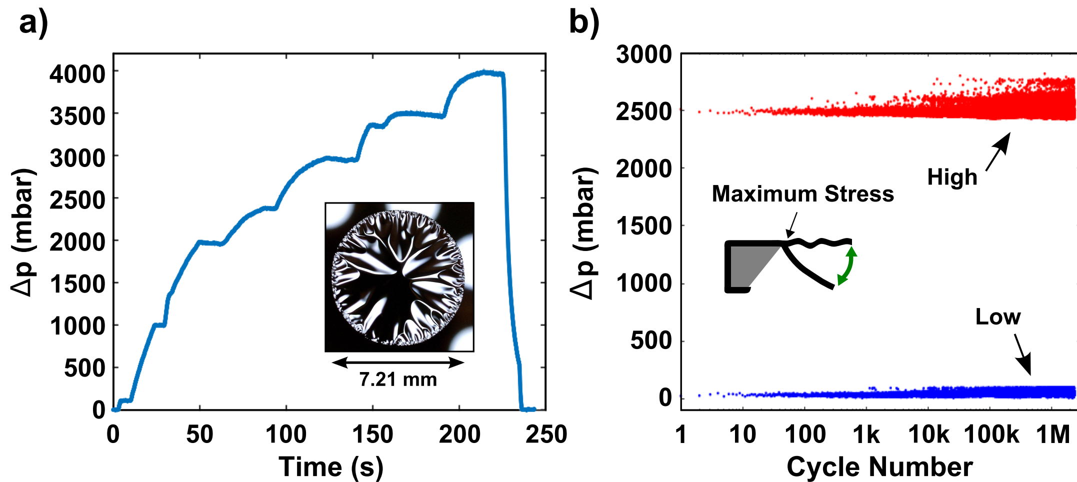

Figure 5.16: The applied differential pressure across the 650 nm thick GC window with an open diameter of 7.2 mm during pressure testing is shown in a). The window did not break and the differential pressure was relieved at the end of the test. The GC x-ray transmission window was subsequently employed for cyclic pressure testing with an increased maximum differential pressure of 2400 mbar and the maximum and minimum differential pressure that were reached for each pressure cycle is shown in b).

The differential pressure was held constant for short intervals in order to verify the leak tightness of the test configuration. The tested window did not fail, instead the differential pressure was relieved after holding the differential pressure of 4 bar for a short time.

Cyclic pressure testing was subsequently performed for the same window with an increased minimum differential pressure of at least 2400 mbar per cycle. The recorded maximum and minimum values of the differential pressure for each of the pressure cycles are shown in figure 5.16 b). Two million cycles did not lead to window failure and subsequent helium leak testing (not shown) verified the window integrity. Cycle testing was performed with a frequency of 3 Hz and a pressure reservoir with a pressure of 3000 mbar versus atmosphere was used, which explains the infrequent overshoots of the applied differential pressure.

5.4.4 X-ray Transmission

X-ray transmission measurements were performed in order to rule out any negative effects of the wafer scale GC deposition process. The measured x-ray transmission of a 650 nm thick GC window is shown in figure 5.17 a).

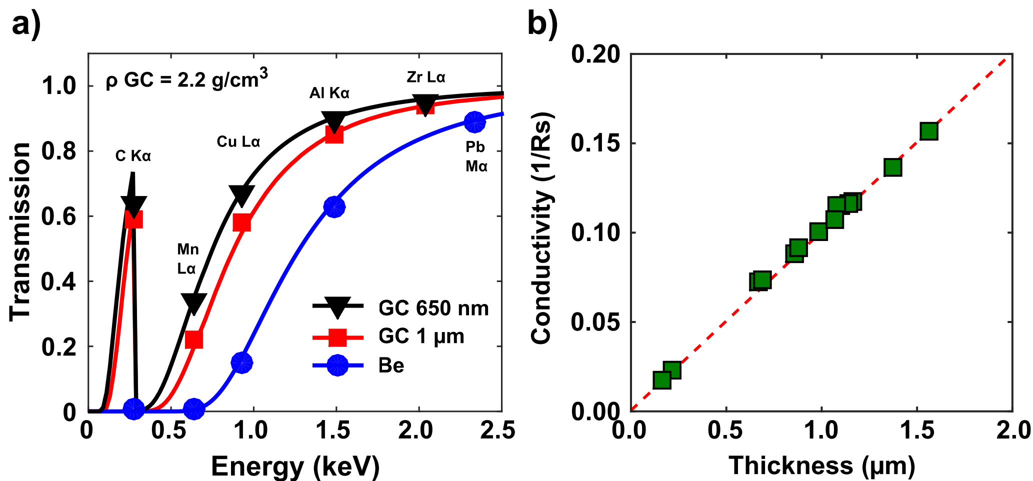

Figure 5.17: The measured x-ray transmission of a 650 nm thick GC window that has been fabricated using the wafer scale deposition process is given in a). The transmission of the discussed GC window with a thickness of 1 μm and of a Be window are included as a reference. The sheet conductivity of the GC material for the corresponding thickness, as deposited with the wafer scale deposition system is shown in b). The linear dependency is indicated by the dashed line of best fit and corresponds to a bulk resistivity of 1 mΩ cm.

The measured x-ray transmission of a 1 μm thick GC window, that was fabri-

cated using the single sample deposition process, and of a Be window are included as references. The measured data points were supplemented by simulated transmission values assuming a GC density of $2.2\,\mathrm{g/cm^3}$ employing the web applet supplied by the CXRO and indicates a similar GC density for both deposition processes.

5.4.5 Electrical Conductivity

The electrical conductivity of the GC material deposited by the waver scale deposition process was measured using the scheme discussed in Chapter 2, and a linear dependency of the sheet conductivity versus the GC thickness was identified, as shown in figure 5.17 b). The bulk resistivity of the GC material was subsequently calculated and determined to be $1\,\mathrm{m\Omega\,cm}$.

6 Discussion

6.1 Graphenic Carbon as a Material for X-ray Transmission Windows: Replacing Beryllium

GC x-ray transmission windows with a GC thickness of 1 µm were shown to not only fulfill the requirements of the x-ray transmission windows discussed in Chapter 2, but also supersede the benchmark properties of Be windows for the given application, as shown in the previous chapter. Foremostly, the presented GC x-ray transmission windows exhibit a higher x-ray transmission than Be windows for x-ray energies below 2 keV. A photograph of the first prototype SDD x-ray detector modules incorporating a GC x-ray transmission window is presented in figure 6.1 a). The inside of the detector housing was evacuated and the free standing GC film therefore deflected downwards.

A prototype SDD module incorporating a GC x-ray transmission window was used to record the EDS spectrum of a polytetrafluoroethylene (PTFE) sample. PTFE is a synthetic fluoropolymer and composed of carbon and fluorine. The high transmission of the GC window for energies below 2 keV allows the detection of the $K\alpha$ radiation originating from the elements carbon and fluorine, which is not possible with a Be window. The EDS spectrum obtained from a PTFE sample, with the SDD detector module incorporating a GC x-ray transmission window, is shown in figure 6.1 b). The spectrum exhibits high peak intensities for the energies corresponding to the $C\ K\alpha$ (0.277 keV) and $F\ K\alpha$ (0.677 keV) lines and the peaks can clearly be identified. A significant signal increase is apparent if the spectrum is compared to a spectrum obtained using a detector module incorporating a Be window, at otherwise identical conditions. The silicon and copper peaks are assumed to have originated from the sample holder and both spectra were normalized to the intensity of the silicon peak for better comparability. This is seen valid as the transmission of the corresponding $Si\ K\alpha$ (1.74 keV) radiation is higher for the GC window compared to a Be window.

The proposed GC x-ray transmission windows therefore not only replace the toxic beryllium but also offer the advantage of obtaining higher count rates for the $K\alpha$ radiation of light elements.

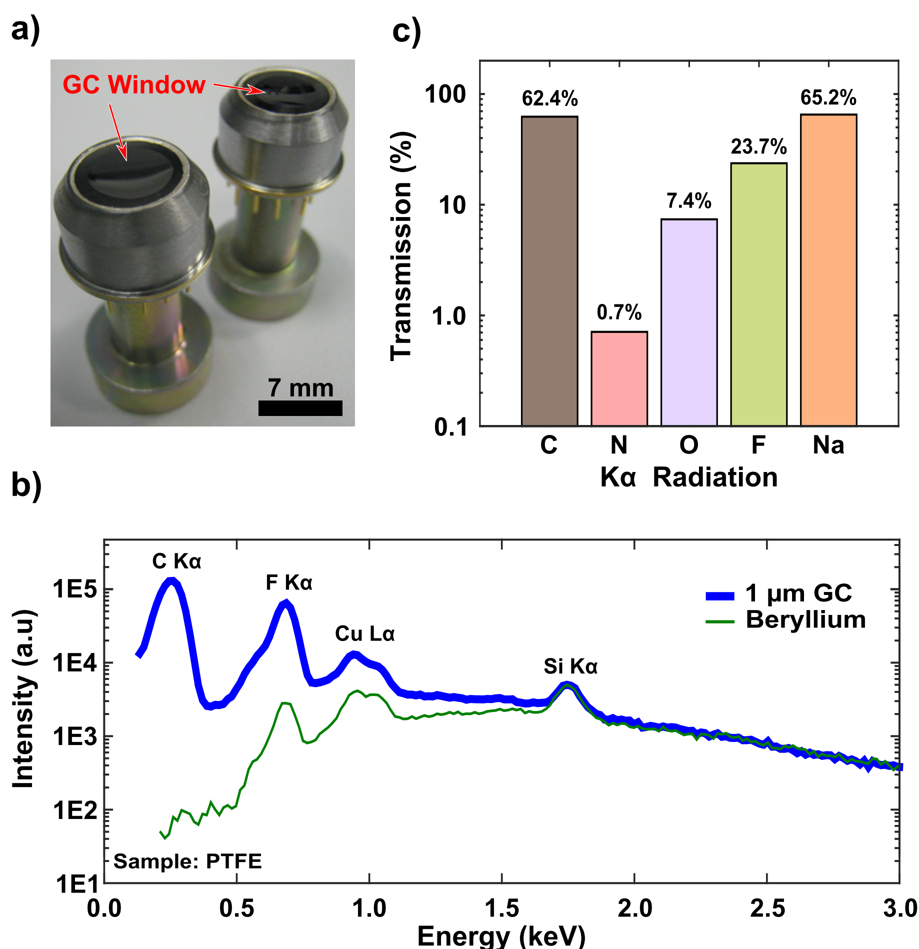

Figure 6.1: A photograph of the first prototype SDD modules incorporating a GC x-ray transmission window is shown in a). The measured EDS spectra of a PTFE sample, as obtained with a detector module incorporating a GC and with a detector module incorporating a Be x-ray transmission window, are given in b) and demonstrate the improved x-ray transmission of the GC x-ray transmission windows. The carbon and fluorine peaks are clearly visible and exhibit an increased intensity. The copper and silicon peaks are assumed to originate from the sample holder. The calculated transmission of the $K\alpha$ radiation for the light elements carbon (C), nitrogen (N), oxygen (O), fluorine (F) and sodium (Na) are demonstrated in c) for a 1 µm thick GC window.

The calculated x-ray transmission of a 1 µm thick GC window for the $K\alpha$ radiation of the elements carbon, nitrogen, oxygen, fluorine and sodium are given in figure 6.1 c). The increased transmission therefore allows the detection of the elements carbon, oxygen and to some extend even nitrogen using a 1 µm thick GC window, if the measurements are performed in a vacuum environment. This is highly attractive for the user as especially carbon, nitrogen and oxygen are of interest, in for example semiconductor material sciences, and in this case the 1 µm thick GC window could avoid the necessity of low energy x-ray transmission windows. In the case of handheld applications, fluorine is of particular interest, as the energy of the $F\ K\alpha$ radiation is sufficiently high to penetrate small distances in air. Handheld devices incorporating a 1 µm thick GC window could therefore be used to extend the detection limit to fluorine, especially if helium purging is used.

A GC thickness of 1 µm was chosen as a reference thickness for the prototype modules as an increased optical transmission, compared to the reference Be windows, was observed for lower GC thicknesses. The optical and infrared transmission of the GC material was therefore identified as the limiting factor regarding the GC thickness. The high light blocking ability of Be windows is a side effect of the large Be thickness of at least 8 µm that is necessary to obtain a helium leak tight window configuration. It remains to be seen if such high levels of light blocking are truly necessary for all applications. If not, this would allow to further reduce the GC thickness of the GC x-ray transmission windows, leading to an even higher x-ray transmission.

Table 6.1 summarizes the extracted window properties of GC x-ray transmission windows with a GC thickness of 1 µm and an open diameter of 7 mm. The cell coloration green is chosen for the GC window properties that represent a significant improvement compared to Be windows and includes the increased x-ray transmission, the high resilience against material fatigue, the high thickness control and non-toxicity. The red cell coloration indicates the main problems of Be windows, including the toxicity and poor thickness control. The novel window material allows for an improved x-ray transmission, exhibits an excellent mechanical stability and a high resilience against material fatigue, a high intrinsic chemical stability against most chemical compounds and the developed deposition process allows for a much better control of the window thickness compared to Be windows. In addition, the replacement of the toxic beryllium material would finally allow to repair SDD detector modules after a window failure, which is currently not possible as the broken detector modules are classified as hazardous waste. The subsequent system downtime due to the required decontamination of the measurement environment after a beryllium window failure is consequently also ruled out, improving the overall availability of the measurement systems.

Table 6.1: Summarized properties of a commercial DuraCoat Be window with a specified thickness of 8 µm and a window diameter of 7 mm, as specified in references [44, 56], and of a GC x-ray transmission window with a thickness of 1 µm and an open diameter of 7 mm.

Window Property	DuraCoat Beryllium	Graphenic Carbon
X-ray Transmission	$> 80\ \%\ for\ E > 1.7\ keV$	$> 90\ \%\ for\ E > 1.7\ keV$
Pressure Stability	$> 2\ bar$	$> 2\ bar$
Helium Leak Rate	$< 1 \times 10^{-10}\ \frac{mbar\ L}{s}$	$< 1 \times 10^{-10}\ \frac{mbar\ L}{s}$
Fill Factor	$100\ \%$	$100\ \%$
Pressure Cycle Fatigue	$> 20k\ @\ \Delta p = 1\ bar$	$> 10M\ @\ \Delta p = 1.2\ bar$
Light Blocking Factor	$> 10^{11}$	$> 10^{11}$
Thickness Tolerance	$-\ 0\ \mu m\ /\ +\ 5\ \mu m$	$< 10\ nm$
Chemical Resistance	High	High
Electrical Resistivity	$< 4 \times 10^{4}\ \Omega\, cm$	$1\ m\Omega\, cm$
Non-Toxic	No	Yes

6.2 Comparison of the Developed Deposition Processes

The high mechanical strength of the presented GC x-ray transmission windows, especially using the wafer scale deposition process, was demonstrated by burst pressure testing and both developed GC deposition processes allow the fabrication of GC x-ray transmission windows with an open window diameter of 7 mm and a GC thickness of 1 µm that withstand a differential pressure of 2 bar, as shown in figure 6.2 a).

The burst pressure values demonstrate the large mechanical stability increase for the GC films deposited with the the wafer scale deposition system. GC windows with an open diameter of 7.2 mm and a GC thickness of 600 nm to 700 nm were able to withstand a differential pressure of almost 7 bar and therefore exhibit an almost seven-fold increase in stability compared to the GC material deposited with the small scale deposition system. The high mechanical stability of the wafer deposited samples is assumed to arise from the higher processing temperatures that are not available on the small scale deposition system due to the maximum temperature stability of the used quartz ware.

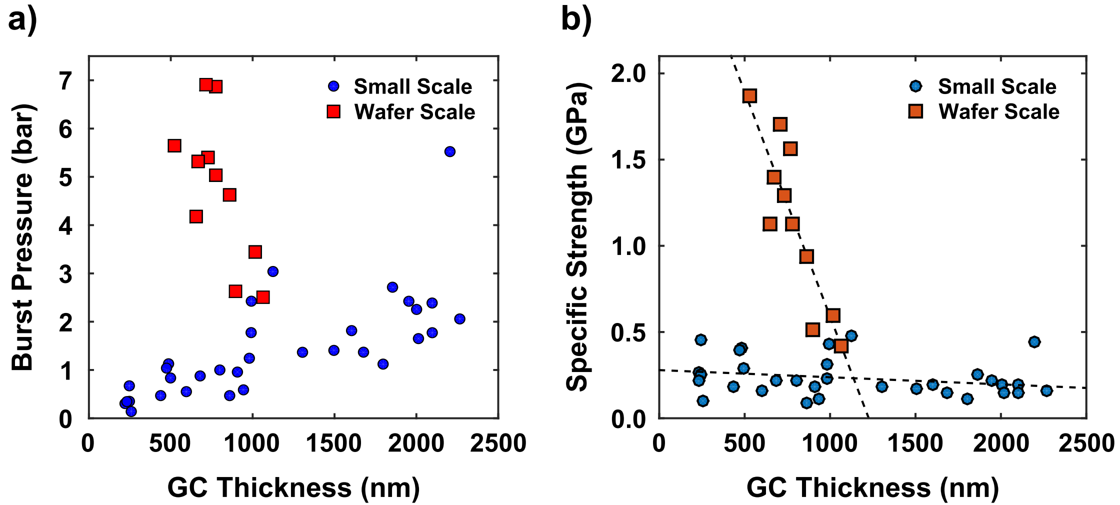

Figure 6.2: The measured burst pressure values of GC x-ray transmission windows with the corresponding GC thickness and an open diameter of 7 mm are given in a) for the two developed GC deposition processes. The extracted specific strength of each of the tested GC windows is shown in b) and the dashed lines indicate the best fit for the two different deposition methods.

None the less, no substantial differences of the GC materials were identified using Raman spectroscopy or cross section SEM images. Even the material density of 2.2 g/cm^3 remained a good fit for the transmission measurements and it is therefore difficult to explain the observed increase of the mechanical stability on a structural level, given the employed measurement schemes. Only bulge testing revealed an increased Young's modulus from approximately 130 GPa to 170 GPa, which is in line with the observed stability enhancement.

While the mechanical strength of the wafer deposited GC material is much higher, the fact that the negative correlation, of the observed specific strength of the GC material and the GC thickness, is much more pronounced indicates a substantial difference in the growth behavior of the GC films, as shown in figure 6.2 b). The large influence of the GC thickness is assumed to arise from a higher compressive stress that is present within the GC material and thus assumed to lead to defect generation within the GC material at reduced GC thicknesses, compared to the GC material deposited with the small scale deposition process. Unfortunately it was not possible to perform wafer bow measurements of the GC samples deposited by the small scale deposition process due to the long, high temperature processing involved in the CVD deposition process that led to a deformation of the silicon substrates. None the less, the performed Raman measurements on both types of deposited GC material indicate a significant increase in the compressive residual stress of the GC material deposited by the wafer scale deposition system.

The developed two step growth process is therefore seen as a route to fabricate GC windows with a large GC thickness, utilizing the high mechanical strength of the wafer scale deposition process, and enables the GC material to be used for x-ray windows with a much larger open diameter that require an even higher mechanical strength.

6.3 Graphenic Carbon as a Window Material for Low Energy X-ray Transmission Windows

The excellent properties of the GC x-ray transmission windows with a GC thickness of 1 µm led to the development of GC low energy x-ray transmission windows. An integrated silicon support bar design allowed the thickness of the GC material to be reduced significantly as demonstrated in Chapter 5. A GC low energy x-ray transmission window with a GC thickness of 140 nm and a silicon bar support grid, with a span width of 1 mm and a bar width of 200 µm, was demonstrated to withstand an atmospheric differential pressure while exhibiting a high transparency for x-ray radiation with an energy below 2 keV. The measured x-ray transmission of the window is shown in figure 6.3 a) and compared to the measured x-ray transmission of a Be window. The GC low energy x-ray window with a GC thickness of 140 nm offers a low energy x-ray transmission superior to commercially available polymer and a similar transmission to current state of the art silicon nitride low energy x-ray transmission windows.

The GC thickness of 140 nm was verified to be helium leak tight and the blocking of visible and infrared radiation was superior compared to a polymer window that incorporates an additional aluminium light blocking layer. The inherent light blocking ability of the GC windows avoids the spectral contamination of the recorded spectrum due to x-ray fluorescence of the light blocking layer and rules out yielding or delamination effects that can deteriorate the light blocking ability of the window and therefore reduce the life time of the detector module [42].

The excellent mechanical strength of the GC material is quantified by using the introduced value of the specific strength, approaching values of more than 1.5 GPa, as discussed in Chapter 5. The calculation method of the figure of merit can subsequently be used to estimate the minimum thickness of a GC low energy x-ray transmission window, if we assume a specific strength of the GC material of 1.5 GPa, a cell width of 1 mm and a required burst pressure of at least 1200 mbar. The resulting minimal GC thickness was calculated using equation 6.1, with Δp_{max} denoting the required burst pressure, r the half width of the cell spacing and s

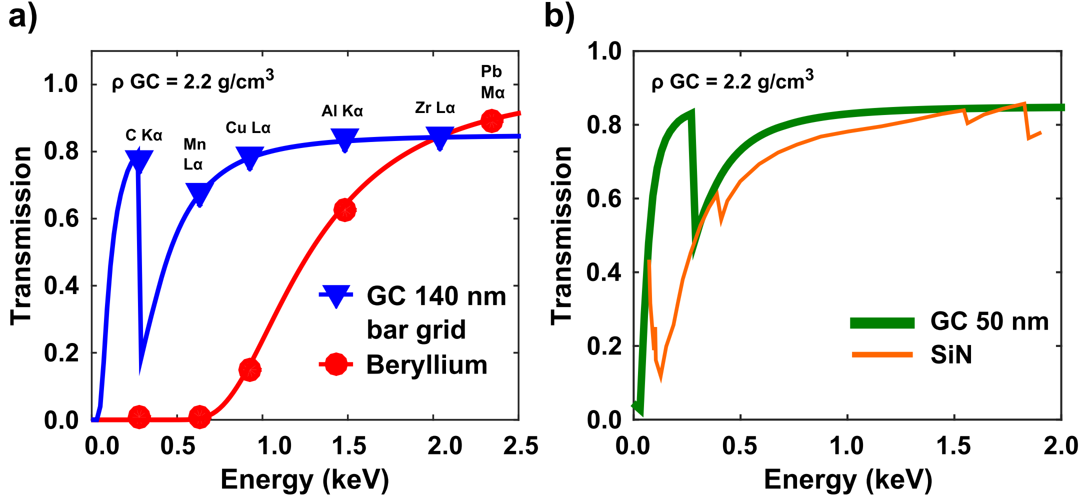

Figure 6.3: The measured x-ray transmission of a 140 nm thick GC low energy x-ray transmission window incorporating a bar grid support structure is shown in a) and compared to a Be window. The x-ray transmission of the same window geometry with a reduced GC thickness of 50 nm was simulated and exhibits a higher x-ray transmission compared to the state of the art fluorescent blind SiN low energy x-ray transmission window [54].

the specific strength of the GC material. The minimal thickness was found to be 20 nm which would lead to a significant increase of the x-ray transmission. The x-ray transmission for a GC low energy x-ray transmission window with the discussed window geometry was simulated and a GC thickness of 50 nm is sufficient to offer a higher x-ray transmission than a SiN low energy transmission window for the relevant energies, as shown in figure 6.3 b) [54].

$$t_{min} = \frac{\Delta p_{max} r}{2s} \tag{6.1}$$

The light blocking ability of such extremely thin GC x-ray transmission windows is significantly reduced compared to 1 µm and 140 nm thick GC x-ray transmission windows and depending on the application an additional light blocking layer might be necessary. This is demonstrated by the photographs shown in figure 6.4 of a GC x-ray transmission window with a GC thickness of approximately 60 nm. By changing the focus of the camera it is possible to visualize the high optical transparency of the GC material at such reduced thicknesses.

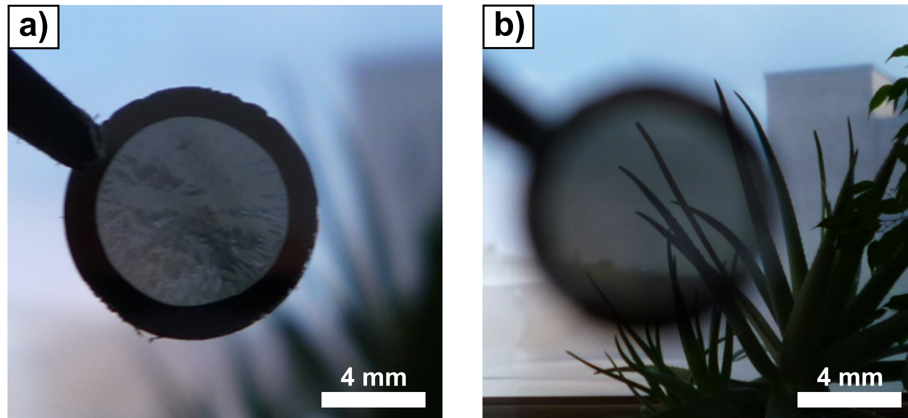

Figure 6.4: A front view photograph of a GC x-ray transmission window with a GC thickness of approximately 60 nm is shown in a). The high optical transparency becomes apparent by shifting the focus point of the camera to the background of the image, as demonstrated in b).

It remains to be seen to which GC thickness a helium leak tight window configuration is given but the small grain size typically found in nano- and polycrystalline graphene materials of only a few nanometers, supports the expectation that even extremely thin GC windows are helium leak tight, as long as the presence of pin holes is avoided. This was supported by the fact that no difference in the measured helium leak rates was found for windows as thin as 140 nm compared to 1 µm or 2 µm thick GC windows.

It is therefore assumed that the x-ray transmission of GC low energy x-ray transmission windows can still be significantly increased given the observed mechanical stability of the GC material.

6.4 Material Properties of the Graphenic Carbon Material

Bulge testing of rectangular GC thin films, as discussed in Chapter 5, resulted in a calculated maximum stress value of 1.4 GPa at a differential pressure of 950 mbar and a GC thickness of 140 nm. It should be noted that the GC thin film was still intact at the given differential pressure and the maximum stress value therefore has to be expected to be even higher at the pressure required to induce mechanical failure. Xiang et al. [216] have postulated that the maximum value of the stress-strain curve of rectangular thin films during bulge testing, corresponds to the ultimate tensile strength of the material. This is not confirmed by the performed FEM simulations, as a significant increase of the stress value was observed

near the window frame and window failure assumed to occur in this region. The calculated value of 1.4 GPa is therefore interpreted as a lower limit of the ultimate tensile strength of the deposited GC material. None the less, this value is still substantially larger than the values found in literature for beryllium (454 MPa) and if we incorporate the simulation results, indicating an approximately five fold increase of the stress near the window frame compared to the calculated values, as discussed in Chapter 5, is increased to 7.0 GPa [43].

The material constants obtained from bulge testing are seen as a rough estimate as the systematic error due to the compressive stress of the GC material is unknown. None the less, the Raman spectroscopy measurements indicate a similar value for the Young's modulus of the GC material and the values therefore seen as sufficiently reliable to verify the significantly higher value of the Young's modulus of the GC material compared to the values commonly reported for PyC in literature, which are found in the range of 10 GPa to 45 GPa [217]. This validates the assumptions made in Chapter 3 and moves the GC material closer towards nano- and polycrystalline graphene and is seen as the origin of the astonishing mechanical properties of the GC x-ray transmission windows.

The tested GC x-ray transmission windows exhibited a high resilience against dynamic loading and material fatigue. This is of importance as dynamic stress occurs during venting of vacuum applications or during handling of the detector module throughout the detector lifetime.

The identified material properties of the GC material are summarized in table 6.2 including the density, the residual compressive stress, the bulk resistivity, the Young's Modulus and the lower limit of the ultimate tensile strength (UTS).

Table 6.2: The extracted material properties of the GC material are summarized.

Density	**Stress**	**Resistivity**	**Young's Modulus**	**UTS**
$2.2\ g/cm^3$	$400 - 500\ MPa$	$1\ m\Omega\, cm$	$130 - 170\ GPa$	$> 1.4\ GPa$

7 Summary and Outlook

This thesis discussed the successful development and realization of x-ray transmission windows incorporating graphenic carbon (GC) as a window material in order to replace toxic beryllium. The basic principles of energy dispersive x-ray spectroscopy and the silicon drift detector technology were introduced and the underlying requirements discussed that make x-ray transmission windows necessary. Depending on the application, x-ray transmission windows need to be extremely thin, mechanically strong, helium leak tight, electrically conductive, composed of low z materials and offer a high absorption in the optical and infrared spectrum. The experimental schemes required to evaluate the properties of x-ray transmission windows were introduced and the results obtained during bulge testing, Raman spectroscopy and FEM simulations discussed.

Graphenic carbon (GC) was identified as a potential x-ray transmission window material by examining the material properties of graphene and pyrolytic carbon in regard to the requirements of x-ray transmission windows. A GC deposition process using silicon substrates was developed utilizing chemical vapor deposition and the identified deposition process parameters result in a highly textured GC material with high mechanical strength. The developed fabrication scheme for the GC x-ray transmission windows provides an integrated silicon window frame and the resulting window configuration exhibits an inherently high adhesion of the GC material and gas tightness. The introduced method allows the fabrication of x-ray transmission windows, with an open window geometry as well as an integrated silicon support structure, that can be directly incorporated into standard detector housings.

The influence of the GC thickness on the mechanical stability of the GC x-ray transmission windows was discussed and a negative correlation observed that limits the GC thickness. This is attributed to the compressive residual stress of the deposited GC material. The wet etching process of the silicon material was identified as a critical aspect during the fabrication of the GC x-ray transmission windows and a two step fabrication process was proposed and validated by fabricating GC x-ray transmission windows with a GC thickness of up to 8 µm. The GC material offers an excellent resilience against material fatigue, which was demonstrated by cyclic pressure testing of GC x-ray transmission windows, and more than 10 million pressure cycles did not lead to window failure. Bulge testing

and Raman spectroscopy were employed to probe the mechanical properties of the GC material and a Young's modulus of up to 170 GPa was identified. FEM simulations were performed in order to understand the implications that arise from the compressive stress of the GC material and an inhomogeneous stress distribution was found, with the maximum stress acting near the window edge. GC x-ray transmission windows with a GC thickness of 1 µm are mechanically strong, helium leak tight, electrically conductive, opaque to visible and infrared light, chemically stable and exhibit an x-ray transmission that is superior to the transmission of Be x-ray transmission windows.

It was demonstrated that the x-ray transparency of GC X-ray transmission windows can be extended to the low energy range by reducing the GC thickness and implementing a silicon support grid, thus allowing the detection of light elements.

The developed deposition process was transferred to a deposition system capable of processing silicon substrates with a diameter of 150 mm. This allows the mass production of GC x-ray transmission windows on an industrial scale and was seen as a prerequisite in order to replace beryllium as a window material for x-ray transmission windows.

GC x-ray transmission windows exhibit excellent properties and not only allow to replace the toxic beryllium material but also offer a superior x-ray transmission. The suitability of graphenic carbon as a window material for x-ray transmission windows was subsequently demonstrated by equipping a vacuum encapsulated SDD detector module with a 1 µm thick GC window. The obtained EDS spectra display an increased peak intensity, compared to spectra obtained with standard beryllium windows, for energies below 2 keV and allows the detection of fluorine and carbon content without the use of a special low energy x-ray transmission window.

To our knowledge this is the first realization of an alternative x-ray transmission window that is capable of replacing beryllium without any negative implications. The developed GC windows are therefore expected to further increase the importance and availability of EDS systems by avoiding the health hazards associated with beryllium while improving the system performance.

Outlook

Further optimization of the GC material seems feasible as the large, apparent differences between the two developed deposition processes indicate a strong dependency of the window strength on the deposition process. A better understanding

of the encountered tear formation, compressive stress and specific strength of the GC material, as well as the influence of the deposition parameters is seen necessary in order to further optimize the mechanical properties of the GC material. The encountered Young's modulus of the GC material is still substantially smaller than the values reported for nano- and polycrystalline graphene and ample room for improvement therefore expected.

The proposed two step growth process for GC x-ray windows with an increased GC thickness allows the fabrication of large diameter GC x-ray transmission windows and is in general seen as a promising route to obtain GC x-ray transmission windows with a high mechanical stability.

Finite element simulations identified a significantly increased stress of the window material in the window frame region. It is therefore assumed that a more elaborate thickness distribution of the GC window material, with an increased thickness near the window region that is gradually decreased towards the window center, could further increase the x-ray transparency of GC x-ray transmission windows, while complying to the mechanical stability requirements.

The presented bar grid window design for GC low energy x-ray transmission windows can be improved further by optimizing the span and support grid width. This would allow for a reduction of the GC thickness and an even higher x-ray transmission for low energy x-ray radiation. In addition, by replacing the radio opaque silicon support structure with an integrated support made from thick GC material, a GC low energy x-ray transmission window with a high fill factor for high energy x-radiation would be obtained. The observed high compressive stress of the GC material poses an obstacle but it is seen as a feasible future improvement of the discussed GC low energy x-ray transmission windows. The amount of compressive stress was found to be process dependent and a better understanding of the stress inducing mechanism as well as the use of alternative substrate materials, with a lower thermal expansion coefficient, is seen as a promising way to obtain stress free, or even tensile stressed, GC material. This would open a manifold of potential applications such as a pellicle material for extreme ultraviolet (EUV) lithography and MEMS or NEMS applications including microphone and loudspeaker devices.

Recent work by Törmä et al. [218] has shown that the excitation of light elements is much more efficient by the use of soft x-ray radiation, which is commonly absorbed by the exit window of x-ray tubes. Replacing the exit window with a high transparency x-ray transmission window, fabricated from the presented GC material, is therefore assumed to improve the excitation efficiency of light elements in EDXRF systems and seen as a further application for the GC x-ray transmis-

sion windows.

This work was conducted in close co-operation with the Munich based company Ketek GmbH and the demonstrated properties of the GC x-ray transmission windows have led to the filing of the patent with the title "X-Ray Radiation Passage Window for a Radiation Detector" under the patent number: US 13/963,928 [219]. The presented wafer scale deposition process of the GC window material demonstrates the scalability to mass production compatible equipment of the deposition process. Ketek is working on the industrial scale fabrication of GC x-ray transmission windows, targeting the replacement of toxic Be windows and the introduction of GC low energy x-ray transmission windows to the market.

Acronyms

a-C	Amorphous Carbon
AFM	Atomic Force Microscopy
Al	Aluminium
Be	Beryllium
BWF	Breit-Wigner-Fano
C	Carbon
CCD	Charge Coupled Detector
CCP	Capacitively Coupled Plasma
CNT	Carbon Nanotube
CTE	Coefficient of Thermal Expansion
Cu	Copper
CVD	Chemical Vapor Deposition
CXRO	Center of X-ray Optics at the Lawrence Berkeley National Laboratory
EDS	Energy Dispersive Spectroscopy
EDXRF	Energy Dispersive X-ray Fluorescence
F	Fluorine
FEM	Finite Element
FF	Fill Factor of X-ray Transmission Window
FWHM	Full Width Half Maximum
GC	Graphenic Carbon
HOPG	Highly Ordered Pyrolytic Graphite
HT-PyC	Highly Textured Pyrolytic Carbon
JFET	Junction Gate Field Effect Transistor

LED	Light Emitting Diode
MEMS	Micro Electro Mechanical Systems
Mn	Manganese
NEMS	Nano Electro Mechanical Systems
PAH	Polycyclic Aromatic Hydrocarbons
PIXE	Particle Induced X-ray Emission
PTFE	Polytetrafluoroethylene
PyC	Pyrolytic Carbon
PyG	Pyrolytic Graphite
RIE	Reactive Ion Etching
RTCVD	Rapid Thermal Chemical Vapor Deposition
SDD	Silicon Drift Device
SEM	Scanning Electron Microscopy
Si(Li)	Lithium Drifted Silicon
SiN	Silicon Nitride
ta-C	Tetrahedral Amorphous Carbon
TEM	Transmission Electron Microscopy
TXRF	Total Reflection X-ray Fluorescence Spectroscopy
UTS	Ultimate Tensile Strength
UV	Ultra-Violet
WDS	Wavelength Dispersive Spectroscopy
WLI	White Light Interferometer
Zr	Zirconium

List of Symbols

I_0	Peak Intensity
L_a	Crystallite Length (nm)
Q^{-1}	Breit-Wigner-Fano Coupling Coefficient
R_{RMS}	Root Mean Square Surface Roughness
R_s	Electrical Sheet Resistance ($\Omega/\Box$)
Δp	Differential Pressure
Γ	Full Width at Half Maximum
Ω	Electrical Resistivity (Ohm)
$\delta\epsilon$	Differential Strain
$\delta\omega$	Differential Wavenumber (cm^{-1})
ϵ	Strain
λ	Wavelength (nm)
μ	Mass Absorption Coefficient
ν	Poisson's Ratio
ω	Wavenumber (cm^{-1})
ω_0	Peak Position (cm^{-1})
ω_E	Average Energy for Electron-Hole Pair Generation in a Semiconductor (eV)
ρ	Bulk Resistivity (Ohm cm)
ρ	Material Density (g/cm^3)
σ	Stress (Pa)
σ_0	Residual Stress (Pa)
n_i	Intrinsic Charge Carrier Density (cm^{-3})
E	Young's Modulus (Pa)
E	Energy (eV)
F	Fano Factor
I	Signal Intensity

K	Surface Curvature
R	Radius of Curvature
r	Radius
T	Temperature (K)
t	Thickness
T(E)	Energy Dependent Transmission
Y	Bi-axial Elastic Modulus (Pa)
Z	Atomic Number

Publications of the Author

[SH15a] S. Huebner, N. Miyakawa, S. Kapser, A. Pahlke, and F. Kreupl, "High Performance X-Ray Transmission Windows Based on Graphenic Carbon," *IEEE Trans. Nucl. Sci.*, vol. 62, no. 2, pp. 588-93, 2015.

[SH15b] S. Huebner, N. Miyakawa, A. Pahlke, and F. Kreupl, "Design and properties of low-energy X-ray transmission windows based on graphenic carbon," *Phys. Status Solidi (b)*, vol. 252, no. 11, pp. 2564-73, 2015. (Invited Paper)

[SH16a] S. Huebner, N. Miyakawa, A. Pahlke, and F. Kreupl, "Performance Improvement of Graphenic Carbon X-ray Transmission Windows," *MRS Advances*, available on CJO2016. doi:10.1557/adv.2016.194.

References

[1] B. G. Lowe and R. A. Sareen, *Semiconductor X-Ray Detectors.* Series in Sensors, CRC Press, Taylor & Francis Group, 2013.

[2] J. Kemmer, "Improvement of detector fabrication by the planar process," *Nuclear Instruments and Methods in Physics Research Section A: Accelerators, Spectrometers, Detectors and Associated Equipment*, vol. 226, no. 1, pp. 89–93, 1984.

[3] G. Bertuccio, L. Fasoli, C. Fiorini, E. Gatti, A. Longoni, M. Sampietro, D. Hauff, J. Kemmer, and R. Richter, "Silicon drift detector with integrated p-JFET for continuous discharge of collected electrons through the gate junction," *Nuclear Instruments and Methods in Physics Research Section A: Accelerators, Spectrometers, Detectors and Associated Equipment*, vol. 377, pp. 352–6, aug 1996.

[4] T. Pantazis, J. Pantazis, A. Huber, and R. Redus, "The historical development of the thermoelectrically cooled X-ray detector and its impact on the portable and hand-held XRF industries (February 2009)," *X-Ray Spectrometry*, vol. 39, no. 2, pp. 90–7, 2010.

[5] E. Van Cleve, B. Lucas, Z. Ganlieli, E. W. Wong, P. Cortes, N. Mehta, D. Cuadra, J. Fong, S. Hansen, A. Kotowski, and C. G. Camara, "A triboelectric closed loop band system for the generation of x-rays," in *SPIE Optical Engineering + Applications* (A. M. Khounsary and C. A. MacDonald, eds.), p. 95900F, International Society for Optics and Photonics, aug 2015.

[6] S. Burgess, X. Li, M. G. Burke, G. Bertali, O. Ciuca, and X. L. Zhong, "Sub-10 nm spatial resolution for SEM-EDS using a novel EDS detector design," in *Microscopy and Microanalysis*, pp. 2–3, 2015.

[7] D. E. Newbury and N. W. M. Ritchie, "Performing elemental microanalysis with high accuracy and high precision by scanning electron microscopy/silicon drift detector energy-dispersive X-ray spectrometry (SEM/SDD-EDS)," *Journal of Materials Science*, vol. 50, pp. 493–518, nov 2015.

[8] C. Strupp, "Beryllium metal II. a review of the available toxicity data.," *The Annals of occupational hygiene*, vol. 55, pp. 43–56, jan 2011.

[9] P. Kuisma-Kursula, "Accuracy, precision and detection limits of SEM-WDS, SEM-EDS and PIXE in the multi-elemental analysis of medieval glass," *X-Ray Spectrometry*, vol. 29, pp. 111–8, jan 2000.

[10] B. K. Agarwal, *X-Ray Spectroscopy: An Introduction.* Springer-Verlag Berlin Heidelberg, 1991.

[11] J. C. Russ, *Fundamentals of Energy Dispersive X-ray Analysis.* Butterworths & Co (Publishers) Ltd, 1984.

[12] R. Jenkins, R. Manne, R. Robin, and C. Senemaud, "IUPAC - nomenclature system for x-ray spectroscopy," *X-Ray Spectrometry*, vol. 20, pp. 149–55, jun 1991.

[13] D. Poole, "4.2.1 X-ray absorption edges, characteristic X-ray lines and fluorescence yields. Kaye & Laby Online. Version 1.0 (2005)," in *Tables of Physical & Chemical Constants (16th edition 1995).*, 2005.

[14] J. H. Hubbell, P. N. Trehan, N. Singh, B. Chand, D. Mehta, M. L. Garg, R. R. Garg, S. Singh, and S. Puri, "A Review, Bibliography, and Tabulation of K, L, and Higher Atomic Shell X-Ray Fluorescence Yields," *Journal of Physical and Chemical Reference Data*, vol. 23, no. 2, pp. 339–64, 1994.

[15] M. Siegbahn, "X-ray Spectroscopy," *The Spectroscopy of X-rays*, pp. 265–76, 1925.

[16] J. A. Bearden, "X-Ray Wavelengths," *Reviews of Modern Physics*, vol. 39, pp. 78–124, jan 1967.

[17] B. Henke, E. Gullikson, and J. Davis, "X-Ray Interactions: Photoabsorption, Scattering, Transmission, and Reflection at E = 50-30,000 eV, Z = 1-92," *Atomic Data and Nuclear Data Tables*, vol. 54, pp. 181–342, jul 1993.

[18] "Information on the test material EDS-TM002 and the BAM software package -EDX Spectrometer Test - for determination of the spectrometer performance," *Federal Institute for Materials Research and Testing - Technical Note*, 2013.

[19] H. Bronk, S. Röhrs, A. Bjeoumikhov, N. Langhoff, J. Schmalz, R. Wedell, H. E. Gorny, A. Herold, and U. Waldschläger, "ArtTAX - A new mobile spectrometer for energy-dispersive micro X-ray fluorescence spectrometry on art and archaeological objects," *Fresenius' Journal of Analytical Chemistry*, vol. 371, no. 3, pp. 307–16, 2001.

[20] A. Berendes, D. Neimke, R. Schumacher, and M. Barth, "A versatile technique for the investigation of gunshot residue patterns on fabrics and other surfaces: m-XRF," *Journal of Forensic Sciences*, vol. 51, no. 5, pp. 1085–90, 2006.

[21] P. Higueras, R. Oyarzun, J. Iraizoz, S. Lorenzo, J. Esbrí, and A. Martínez-Coronado, "Low-cost geochemical surveys for environmental studies in developing countries: Testing a field portable XRF instrument under quasi-realistic conditions," *Journal of Geochemical Exploration*, vol. 113, pp. 3–12, feb 2012.

[22] J. McCarthy, J. Friel, and P. Camus, "Impact of 40 years of technology advances on EDS system performance.," *Microscopy and microanalysis : the official journal of Microscopy Society of America, Microbeam Analysis Society, Microscopical Society of Canada*, vol. 15, pp. 484–90, 2009.

[23] H. M. Mann, J. W. Haslett, and F. J. Janarek, "Lithium-Drifted p-i-n Junction Detectors," *IRE Transactions on Nuclear Science*, vol. 9, pp. 43–54, aug 1962.

[24] D. Schlosser, P. Lechner, G. Lutz, A. Niculae, H. Soltau, L. Strüder, R. Eckhardt, K. Hermenau, G. Schaller, F. Schopper, O. Jaritschin, A. Liebel, A. Simsek, C. Fiorini, and A. Longoni, "Expanding the detection efficiency of silicon drift detectors," *Nuclear Instruments and Methods in Physics Research Section A: Accelerators, Spectrometers, Detectors and Associated Equipment*, vol. 624, pp. 270–6, dec 2010.

[25] L. Bombelli, R. Quaglia, C. Fiorini, R. Alberti, and T. Frizzi, "A Multichannel Integrated Readout Circuit for High Throughput X-Ray Spectroscopy With Silicon Drift Detectors," *IEEE Transactions on Nuclear Science*, vol. 60, pp. 430–6, feb 2013.

[26] F. Scholze, H. Henneken, P. Kuschnerus, H. Rabus, M. Richter, and G. Ulm, "Determination of the electron hole pair creation energy for semiconductors from the spectral responsivity of photodiodes," *Nuclear Instruments and Methods in Physics Research Section A: Accelerators, Spectrometers, Detectors and Associated Equipment*, vol. 439, pp. 208–15, jan 2000.

[27] U. Fano, "Ionization Yield of Radiations. II. The Fluctuations of the Number of Ions," *Physical Review*, vol. 72, pp. 26–9, jul 1947.

[28] B. Lowe and R. Sareen, "A measurement of the electron hole pair creation energy and the Fano factor in silicon for 5.9 keV X-rays and their temperature dependence in the range 80 - 270 K," *Nuclear Instruments and Methods*

in Physics Research Section A: Accelerators, Spectrometers, Detectors and Associated Equipment, vol. 576, pp. 367–70, jun 2007.

[29] M. Mazziotta, "Electron - hole pair creation energy and Fano factor temperature dependence in silicon," *Nuclear Instruments and Methods in Physics Research Section A: Accelerators, Spectrometers, Detectors and Associated Equipment*, vol. 584, pp. 436–9, jan 2008.

[30] G. Fraser, A. Abbey, A. Holland, K. McCarthy, A. Owens, and A. Wells, "The X-ray energy response of silicon Part A. Theory," *Nuclear Instruments and Methods in Physics Research Section A: Accelerators, Spectrometers, Detectors and Associated Equipment*, vol. 350, pp. 368–78, oct 1994.

[31] R. Redus and A. Huber, "Figure of merit for spectrometers for EDXRF," *X-Ray Spectrometry*, vol. 41, no. 6, pp. 401–9, 2012.

[32] "VITUS Silicon Drift Detector (SDD) Modules: KETEK GmbH," *Retrieved from http://www.ketek.net/products/vitus-sdd/ (2016-03-15).*

[33] A. B. Sproul and M. A. Green, "Improved value for the silicon intrinsic carrier concentration from 275 to 375 K," *Journal of Applied Physics*, vol. 70, no. 2, pp. 846–54, 1991.

[34] E. Gatti and P. Rehak, "Semiconductor drift chamber - An application of a novel charge transport scheme," *Nuclear Instruments and Methods in Physics Research*, vol. 225, no. 3, pp. 608–14, 1984.

[35] P. Lechner, C. Fiorini, R. Hartmann, J. Kemmer, N. Krause, P. Leutenegger, A. Longoni, H. Soltau, D. Stötter, R. Stötter, L. Strüder, and U. Weber, "Silicon Drift Detectors for high count rate X-ray spectroscopy at room temperature," *Nuclear Instruments and Methods in Physics Research, Section A: Accelerators, Spectrometers, Detectors and Associated Equipment*, vol. 458, no. 1-2, pp. 281–7, 2001.

[36] P. Lechner, A. Pahlke, and H. Soltau, "Novel high-resolution silicon drift detectors," *X-Ray Spectrometry*, vol. 33, pp. 256–61, jul 2004.

[37] C. Guazzoni, "The first 25 years of silicon drift detectors: A personal view," *Nuclear Instruments and Methods in Physics Research Section A: Accelerators, Spectrometers, Detectors and Associated Equipment*, vol. 624, pp. 247–54, dec 2010.

[38] "Filter Transmission," *http://henke.lbl.gov/optical_constants/filter2.html (15.03.2016).*

[39] S. B. Riffat and X. Ma, "Improving the coefficient of performance of thermoelectric cooling systems: A review," *International Journal of Energy Research*, vol. 28, no. 9, pp. 753–68, 2004.

[40] M. Alvisi, M. Blome, M. Griepentrog, V.-D. Hodoroaba, P. Karduck, M. Mostert, M. Nacucchi, M. Procop, M. Rohde, F. Scholze, P. Statham, R. Terborg, and J.-F. Thiot, "The determination of the efficiency of energy dispersive X-ray spectrometers by a new reference material.," *Microscopy and Microanalysis*, vol. 12, no. 5, pp. 406–15, 2006.

[41] W. Bludau, A. Onton, and W. Heinke, "Temperature dependence of the band gap of silicon," *Journal of Applied Physics*, vol. 45, pp. 1846–8, oct 1974.

[42] P. Torma and H. Sipila, "Ultra-thin silicon nitride X-ray windows," *IEEE Transactions on Nuclear Science*, vol. 60, no. 2, pp. 1311–4, 2013.

[43] A. J. Stonehouse, "Physics and chemistry of beryllium," *Journal of Vacuum Science & Technology A: Vacuum, Surfaces, and Films*, vol. 4, no. 3, pp. 1163–70, 1986.

[44] M. Harker, "Corrosion Resistance of DuraBeryllium Plus X-ray Windows Part 1 - App and Tech Notes," *Moxtek*, 2014.

[45] M. W. Lund, "Current Trends in Si(Li) Detector Windows for Light Element Analysis," in *X-Ray Spectrometry in Electron Beam Instruments SE - 3* (D. Williams, J. Goldstein, and D. Newbury, eds.), pp. 21–31, Springer US, 1995.

[46] V. P. Viitanen, R. Mutikainen, S. Nenonen, and P. Partanen, "Comparison of ultrathin x-ray window designs.," *Journal of X-ray science and technology*, vol. 4, pp. 182–90, jan 1994.

[47] M. C. Roberts and E. C. Anderson, "Light Rejection Evaluation of Ultrathin Polymer EDS Windows," *Microscopy and Microanalysis*, vol. 10, no. S02, pp. 924–5, 2004.

[48] D. Brough, *Investigation of Low Stress Silicon Nitride as a Replacement Material for Beryllium in X-ray Windows.* Master thesis, Brigham Young University, 2012.

[49] X. Ying, J. Luo, P. Wang, M. Cui, Y. Zhao, G. Li, and P. Zhu, "Ultra-thin freestanding diamond window for soft X-ray optics," *Diamond and Related Materials*, vol. 12, pp. 719–22, mar 2003.

[50] X. Ying and X. Xu, "CVD diamond thin film for IR optics and X-ray optics," *Thin solid films*, vol. 368, pp. 297–9, 2000.

[51] D. K. Reinhard, T. A. Grotjohn, M. Becker, M. K. Yaran, T. Schuelke, and J. Asmussen, "Fabrication and properties of ultranano, nano, and microcrystalline diamond membranes and sheets," *Journal of Vacuum Science & Technology B: Microelectronics and Nanometer Structures*, vol. 22, no. 6, pp. 2811–7, 2004.

[52] F. Scholze and M. Procop, "Detection efficiency of energy-dispersive detectors with low-energy windows," *X-Ray Spectrometry*, vol. 34, pp. 473–6, nov 2005.

[53] "Ultra thin AP3 X-ray Windows, Datasheet, WIN-DATA-1001a, Rev E," *Moxtek*, 2016.

[54] P. T. Torma, J. Kostamo, H. Sipila, M. Mattila, P. Kostamo, E. Kostamo, H. Lipsanen, C. Laubis, F. Scholze, N. Nelms, B. Shortt, and M. Bavdaz, "Performance and properties of ultra-thin silicon nitride X-ray windows," *IEEE Transactions on Nuclear Science*, vol. 61, no. 1, pp. 695–9, 2014.

[55] J. Campbell, N. Boyd, N. Grassi, P. Bonnick, and J. Maxwell, "The Guelph PIXE software package IV," *Nuclear Instruments and Methods in Physics Research Section B: Beam Interactions with Materials and Atoms*, vol. 268, pp. 3356–63, oct 2010.

[56] "DuraBeryllium X-ray Windows Datasheet, WIN-DATA-1003, Rev C," *Moxtek*, 2016.

[57] J. Rafaelsen, T. Nylese, M. Bolorizadeh, and V. Carlino, "Windowless , Silicon Nitride window and Polymer window EDS detectors : Changes in Sensitivity and Detectable Limits," *Microscopy and Microanalysis*, vol. 21, pp. 1645–6, 2015.

[58] D. Kriebel, J. D. Brain, N. L. Sprince, and H. Kazemi, "The Pulmonary Toxicity of Beryllium," *American Review of Respiratory Disease*, vol. 137, pp. 464–73, feb 1988.

[59] M. Wick, "Chronic beryllioisis - Case 293," *https://www.flickr.com/photos/pulmonary_pathology/15528999565/in/photostream/, retrieved jan 2016.*

[60] K. S. Novoselov, A. K. Geim, S. V. Morozov, D. Jiang, Y. Zhang, S. V. Dubonos, I. V. Grigorieva, and A. A. Firsov, "Electric field effect in atomically thin carbon films.," *Science*, vol. 306, no. 5696, pp. 666–9, 2004.

[61] M. Peplow, "Graphene booms in factories but lacks a killer app.," *Nature*, vol. 522, pp. 268–9, jun 2015.

[62] F. Schwierz, "Graphene transistors: Status, prospects, and problems," *Proceedings of the IEEE*, vol. 101, pp. 1567–84, jul 2013.

[63] C. Lee, X. Wei, J. W. Kysar, and J. Hone, "Measurement of the elastic properties and intrinsic strength of monolayer graphene.," *Science*, vol. 321, pp. 385–8, jul 2008.

[64] K. S. Kim, Y. Zhao, H. Jang, S. Y. Lee, J. M. Kim, K. S. Kim, J.-H. Ahn, P. Kim, J.-Y. Choi, and B. H. Hong, "Large-scale pattern growth of graphene films for stretchable transparent electrodes.," *Nature*, vol. 457, pp. 706–10, feb 2009.

[65] G. Jo, M. Choe, S. Lee, W. Park, Y. H. Kahng, and T. Lee, "The application of graphene as electrodes in electrical and optical devices," *Nanotechnology*, vol. 23, p. 112001, mar 2012.

[66] J. S. Bunch, S. S. Verbridge, J. S. Alden, A. M. Van Der Zande, J. M. Parpia, H. G. Craighead, and P. L. McEuen, "Impermeable atomic membranes from graphene sheets," *Nano Letters*, vol. 8, pp. 2458–62, aug 2008.

[67] A. K. Geim and K. S. Novoselov, "The rise of graphene.," *Nature Materials*, vol. 6, pp. 183–91, mar 2007.

[68] J. Hone, "Graphene nanoelectromechanical systems," *Proceedings of the IEEE*, vol. 101, pp. 1766–79, jul 2013.

[69] Y.-M. Chen, S.-M. He, C.-H. Huang, C.-C. Huang, W.-P. Shih, C.-L. Chu, J. Kong, J. Li, and C. Y. Su, "Ultra-large suspended graphene as highly elastic membrane for capacitive pressure sensor," *Nanoscale*, vol. 8, pp. 3555–64, jan 2016.

[70] R. Raccichini, A. Varzi, S. Passerini, and B. Scrosati, "The role of graphene for electrochemical energy storage.," *Nature Materials*, vol. 14, no. 3, pp. 271–9, 2015.

[71] F. Yavari and N. Koratkar, "Graphene-Based Chemical Sensors.," *The journal of physical chemistry letters*, vol. 3, pp. 1746–53, jul 2012.

[72] S. Stankovich, D. A. Dikin, G. H. B. Dommett, K. M. Kohlhaas, E. J. Zimney, E. A. Stach, R. D. Piner, S. T. Nguyen, and R. S. Ruoff, "Graphene-based composite materials.," *Nature*, vol. 442, pp. 282–6, jul 2006.

[73] X. Huang, X. Qi, F. Boey, and H. Zhang, "Graphene-based composites.," *Chemical Society reviews*, vol. 41, pp. 666–86, jan 2012.

[74] R. J. Young, I. A. Kinloch, L. Gong, and K. S. Novoselov, "The mechanics of graphene nanocomposites: A review," *Composites Science and Technology*, vol. 72, no. 12, pp. 1459–76, 2012.

[75] V. Berry, "Impermeability of graphene and its applications," *Carbon*, vol. 62, pp. 1–10, oct 2013.

[76] "Graphene - The worldwide patent landscape in 2015," *UK Intellectual Property Office*, 2015.

[77] A. K. Geim, "Graphene: status and prospects.," *Science*, vol. 324, pp. 1530–4, jun 2009.

[78] D. O'Hara, "Method of making graphene sheets and applications thereof," *U.S. Patent 12,589,897, issued October 30, 2009.*

[79] C. Berger, Z. Song, T. Li, X. Li, A. Y. Ogbazghi, R. Feng, Z. Dai, A. N. Marchenkov, E. H. Conrad, P. N. First, and W. A. de Heer, "Ultrathin Epitaxial Graphite - 2D Electron Gas Properties and a Route toward Graphene-based Nanoelectronics," *The Journal of Physical Chemistry B*, vol. 108, pp. 19912–6, dec 2004.

[80] K. V. Emtsev, A. Bostwick, K. Horn, J. Jobst, G. L. Kellogg, L. Ley, J. L. McChesney, T. Ohta, S. A. Reshanov, J. Röhrl, E. Rotenberg, A. K. Schmid, D. Waldmann, H. B. Weber, and T. Seyller, "Towards wafer-size graphene layers by atmospheric pressure graphitization of silicon carbide.," *Nature Materials*, vol. 8, pp. 203–7, mar 2009.

[81] D. R. Dreyer, S. Park, C. W. Bielawski, and R. S. Ruoff, "The chemistry of graphene oxide.," *Chemical Society reviews*, vol. 39, pp. 228–40, jan 2010.

[82] Y. Hernandez, V. Nicolosi, M. Lotya, F. M. Blighe, Z. Sun, S. De, I. T. McGovern, B. Holland, M. Byrne, Y. K. Gun'Ko, J. J. Boland, P. Niraj, G. Duesberg, S. Krishnamurthy, R. Goodhue, J. Hutchison, V. Scardaci, A. C. Ferrari, and J. N. Coleman, "High-yield production of graphene by liquid-phase exfoliation of graphite.," *Nature nanotechnology*, vol. 3, pp. 563–8, sep 2008.

[83] X. Chen, L. Zhang, and S. Chen, "Large area CVD growth of graphene," *Synthetic Metals*, vol. 210, no. Part A, pp. 95–108, 2015.

[84] I. Pasternak, M. Wesolowski, I. Jozwik, M. Lukosius, G. Lupina, P. Dabrowski, J. M. Baranowski, and W. Strupinski, “Graphene growth on Ge(100)/Si(100) substrates by CVD method.,” *Scientific Reports*, vol. 6, jan 2016.

[85] X. Wang, L. Zhi, and K. Müllen, “Transparent, conductive graphene electrodes for dye-sensitized solar cells.,” *Nano Letters*, vol. 8, pp. 323–7, jan 2008.

[86] X. Li, W. Cai, J. An, S. Kim, J. Nah, D. Yang, R. Piner, A. Velamakanni, I. Jung, E. Tutuc, S. K. Banerjee, L. Colombo, and R. S. Ruoff, “Large-area synthesis of high-quality and uniform graphene films on copper foils.,” *Science*, vol. 324, pp. 1312–4, jun 2009.

[87] L. Huang, Q. Chang, G. Guo, Y. Liu, Y. Xie, T. Wang, B. Ling, and H. Yang, “Synthesis of high-quality graphene films on nickel foils by rapid thermal chemical vapor deposition,” *Carbon*, vol. 50, pp. 551–6, feb 2012.

[88] S. D. Robertson, “Graphite Formation from Low Temperature Pyrolysis of Methane over some Transition Metal Surfaces,” *Nature*, vol. 224, pp. 177–8, 1969.

[89] J.-H. Lee, E. K. Lee, W.-J. Joo, Y. Jang, B.-S. Kim, J. Y. Lim, S.-H. Choi, S. J. Ahn, J. R. Ahn, M.-H. Park, C.-W. Yang, B. L. Choi, S.-W. Hwang, and D. Whang, “Wafer-Scale Growth of Single-Crystal Monolayer Graphene on Reusable Hydrogen-Terminated Germanium.,” *Science*, vol. 344, pp. 286–9, apr 2014.

[90] A. V. Zaretski and D. J. Lipomi, “Processes for non-destructive transfer of graphene: widening the bottleneck for industrial scale production,” *Nanoscale*, no. 7, pp. 9963–9, 2015.

[91] S. P. Koenig, N. G. Boddeti, M. L. Dunn, and J. S. Bunch, “Ultrastrong adhesion of graphene membranes,” *Nature Nanotechnology*, vol. 6, pp. 543–6, sep 2011.

[92] G. Hong, Q.-H. Wu, J. Ren, and S.-T. Lee, “Mechanism of non-metal catalytic growth of graphene on silicon,” *Applied Physics Letters*, vol. 100, p. 231604, jun 2012.

[93] I. H. Son, J. Hwan Park, S. Kwon, S. Park, M. H. Rümmeli, A. Bachmatiuk, H. J. Song, J. Ku, J. W. Choi, J.-m. Choi, S.-G. Doo, and H. Chang, “Silicon carbide-free graphene growth on silicon for lithium-ion battery with high volumetric energy density,” *Nature Communications*, vol. 6, p. 7393, 2015.

[94] J. Sun, N. Lindvall, M. T. Cole, T. Wang, T. J. Booth, P. Boggild, K. B. K. Teo, J. Liu, and A. Yurgens, "Controllable chemical vapor deposition of large area uniform nanocrystalline graphene directly on silicon dioxide," *Journal of Applied Physics*, vol. 111, p. 044103, feb 2012.

[95] J. Hwang, M. Kim, D. Campbell, H. A. Alsalman, J. Y. Kwak, S. Shivaraman, A. R. Woll, A. K. Singh, R. G. Hennig, S. Gorantla, M. H. Rümmeli, and M. G. Spencer, "van der Waals Epitaxial Growth of Graphene on Sapphire by Chemical Vapor Deposition without a Metal Catalyst.," *ACS nano*, vol. 7, pp. 385–95, jan 2013.

[96] J. Sun, N. Lindvall, M. T. Cole, K. B. K. Teo, and A. Yurgens, "Large-area uniform graphene-like thin films grown by chemical vapor deposition directly on silicon nitride," *Applied Physics Letters*, vol. 98, p. 252107, jun 2011.

[97] J. Chen, Y. Guo, Y. Wen, L. Huang, Y. Xue, D. Geng, B. Wu, B. Luo, G. Yu, and Y. Liu, "Two-stage metal-catalyst-free growth of high-quality polycrystalline graphene films on silicon nitride substrates.," *Advanced Materials*, vol. 25, pp. 992–7, feb 2013.

[98] W. Yang, C. He, L. Zhang, Y. Wang, Z. Shi, M. Cheng, G. Xie, D. Wang, R. Yang, D. Shi, and G. Zhang, "Growth, characterization, and properties of nanographene.," *Small*, vol. 8, pp. 1429–35, may 2012.

[99] J. Ribeiro-Soares, M. Oliveros, C. Garin, M. David, L. Martins, C. Almeida, E. Martins-Ferreira, K. Takai, T. Enoki, R. Magalhães-Paniago, A. Malachias, A. Jorio, B. Archanjo, C. Achete, and L. Cançado, "Structural analysis of polycrystalline graphene systems by Raman spectroscopy," *Carbon*, vol. 95, pp. 646–52, 2015.

[100] A. Bianco, H.-M. Cheng, T. Enoki, Y. Gogotsi, R. H. Hurt, N. Koratkar, T. Kyotani, M. Monthioux, C. R. Park, J. M. Tascon, and J. Zhang, "All in the graphene family - A recommended nomenclature for two-dimensional carbon materials," *Carbon*, vol. 65, pp. 1–6, dec 2013.

[101] H. Medina, Y.-C. Lin, C. Jin, C.-C. Lu, C.-H. Yeh, K.-P. Huang, K. Suenaga, J. Robertson, and P.-W. Chiu, "Metal-Free Growth of Nanographene on Silicon Oxides for Transparent Conducting Applications," *Advanced Functional Materials*, vol. 22, pp. 2123–8, may 2012.

[102] T. Zhang, X. Li, S. Kadkhodaei, and H. Gao, "Flaw insensitive fracture in nanocrystalline graphene.," *Nano Letters*, vol. 12, pp. 4605–10, sep 2012.

[103] P. Zhang, L. Ma, F. Fan, Z. Zeng, C. Peng, P. E. Loya, Z. Liu, Y. Gong, J. Zhang, X. Zhang, P. M. Ajayan, T. Zhu, and J. Lou, "Fracture toughness of graphene," *Nature Communications*, vol. 5, pp. 1–7, 2014.

[104] S. M. Wiederhorn, "Brittle Fracture and Toughening Mechanisms in Ceramics," *Annual Review of Materials Science*, vol. 14, pp. 373–403, 1984.

[105] S. Chen, L. Brown, M. Levendorf, W. Cai, S.-Y. Ju, J. Edgeworth, X. Li, C. W. Magnuson, A. Velamakanni, R. D. Piner, J. Kang, J. Park, and R. S. Ruoff, "Oxidation resistance of graphene-coated Cu and Cu/Ni alloy.," *ACS nano*, vol. 5, pp. 1321–7, feb 2011.

[106] M. Schriver, W. Regan, W. J. Gannett, A. M. Zaniewski, M. F. Crommie, and A. Zettl, "Graphene as a long-term metal oxidation barrier: worse than nothing.," *ACS nano*, vol. 7, pp. 5763–8, jul 2013.

[107] G. I. Dovbeshko, V. R. Romanyuk, D. V. Pidgirnyi, V. V. Cherepanov, E. O. Andreev, V. M. Levin, P. P. Kuzhir, T. Kaplas, and Y. P. Svirko, "Optical Properties of Pyrolytic Carbon Films Versus Graphite and Graphene.," *Nanoscale research letters*, vol. 10, pp. 1–6, dec 2015.

[108] A. C. Thompson, J. Kirz, D. T. Attwood, E. M. Gullikson, M. R. Howells, J. B. Kortright, Y. Liu, A. L. Robinson, J. H. Underwood, K.-J. Kim, I. Lindau, P. Pianetta, H. Winick, G. P. Williams, and J. H. Scofield, *X-ray Data Booklet.* 2009.

[109] J. R. Davis, ed., *Tensile Testing, 2nd Edition.* ASM International, 2004.

[110] C. Bathias and A. Pineau, *Fatigue of Materials and Structures.* John Wiley & Sons, 2013.

[111] A. Nerken, "History of helium leak detection," *Journal of Vacuum Science & Technology A: Vacuum, Surfaces, and Films*, vol. 9, pp. 2036–8, may 1991.

[112] M. Norton, A. G. Amillo, and R. Galleano, "Comparison of solar spectral irradiance measurements using the average photon energy parameter," *Solar Energy*, vol. 120, pp. 337–44, oct 2015.

[113] J. Dohan and W. Masschelein, "The Photochemical Generation of Ozone : Present State-of-the-Art," *Ozone: Science & Engineering*, vol. 9, pp. 315–34, sep 1987.

[114] S. Y. Zhou, Ç. Ö. Girit, a. Scholl, C. J. Jozwiak, D. a. Siegel, P. Yu, J. T. Robinson, F. Wang, a. Zettl, and a. Lanzara, "Instability of two-dimensional graphene: Breaking sp2 bonds with soft x rays," *Physical Review B - Condensed Matter and Materials Physics*, vol. 80, no. 12, pp. 1–4, 2009.

[115] F. Kreupl, D. E. Perea, Y. Jung, J. B. Hannon, M. Reed, W. Sinke, and S. T. Picraux, *Carbon-based materials as key-enabler for - More Than Moore -*. Cambridge, U.K., Cambridge Univ. Press, 2011.

[116] G. J. Simpson, D. L. Sedin, and K. L. Rowlen, "Surface Roughness by Contact versus Tapping Mode Atomic Force Microscopy," *Langmuir*, vol. 15, pp. 1429–34, feb 1999.

[117] C. Y. Poon and B. Bhushan, "Comparison of surface roughness measurements by stylus profiler, AFM and non-contact optical profiler," *Wear*, vol. 190, pp. 76–88, nov 1995.

[118] G. Binnig and C. F. Quate, "Atomic Force Microscope," *Physical Review Letters*, vol. 56, pp. 930–3, mar 1986.

[119] T. Ando, "High-speed atomic force microscopy coming of age.," *Nanotechnology*, vol. 23, p. 062001, feb 2012.

[120] E. Gadelmawla, M. Koura, T. Maksoud, I. Elewa, and H. Soliman, "Roughness parameters," *Journal of Materials Processing Technology*, vol. 123, pp. 133–45, apr 2002.

[121] M. S. Dresselhaus, A. Jorio, M. Hofmann, G. Dresselhaus, and R. Saito, "Perspectives on Carbon Nanotubes and Graphene Raman Spectroscopy," *Nano Letters*, vol. 10, no. 3, pp. 751–8, 2010.

[122] A. C. Ferrari and J. Robertson, "Interpretation of Raman spectra of disordered and amorphous carbon," *Physical Review B*, vol. 61, pp. 14095–107, may 2000.

[123] P. Mallet-Ladeira, P. Puech, C. Toulouse, M. Cazayous, N. Ratel-Ramond, P. Weisbecker, G. L. Vignoles, and M. Monthioux, "A Raman study to obtain crystallite size of carbon materials: A better alternative to the Tuinstra - Koenig law," *Carbon*, vol. 80, pp. 629–39, dec 2014.

[124] M. S. Dresselhaus, G. Dresselhaus, R. Saito, and A. Jorio, "Raman spectroscopy of carbon nanotubes," *Physics Reports*, vol. 409, no. 2, pp. 47–99, 2005.

[125] A. C. Ferrari and D. M. Basko, "Raman spectroscopy as a versatile tool for studying the properties of graphene.," *Nature nanotechnology*, vol. 8, pp. 235–46, apr 2013.

[126] C. Thomsen and S. Reich, "Double Resonant Raman Scattering in Graphite," *Physical Review Letters*, vol. 85, no. 24, pp. 5214–7, 2000.

[127] A. C. Ferrari, “Raman spectroscopy of graphene and graphite: Disorder, electronâ€“phonon coupling, doping and nonadiabatic effects,” *Solid State Communications*, vol. 143, pp. 47–57, jul 2007.

[128] A. Cuesta, P. Dhamelincourt, J. Laureyns, A. Martínez-Alonso, and J. Tascón, “Raman microprobe studies on carbon materials,” *Carbon*, vol. 32, no. 8, pp. 1523–32, 1994.

[129] C. Castiglioni, C. Mapelli, F. Negri, and G. Zerbi, “Origin of the D line in the Raman spectrum of graphite: A study based on Raman frequencies and intensities of polycyclic aromatic hydrocarbon molecules,” *The Journal of Chemical Physics*, vol. 114, pp. 963–74, jan 2001.

[130] M. A. Pimenta, G. Dresselhaus, M. S. Dresselhaus, L. G. Cançado, A. Jorio, and R. Saito, “Studying disorder in graphite-based systems by Raman spectroscopy.,” *Physical Chemistry Chemical Physics*, vol. 9, pp. 1276–91, mar 2007.

[131] F. Tuinstra and J. L. Koenig, “Raman Spectrum of Graphite,” *The Journal of Chemical Physics*, vol. 53, pp. 1126–30, sep 1970.

[132] M. J. Matthews, M. A. Pimenta, G. Dresselhaus, M. S. Dresselhaus, and M. Endo, “Origin of dispersive effects of the Raman D band in carbon materials,” *Physical Review B*, vol. 59, pp. R6585–R8, mar 1999.

[133] G. A. Zickler, B. Smarsly, N. Gierlinger, H. Peterlik, and O. Paris, “A reconsideration of the relationship between the crystallite size La of carbons determined by X-ray diffraction and Raman spectroscopy,” *Carbon*, vol. 44, pp. 3239–46, dec 2006.

[134] D. Xiaoli and S. Katuo, “High-accuracy absolute distance measurement by means of wavelength scanning heterodyne interferometry,” *Measurement Science and Technology*, vol. 9, pp. 1031–5, jul 1998.

[135] U. Schnell, E. Zimmermann, and R. Dandliker, “Absolute distance measurement with synchronously sampled white-light channelled spectrum interferometry,” *Pure and Applied Optics: Journal of the European Optical Society Part A*, vol. 4, pp. 643–51, sep 1995.

[136] J. Schmit, “3D Interferometric Microscope for Topography and Real Color Imaging in Industrial Applications,” in *2014 International Symposium on Optomechatronic Technologies*, 2014.

[137] R. W. Chabay and B. A. Sherwood, *Matter and Interactions, 3rd Edition.* John Wiley & Sons, 2011.

[138] D. Armani, C. Liu, and N. Aluru, "Re-configurable fluid circuits by PDMS elastomer micromachining," *IEEE International MEMS '99 Twelfth IEEE International Conference on Micro Electro Mechanical Systems*, pp. 222–7, 1999.

[139] O. L. Blakslee, D. G. Proctor, E. J. Seldin, G. B. Spence, and T. Weng, "Elastic Constants of Compression of Annealed Pyrolytic Graphite," *Journal of Applied Physics*, vol. 41, no. 8, pp. 3373–82, 1970.

[140] D. Metten, F. Federspiel, M. Romeo, and S. Berciaud, "All-Optical Blister Test of Suspended Graphene Using Micro-Raman Spectroscopy," *Physical Review Applied*, vol. 054008, pp. 1–11, 2014.

[141] L. B. Freund and S. Suresh, *Thin Film Materials: Stress, Defect Formation and Surface Evolution.* Cambridge University Press, 2008.

[142] A. K. Varshneya, "Chemical Strengthening of Glass: Lessons Learned and Yet To Be Learned," *International Journal of Applied Glass Science*, vol. 1, pp. 131–42, mar 2010.

[143] C. A. Taylor, M. F. Wayne, and W. K. S. Chiu, "Residual stress measurement in thin carbon films by Raman spectroscopy and nanoindentation," *Thin Solid Films*, vol. 429, pp. 190–200, apr 2003.

[144] J. Yang, H. Kahn, A. Q. He, S. M. Phillips, and A. H. Heuer, "New technique for producing large-area as-deposited zero-stress LPCVD polysilicon films: the MultiPoly process," *Journal of Microelectromechanical Systems*, vol. 9, no. 4, pp. 485–94, 2000.

[145] V. Ziebart, O. Paul, and H. Baltes, "Strongly buckled square micromachined membranes," *Journal of Microelectromechanical Systems*, vol. 8, no. 4, pp. 423–32, 1999.

[146] Y. Toivola, J. Thurn, R. F. Cook, G. Cibuzar, and K. Roberts, "Influence of deposition conditions on mechanical properties of low-pressure chemical vapor deposited low-stress silicon nitride films," *Journal of Applied Physics*, vol. 94, pp. 6915–22, oct 2003.

[147] J. S. Mitchell, C. A. Zorman, T. Kicher, S. Roy, and M. Mehregany, "Examination of Bulge Test for Determining Residual Stress, Young's Modulus, and Poisson's Ratio of 3C-SiC Thin Films," *Journal of Aerospace Engineering*, vol. 16, no. 2, pp. 46–54, 2003.

[148] A. Catlin and W. P. Walker, "Mechanical Properties of Thin Single-Crystal Gold Films," *Journal of Applied Physics*, vol. 31, no. 12, p. 2135, 1960.

[149] T. Kramer and O. Paul, "Surface Micromachined Ring Test Structures to Determine Mechanical Properties of Compressive Thin Films," *Sensors & Actuators A-Physical*, vol. 92, pp. 292–8, 2001.

[150] M. K. Small and W. Nix, "Analysis of the accuracy of the bulge test in determining the mechanical properties of thin films," *Journal of Materials Research*, vol. 7, no. 06, pp. 1553–63, 1992.

[151] J. Pan, P. Lin, F. Maseeh, and S. Senturia, "Verification of FEM analysis of load-deflection methods for measuring mechanical properties of thin films," *IEEE 4th Technical Digest on Solid-State Sensor and Actuator Workshop*, 1990.

[152] J. Vlassak and W. Nix, "A new bulge test technique for the determination of Young's modulus and Poisson's ratio of thin films," *Journal of Materials Research*, vol. 7, no. August, pp. 3242–9, 1992.

[153] Y. Xiang, X. Chen, and J. J. Vlassak, "Plane-strain bulge test for thin films," *Journal of Materials Research*, vol. 20, no. 09, pp. 2360–70, 2005.

[154] T. Sharda, T. Soga, T. Jimbo, and M. Umeno, "Highly stressed carbon film coatings on silicon: Potential applications," *Applied Physics Letters*, vol. 80, no. 16, pp. 2880–2, 2002.

[155] R. L. Edwards, G. Coles, and W. N. Sharpe, "Comparison of tensile and bulge tests for thin-film silicon nitride," *Experimental Mechanics*, vol. 44, pp. 49–54, feb 2004.

[156] C. Cooper, R. Young, and M. Halsall, "Investigation into the deformation of carbon nanotubes and their composites through the use of Raman spectroscopy," *Composites Part A: Applied Science and Manufacturing*, vol. 32, pp. 401–11, mar 2001.

[157] J.-U. Lee, D. Yoon, and H. Cheong, "Estimation of Young's modulus of graphene by Raman spectroscopy.," *Nano letters*, vol. 12, pp. 4444–8, sep 2012.

[158] T. M. G. Mohiuddin, a. Lombardo, R. R. Nair, a. Bonetti, G. Savini, R. Jalil, N. Bonini, D. M. Basko, C. Galiotis, N. Marzari, K. S. Novoselov, a. K. Geim, and a. C. Ferrari, "Uniaxial strain in graphene by Raman spectroscopy: G peak splitting, Grüneisen parameters, and sample orientation," *Physical Review B - Condensed Matter and Materials Physics*, vol. 79, no. 20, pp. 1–8, 2009.

[159] Y. C. Cheng, Z. Y. Zhu, G. S. Huang, and U. Schwingenschlögl, "Grüneisen parameter of the G mode of strained monolayer graphene," *Physical Review B - Condensed Matter and Materials Physics*, vol. 83, no. 11, pp. 1–5, 2011.

[160] S. Tamulevičius, "Stress and strain in the vacuum deposited thin films," *Vacuum*, vol. 51, pp. 127–39, oct 1998.

[161] G. G. Stoney, "The Tension of Metallic Films Deposited by Electrolysis," *Proceedings of the Royal Society of London. Series A, Containing Papers of a Mathematical and Physical Character*, vol. 82, no. 553, pp. 172–5, 1909.

[162] C. A. Klein, "How accurate are Stoney's equation and recent modifications," *Journal of Applied Physics*, vol. 88, pp. 5487–9, nov 2000.

[163] W. A. Brantley, "Calculated elastic constants for stress problems associated with semiconductor devices," *Journal of Applied Physics*, vol. 44, no. 1, pp. 534–5, 1973.

[164] F. M. Smits, "Measurements of Sheet Resistivity with the Four-Point Probe," *Bell System Technical Journal*, vol. 37, no. 3, pp. 711–8, 1958.

[165] N. McEvoy, N. Peltekis, S. Kumar, E. Rezvani, H. Nolan, G. P. Keeley, W. J. Blau, and G. S. Duesberg, "Synthesis and analysis of thin conducting pyrolytic carbon films," *Carbon*, vol. 50, pp. 1216–26, mar 2012.

[166] J. Sun, M. T. Cole, N. Lindvall, K. B. K. Teo, and A. Yurgens, "Noncatalytic chemical vapor deposition of graphene on high-temperature substrates for transparent electrodes," *Applied Physics Letters*, vol. 100, p. 022102, jan 2012.

[167] T. Kaplas and Y. Svirko, "Direct deposition of semitransparent conducting pyrolytic carbon films," *Journal of Nanophotonics*, vol. 6, no. 1, p. 061703, 2012.

[168] G. S. Duesberg, H.-Y. Kim, K. Lee, N. McEvoy, S. Winters, and C. Yim, "Investigation of carbon-silicon schottky diodes and their use as chemical sensors," *Solid-State Device Research Conference (ESSDERC), 2013 Proceedings of the European*, pp. 85–90, 2013.

[169] A. P. Graham, G. Schindler, G. S. Duesberg, T. Lutz, and W. Weber, "An investigation of the electrical properties of pyrolytic carbon in reduced dimensions: Vias and wires," *Journal of Applied Physics*, vol. 107, no. 11, p. 114316, 2010.

[170] J. Pappis and S. L. Blum, "Properties of Pyrolytic Graphite," *Journal of the American Ceramic Society*, vol. 44, pp. 592–7, dec 1961.

[171] M. L. Kaplan, P. H. Schmidt, C.-H. Chen, and W. M. Walsh, "Carbon films with relatively high conductivity," *Applied Physics Letters*, vol. 36, no. 10, pp. 867–9, 1980.

[172] J. Isberg, "High Carrier Mobility in Single-Crystal Plasma-Deposited Diamond," *Science*, vol. 297, no. 5587, pp. 1670–2, 2002.

[173] M. Inagaki and F. Kang, *Materials Science and Engineering of Carbon: Fundamentals (Second Edition).* Elsevier, 2014.

[174] D. R. Mckenzie, R. C. Mcphedran, N. Savvides, and L. C. Botten, "Properties and structure of amorphous hydrogenated carbon films," *Philosophical Magazine Part B*, vol. 48, pp. 341–64, dec 1983.

[175] H. Li, B. W. Sheldon, A. Kothari, Z. Ban, and B. L. Walden, "Stress evolution in nanocrystalline diamond films produced by chemical vapor deposition," *Journal of Applied Physics*, vol. 100, no. 9, p. 094309, 2006.

[176] H. D. Espinosa, B. Peng, N. Moldovan, T. A. Friedmann, X. Xiao, D. C. Mancini, O. Auciello, J. Carlisle, C. A. Zorman, and M. Merhegany, "Elasticity, strength, and toughness of single crystal silicon carbide, ultrananocrystalline diamond, and hydrogen-free tetrahedral amorphous carbon," *Applied Physics Letters*, vol. 89, no. 7, p. 073111, 2006.

[177] J. Robertson, "Diamond-like amorphous carbon," *Materials Science and Engineering: R: Reports*, vol. 37, pp. 129–281, may 2002.

[178] M. Guellali, R. Oberacker, and M. Hoffmann, "Influence of heat treatment on microstructure and properties of highly textured pyrocarbons deposited during CVD at about 1100 C and above 2000 C," *Composites Science and Technology*, vol. 68, pp. 1122–30, apr 2008.

[179] W. A. Bone and H. F. Coward, "CXVII. -The thermal decomposition of hydrocarbons. Part I. [Methane, ethane, ethylene, and acetylene.]," *J. Chem. Soc., Trans.*, vol. 93, pp. 1197–225, jan 1908.

[180] L. Huang, X. Cui, B. White, and S. P. Oâ€˜Brien, "Long and Oriented Single-Walled Carbon Nanotubes Grown by Ethanol Chemical Vapor Deposition," *The Journal of Physical Chemistry B*, vol. 108, pp. 16451–6, oct 2004.

[181] C. Guéret, M. Daroux, and F. Billaud, "Methane pyrolysis: thermodynamics," *Chemical Engineering Science*, vol. 52, no. 5, pp. 815–27, 1997.

[182] A. Becker and K. Hüttinger, “Chemistry and kinetics of chemical vapor deposition of pyrocarbon - II pyrocarbon deposition from ethylene, acetylene and 1,3-butadiene in the low temperature regime,” *Carbon*, vol. 36, pp. 177–99, jan 1998.

[183] Z. J. Hu and K. J. Hüttinger, “Mechanisms of carbon deposition - a kinetic approach,” *Carbon*, vol. 40, pp. 624–8, apr 2002.

[184] K. Norinaga, O. Deutschmann, and K. J. Hüttinger, “Analysis of gas phase compounds in chemical vapor deposition of carbon from light hydrocarbons,” *Carbon*, vol. 44, no. 9, pp. 1790–800, 2006.

[185] Z. J. Hu, W. G. Zhang, K. J. Hüttinger, B. Reznik, and D. Gerthsen, “Influence of pressure, temperature and surface area/volume ratio on the texture of pyrolytic carbon deposited from methane,” *Carbon*, vol. 41, no. 4, pp. 749–58, 2003.

[186] V. De Pauw, S. Kalhöfer, and D. Gerthsen, “Influence of the deposition parameters on the texture of pyrolytic carbon layers deposited on planar substrates,” *Carbon*, vol. 42, pp. 279–86, jan 2004.

[187] M. Kumagai, N. Uchiyama, E. Ohmura, R. Sugiura, K. Atsumi, and K. Fukumitsu, “Advanced dicing technology for semiconductor wafer - Stealth Dicing,” in *2006 IEEE International Symposium on Semiconductor Manufacturing*, pp. 215–8, sep 2006.

[188] S. S. Iyer, M. Arienzo, and E. de Fresart, “Low-temperature silicon cleaning via hydrogen passivation and conditions for epitaxy,” *Applied Physics Letters*, vol. 57, p. 893, aug 1990.

[189] M. Morita, T. Ohmi, E. Hasegawa, M. Kawakami, and M. Ohwada, “Growth of native oxide on a silicon surface,” *Journal of Applied Physics*, vol. 68, p. 1272, aug 1990.

[190] V. De Pauw, A. Collin, W. Send, J. Hawecker, D. Gerthsen, A. Pfrang, and T. Schimmel, “Deposition rates during the early stages of pyrolytic carbon deposition in a hot-wall reactor and the development of texture,” *Carbon*, vol. 44, pp. 3091–101, nov 2006.

[191] H. Richter and J. Howard, “Formation of polycyclic aromatic hydrocarbons and their growth to soot - a review of chemical reaction pathways,” *Progress in Energy and Combustion Science*, vol. 26, pp. 565–608, aug 2000.

[192] J. Bokros, “The structure of pyrolytic carbon deposited in a fluidized bed,” *Carbon*, vol. 3, pp. 17–29, jul 1965.

[193] S. Oh and J.-Y. Lee, "A study on the formation of soot in pyrolytic carbon deposited in a tumbling bed and its effects on mechanical properties," *Carbon*, vol. 24, no. 4, pp. 411–5, 1986.

[194] M. C. Ozturk, F. Y. Sorrell, J. J. Wortman, F. S. Johnson, and D. T. Grider, "Manufacturability issues in rapid thermal chemical vapor deposition," *IEEE Transactions on Semiconductor Manufacturing*, vol. 4, pp. 155–65, may 1991.

[195] Y. Nishi and R. Doering, eds., *Handbook of Semiconductor Manufacturing Technology, Second Edition.* Boca Raton: CRC Press, Taylor & Francis Group, 2007.

[196] J.-P. Zöllner, G. Eichhorn, V. Cimalla, J. Bozmarov, P. Zaumseil, and H. Kürschner, "Slip generation during rapid thermal processing," *Physica Status Solidi (a)*, vol. 156, pp. 63–70, jul 1996.

[197] B.-J. Cho and C.-K. Kim, "Elimination of slips on silicon wafer edge in rapid thermal process by using a ring oxide," *Journal of Applied Physics*, vol. 67, no. 12, p. 7583, 1990.

[198] R. Kakoschke, E. Bussmann, and H. Föll, "The appearance of spatially nonuniform temperature distributions during rapid thermal processing," *Applied Physics A*, vol. 52, no. 1, pp. 52–9, 1991.

[199] W. S. Yoo, T. Fukada, I. Yokoyama, K. Kang, and N. Takahashi, "Thermal Behavior of Large-Diameter Silicon Wafers during High-Temperature Rapid Thermal Processing in Single Wafer Furnace," *Japanese Journal of Applied Physics*, vol. 41, pp. 4442–9, jul 2002.

[200] P.-O. Logerais, O. Riou, F. Delaleux, J.-F. Durastanti, and A. Bouteville, "Improvement of temperature homogeneity of a silicon wafer heated in a rapid thermal system (RTP: Rapid Thermal Process) by a filtering window," *Applied Thermal Engineering*, vol. 77, pp. 76–89, feb 2015.

[201] R. Gyurcsik, T. Riley, and F. Sorrell, "A model for rapid thermal processing: achieving uniformity through lamp control," *IEEE Transactions on Semiconductor Manufacturing*, vol. 4, no. 1, pp. 9–13, 1991.

[202] A. Wieber, J. Guzman, and E. Wolf, "An STM study of phosphoric acid inhibition of the oxidation of HOPG and carbon catalyzed by alkali salts," *Carbon*, vol. 44, pp. 2069–79, aug 2006.

[203] "OSRAM XERADEX SEMI Applications, Datasheet, ENGR_BLTN29," *Osram Sylvania*, 2004.

[204] X. Lu, H. Huang, N. Nemchuk, and R. S. Ruoff, "Patterning of highly oriented pyrolytic graphite by oxygen plasma etching," *Applied Physics Letters*, vol. 75, p. 193, jul 1999.

[205] G. T. A. Kovacs, N. I. Maluf, and K. E. Petersen, "Bulk micromachining of silicon," *Proceedings of the IEEE*, vol. 86, no. 8, pp. 1536–51, 1998.

[206] P. Pal and S. S. Singh, "A New Model for the Etching Characteristics of Corners Formed by Si {111} Planes on Si {110} Wafer Surface," *Engineering*, vol. 5, pp. 1–8, 2013.

[207] I. Zubel and M. Kramkowska, "The effect of isopropyl alcohol on etching rate and roughness of (1 0 0) Si surface etched in KOH and TMAH solutions," *Sensors and Actuators A: Physical*, vol. 93, pp. 138–47, sep 2001.

[208] I. Barycka and I. Zubel, "Silicon anisotropic etching in KOH-isopropanol etchant," *Sensors and Actuators A: Physical*, vol. 48, pp. 229–38, may 1995.

[209] I. Zubel and M. Kramkowska, "The effect of alcohol additives on etching characteristics in KOH solutions," *Sensors and Actuators A: Physical*, vol. 101, pp. 255–61, oct 2002.

[210] I. Zubel and M. Kramkowska, "Etch rates and morphology of silicon (h k l) surfaces etched in KOH and KOH saturated with isopropanol solutions," *Sensors and Actuators A: Physical*, vol. 115, pp. 549–56, sep 2004.

[211] D. L. Kendall, "Vertical Etching of Silicon at very High Aspect Ratios," *Annual Review of Materials Science*, vol. 9, pp. 373–403, aug 1979.

[212] B. Wu, A. Kumar, and S. Pamarthy, "High aspect ratio silicon etch: A review," *Journal of Applied Physics*, vol. 108, p. 051101, sep 2010.

[213] R. K. Singh, D. R. Gilbert, J. Fitz-Gerald, S. Harkness, and D. G. Lee, "Engineered Interfaces for Adherent Diamond Coatings on Large Thermal-Expansion Coefficient Mismatched Substrates," *Science*, vol. 272, pp. 396–8, apr 1996.

[214] J.-h. Jeong, S.-Y. Lee, W.-S. Lee, Y.-J. Baik, and D. Kwon, "Mechanical analysis for crack-free release of chemical-vapor-deposited diamond wafers," *Diamond and Related Materials*, vol. 11, pp. 1597–605, aug 2002.

[215] W. W. Tyler and A. C. Wilson, "Thermal Conductivity, Electrical Resistivity, and Thermoelectric Power of Graphite," *Physical Review*, vol. 89, pp. 870–5, feb 1953.

[216] Y. Xiang, T. Tsui, J. Vlassak, and A. McKerrow, "Measuring the elastic modulus and ultimate strength of low-k dielectric materials by means of the bulge test," *Proceedings of the IEEE 2004 International Interconnect Technology Conference (IEEE Cat. No.04TH8729)*, pp. 1–3, 2004.

[217] E. López-Honorato, P. J. Meadows, P. Xiao, G. Marsh, and T. J. Abram, "Structure and mechanical properties of pyrolytic carbon produced by fluidized bed chemical vapor deposition," *Nuclear Engineering and Design*, vol. 238, no. 11, pp. 3121–8, 2008.

[218] P. Törmä, H. Sipilä, T. Koskinen, and M. Mattila, "Technology development for soft X-ray spectroscopy," *Spectrochimica Acta Part B: Atomic Spectroscopy*, vol. 119, pp. 36–40, may 2016.

[219] A. Pahlke, R. Fojt, and N. Miyakawa, "X-Ray Radiation Passage Window for a Radiation Detector," *U.S. Patent 13 963 928*, 2012.

Danksagung

Die vorliegende Arbeit wurde finanziell unterstützt durch das Bayerisches Staatsministerium für Wirtschaft und Medien, Energie und Technologie im Rahmen des Zentralen Innovationsprogramm Mittelstand (ZIM) unter der Projektnummer MST-1210-0006/BAY 177/001.

Ich möchte diese Gelegenheit nutzen um mich bei meinem Doktorvater Prof. Franz Kreupl, nicht nur für die organisatorische, sondern vor allem für die fachliche Betreuung zu bedanken und für die Möglichkeit von seiner langjährigen Erfahrung im Bereich der Halbleitertechnologie zu profitieren.

Des Weiteren geht besonderer Dank an Natsuki Miyakawa für unsere enge Zusammenarbeit im Laufe des Projekts. Insgesamt möchte ich mich ausdrücklich für die hervorragende Zusammenarbeit mit der Firma Ketek im Allgemeinen und bei Silvia Wallner, Reinhard Fojt und Andreas Pahlke im Speziellen bedanken. Vielen Dank für eure Unterstützung und die unbürokratische Herangehensweise. Ich wünsche euch weiterhin viel Erfolg, insbesondere mit dem Projekt Graphenster!
Ein großes Dankeschön geht ebenfalls an Prof. Doris Schmitt-Landsiedel und den Rest der wissenschaftlichen Mitarbeitern am LTE für die angenehme Arbeitsatmosphäre, sowie insbesondere an Silke Boche für das geduldige Warten auf die Teflonhalter und die hervorragende Unterstützung im Reinraumlabor, an Markus Becherer und Werner Kraus für ihre wertvolle Unterstützung dank ihrer langjährigen Erfahrung bezüglich der verwendeten Anlagen, Wolfgang Pielock und Karl Demmel für die allzeitige Hilfsbereitschaft und passgenaue Anfertigung jeglicher Sonderbauteile sowie Rainer Emling und Christoph Klösters für die Instandhaltung und Unterstützung bei allerlei technischen Problemen. Selbstverständlich gilt Frau Cutrupia und Frau Giunta ein besonderes Dankeschön für die Unterstützung durch das Sekretariat. Vielen Dank an Lukas Holzbauer für die hervorragende Arbeit und Unterstützung im Verlauf dieser Promotion, ich hoffe dass die entwickelten Messsysteme noch lange im Einsatz bleiben!

Zu guter Letzt möchte ich mich bei meinen Kollegen Max Stelzer, Stefan Kapser und Mohanad Zaki bedanken, ohne euch wäre die Promotion nicht möglich gewesen, vielen Dank für die angenehme Arbeitsatmosphäre und allzeitige Hilfsbereitschaft!

Erklärung:

Ich versichere, dass ich die Arbeit ohne fremde Hilfe und ohne Benutzung anderer als der von mir angegebenen Quellen angefertigt habe und dass die Arbeit in gleicher oder ähnlicher Form noch keiner Prüfungsbehörde vorgelegen hat und von dieser als Teil einer Prüfungsleistung angenommen wurde.

Alle Ausführungen, die wörtlich oder sinngemäß übernommen wurden, sind als solche gekennzeichnet.

München, den